Locally measured quasi-elastic deformation properties of geomaterials under torsional shear and triaxial loadings

ねじり・三軸載荷条件下における地盤材料の局所計測による弾性的変形特性

by

Laddu Indika Nalin De Silva

A thesis submitted in partial fulfillment of the requirements

for the degree of

Master of Engineering

Signature	Date	Seal
Advisor:		
Co-Advisor:		

Department of Civil Engineering
University of Tokyo
Tokyo, Japan
September, 2004

ABSTRACT

Quasi-elastic and global deformation properties of Toyoura sand and Hime gravel were thoroughly investigated using the recently developed high capacity medium sized hollow cylinder apparatus. A modified version of Pin-typed Local Deformation Transducer (PLDT) was introduced to evaluate local deformation properties in hollow cylinder specimens.

A series of drained triaxial and torsional tests were conducted on both Toyoura sand and Hime gravel specimens at different densities using the modified version of PLDT system as the local strain measurement technique. Stress paths include isotropic consolidation followed by triaxial compression with small vertical and torsional cyclic loading at different stress levels. From the results, it was confirmed that the modified version of PLDT system could be successfully used to evaluate quasi-elastic deformation properties in hollow cylinder specimens.

Locally and externally measured Young's modulus of both Toyoura sand and Hime gravel shows almost similar results with an average difference of 2 %, while locally measured shear modulus of Toyoura is on average 15 % less than externally measured one. In contrast, there was no significant difference observed in locally and externally measured shear moduli of Hime gravel. It seems that effects of end restraint on the Young's modulus was small compared to shear modulus.

Results from both local and external transducers show an increasing trend of Young's and shear moduli with the density at the same stress level. The applicability of different void ratio functions proposed in the literature for the comparison of Young's and shear moduli at different densities was checked. It was confirmed that the void ratio function proposed by Hardin and Richart (1963) for granular materials is the most appropriate for both Toyoura sand and Hime gravel.

It was confirmed that Young's and shear moduli normalized by void ratio function *f(e)* can be expressed as functions of $\sigma'_z{}^m$ and $(\sigma'_z * \sigma'_\theta)^{0.5n}$, respectively, where *m* and *n* are parameters regarding stress state dependency. Both local and external measurements give similar *m* and *n* values for all the tests of Toyoura sand and Hime gravel, respectively. A

sudden degradation of shear modulus during triaxial compression at principal stress ratios greater than three was observed in Toyoura sand, while that of Hime gravel shows a gradual degradation after principal stress ratios become greater than three. Young's modulus values show almost no degradation. This behavior was observed in both local and external measurements giving evidences of damage to the soil structure at large principal stress ratios.

One test on Toyoura sand was conducted to investigate the effects of shear stress level on Young's and shear moduli of Toyoura sand. It was observed that there was a little effect of shear stress level on Young's and shear moduli until the principal stress ratio greater than 2.2. After that a gradual degradation of both Young's and shear moduli was observed, giving evidences of possible damage to the soil structure due to large shear stress.

Two different pluviation techniques were adopted in preparing the sand specimens to investigate the effects of different pluviation techniques on global behavior of sand. It was confirmed that the specimens prepared by pluviating sand in alternative clock-wise and counter clock-wise directions show a significantly large circumferential strain (ε_θ) compared to specimens prepared by pluviating sand in radial direction. In which, sand particles were pluviated predominantly and repeatedly in the radial direction, while traveling a pluviator slowly in the circumferential direction. The traveling of sand from nozzle along the circumferential direction was reversed when each cycle had been completed. This suggests that the uniformity of specimens is higher when prepared by pluviating sand in radial direction. But still a significant difference between ε_θ and ε_z can be observed in Toyoura sand specimens even though they were prepared by pluviating sand in radial direction. On the other hand, Hime gravel specimens, although they were prepared by pluviating gravel in alternative clock-wise and counter clock-wise directions, show almost similar ε_θ and ε_z. This may be because the shape of Hime gravel is sub-round. Therefore the orientation of the particle is not important and hence more uniform specimen could be obtained. However, more verification is necessary to conclude this.

In order to understand the possible reasons for the difference in locally and externally measured shear modulus of Toyoura sand, a simple model of the hollow cylinder specimen was created and a 3-D elastic FEM analysis was performed by subjecting the model into vertical and torsional displacements. Analysis was performed in two cases: a model without

considering the effects of the blades on the top cap and pedestal and a model with the blades. The distribution of vertical and shear stresses along the model specimen obtained from the results, and manual evaluation of local and external strains by implementing the same procedure as the PLDT system suggest that, the difference in locally and externally measured shear modulus cannot be explained only by considering the effects of end restraint alone although it has some effect.

ACKNOWLEDGEMENT

First and foremost I wish to forward my deepest heartfelt gratitude to my supervising professor, Professor Junichi Koseki, Institute of Industrial Science, The university of Tokyo, for his kindhearted guidance, constructive criticisms, amazing patience, and valuable suggestions to make this research a reality. Without his help and attention, this task would have not been a reality. Japan is totally different from my homeland, Sri Lanka in terms of lifestyle, culture, academic life and so on. In addition, I had a very little exposure to advanced laboratory testing of soils before coming to Japan also. Therefore my first few months in Japan was full of disappointments, discouraging experiences, unexpected problems both in my academic and day to day life. It was Professor Junichi Koseki's warmhearted care and attention which helped me not only to overcome those early stage difficulties but also it grew on me an ever lasting love to Japan, Japanese people and laboratory soil testing. Furthermore, his meeting changed my way of thinking, way of writing, and way of approaching into a problem drastically in a qualitative manner.

I am also very much thankful to Assistant Professor Taro Uchimura, Geotechnical engineering laboratory, The University of Tokyo, for devoting his valuable time and effort in giving valuable suggestions and constructive criticisms both in my research and in compiling this manuscript.

My special appreciation goes to Mr. Takeshi Sato, Koseki Laboratory, The University of Tokyo, for his highly cooperative helps in assembling the apparatus, wiring for amplifiers and transducers, teaching me the basic procedures of laboratoty soil testing, and advising on trouble shooting. I gained a lot of knowledge from him not only about conducting experiments but also about workshop techniques such as drilling, filing, grinding, making sensors and so on.

Mr. Tutomu Namikawa, University of Tokyo, taught me a lot about elastic modeling and he helped me to conduct FEM analysis using his company facilities. I am very much thankful to him for all the kind supports and efforts.

I am grateful to Miss Michie Torimitsu, the secretary of Koseki laboratory for her friendly movement and understanding in numerous ways during the course of my study. Her helps were essential for the smooth progress of my day-to-day academic activities. Miss Tsusumi who joined Koseki laboratory in the latter part of my stay, helped me to solve many problems

regarding the security of my computer and the use of network. I would like to thank them for all the helps.

My appreciation goes to Dr. Lin Wang, Chuo Kaihatsu Cooperation, for developing the user friendly Windows based control program of the newly assembled apparatus. His voluntary contribution in modifying the program and helping hands in troubleshooting is highly appreciated.

I wish to express my gratitude to Mr. Sajaad Maqbool, a senior graduate student of Koseki laboratorty for his helps in many ways. From the very first day, when I met him at the Tokyo city air terminal to the end of my stay in Japan, he helped me a lot in both academic and daily life. Without his co-operation and helps, my two-year stay in Japan would have been a very tough period. Dr. Nguyen HongNam, who was a senior student of Koseki laboratory, taught me a lot about PLDTs and torsional shear apparatus. Mr. Le Quang Anh Dan shared some of his knowledge about hollow cylinder apparatuses and programming in N88 basic with me. I am thankful to both of them for their contribution. In addition, all my colleagues of Koseki laboratory forward their helping hands on me. Especially Mr. Kato, Miss. Hashiguchi, Mr. Mihira, Mr. Itou and Mr. Komoto helped me to get through all the paper works. Their kind and cooperative supports during my stay is highly appreciated.

This is my first ever long stay, which I stayed without the association of my family. Therefore without the dedication of my father, mother and other family members, most of my ambitions may not be fulfilled. I am very much grateful to them for undergoing those hardships in making a smooth way for my stay in Japan.

I would like to thank all my friends both in Japan and in Sri Lanka for keeping our friendships alive by sending mails and letters, giving calls, and etc. Their frequent contacts helped me to get rid of the home sick, which I felt during the first few months of my stay in Japan.

Finally, I wish to express my special gratitude for the Asian Development Bank, for providing me the necessary financial assistance for my studies in Japan.

TABLE OF CONTENTS

CHAPTER 1: INTRODUCTION

1.1 Background

1.1.1 Hollow cylinder specimen with local strain measurements

It is well known that the deformation of ground under normal working loads is less than 0.1% of strain. Since soils are showing linear elastic stress-strain behavior at very small strain levels (less than 0.001%), small strain stiffnesses of geomaterials, also known as quasi-elastic deformation properties such as Young's modulus and shear modulus are very important parameters in the design of geotechnical engineering structures. Therefore it can be seen that a large attention is paid for the accurate determination of these properties in the field. Down-hole survey and cross-hole survey are commonly used in the field determination of quasi-elastic shear modulus of soil and the values obtained from those are used as the reference shear modulus values for a particular engineering application such as a dynamic response analysis or a static loading/unloading situation (eg., embankment or excavation). It should be noted that the relationship between shear modulus measured dynamically and statically is not well understood, and the use of dynamically obtained soil strength parameters for analyzing static loading situations is not yet fully validated.

Among the soil testing apparatuses used in the geotechnical engineering laboratories around the world, hollow cylinder apparatus is a very effective tool in simulating the actual working condition of soil with general stress paths including rotation of principal stress axes (Saada, 1988).

On the other hand, with the development of small strain measuring techniques such as inclinometer (Burland. 1989), LDT (Goto et al, 1991; Tatsuoka et al, 1997), proximity transducers etc, it has now become possible to measure small strains in the order of less than 0.001% both locally and externally in the laboratory. But system compliance problems such as misalignment, bedding error and end restraint effect cause some unreliability on the externally measured deformation properties. Therefore, local strain measurement is becoming popular among the researchers due to its closeness to the actual strains. Since soil behavior can be considered as elastic at strain levels less than 0.001%, the measument of such small strain is very important in understanding the quasi-elastic deformation properties of soils such as Young's modulus and shear modulus. Although the above-mentioned techniques are well suited for triaxial testing routines of soils, some modifications are needed to use them in hollow cylinder specimens. The change in curvature and the change in measuring direction of the specimen create many problems for conventional local deformation measuring techniques when applied to hollow cylinder specimens.

Hong Nam & Koseki (2001) developed a new local strain measuring technique (Pin-typed Local Deformation Transducer, PLDT) to be employed in the hollow cylinder specimens. It consists of three local deformation transducers with pinned ends (PLDTs). They are arranged in a triangular shape using hinges directly attached to the specimen. One such hinge supports two PLDTs. This technique can be effectively used in hollow cylinder specimens with larger outer diameter (>= 20cm) to obtain four strain components of the specimen (ε_z, ε_r, ε_θ, γ) locally.

When this technique was applied to specimens with outer diameter less than 20 cm, it was observed that the larger curvature of the specimen made it very difficult to arrange the three PLDTs in a triangular shape with one common hinge for two LDTs. In addition, it was not possible to set the diagonal PLDT at an angle of approximately 45^0 to the horizontal, and large reaction force at the hinge caused by two PLDTs may damage the hinge at large stress levels as well. In order to overcome these problems, it is vital to modify the current PLDT arrangement to suit for specimens with smaller dimensions and check its consistency against conventional external strain measurement techniques.

On the other hand, it was observed by Hong Nam and Koseki (2004) that the effects of end restraint on shear modulus was significant compared to that of Young's modulus in the torsional shear tests. This resulted in lower shear modulus when measured locally. Since local measurement is close to the actual value, it is important to thoroughly investigate this phenomenon for other soils as well because in the actual practice, designers may rely on the shear modulus, which was measured using external transducers only. Therefore over estimation of shear modulus using external transducers may yield to over-estimation of safety of a particular structure. Therefore it is vital to understand the consequences and if possible give some guideline for revising the current soil property characterization procedure.

1.1.2 Degradation of shear modulus at large stress ratios

The recently assembled medium sized high capacity hollow cylinder apparatus at Institute of Industrial Science (IIS), University of Tokyo, Japan, is capable of testing specimens with various sizes up to 20cm in outer diameter, 12cm in inner diameter and 30cm in height. High capacity and large size of the apparatus makes it possible to test geomaterials with larger particle sizes such as gravel. It should be noted that there are very limited data on gravel in torsional shear with static local measurements. Previous studies by Ono (2000), Koseki (2001), Hong Nam (2004), revealed a sudden degradation of shear modulus of sand at principal stress ratio greater than three using hollow cylinder apparatus. Therefore it is important to check the validity of this phenomenon for gravel as well.

1.2 Scope of the Study

In view of the background mentioned above, the present study aims at the following scopes:

1. Modify the triangular PLDT system with common hinges in order to use for the specimens with smaller outer dimeter (less than 20 cm).

2. Investigate the stress state dependency of quasi-elastic deformation properties of sand and gravel at various densities using the modified version of PLDT system as the local strain measument technique.

3. Compare the locally measured quasi-elastic and global deformations with externally measured ones.

4. Investigate the sudden degradation of shear modulus of sand and gravel at large principal stress ratios for various densities.

5. Investigate the effects of shear stress level on Young's and shear moduli

6. Simulate the small strain behavior of hollow cylinder specimen using FEM and try to understand the possible reasons for the difference in locally and externally measured shear modulus.

CHAPTER 2: SPECIMEN PREPERATION AND APPARATUS

2.1 Test materials

A summary of the materials used is listed in Table 2.1.

2.1.1 Toyoura sand

Toyoura sand is fine (D_{50} = 0.162 mm, D_{max} = 0.4 mm), uniform sand that has been widely used in geotechnical engineering laboratories all over Japan. Toyoura sand Batch G was used for the present study. The maximum void ratio e_{max} is 0.975 and the minimum void ratio e_{min} is 0.561. All the specimens were prepared by air pluviation technique and pouring height was changed from 0.1m to 1m to prepare specimens with initial dry densities varying from 1.443 g/cm^3 to 1.61 g/cm^3. In terms of relative density it is between 38.2 % and 90.6%. Pouring height was kept constant during the course of pluviation to obtain a uniform specimen. In the first five tests pluviation was done in alternative clock-wise and counter clock-wise directions. In the rest of the tests pluviation was done in alternative radial direction, while moving the nozzle gradually in the alternative clock-wise and counter clock-wise directions as well. Refer to Fig.2.3 for the schematic diagram of these pluviation procedures. All the Toyoura sand specimens have dimensions of 15 cm in outer diameter, 9 cm in inner diameter and 30 cm in height.

2.1.2 Hime Gravel

Japanese originated Hime gravel has a D_{50} of 1.73mm and D_{max} of 3.30 mm. The maximum void ratio e_{max} is 0.709 and the minimum void ratio e_{min} is 0.480. Specimen preparation method was exactly the same as Toyoura sand specimens. A pluviator with larger opening about 5 mm in width was used for pluviating gravel particles. All the materials were tested at dry state under drained condition to obtain drained quasi-elastic deformation properties. All the Hime gravel specimens have dimensions of 20 cm in outer diameter, 12 cm in inner diameter and 30 cm in height.

2.2 Specimen preparation

Refer to Appendix to view the photos of each step in specimen preparation.

First the inner latex membrane of 0.3 mm thickness, which was manufactured by Katouno Company, was placed over a metal ring, which has a rubber O-ring at the top. It provides better protection to apply small amount of grease on the rubber O-ring before the membrane was placed. Then the metal ring together with membrane was kept on the apparatus base and the hollow pedestal was put over the metal ring while taking the inner membrane out from the hole of the pedestal. Care was taken not to damage the membrane at all the time. Then the pedestal was screwed into the apparatus base firmly. After that the inner mould could be set. Inner mould consists of four metal parts, which makes a perfect cylinder, a steel ring to keep the four parts together and a steel rod screwed at the end to keep the inner mould fixed in position. All the four parts of the inner mould was placed inside the inner membrane, which comes out from the pedestal and the mould was fixed using the ring and rod firmly.

Next step after setting the inner mould was to put the outer latex membrane of same thickness as the inner membrane over the outer diameter of the pedestal. Then the gap between outer membrane and pedestal was sealed by using a rubber band and a rubber O-ring. After that outer mould could be fixed. The outer mould consists of two symmetrical steel parts with two clamps to tighten them together. Small amount of grease should be applied along the edges of the outer mould parts before fixing it. After fixing the outer mould, the extra part of

the outer membrane was put over the outer mould and it was ensured that the gap between outer membrane and the outer mould was perfectly sealed. After that a vacuum of 30 kPa was applied to the space between outer membrane and outer mould.

Moulds were ready for pluviation after those steps. Before pluviation, some measures were taken to collect the waste material that didn't go into the space between inner and outer membranes. This step was necessary to obtain the weight of the specimen. The funnel containing test material was kept over the space between inner and outer membranes and the material was allowed to fall freely while keeping the falling head constant. In this study, falling height of each specimen was changed between 0.1m – 1m to obtain specimens with various densities. The direction of funnel movement was changed alternatively between clockwise and anti-clockwise (Fig.2.3) and an attempt was taken to keep the top surface of the specimen horizontal during pouring to minimize the inhomogeinity. In some experiments of this study, pluviation was done in the radial direction (Fig.2.3) instead of alternate clockwise and counter-clockwise directions to check the effects of different pluviation techniques. After pluviating the material to the full height of the specimen, the top surface of the specimen was leveled horizontally using a metal strip and the waste material was collected and weighted.

Next step was to place the top cap over the specimen. First the top cap guider was fixed to one of the four steel poles that come from the base of the apparatus. Then a steel cable with four bolts attached to one end and dead weight attached to the other end was attached to the top cap using the four bolts. After that the cable attached to the top cap was put over the pulleys of the guider and balanced using counter balances. Horizontality of the top cap surface was maintained by adjusting the four bolts before it was placed on the specimen top surface. Then the top cap was placed very carefully over the specimen until it just touched the top surface while ensuring the symmetry of the specimen. Two clamps were then fixed symmetrically to two steel poles and the top cap was held in position by attaching it to the clamps using bolts. After that the extra part of the inner membrane was put over the top cap inner ring and the extra part of the outer membrane was put over the top cap outer ring. Specimen inside was perfectly sealed by using rubber bands, covering the inner and outer rings of the top cap. Next the counter balance was applied again and the clamps were removed. After that, a vacuum of 30kPa was applied to the specimen inside and the outer mould was removed. Then the top cap was clamped again and the inner mould was removed.

After that the upper part of the top cap was connected firmly to the top cap. It should be noted that the upper part of the top cap is fixed to the loading shaft. Setting of the transducers was done next and after that the specimen was covered with the cell. Finally, the cell pressure was increased gradually up to 30 kPa, while reducing the vacuum applied to the specimen down to the atmospheric pressure, in order to maintain the same effective stress. When changing the vacuum into cell pressure, the dead weight above the specimen should be counter balanced properly.

2.3 Apparatus

2.3.1 High capacity medium sized hollow cylinder apparatus

2.3.1.1 Vertical and torsional loading systems

Recently developed high capacity medium sized hollow cylinder apparatus at Institute of Industrial Science (IIS), The University of Tokyo, Japan is schematically shown in Fig. 2.1a, 2.1b and Fig. 2.2. Fig. 2.1a illustrates the specimen, triaxial cell and transducers for the specimen with outer diameter of 20 cm, inner diameter of 12 cm and height of 30 cm. Figure 2.1b shows the specimen with outer diameter of 15 cm, inner diameter of 9 cm and height of 30 cm. Vertical and torsional loading system is schematically shown in Fig. 2.2. Vertical and torsional loading capacities of the system are 15 kN and 0.3 kN.m respectively. This higher loading capacity of the system enables to investigate the properties of soils with larger particles such as gravel. It enables to apply deviator and torsional shear stress up to 740 kPa and 180 kPa, respectively, on the specimen with outer diameter of 20 cm, inner diameter of 12 cm and height of 30 cm.

The axial loading system consists of an AC servomotor, a reduction gear system with two gears, electro magnetic clutches and brakes and a ball screw with a pre pressured nut. The motor always drives in one direction. Simultaneously, the upper gear is rotating in one direction and the lower gear is rotating in the opposite direction. The movement of the loading piston is switched from downwards to upwards without any backlash by using the electric clutch (Koseki et al., 2004).

Torsional loading system also consists of similar devices. Torque is transmitted to the loading shaft by means of a metal band. Both vertical and torsional loading systems are designed to have nearly zero backlash. These loading systems are controlled independently by using two 12-bit D-A converters named PCN 3098 made by PC Technology Company.

Cell pressure is applied through an electro-pneumatic transducer (E/P) with a capacity of 1000kPa. Inner and outer cell pressures were kept constant throughout the tests in the present study. Control of cell pressure and loading system can be fully computerized. Back pressure was kept equal to atmospheric pressure during the present study.

This apparatus is capable of testing specimens with various dimensions ranging from 20 cm outer diameter, 12 cm in inner diameter and 30 cm in height to 15 cm in outer diameter, 9 cm in inner diameter and 30 cm in height. It should be noted that this apparatus is capable in testing in-situ frozen specimens, as they are usually available in the form of cylinders with an outer diameter of 15 cm.

2.3.1.2 Data acquisition system

Analog electric signals from the transducers are amplified using Kyowa DPM 600 series dynamic strain amplifiers and converted into digital signals using two 16-bit Contec AD 16-16EH A-D converters. These data are then stored in the computer.

The apparatus is automatically controlled by software called Digit Show developed by Lin Wang (Chuo Kaihatsu limited). It is Windows based control program written in visual C++. After initializing the A/D and D/A boards, two files can be assigned to save voltage data and calculated data. Then a file contains calibration factors of all the control channels should be opened. Output from the load cell is used by the program to control axial and shear stresses while outputs from external transducers and potentiometers are used as control channels for axial and shear strains respectively. This program is capable of controlling any monotonic loading path automatically. After inputting the target cell pressure and axial stress, program controls the loading system of the apparatus accordingly. Axial and torsional small cyclic loading can be controlled either by stress amplitude or strain amplitude after adjusting the relavant motor speeds. In the present study, isotropic consolidation data and small cyclic loading data are saved in separate files for less ambiguity.

2.3.1.3 Measurement of stresses, strains and volume change

This system has 16 measuring channels in total to measure stresses, strains and volume change. Two channels for load cell and external displacement transducers (EDT), one channel for potentiometer, high capacity differential pressure transducer (HCDPT) and low capacity differential pressure transducer (LCDPT), three channels for proximity transducers (Gap sensors) and six channels for pin-typed local deformation transducers (PLDT). The function of each transducer is described below.

Load cell - A two-component load cell with negligible coupling effect (no effect of axial load for torque and vise versa) located inside the cell is used in this apparatus. It has a vertical loading capacity of 15 kN and a torsional loading capacity of 0.3 kN.m.

HCDPT - Measurement of cell pressure is done using this transducer. It is capable of measuring up to a maximum of 600kPa.

LCDPT -Change of volume inside the specimen in drained tests on saturated specimens is measured using this transducer.

EDT - Measurement of axial strains outside the cell is done by using two EDTs located symmetrically along the loading shaft.

Gap sensors - Three gap sensors (probe of PU-09 and amplifier 5509) ranged 4 mm are located inside the cell. Two of them are fixed vertically and targeted to the top cap to measure axial strain and the other one is fixed horizontally and targeted to a vertical steel plate fixed to the top cap to measure the rotation of the top cap (Refer to Fig 2.4). All the gap sensors manufactured by Applied Electronic Company (AEC).

Potentiometer - One potentiometer having a diameter of 5 cm is attached to the top cap perimeter for measuring large shear strains.

Pin-typed Local Deformation transducers (PLDT) - Figure 2.4 and 2.5 illustrates the layout of the modified version of PLDTs and gap sensors for two specimens employed for this study. Seven PLDTs in total are used in the present study. Manufacturing process of PLDT is as same as the conventional LDTs (Goto et al., 1991), while the only difference is that the ends of the PLDTs are pinned in order to allow for free rotation of the LDT. Conventional LDTs with flat ends cannot be used in hollow cylinder specimens because they cannot withstand any rotation. Refer to Hong Nam 2001 for more details about the working principal, design criteria and performance evaluation of PLDTs.

Original version of PLDT system (Hong Nam., 2001) consists of three PLDTs arranged in a triangle(vertical, horizontal and diagonal) using three hinges attached to the central portion of the specimen. These hinges have a small conical hole to bear the pinned end of PLDT. Each hinge bears two PLDTs. But it was found that the results from this system are not reliable when it is employed in specimens with outer diameter less than 20cm. In addition to that, larger curvature of the specimen makes it very difficult to set the PLDTs in a triangle using common hinges without having excessive bending strains in PLDTs. As a result, large reaction force is applied to the hinges and it causes damage to the specimen-hinge interface at higher stress levels.

Therefore a modified version of PLDT system is employed in the present study. In that, three PLDTs are attached separately using separate hinges and PLDTs are independent of each other. This modification gives more flexibility in setting the system. Although PLDTs are separated, an attempt was made to fix them close to each other. Two additional assumptions ware made for calculating local strains.

I. Vertical component of the diagonal PLDT has the same strain as the vertical PLDT
II. Horizontal component of the diagonal PLDT has the same strain as the horizontal PLDT

By combining the above assumptions with the assumptions used in original version of PLDTs, it is possible to calculate four-strain components ε_z, ε_θ, γ, and ε_r locally. Calculation procedure is described in detail in Chapter 3.

Two sets of modified version of triangular PLDTs were employed in all the tests. They are arranged in opposite sides of a diameter of the specimen. One horizontal PLDT was located

inside the specimens that have dimensions of 20 cm in outer diameter, 12 cm in inner diameter and 30 cm in height. Other specimens that have dimensions of 15 cm in outer diameter, 9 cm in inner diameter and 30 cm in height, only two sets of outer triangular PLDTs were used.

2.4 Experiment program

2.4.1 Preliminary tests on small-sized hollow cylinder apparatus

First series of tests were conducted on air pluviated dry Toyoura sand specimens having outer diameter of 10cm, inner diameter of 6cm and height of 20cm as to get some experience of hollow cylinder apparatus. No local strain measurement was done during this series of tests. One external deformation transducer was used for axial strain measurement and one potentiometer was used for the measurement of rotation of specimen.

The control program of the small-sized hollow cylinder apparatus which was programmed by Yoshida, designed to perform cyclic loading between given strain levels. Therefore this program was first modified in order to perform cyclic loading between given stress levels. Then a series of large cyclic shear tests were performed. Twenty large shear stress cycles between $\tau = 0$ kPa and 60 kPa was applied to each specimen by varying the loading speed while keeping the vertical and horizontal effective stresses constant at 100 kPa. In some tests, an attempt was given to apply small cycles at different stress levels to calculate shear modulus of soil. But it was confirmed that this apparatus is not capable of applying small cycles in the range of single amplitude of $\gamma = 0.0015\%$ due to the backlash of the loading system, as typically shown in Fig. 2.31

2.4.2 Tests on high capacity medium-sized hollow cylinder apparatus

The newly assembled medium-sized hollow cylinder apparatus was used for the second series of tests. This apparatus is characterized by its high capacity. It is capable of testing specimens with various dimensions ranging from 15cm of outer diameter, 9 cm of inner diameter and 30 cm of height to 20 cm of outer diameter, 12 cm of inner diameter and 30 cm of height. More

importantly, this apparatus can be used to conduct tests on in-situ frozen samples, as they are also available in 15cm of outer diameter and 30 cm of height.

Two materials namely, Toyoura sand and Hime gravel were used for the present study. Table 2.2a and Table 2.2b illustrates the specimen details and their stress paths. Density of specimens was varied to check the effects of density on quasi-elastic deformation properties. Three different stress paths were used to investigate the effects of different stress levels. First each specimen was subjected to isotropic loading and unloading. Small cyclic vertical and torsional loading was performed at the end of each 50 kPa increment to calculate Young's and shear modulus. Then some specimens were subjected to triaxial compression while keeping the horizontal stress constant. Again, small cyclic loading in both vertical and torsional directions was applied at the end of each 25 kPa vertical stress increment. In one test (test LIN14), large shear stress was applied to the specimen after the isotropic consolidation and small cyclic loading was applied at the end of each 10kPa shear stress increment.

2.5 Calibration of Transducers

Fig. 2.7 through Fig. 2.30 illustrate the calibration curves of transducers employed in medium-sized hollow cylinder apparatus. Calibration of load cell for axial and torsional loads were conducted by resting the load cell and top cap on a rubber dummy. Fig. 2.6 shows the calibration procedure for PLDTs. Gap sensors and potentiometers were also calibrated using the same calibration platform.

Table 2.1: List of test materials

Material	Origin	D_{50} (mm)	U_c	G_s	e_{max}	e_{min}	Grain Shape
Toyoura sand	Japan	0.162	1.46	2.635	0.975	0.561	Sub-granular
Hime gravel	Japan	1.730	1.33	2.650	0.709	0.480	Sub-round

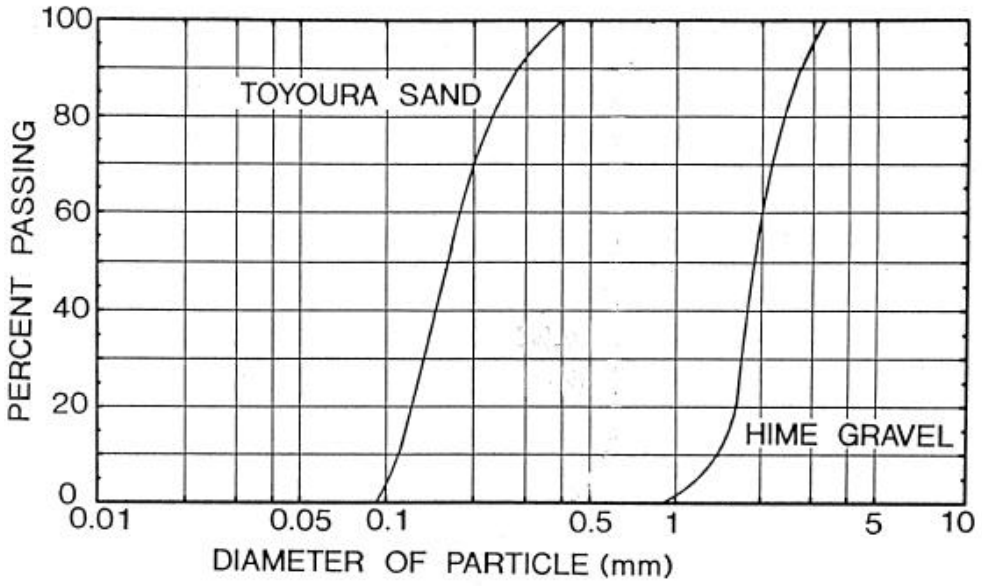

Fig. 2.1 Gradation curves of Toyoura sand and Hime gravel

Table 2.2a Details of Toyoura sand specimens

Test	Specimen dimensions (cm) (Do * Di * H)	Dry density (g/cm^3)	Initial void ratio	Relative density (%)	Local strains	Stress path (kPa)
LIN2	15 * 9 * 30	1.536	0.715	68.4	Original PLDT	IC ($\sigma'_z = \sigma'_\theta = 30 \sim 450 \sim 200$) TC ($\sigma'_\theta = 200$, $\sigma'_z = 200 \sim 400$)
LIN3	15 * 9 * 30	1.532	0.720	67.2	Original PLDT	IC ($\sigma'_z = \sigma'_\theta = 30 \sim 450 \sim 200$) TC ($\sigma'_\theta = 200$, $\sigma'_z = 200 \sim 400$)
LIN4	15 * 9 * 30	1.545	0.706	71.2	Original PLDT	IC ($\sigma'_z = \sigma'_\theta = 30 \sim 450 \sim 200$) TC ($\sigma'_\theta = 200$, $\sigma'_z = 200 \sim 400$)
LIN5	15 * 9 * 30	1.610	0.635	90.6	Modified PLDT	IC ($\sigma'_z = \sigma'_\theta = 30 \sim 450 \sim 100$) TC ($\sigma'_\theta = 100$, $\sigma'_z = 100 \sim 300$)
LIN6	15 * 9 * 30	1.612	0.634	90.6	Modified PLDT	IC ($\sigma'_z = \sigma'_\theta = 30 \sim 400 \sim 50$) TC ($\sigma'_\theta = 50$, $\sigma'_z = 50 \sim 250$)
LIN7	15 * 9 * 30	1.557	0.692	74.8	Modified PLDT	IC ($\sigma'_z = \sigma'_\theta = 30 \sim 400 \sim 50$) TC ($\sigma'_\theta = 50$, $\sigma'_z = 50 \sim 250$)
LIN8	15 * 9 * 30	1.593	0.654	85.3	Modified PLDT	IC ($\sigma'_z = \sigma'_\theta = 30 \sim 400 \sim 50$) TC ($\sigma'_\theta = 50$, $\sigma'_z = 50 \sim 250$)
LIN9	15 * 9 * 30	1.551	0.699	72.8	Modified PLDT	IC ($\sigma'_z = \sigma'_\theta = 50 \sim 400 \sim 50$) TC ($\sigma'_\theta = 50$, $\sigma'_z = 50 \sim 250$)
LIN10	15 * 9 * 30	1.612	0.635	90.6	Modified PLDT	IC ($\sigma'_z = \sigma'_\theta = 30 \sim 400 \sim 150$) TSI ($\sigma'_z = \sigma'_\theta = 150$, $\tau_{z\theta} = 0 \sim 92$) ALT ($\sigma'_\theta = 150$, $\tau_{z\theta} = 92$, $\sigma'_z = 150 \sim 400$)
LIN14	15 * 9 * 30	1.443	0.826	38.2	Modified PLDT	IC ($\sigma'_z = \sigma'_\theta = 60 \sim 400 \sim 150$) TSI ($\sigma'_z = \sigma'_\theta = 150$, $\tau_{z\theta} = 0 \sim 65$)

Table 2.2b Details of Hime gravel specimens

Test	Specimen dimensions (cm) (Do * Di * H)	Dry density (g/cm^3)	Initial void ratio	Relative density (%)	Local strains	Stress path (kPa)
LIN11	20 * 12 * 30	1.761	0.505	89.2	Modified PLDT	IC ($\sigma'_z = \sigma'_\theta$ = 50 ~ 400 ~ 40) TC (σ'_θ = 40, σ'_z = 40 ~ 200)
LIN12	20 * 12 * 30	1.735	0.527	79.4	Modified PLDT	IC ($\sigma'_z = \sigma'_\theta$ = 50 ~ 400 ~ 50) TC (σ'_θ = 50, σ'_z = 50 ~ 250)
LIN13	20 * 12 * 30	1.737	0.525	80.3	Modified PLDT	IC ($\sigma'_z = \sigma'_\theta$ = 60 ~ 400 ~ 50) TC (σ'_θ = 50, σ'_z = 50 ~ 250)
LIN15	20 * 12 * 30	1.725	0.536	75.5	Modified PLDT	IC ($\sigma'_z = \sigma'_\theta$ = 60 ~ 400 ~ 50) TC (σ'_θ = 50, σ'_z = 50 ~ 250)

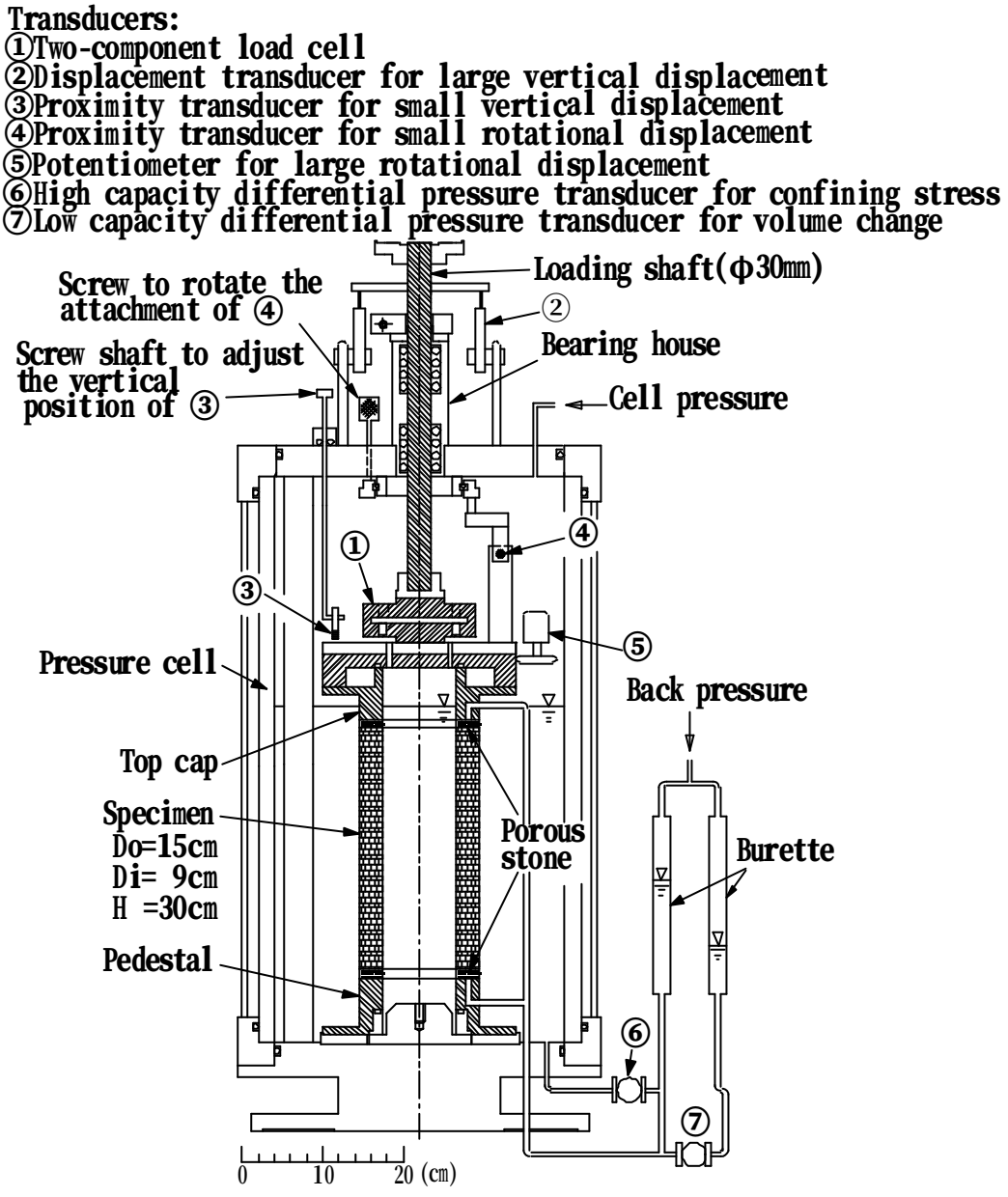

Fig. 2.1a Triaxial cell and transducers for hollow cylinder specimen 1

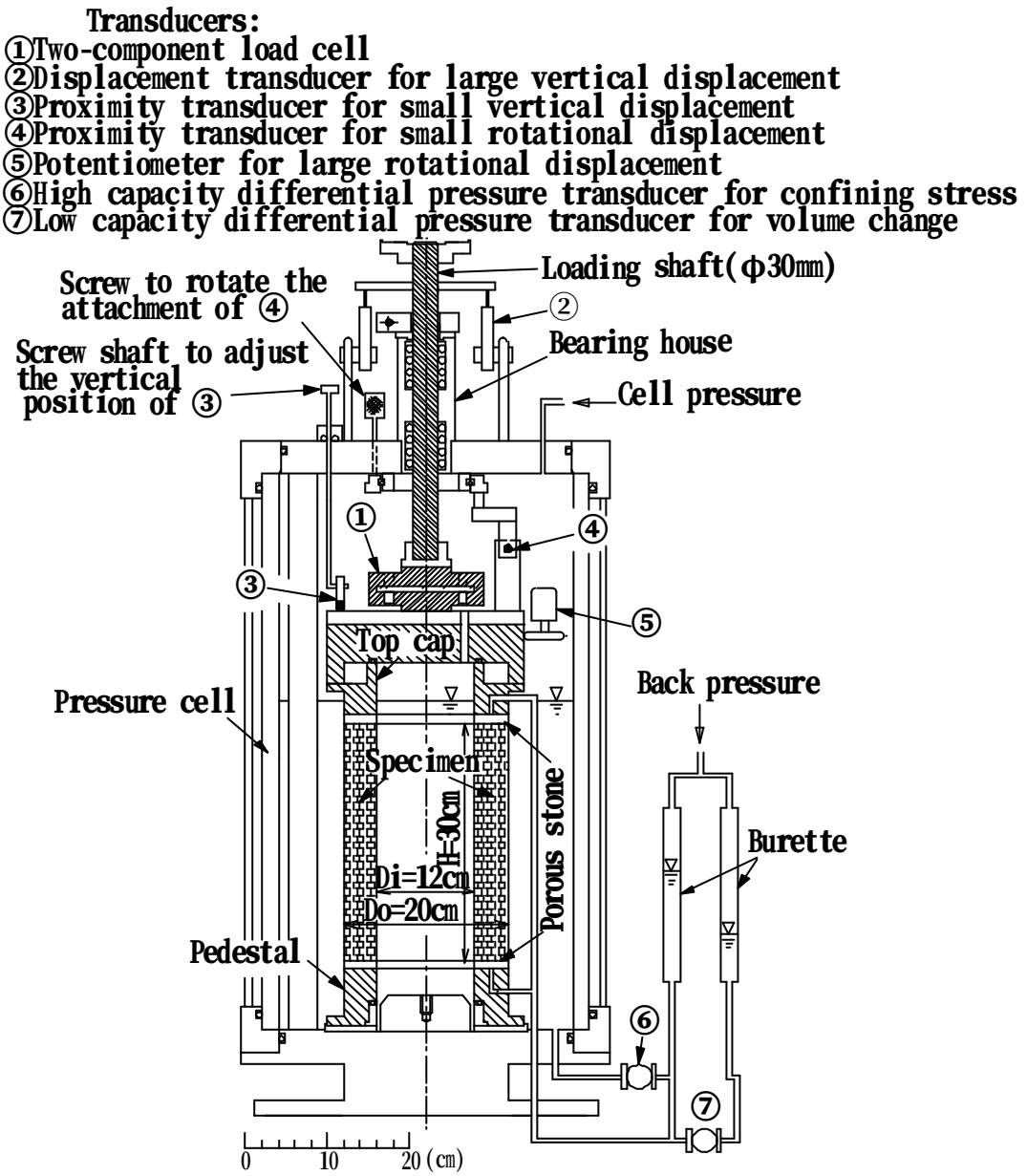

Fig. 2.1b Triaxial cell and transducers for hollow cylinder specimen 2

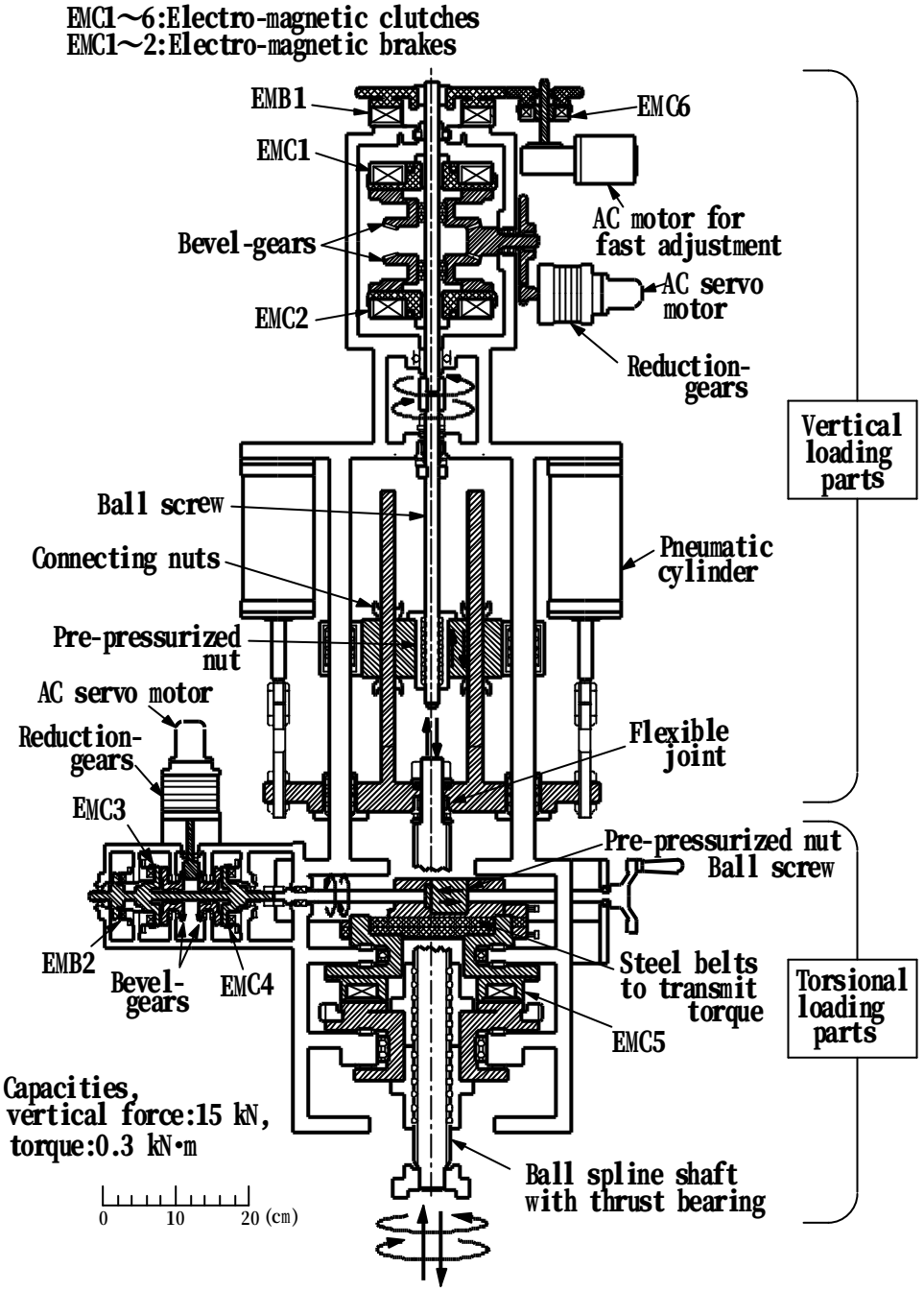

Fig. 2.2 Axial and torsional loading system

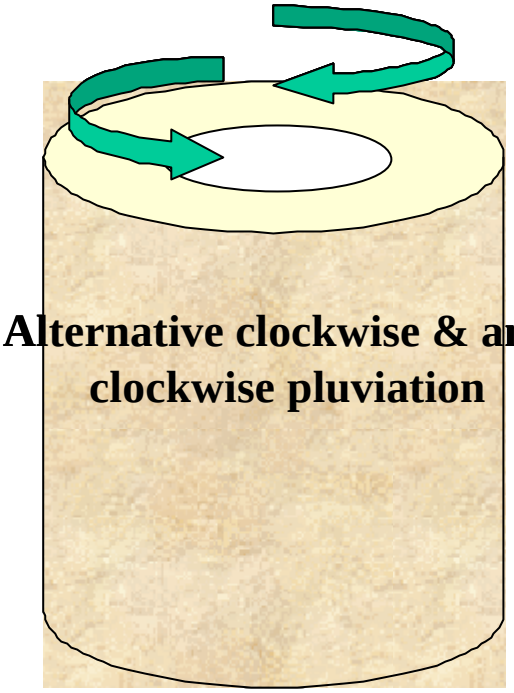

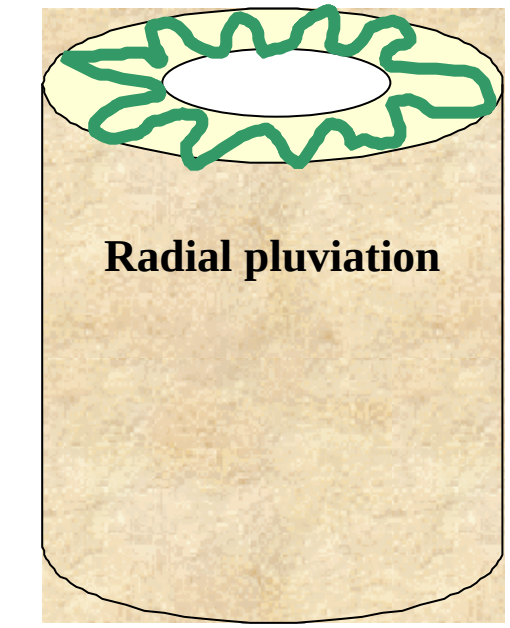

Fig. 2.3 Different pluviation techniques

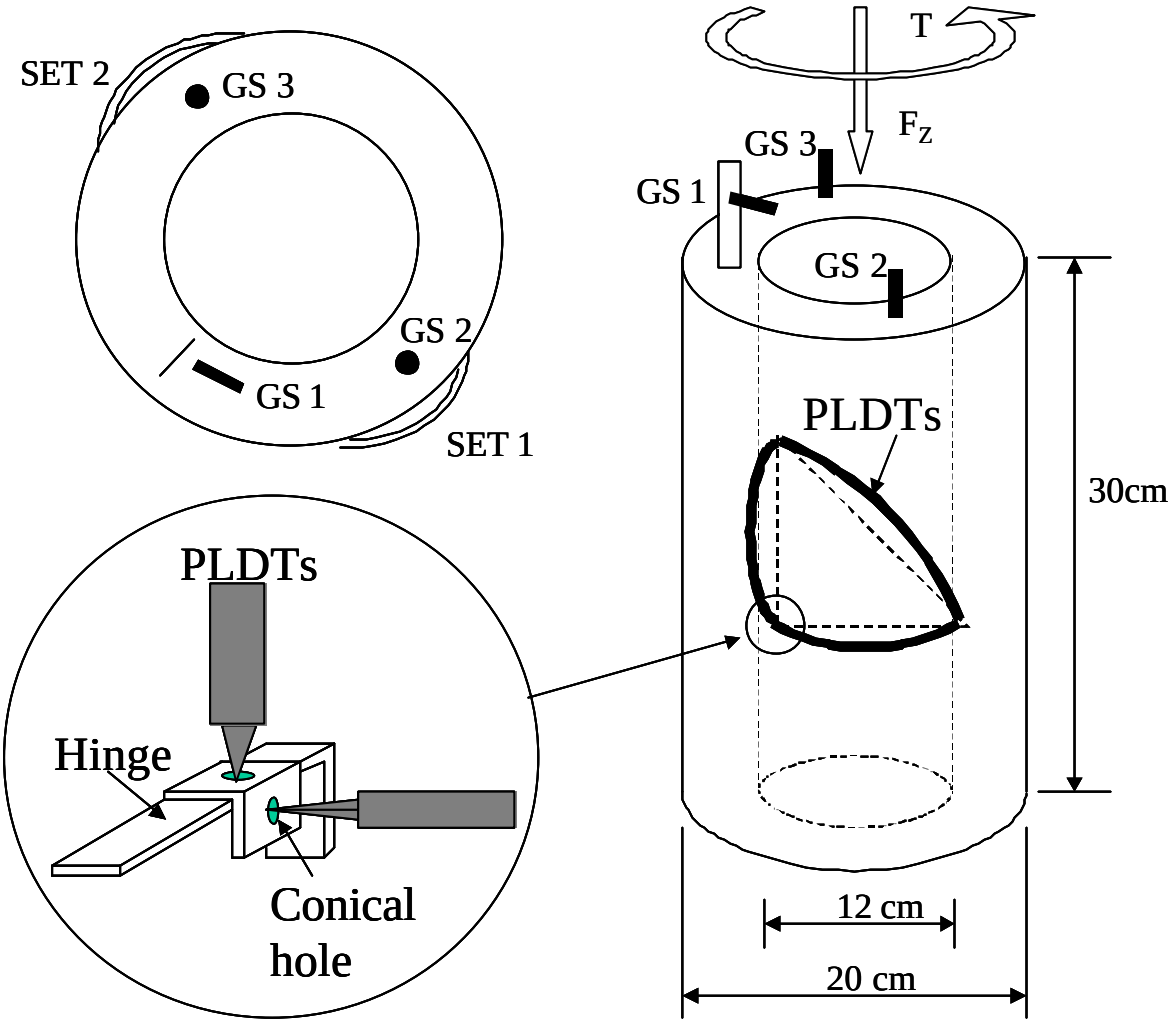

Fig. 2.4 Layout of the original version of PLDTs and gap sensors

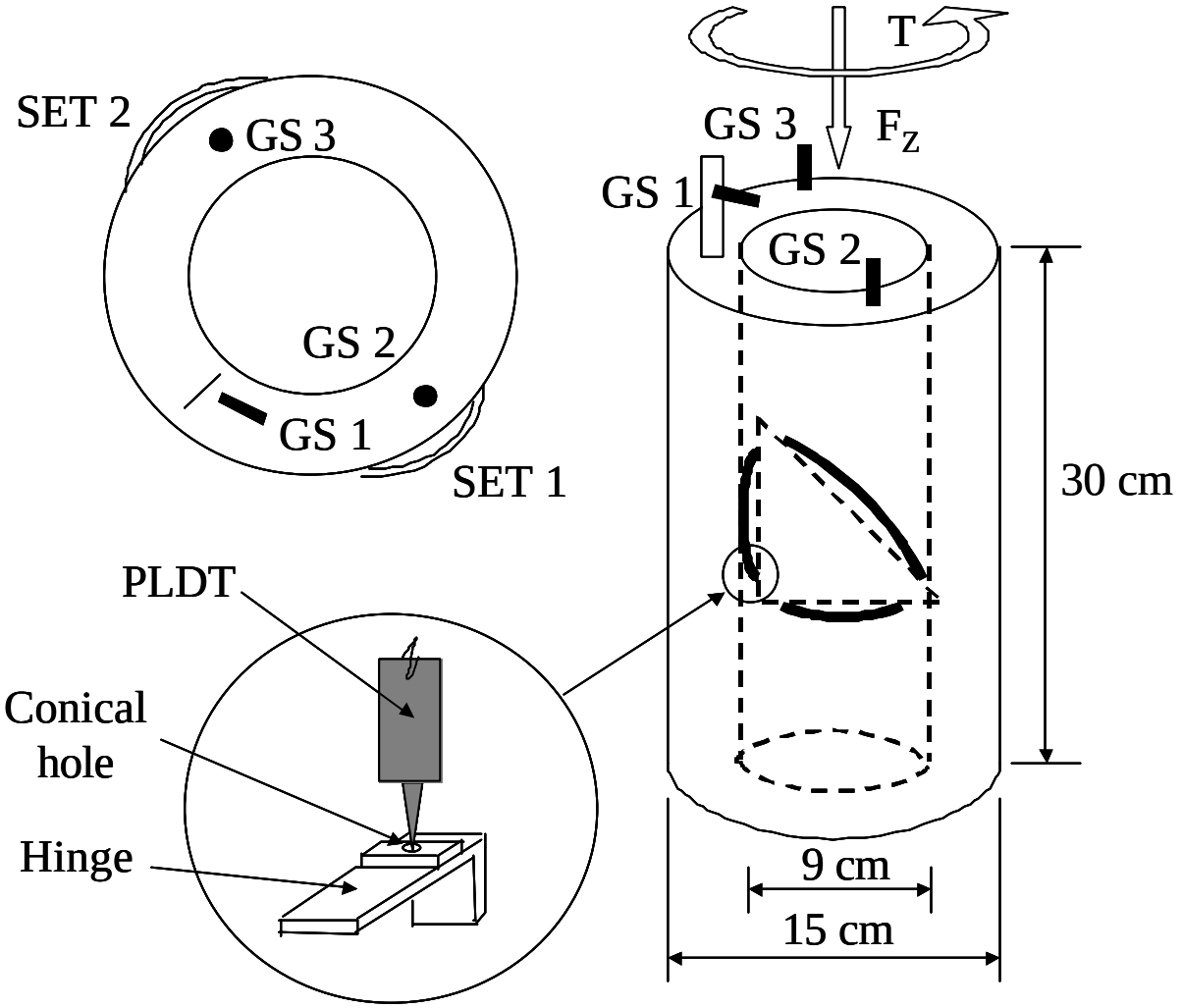

Fig. 2.5 Layout of the modified version of PLDTs and gap sensors

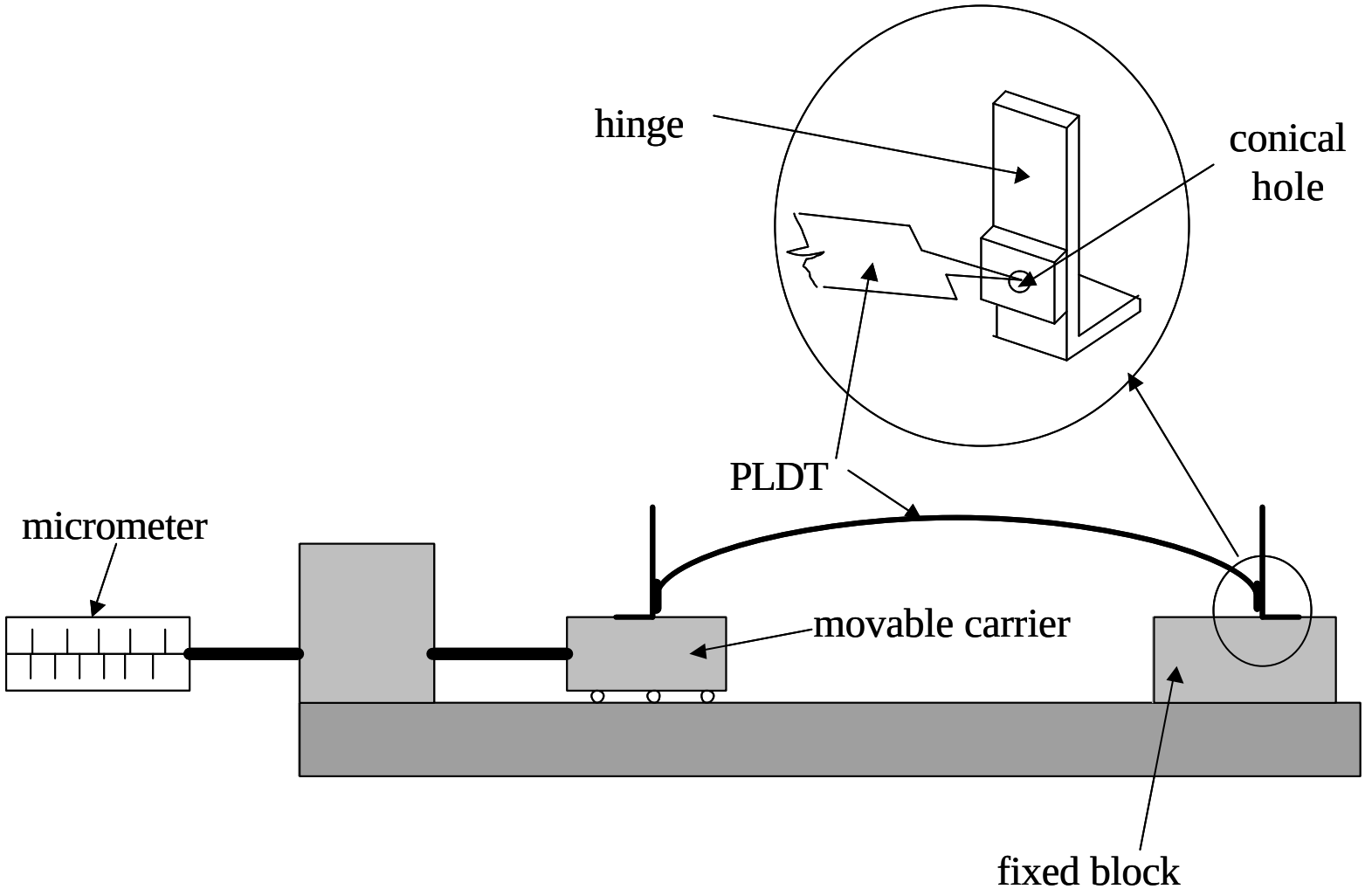

Fig. 2.6 Calibration of PLDT

Calibration curves of transducers in medium-sized hollow cylinder apparatus

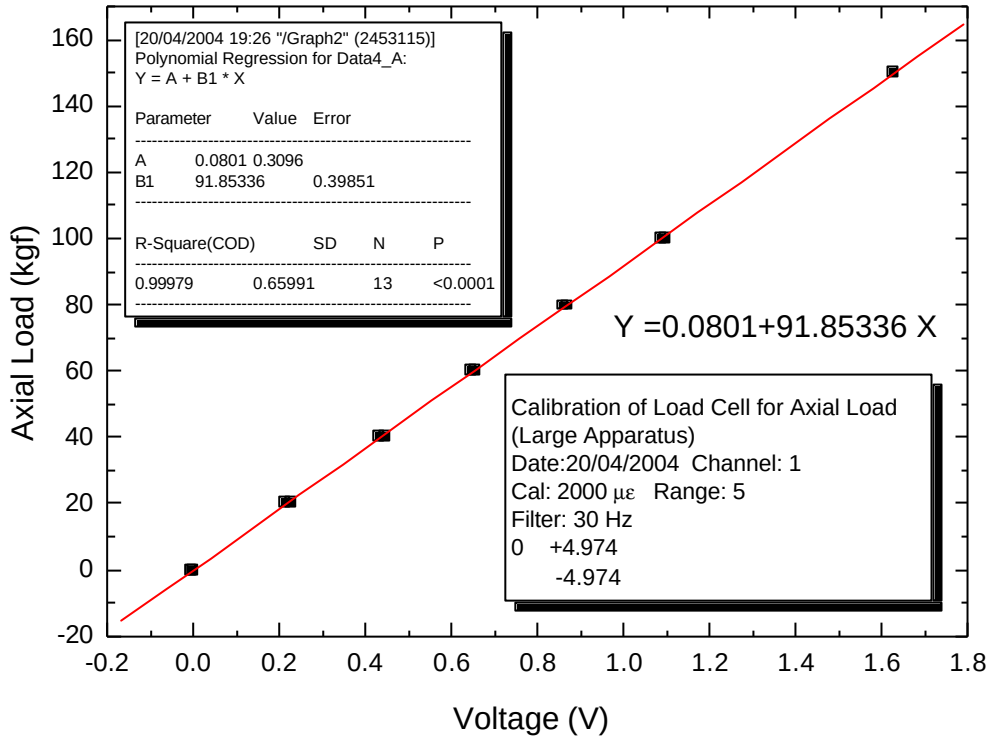

Fig. 2.7 Calibration curve of load cell for axial load

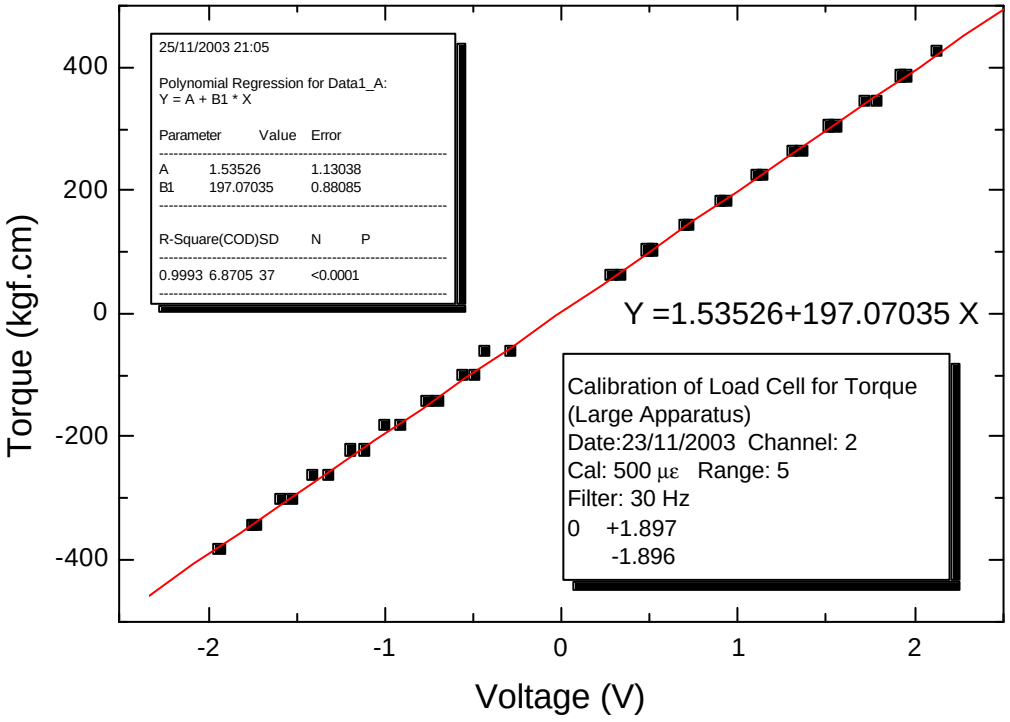

Fig. 2.8 Calibration curve of load cell for torque

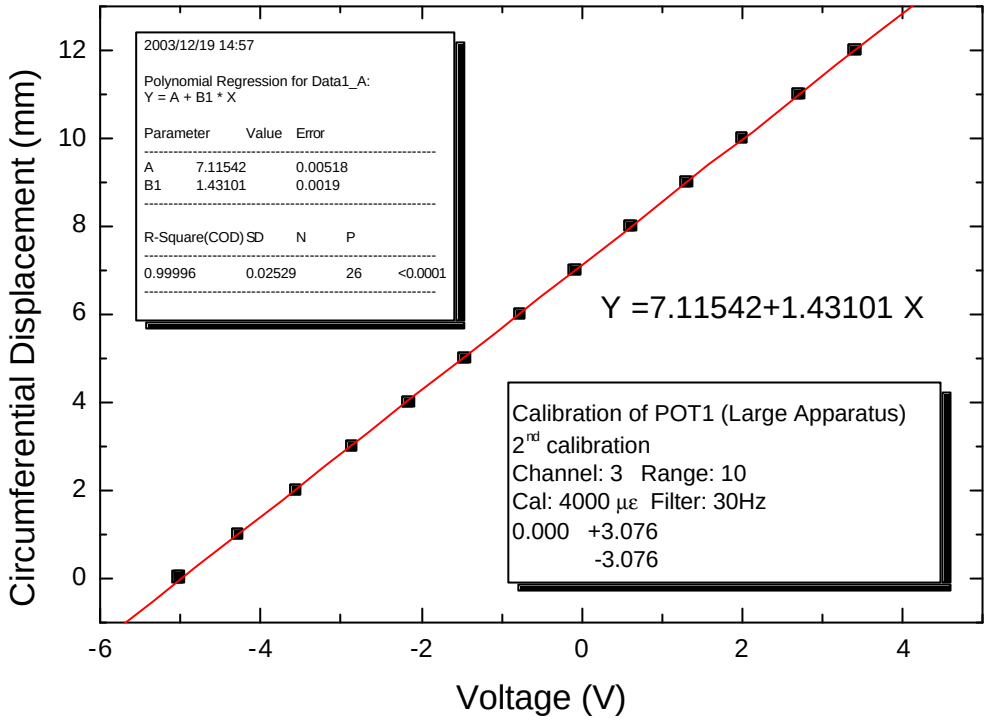

Fig. 2.9 Calibration curve of potentiometer 1 (POT1)

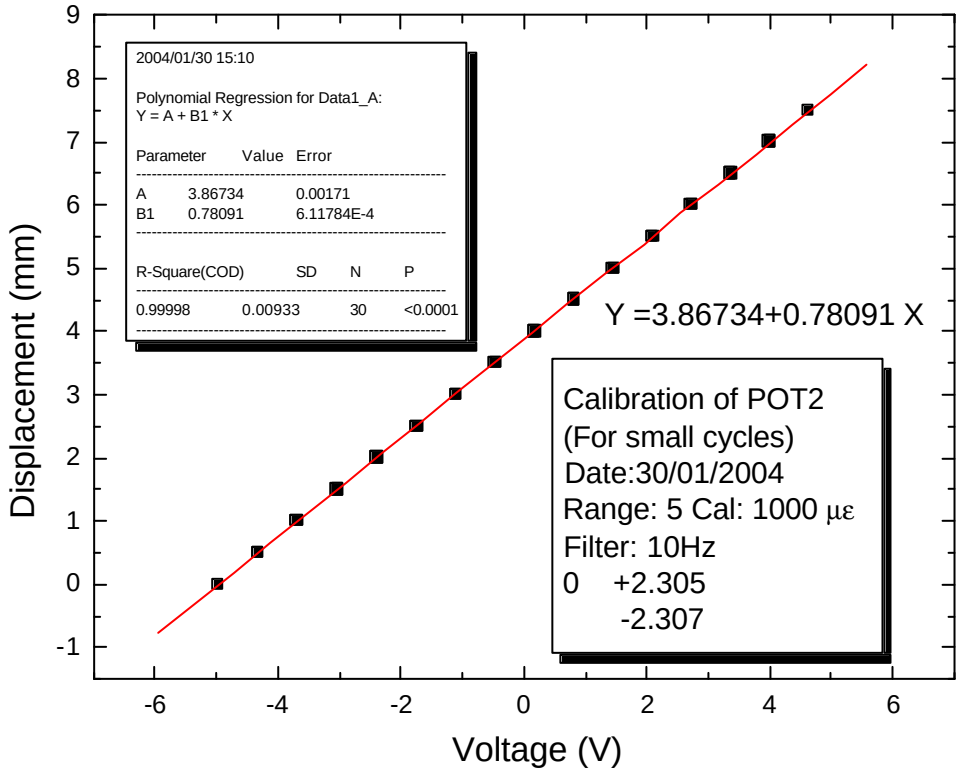

Fig. 2.10 Calibration curve of potentiometer 2 (POT2)

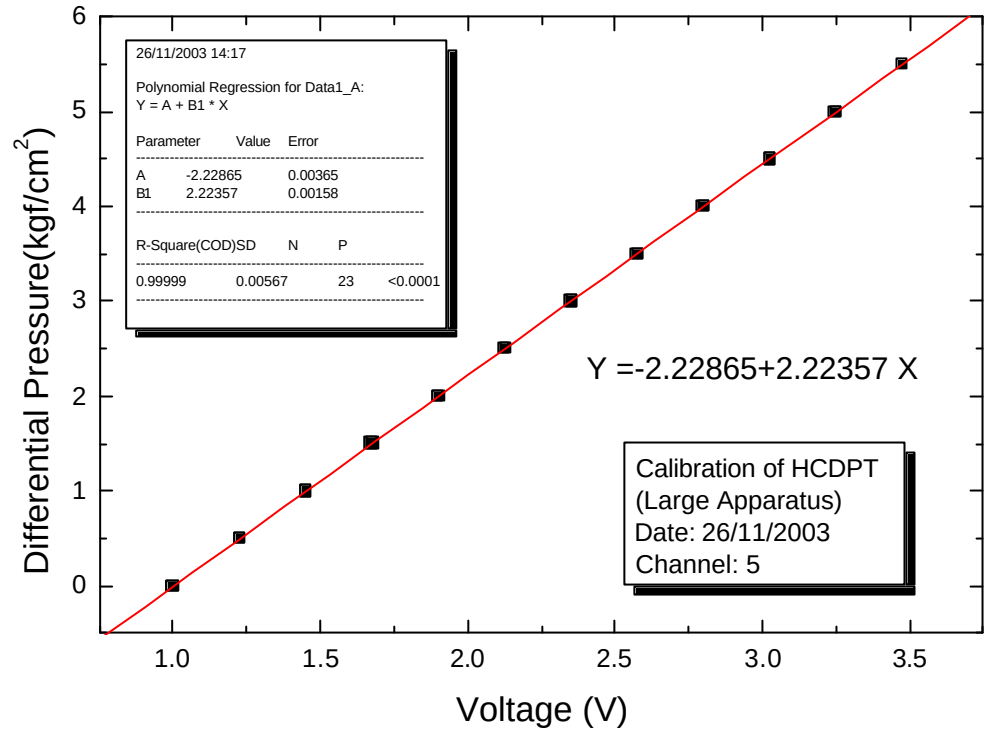

Fig. 2.11 Calibration curve of HCDPT

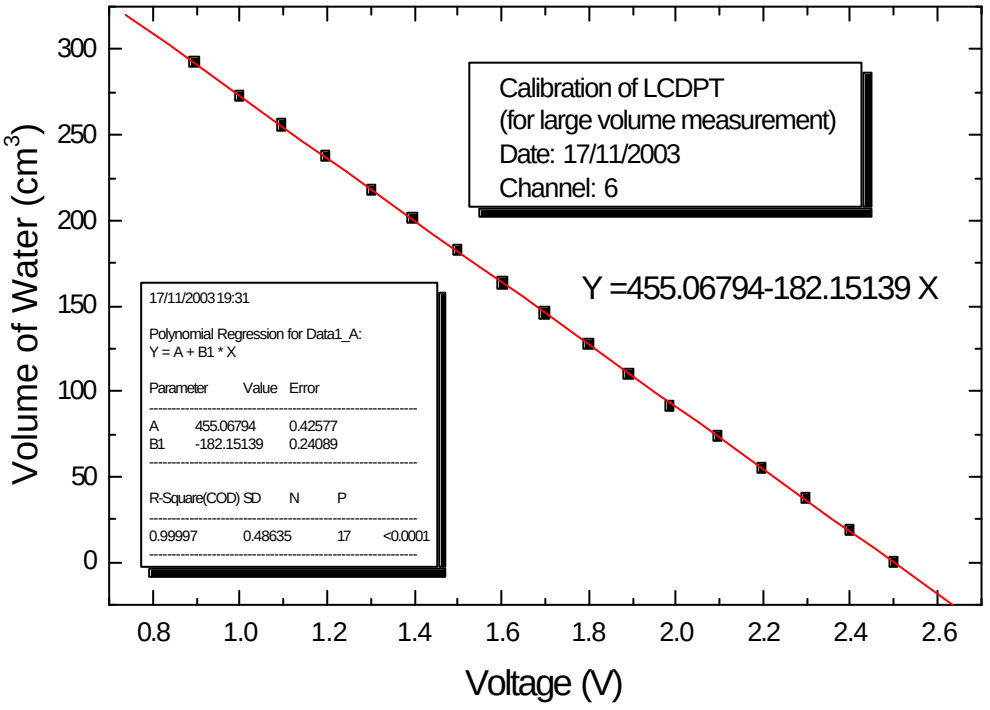

Fig. 2.12 Calibration curve of LCDPT for large volume measurement

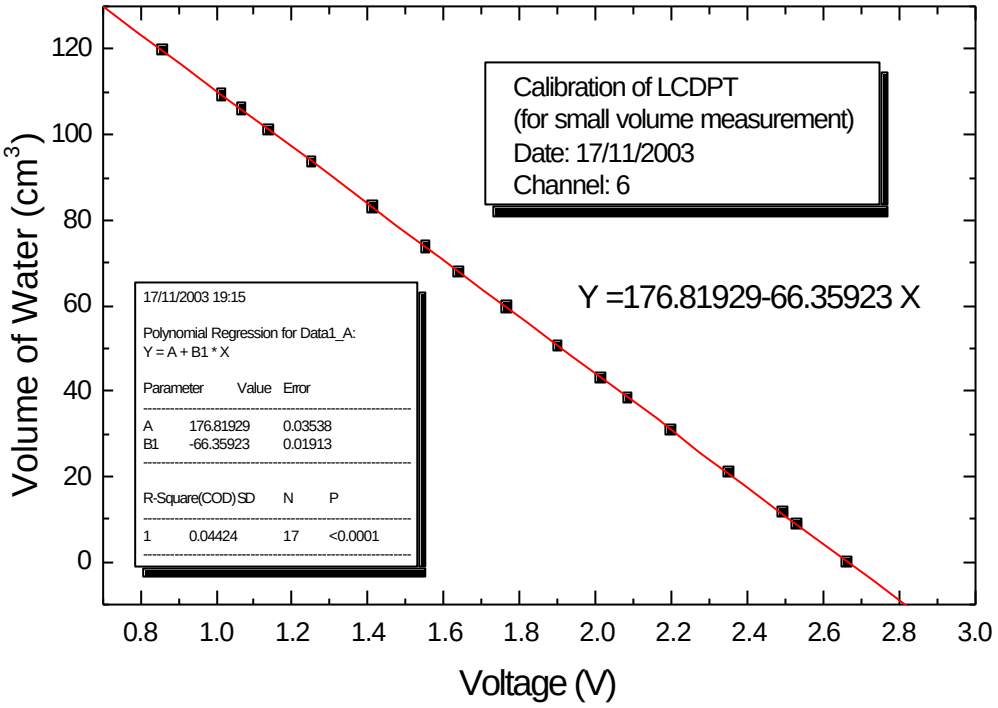

Fig. 2.13 Calibration curve of LCDPT for small volume

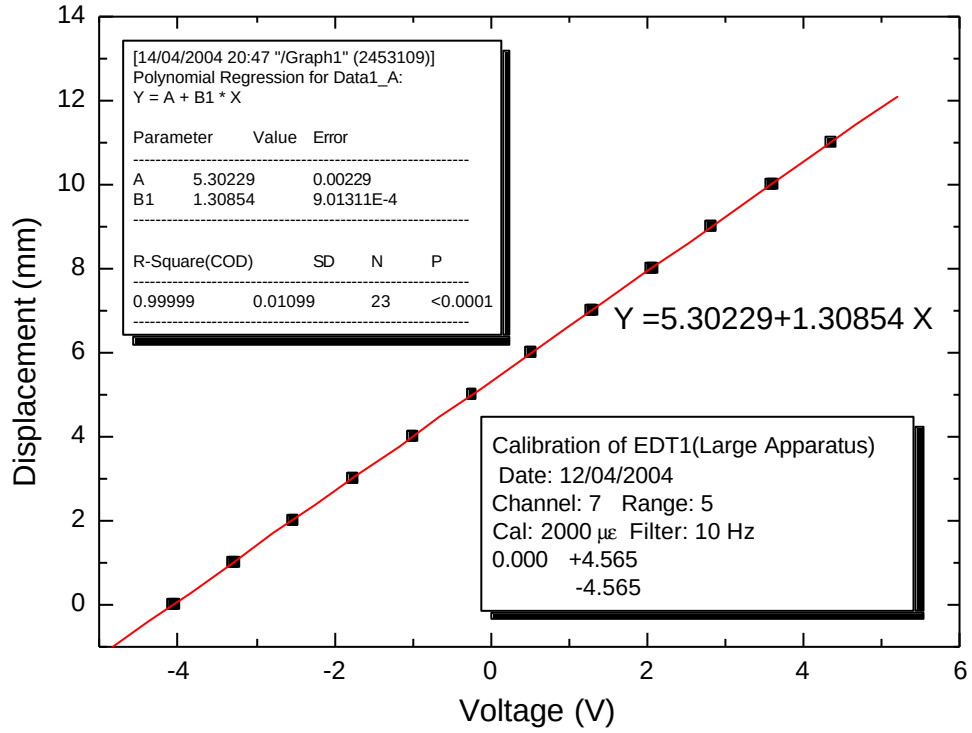

Fig. 2.14 Calibration curve of external transducer1 (EDT1)

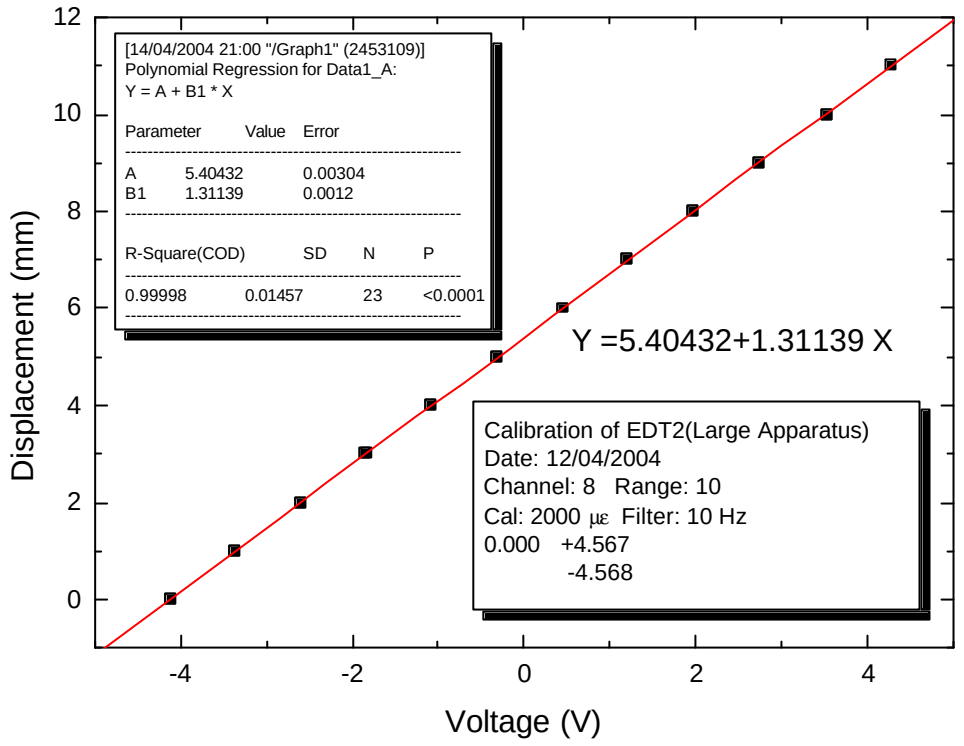

Fig. 2.15 Calibration curve of external transducer2 (EDT2)

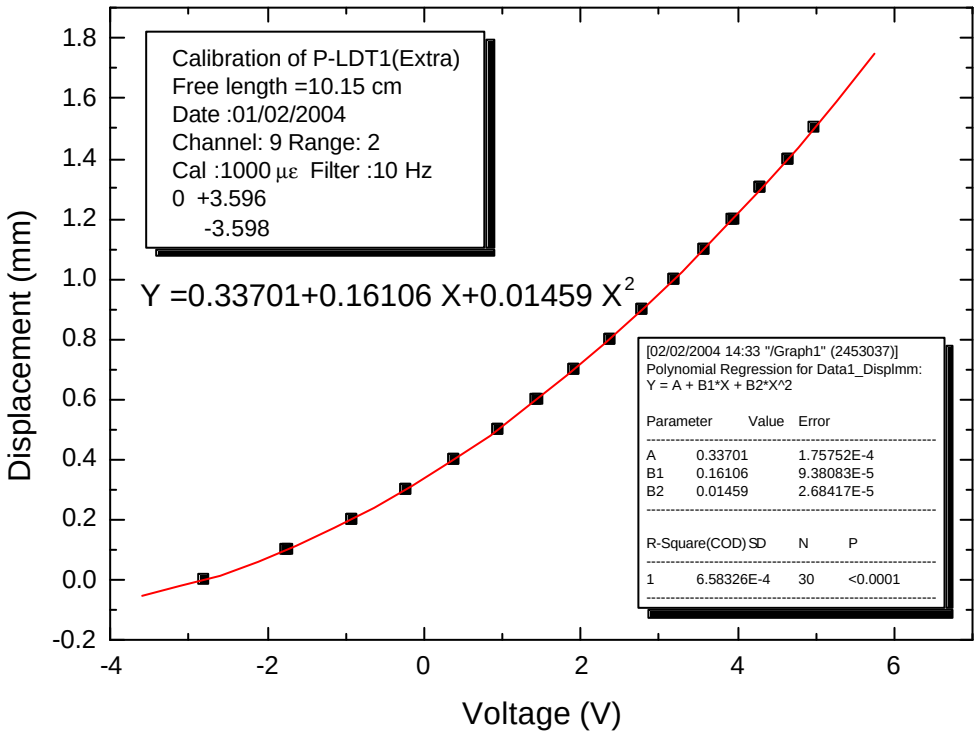

Fig. 2.16 Calibration curve of PLDT 1 (Extra)

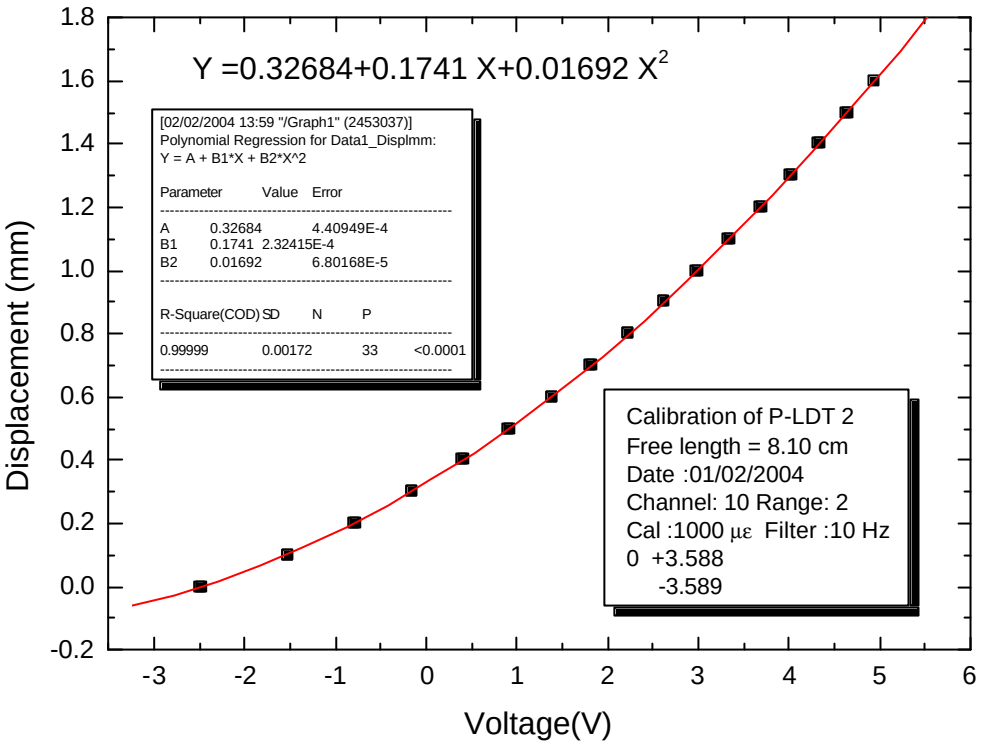

Fig. 2.17 Calibration curve of PLDT 2

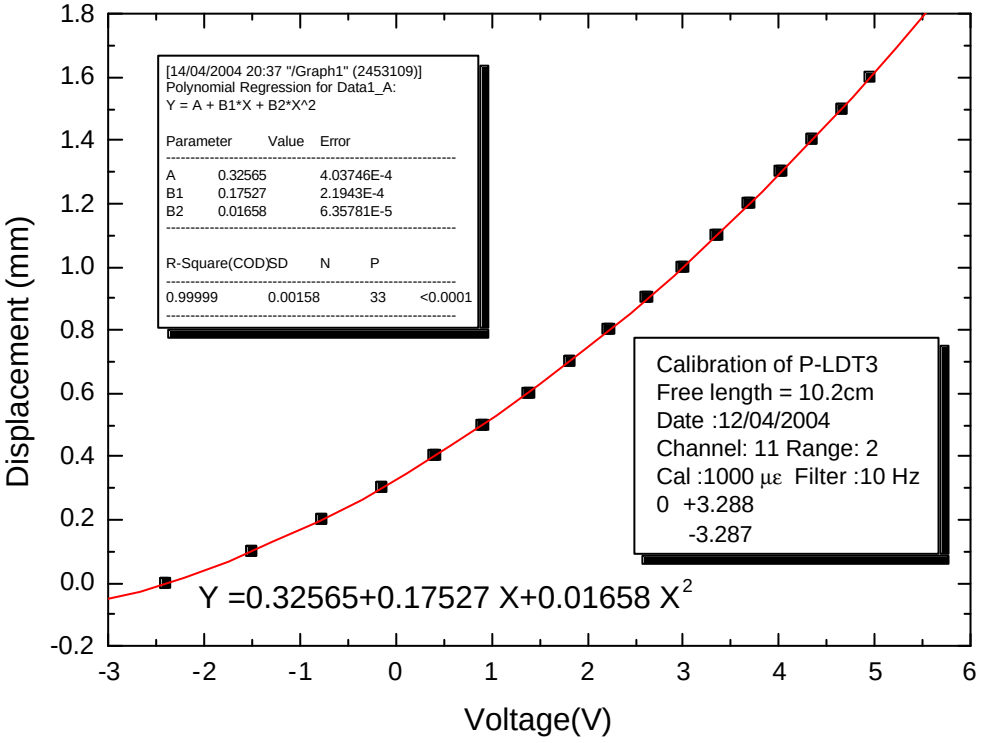

Fig. 2.18 Calibration curve of PLDT 3

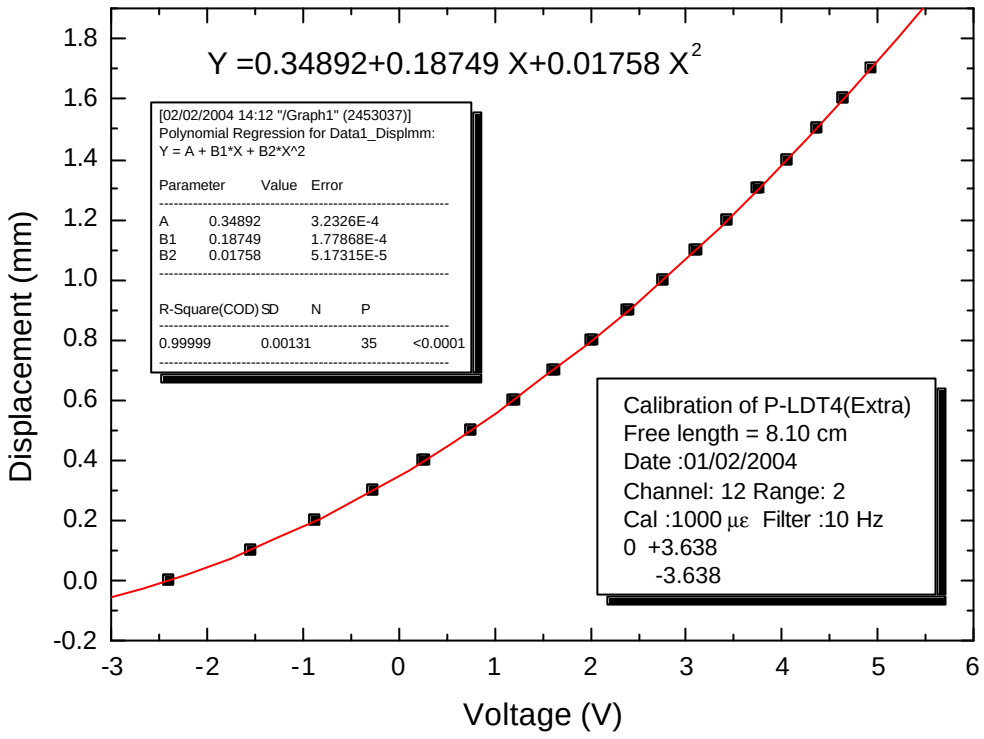

Fig. 2.19 Calibration curve of PLDT 4 (Extra)

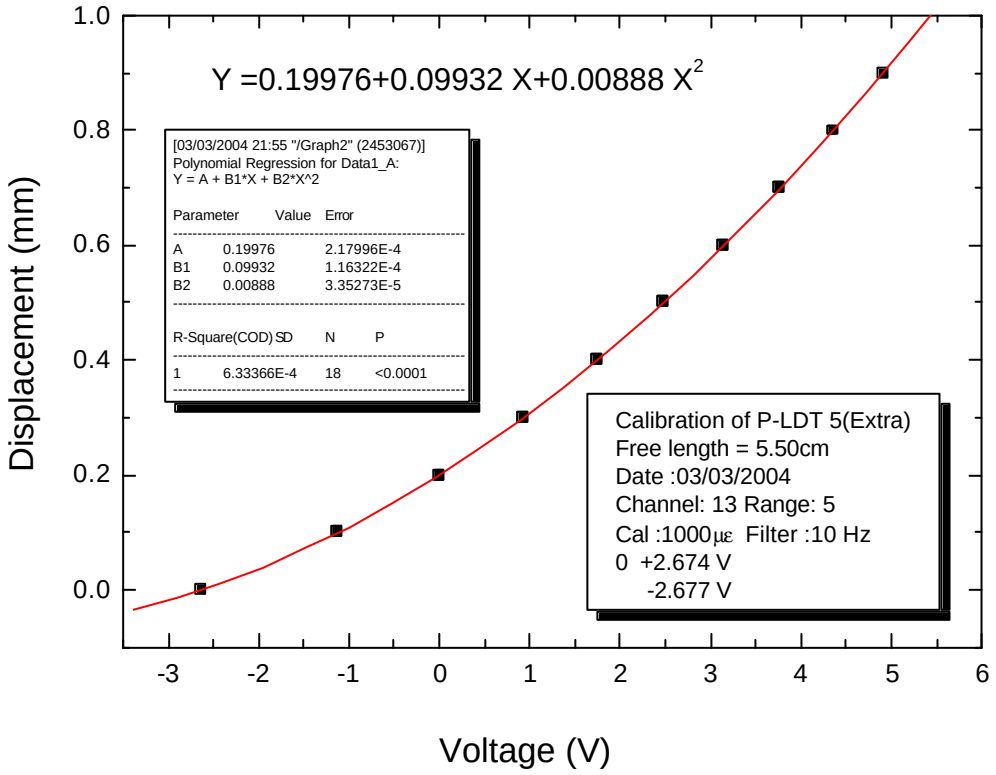

Fig. 2.20 Calibration curve of PLDT 5 (Extra)(small range)

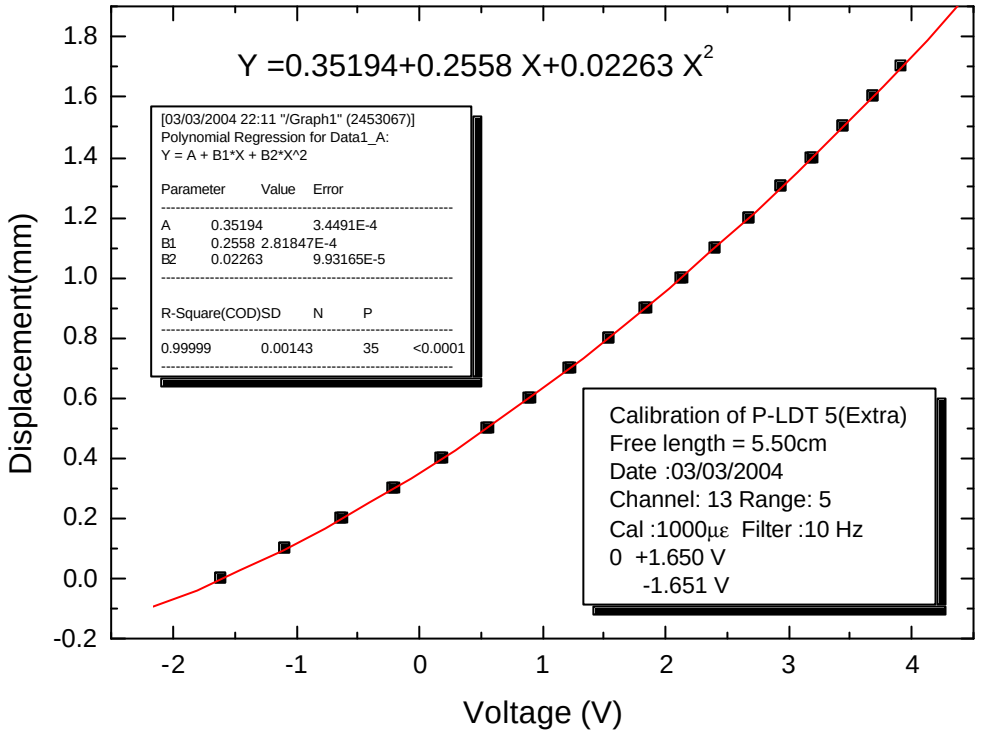

Fig. 2.21 Calibration curve of PLDT 5 (Extra)(large range)

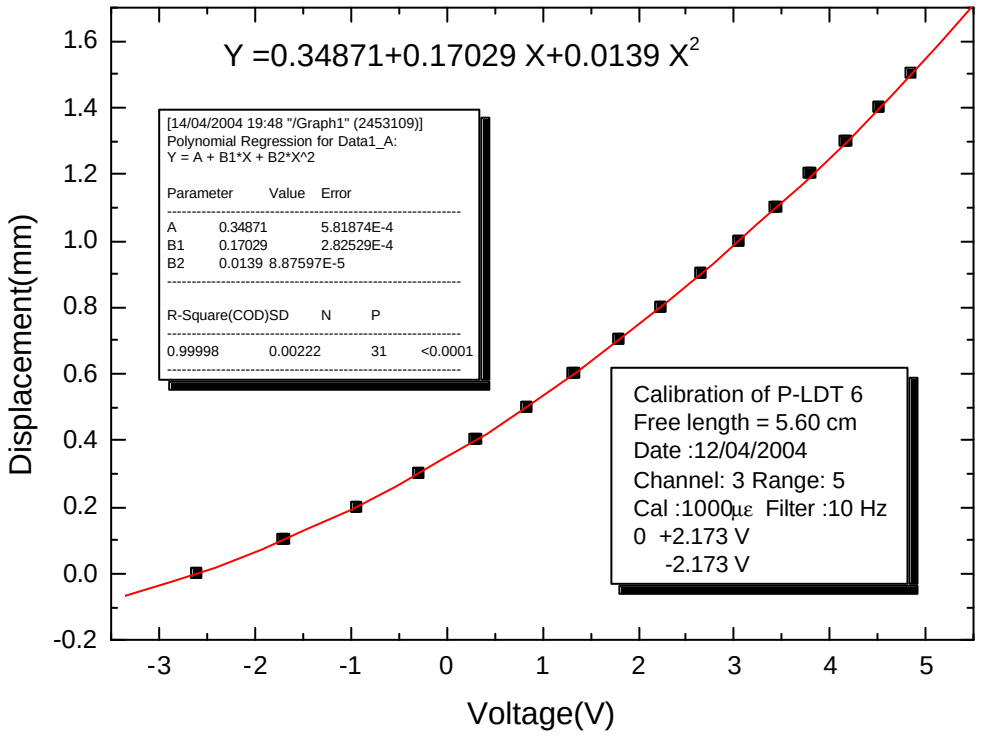

Fig. 2.22 Calibration curve of PLDT 6 (Extra)

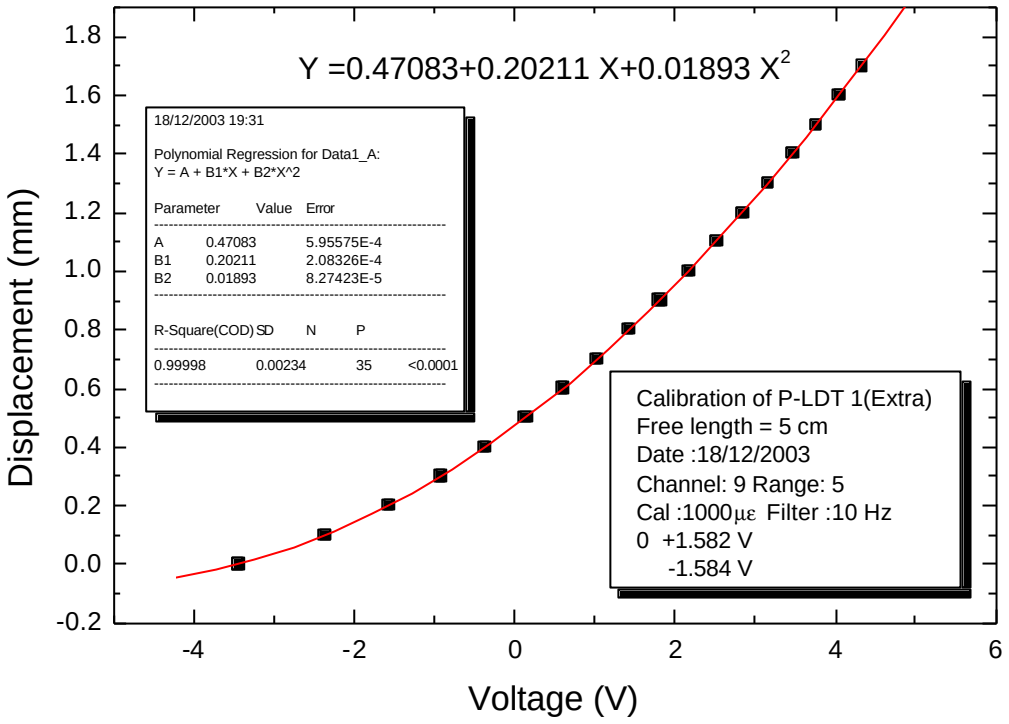

Fig. 2.23 Calibration curve of PLDT 1 (Extra)(5cm)

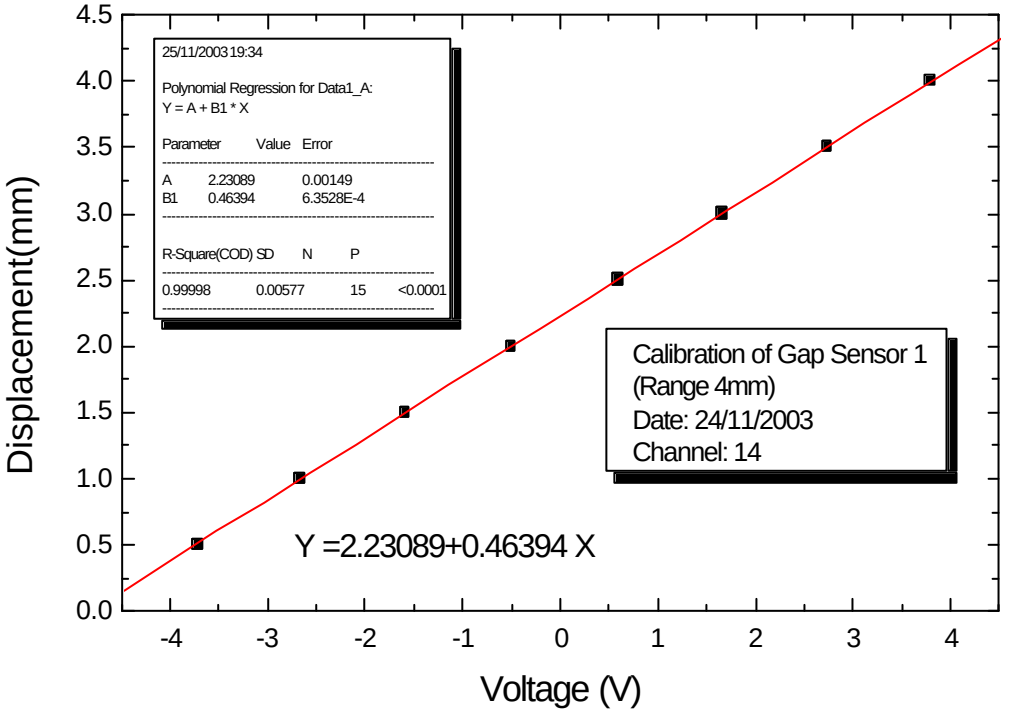

Fig. 2.24 Calibration curve of Gap Sensor 1 (GS1)

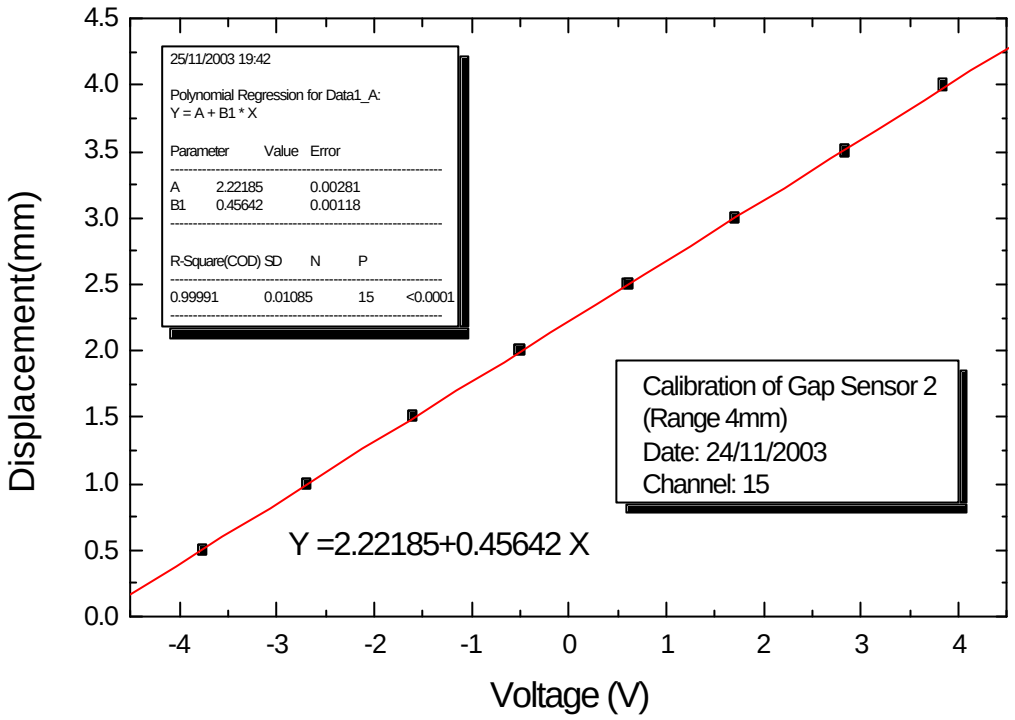

Fig. 2.25 Calibration curve of Gap Sensor 2 (GS2)

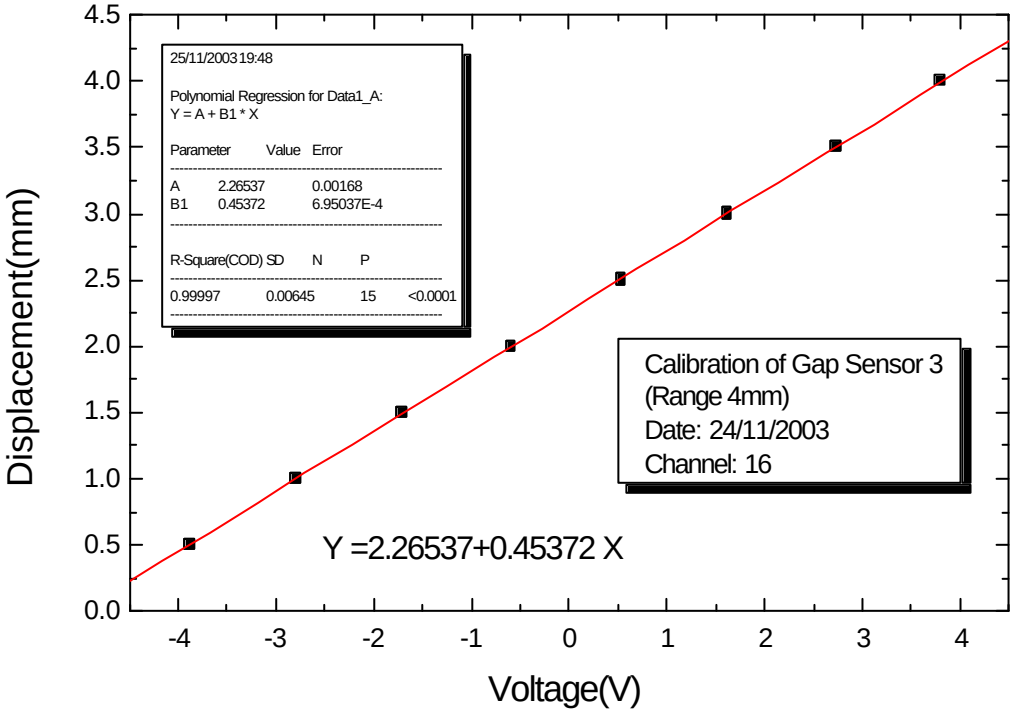

Fig. 2.26 Calibration curve of Gap Sensor 3 (GS3)

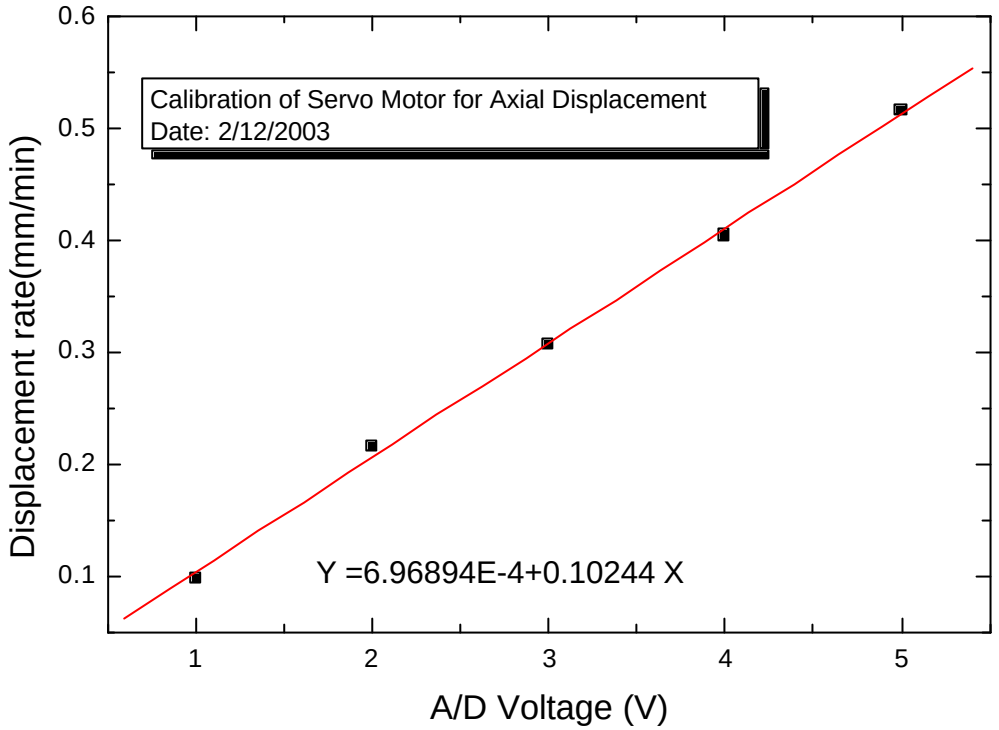

Fig. 2.27 Calibration curve of servomotor for axial displacement rate

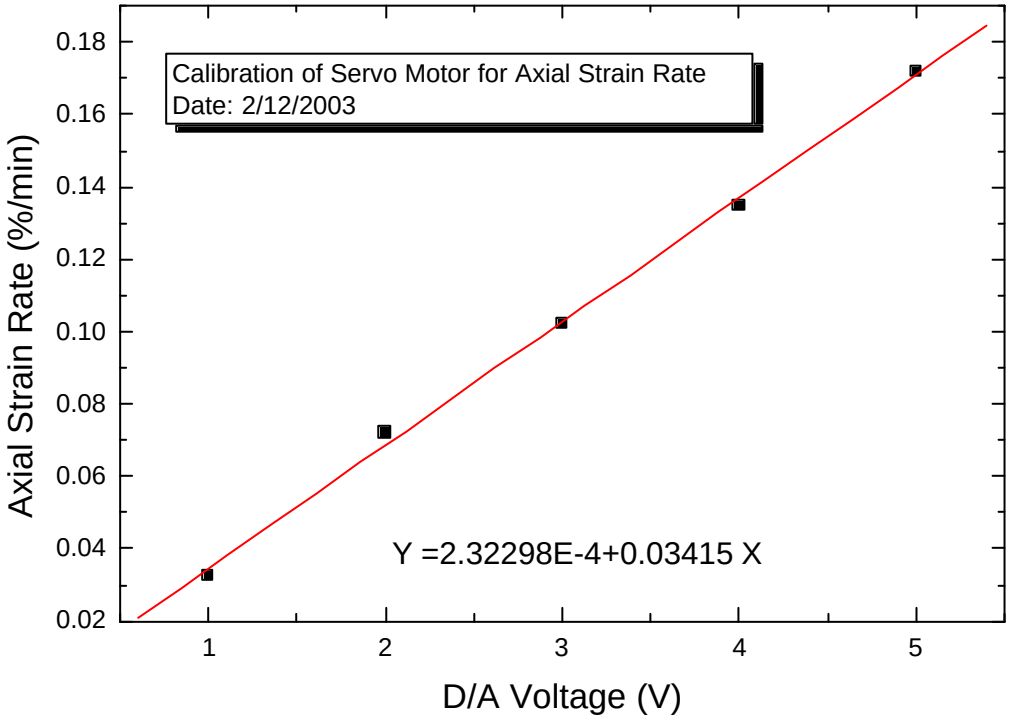

Fig. 2.28 Calibration curve of servomotor for axial strain rate

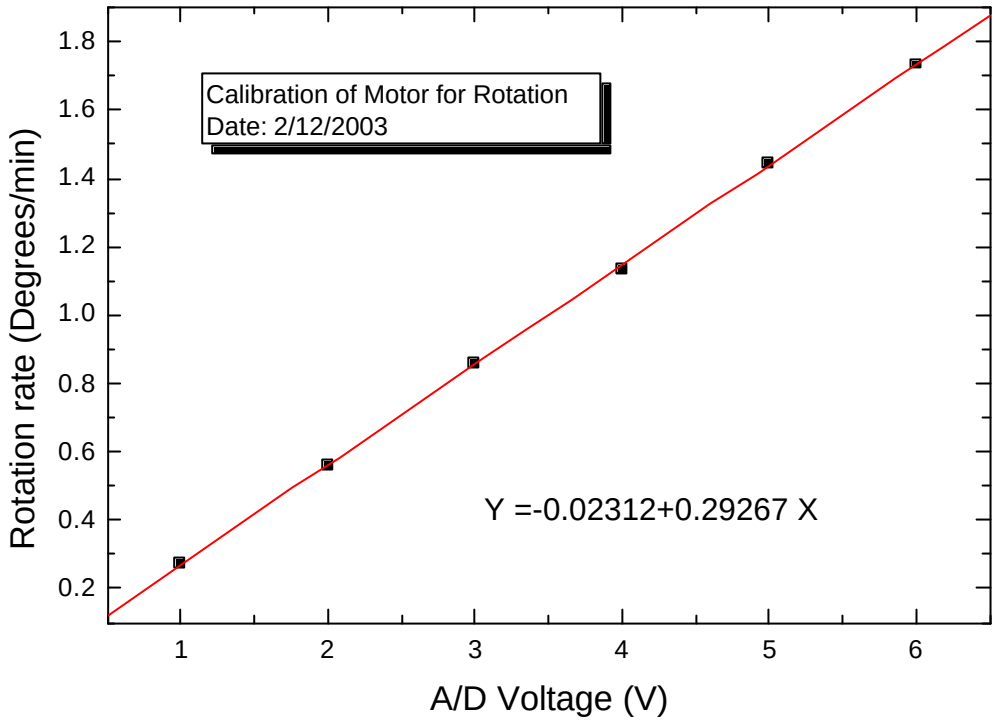

Fig. 2.29 Calibration curve of servomotor for rotation rate

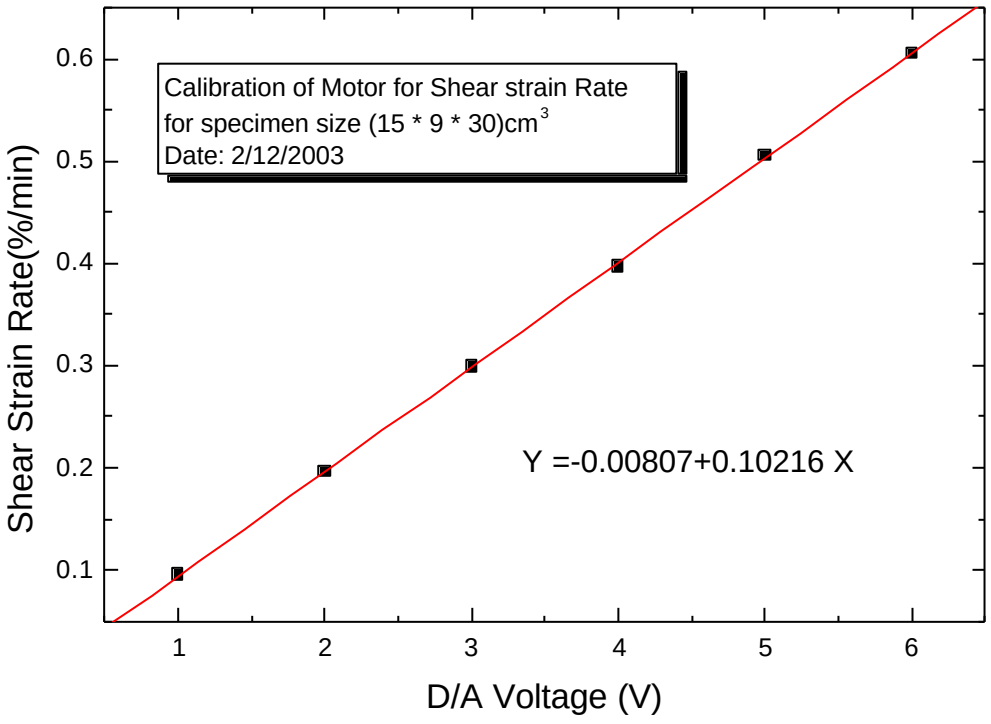

Fig. 2.30 Calibration curve of servomotor for shear strain rate

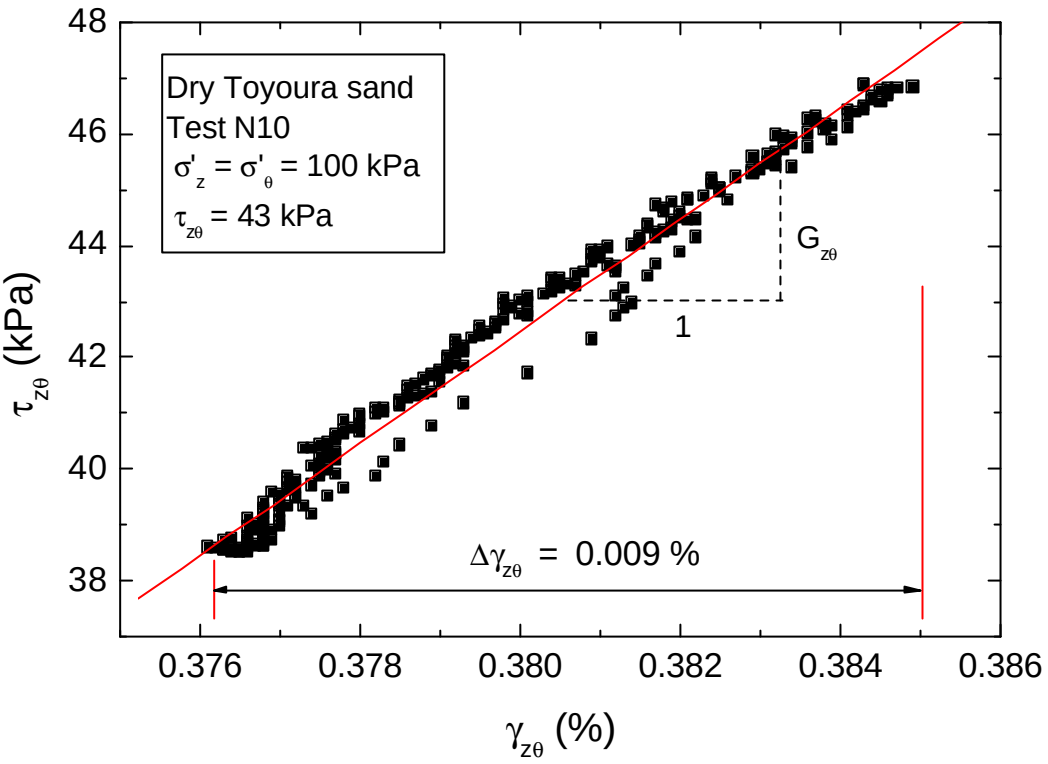

Fig. 2.31 Typical evaluation of shear modulus using small-sized HCA

CHAPTER 3: FORMULATION OF STRESSES AND STRAINS IN HOLLOW CYLINDER SPECIMEN

3.1 Background

Torsional shear tests on hollow cylinder specimens have the advantage of individual control of vertical normal stress, cell pressure and applied shear stress in producing more general stress conditions than those in the conventional triaxial or plane strain tests including rotation of principal stress axes (Tatsuoka et al, 1986). However, formulations of average stresses and strains of the specimen are based on many assumptions because the behavior of soil is not well understood for the moment. Therefore there is no concrete agreement among researchers on the formulation of stresses and strains. Most researchers assume the linear elasticity of the material when calculating radial and circumferential stresses (σ_r and σ_θ) and perfect plasticity when calculating shear stresses (Hight et al, 1983; Saada, 1980). On the other hand, specimen non-uniformity, end restraint effect and system compliance make the stress distribution over the specimen highly complicated.

Calculation of strains that are measured externally assumes a uniform deformation over the specimen, which may not be true. In addition, changes of specimen diameter (both outer and inner) cannot be measured easily using external transducers. Therefore it is taken into account by assuming a proportional change of outer and inner diameter (JGS, 1998). Furthermore, the effect of end restraint and bedding error is crucial in external measurements when the contact between the top cap and specimen top surface is made improperly. Therefore local

measurement of strains locally is gaining popularity among researchers due to its closeness to the real measurements. A technique for local measurement of strains in hollow cylinder apparatus using three pin-typed local deformation transducers (PLDT) was introduced recently (Hong Nam, et al 2001). The original version of PLDT system consists of three PLDTs arranged in a triangle. PLDTs are attached to the specimen using special hinges and one hinge supports two ends of PLDTs. Refer to Master thesis of Hong Nam (2001) for more details on original version of PLDTs. But in the present study, when this system is applied to specimens with outer diameter less than 20 cm, it was found that the larger curvature of the specimen creates problems in arranging the PLDTs using common hinges. Therefore this problem was solved by modifying the original version of PLDT system by separating the three PLDTs using separate hinges. In the modified system, one hinge supports only one end of PLDT. It gives more flexibility in arranging them on the specimen. This chapter describes the formulation of stresses and formulation of local strains using the modified version of PLDTs in detail.

3.2 Void ratio and relative density

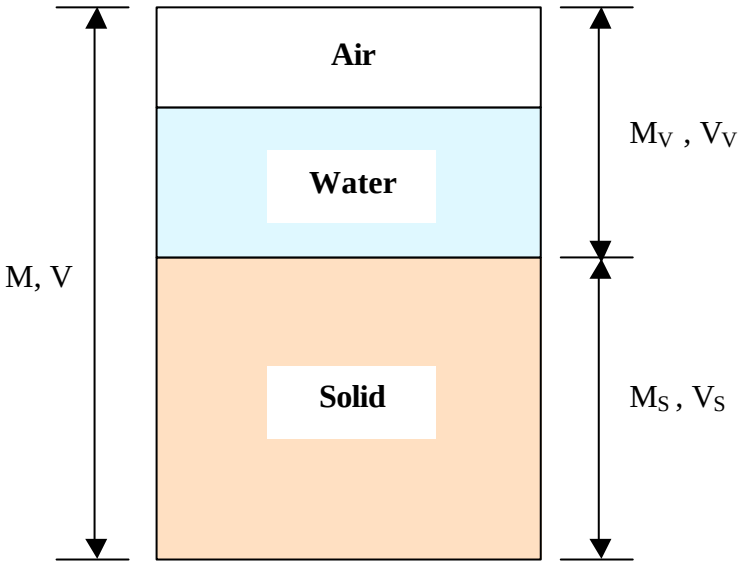

Fig. 3.1 Phase diagram of soil

Void ratio is defined as,

$$e = \frac{V_V}{V_S} = \frac{V - V_S}{V_S} \qquad (3\text{-}1)$$

Where, V_V is the volume of voids, V_S is the volume of solids and V is the total volume of the specimen.

$$\Rightarrow \frac{V}{V_S} = 1 + e \qquad (3\text{-}2)$$

by taking the derivative,

$$de = \frac{dV_S}{V_S} \qquad (3\text{-}3)$$

Assuming solid soil particles are incompressible ($dV_S = 0$) the following expression can be obtained.

$$dV = dV_V$$

$$de = -\frac{dV}{V_S} = -\frac{(1+e)}{V} dV = -(1+e) de_{vol} \qquad (3\text{-}4)$$

After integrating,

$$\int_{e_0}^{e} -\frac{de}{(1+e)} = \int_{e_0}^{e_{vol}} de_{vol}$$

$$\Rightarrow e_{vol} = \ln \frac{(1+e_0)}{(1+e)} \qquad (3\text{-}5)$$

$$\Rightarrow e = \frac{(1+e_0)}{\exp(e_{vol})} - 1$$

In case of dry soil where there is no water,

$$M = M_S \text{ (assuming weight of air is negligible)}$$

Where M is the total mass of soil and M_S is the weight of solids

Eq. (3-2) gives,

$$\Rightarrow \frac{V}{V_S} = 1 + e$$

$$\Rightarrow \frac{M}{V_S} \times \frac{V}{M} = 1 + e$$

$$\Rightarrow \frac{M_S}{V_S} \times \frac{V}{M} = 1 + e \quad (M_S = M \text{ for dry soil})$$

By definition,

$$\frac{M_S}{V_S} = G_S \text{ (Specific gravity of soil)} \quad \text{and} \quad \frac{M}{V} = r \text{ (Dry density of soil)}$$

$$\Rightarrow \frac{G_S}{r} = 1 + e \quad \Rightarrow \quad e = \frac{G_S}{r} - 1 \qquad (3\text{-}6)$$

Relative density (Dr) of soil is defined as,

$$D_r = \frac{(e_{\max} - e)}{(e_{\max} - e_{\min})} \times 100(\%) \qquad (3\text{-}7)$$

3.2.1 Void ratio functions

Void ratio function is used to compare the quasi-elastic deformation properties among specimens with different void ratios. Following are some of the widely used proposals for void ratio functions.

$f(e) = \frac{(2.17 - e)^2}{(1 + e)}$ (Hardin and Richart, 1963)

$f(e) = \frac{(2.97 - e)^2}{(1 + e)}$ (Hardin and Richart, 1963)

$f(e) = \frac{1}{e^{1/3}}$ (Jamiolkowski et al, 1991)

$f(e) = e^{-2.4}$ (Shibuya et al, 1997)

$f(e) = \frac{(7.32 - e)^2}{(1 + e)}$ (Kokusho et al, 1985)

In the present study, the applicability of all the above mentioned void ratio functions for Toyoura sand and Hime gravel specimens was checked

3.3 Stress formulation

As shown in Figure 3.2, external loads acting on the hollow cylinder specimen are known to be the axial load F_z, torque T, inner cell pressure P_i and outer cell pressure P_o. Therefore hollow cylinder specimens have four degrees of freedom from the point of view of loads. The four surface tractions induce four stress components in a soil element and therefore four corresponding strain components. The four stresses are radial stress s_r, circumferential stress s_q, axial stress s_z and shear stress t_{zq}. Corresponding strain components are ε_r, ε_θ, ε_z, $\gamma_{z\theta}$, respectivily.

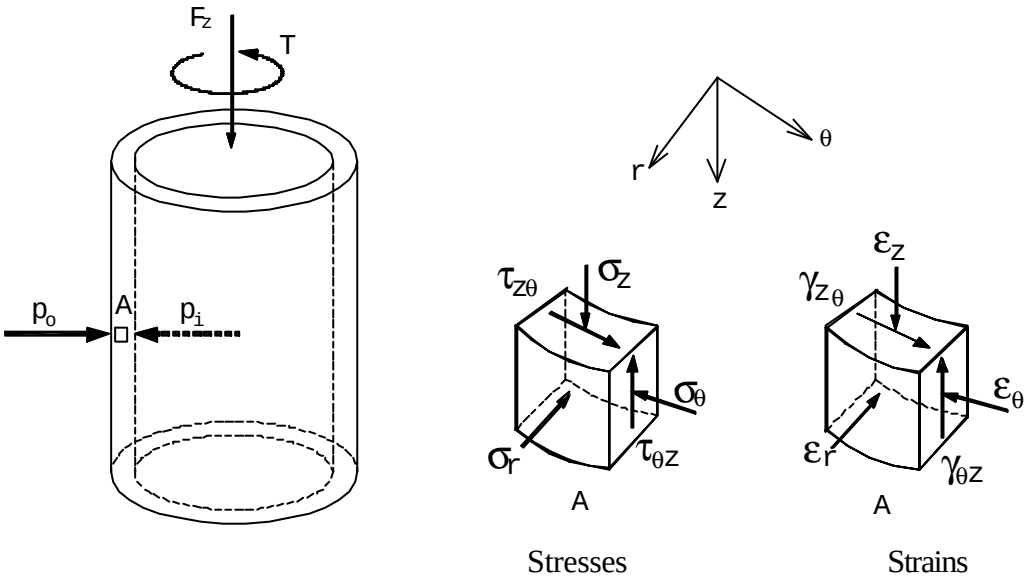

Fig. 3.2. Stresses and strains in soil element A

3.3.1 Radial and circumferential stresses s_r and s_q

It should be noted that the actual distribution of stresses in the specimen is very complicated due to the end restraint effect and bedding error. Timoshenko and Goodier (1970) gave a solution to the problem of a right hollow cylinder subjected to uniform inner pressure p_i and outer pressure p_o. Stress distribution is assumed to be symmetrical with respect to the axis z of the hollow cylinder and the stress components do not depend on radial angle q and are a

function of radius r only. As a result, shear stress t_{rq} is equal to 0. The equation of equilibrium in the radial direction yields,

$$\frac{\partial s_r}{\partial r} + \frac{s_r - s_q}{r} + w = 0 \qquad (3\text{-}8)$$

in which w is body force. When w equals to 0, eq. (3-8) is satisfied by the following,

$$s_r = \frac{B}{r^2} + 2C \qquad (3\text{-}9)$$

$$s_q = -\frac{B}{r^2} + 2C \qquad (3\text{-}10)$$

Where B and C are constants, which can be obtained from the following boundary conditions.

$$s_r|_{r=R_i} = p_i \qquad (3\text{-}11)$$

$$s_r|_{r=R_o} = p_o \qquad (3\text{-}12)$$

Where R_o and R_i denote current outer and inner radii of the specimen, respectively.

By substituting eq. (3-11) and eq. (3-12) into eq. (3-9) and eq. (3-8), we get,

$$s_r = \frac{p_o R_o^2 - p_i R_i^2}{R_o^2 - R_i^2} - \frac{R_i^2 R_o^2 (p_o - p_i)}{R_o^2 - R_i^2}\frac{1}{r^2} \qquad (3\text{-}13)$$

$$s_q = \frac{p_o R_o^2 - p_i R_i^2}{R_o^2 - R_i^2} + \frac{R_i^2 R_o^2 (p_o - p_i)}{R_o^2 - R_i^2}\frac{1}{r^2} \qquad (3\text{-}14)$$

Average stress components are computed with weighting and without weighting (Ampadu, 1991) as follows.

Averaging without weighting

$$\bar{s}_r = \frac{\int_{R_i}^{R_o} s_r\, dr}{\int_{R_i}^{R_o} dr} \qquad (3\text{-}15) \qquad\qquad \bar{s}_q = \frac{\int_{R_i}^{R_o} s_q\, dr}{\int_{R_i}^{R_o} dr} \qquad (3\text{-}16)$$

By substituting eq. (3-13) into eq. (3-15) and eq. (3-14) into eq. (3-16), we get,

$$\bar{s}_r = \frac{p_o R_o + p_i R_i}{R_o + R_i} \qquad (3\text{-}17)$$

$$\bar{s}_q = \frac{p_o R_o - p_i R_i}{R_o - R_i} \qquad (3\text{-}18)$$

These equations were commonly used by a number of researchers such as Hight et al. (1983) and Saada (1988).

Averaging with weighting

$$\int_{R_i}^{R_o} s_r\, r\, dr = \int_{R_i}^{R_o} \bar{s}_r\, r\, dr \qquad (3\text{-}19) \qquad\qquad \int_{R_i}^{R_o} s_q\, r\, dr = \int_{R_i}^{R_o} \bar{s}_q\, r\, dr \qquad (3\text{-}20)$$

$$\bar{s}_r = \frac{\int_{R_i}^{R_o} s_r\, r\, dr}{\int_{R_i}^{R_o} r\, dr} \qquad (3\text{-}21) \qquad\qquad \bar{s}_q = \frac{\int_{R_i}^{R_o} s_q\, r\, dr}{\int_{R_i}^{R_o} r\, dr} \qquad (3\text{-}22)$$

By substituting eq. (3-13) into eq. (3-21) and eq. (3-14) into eq. (3-22), we get

$$\bar{s}_r = \frac{p_o R^2_o - p_i R^2_i}{R^2_o - R^2_i} - \frac{2R^2_i R^2_o (p_o - p_i)}{(R^2_o - R^2_i)^2} \ln\left(\frac{R_o}{R_i}\right) \quad (3\text{-}23)$$

$$\bar{s}_q = \frac{p_o R^2_o - p_i R^2_i}{R^2_o - R^2_i} + \frac{2R^2_i R^2_o (p_o - p_i)}{(R^2_o - R^2_i)^2} \ln\left(\frac{R_o}{R_i}\right) \quad (3\text{-}24)$$

Miura et al. (1986a) used the assumption relating to linear variation of radial stress and equilibrium condition to obtain average stresses in different forms.

In this study, the outer and inner cell pressures are kept equal to each other ($p_i = p_o$), therefore, eqs. (3-17) and (3-18) yield $\bar{s}_r = \bar{s}_q = p_o$, which can be also derived from eqs. (3-23) and eqs. (3-24).

3.3.2 Vertical stress s_z

Average vertical stress at the middle height of the specimen can be computed as follows:

$$\bar{s}_z = \frac{LC}{A} + s_h + s_g + s_{mem} \quad (3\text{-}25)$$

In which :

LC : Axial load detected by the inner load cell,

A: Cross-sectional area of the specimen,

$A = p(R_o^2 - R_i^2)$,

s_h : Horizontal stress ($= s_r = s_q$),

s_g : Overburden stress of the specimen due to its self-weight at its middle height,

$s_g = g_d H/2$

g_d : Unit weight of the specimen,

H: Height of the specimen,

s_{mem} : Correction for membrane stress (Tatsuoka et al., 1986),

If $\varepsilon_z > 0$, $\sigma_{mem} = 0$

If $\varepsilon_z < 0$, $\sigma_{mem} = -\frac{3}{8} \times e_z \times t_{mem} \times \frac{E_{mem}}{(R_o - R_i)}$

Where,

e_z = Axial strain

t_{mem} = Thickness of membrane = 0.031 cm

E_{mem} = Young's modulus of membrane = 1492.11 kPa

Note that the output from the inner load cell is initialized at the isotropic stress state ($s_z = s_q = s_r$).

3.3.3 Shear stress t_{zq}

Shear stress t_{zq} acting on a soil element with the area $dA = r\,dq\,dr$ can be computed as follows.

$$dT = t_{zq} r^2 dq dr$$

$$T = \int_{R_i}^{R_o} \int_0^{2p} t_{zq} r^2 dq dr$$

$$T = 2p \int_{R_i}^{R_o} t_{zq} r^2 dr$$

If the material is perfectly plastic, then the distribution of shear stress is uniform and constant. Thus, we get

$$T = 2p\, t_{zq} \int_{R_i}^{R_o} r^2 dr$$

$$T = \frac{2}{3} p\, t_{zq} \left(R_o^{\,3} - R_i^{\,3} \right)$$

$$t_{zq} = \frac{3T}{2p\left(R_o^{\,3} - R_i^{\,3} \right)} \qquad \text{(3-26)}$$

If the material is linear elastic, then the distribution of shear stress is linear along the radial direction. In this case, by defining t_{max} as the shear stress at $r = R_o$, the shear stress at any distance can be computed by the following equation.

$$t_{zq} = \left(\frac{t_{\max}}{R_o} \right) r$$

The average shear stress $\bar{t}^*_{zq}$ can be computed by the following equation.

$$\overline{t}^*_{zq} \int_{R_i}^{R_o} r^2 dr = \int_{R_i}^{R_o} \frac{t_{\max}}{R_o} r^3 dr$$

$$\overline{t}^*_{zq} = \frac{3}{4} \frac{t_{\max}}{R_o} \left(\frac{R_o^4 - R_i^4}{R_o^3 - R_i^3} \right) \quad (3\text{-}27)$$

On the other hand, if the equivalent shear stress that gives the same shear force as the linearly distributed shear stress is considered, then the average shear stress $\bar{t}^{**}_{zq}$ can be computed as follows.

$$\bar{t}^{**}_{zq} = \frac{1}{2} \frac{t_{\max}}{R_o} (R_o + R_i) \quad (3\text{-}28)$$

By equating eqs. (3-26) and (3-27) to get t_{max} and substituting it into the eq. (3-28), we get

$$\bar{t}^{**}_{zq} = \frac{T}{p (R_o - R_i)(R_o^2 + R_i^2)} \quad (3\text{-}29)$$

In this study, shear stress is averaged from eqs. (3-29) and (3-26) as shown below.

$$\bar{t}_{zq} = \frac{1}{2} \left[\frac{3T}{2p (R_o^3 - R_i^3)} + \frac{T}{p (R_o - R_i)(R_o^2 + R_i^2)} \right] \quad (3\text{-}30)$$

$$T = T_{LC} + T_{mem}$$

Where,

T_{LC} = Torque detected by the inner load cell

$$T_{mem} = -2 \times \frac{p}{3} \times t_{mem} \times \frac{E_{mem}}{H} \times angle \cdot of \cdot rotation \times \left(R_o^{\ 3} + R_i^{\ 3} \right)$$

Angle of rotation is detected from the potentiometer

3.3.4 Principal stresses

Principal stresses can be computed from the four stress components.

$$s_1 = \frac{s_Z + s_q}{2} + \sqrt{\frac{(s_Z - s_q)^2}{2} + (t_{zq})^2} \qquad (3\text{-}31)$$

$$s_2 = s_r \qquad (3\text{-}32)$$

$$s_3 = \frac{s_Z + s_q}{2} - \sqrt{\frac{(s_Z - s_q)^2}{2} + (t_{zq})^2} \qquad (3\text{-}33)$$

The angle d between the direction of the major principal stress s_1 with the vertical direction is calculated by

$$d = \frac{1}{2} \arctan \frac{2t_{zq}}{s_z - s_q} \qquad (3\text{-}34)$$

3.3.5 Stress – nonuniformity coefficients

The stress-strain nonuniformity depends on a number of factors such as stress state, specimen size and dimension, and material constitutive law. Several coefficients have been proposed as follows.

Hight et al. (1983) proposed the following criteria on normalized parameter b_1 and nonuniformity stress parameter b_3.

$$b_1 = \frac{\overline{|s^* - \bar{s}|}}{s_L} < 0.11 \qquad (3\text{-}35)$$

$$b_3 = \frac{\int_{R_i}^{R_o} |s(r) - \overline{s^*}| dr}{(R_o - R_i) s_L} < 0.11 \qquad (3\text{-}36)$$

$\overline{s^*}$: Real average

$\bar{s}$: Calculated average

s_L : Stress level

However, Vaid et al. (1990) criticized these parameters, and proposed another criterion using the parameter b_R in terms of nonuniformity in principal stress ratio

$$b_R = [(s'_1/s'_3)_{\max} - (s'_1/s'_3)_{\min}]/(s'_1/s'_3)_{av} < 0.2 \qquad (3\text{-}37)$$

Yoshimine et al. (1998) also suggested the following parameter relating to the nonuniformity of radial stress s_r without giving concrete criteria for evaluating the nonuniformity based on it.

$$\frac{p_o - p_i}{s_r} = \frac{-(b - \sin^2 d)}{\sin 2d}\left(\frac{R_o}{R_i} - \frac{R_i}{R_o}\right)\frac{t_{zq}}{s_r} \qquad (3\text{-}38)$$

Eq. (3-38) can be rewritten in the following form.

$$\frac{p_o - p_i}{s_r} = -(b - \sin^2 d)\left(\frac{R_o}{R_i} - \frac{R_i}{R_o}\right)\frac{\sin f_{mob}}{1 + (2b-1)\sin f_{mob}}$$

In which f_{mob} is the mobilized angle of friction, and

b is the intermediate principal stress coefficient defined as $b = (s_2 - s_3)/(s_1 - s_3)$.

In the present study, the outer and inner cell pressures were kept equal ($p_o = p_i$)

3.4 Strain formulation

Axial strain e_z, radial strain e_r, circumferential strain e_q, and shear strain g_{zq} are the four strain components of the soil element to be determined. As shown in Fig. 3.3, e_r and e_q of a soil element can be calculated from,

$$e_r = -\frac{u + (du/dr)dr - u}{dr} = -\frac{du}{dr} \qquad (3\text{-}39)$$

$$e_q = -\frac{(u + r)dq - rdq}{rdq} = -\frac{u}{r} \qquad (3\text{-}40)$$

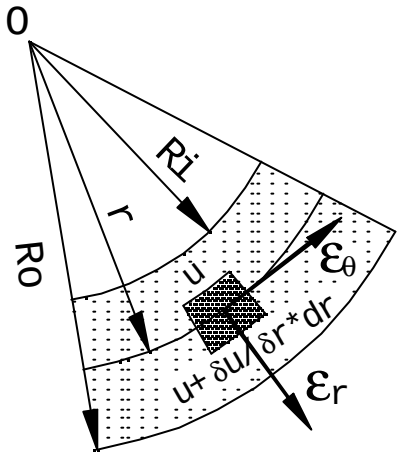

Fig. 3.3. Radial and circumferential strains of a soil element

Combining eqs. (3-39) and (3-40) yields

$$\frac{de_q}{dr} + \frac{1}{r}(e_q - e_r) = 0 \qquad (3\text{-}41)$$

If it is assumed that distribution of u is linear in the radial direction,

$$u = \frac{u_o - u_i}{R_o - R_i} r + \frac{u_i R_o - u_o R_i}{R_o - R_i} \qquad (3\text{-}42)$$

then e_r becomes a constant given by

$$\bar{e}_r = -\frac{u_o - u_i}{R_o - R_i} \qquad (3\text{-}43)$$

And $\bar{e}_q$ can be calculated by

$$\bar{e}_q \int_{R_i}^{R_o} r dr = \int_{R_i}^{R_o} e_q \, r dr = -\int_{R_i}^{R_o} \frac{u}{r} r dr$$

$$\bar{e}_q = -\frac{u_o + u_i}{R_o + R_i} \qquad (3\text{-}44)$$

e_z and g_{zq} can be calculated by

$$e_z = - dw / dz \qquad (3\text{-}45)$$

$$\bar{e}_z = -\frac{\Delta H}{H} \qquad (3\text{-}46)$$

$$g_{zq} = r \, dq / dz \qquad (3\text{-}47)$$

$$\bar{g}_{zq} = \frac{(R_o + R_i)}{2} \frac{\Delta q}{H} \qquad (3\text{-}48)$$

In which, $\bar{e}_z$, $\bar{e}_r$, $\bar{e}_q$, $\bar{g}_{zq}$: Average axial, radial, circumferential, and shear strains of the specimen, respectively

u_o, u_i, w : Displacements in the outer radial, inner radial, and vertical directions, respectively of the specimen

H : Height of the specimen

R_o , R_i: Outer and inner radii of the specimen

Δq : Rotation angle.

As external measurements, displacements in the vertical direction are obtained by a pair of external LVDTs and a pair of vertical gap sensors located symmetrically along a diameter of the specimen. Angle of rotation is measured by using a potentionmeter and a horizontal gap sensor aatached to the top cap of the specimen. Low capacity differential pressure transducer (LCDPT) is used to measure the volume change of the specimen.

Measurement of volume change in the inner cylinder is generally difficult, therefore, one additional assumption is made related to the same ratio of the change in inner and outer radius of the specimen by using following formulae (JGS, 1998).

$$D_i = D_{io}\,[(1-e_{vol})/\,(1-e_z)]^{0.5} \qquad (3\text{-}49)$$

$$D_o = D_{oo}\,[(1-e_{vol})/\,(1-e_z)]^{0.5} \qquad (3\text{-}50)$$

e_{vol} : Volumetric strain of the specimen, normally measured by LCDPT

e_z : Axial strain of the specimen, normally measured by LVDT or gap sensor

D_{io} : Initial inner diameter of the specimen

D_{oo}: Initial outer diameter of the specimen

Local strain measurement technique that were implemented in this study to evaluate e_z, e_r, e_q? and g_{zq} is described in 3.5.

3.5 Local strain measurement

3.5.1 Introduction

Although hollow cylinder apparatus is an effective tool in simulating the actual behavior of soil including rotation of principal stress axes, hollow nature of the specimen makes it difficult to obtain a uniform sample. In addition, system compliance problems such as non-parallality of top cap and specimen top surface and miss-alignment of the specimen yield unreliable strain measurements when using externally attached transducers. To overcome this problem, it is essential to measure strains locally. It should be noted, however, that the use of conventional local deformation transducers (LDT) in hollow cylinder specimens is not possible because the rotation of the specimen can damage the LDT and hinge.

3.5.2 Original version of PLDT

Refer to HongNam (2001 and 2004) for more details about the design criteria of the original version of PLDTs. HongNam and Koseki (2001) introduced a local strain measurement technique that can be applied to the hollow cylinder specimens. This system consists of three LDTs with pinned ends to allow for free rotation at the ends (Fig.3.4). One such LDT is called as pin-typed local deformation transducer (PLDT). Pinned ends of each PLDTs are supported by hinges that are attached directly to the membrane using glue. Each hinge has a conical hole to bear the pinned end of PLDT. Three PLDTs are arranged in a right triangle using three hinges, each supporting two PLDT ends. It is advisable to set the PLDT system at the central one third of the specimen to avoid possible bedding error and end restraint effects. By combining outer triangular PLDT system with an inner triangular PLDT system, it is possible to evaluate the four strain components e_z, e_r, $e_{q?}$ and g_{zq} locally. However the limited working space inside the inner cylinder makes it extremely difficult to set an inner triangular PLDT system. With only outer triangular PLDT system, it is possible to measure three strains e_z, $e_{q?}$ and g_{zq} locally.

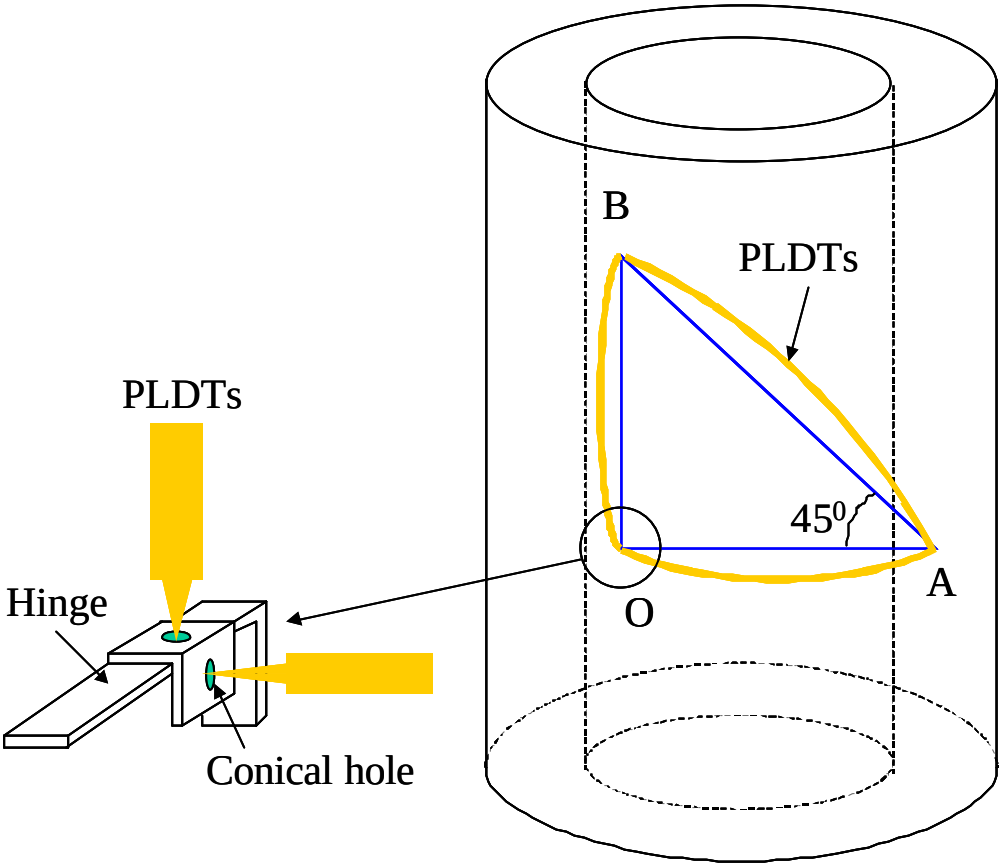

Fig. 3.4. Layout of outer triangular PLDTs in the original version

3.5.3 Formulation of strains using the original version of PLDT system

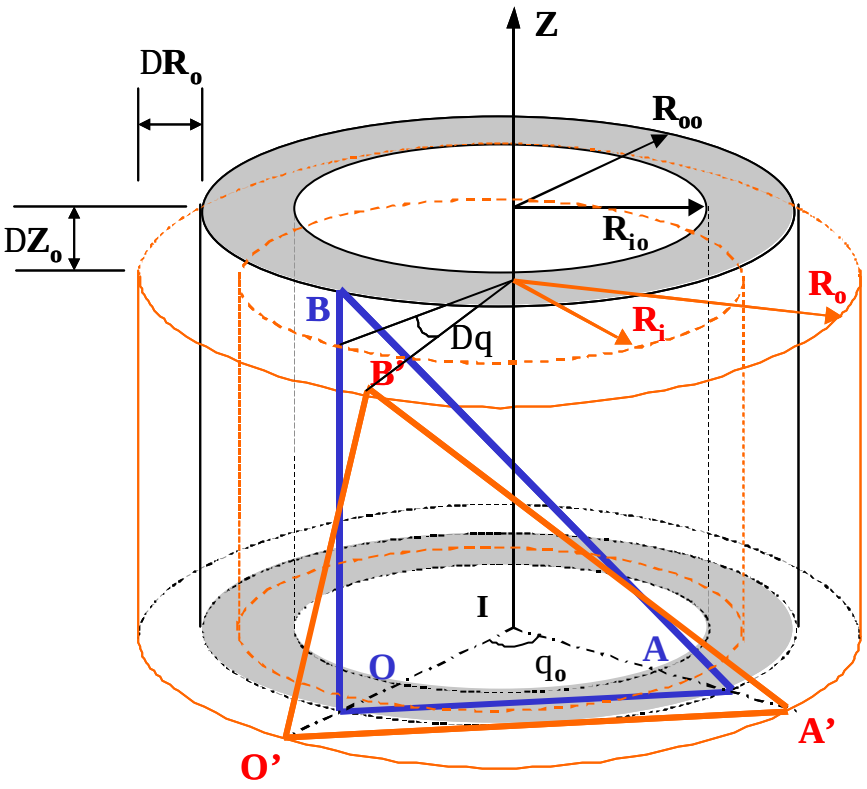

Fig. 3.5. Coordinate system in the original version of PLDTs

Figure 3.5 illustrates the deformation pattern of the portion of specimen that contains the PLDT system. It is assumed that the area of the hinge that is glued to the specimen is negligible and can be considered as a point. Therefore three hinge points O, A and B are creating a right angle triangle at the initial stage. Line OA is parallel to the horizontal plane and line OB is parallel to the vertical plane. After deformation, O, A and B points moved into O', A' and B', respectively. Lengths R_{oo} and R_{io} are the initial outer and inner radii of the specimen, respectively and lengths R_o and R_i are the outer and inner radii of the specimen after deformation, respectively. ΔZ_o, ΔR_o and $\Delta\theta$ are the vertical displacement, change of outer radius and rotation of the specimen portion, respectively.

Three PLDTs can measure the changes in its lengths while loading. Therefore it is possible to obtain lengths O'A', O'B' and A'B' from the calibration curves of PLDTs. But length itself is not enough to formulate strains. Therefore the following two additional assumptions were made.

- The central angle OIA (q_o) made of two ends (O and A) of the horizontal P-LDTs and the intersection (I) of the horizontal plane (containing them) and the symmetrical vertical axis z of the specimen is constant, and
- The specimen remains right hollow cylinder in shape.

Spherical coordinate system (r, q, Z) is used. Outer triangular P-LDT system is considered and r axis is taken to coincide with radial vector IO. Additionally, horizontal plane containing line IO is taken as Z = 0 plane.

At the initial time t_o, the coordinates of 3 points O, A, B are as follows (Fig. 3.5).

O (R_{oo}, 0, 0)

A (R_{oo}, q_o, 0)

B (R_{oo}, 0, Z_{oo})

In which, R_{oo}, q_o, Z_{oo} are the initial outer radius, central angle OIA and vertical distance $\overline{OB}$, respectively.

At the time t, the three points O, A and B move to new positions: O', A' and B', respectively with the corresponding coordinates as shown below.

O' ($R_{oo} + \Delta R_o$, 0, 0) = (R_o, 0, 0)

A' ($R_{oo} + \Delta R_o$, q_o, 0) = (R_o, q_o, 0)

B' ($R_{oo} + \Delta R_o$, q, $Z_{oo} + \Delta Z_o$) = (R_o, q, Z_o)

$$\overline{O'A'} = 2R_o \sin(q_o/2) \rightarrow R_o = \overline{O'A'}/[2\sin(q_o/2)] = \overline{O'A'}\ R_{oo}/\overline{OA} \qquad (3\text{-}51)$$

$$\Delta R_o = R_o - R_{oo} = R_{oo}\,(\overline{O'A'}/\overline{OA} - 1) \qquad (3\text{-}52)$$

Eq. (3-52) shows that horizontal P-LDT can measure the change in the outer radius of the specimen.

$$\overline{O'B'} = [(R_o \cos q - R_o \cos 0)^2 + R_o^2(\sin q - \sin 0)^2 + (Z_o - 0)^2]^{0.5}$$

$$= [2 R_o^2 (1-\cos q) + Z_o^2]^{0.5} \quad (3\text{-}53)$$

$$\overline{A'B'} = \{2 R_o^2 [1- \cos(q - (0 + q_o))] + (Z_o - 0)^2\}^{0.5}$$

$$= \{2 R_o^2 [1 - \cos(q - q_o)] + Z_o^2\}^{0.5} \quad (3\text{-}54)$$

From eq. (3-53) and eq. (3-54), we get:

$$Z_o^2 = \overline{O'B'}^2 - 2 R_o^2 (1 - \cos q) = \overline{A'B'}^2 - 2 R_o^2 [1 - \cos(q - q_o)] \quad (3\text{-}55)$$

$$\overline{A'B'}^2 - \overline{O'B'}^2 = 2 R_o^2 [1 - \cos(q - q_o)] - 2 R_o^2 (1 - \cos q)$$

$$\cos q - \cos(q - q_o) = (\overline{A'B'}^2 - \overline{O'B'}^2) / (2R_o^2)$$

$$-2 \sin(q - q_o/2) \sin(q_o/2) = (\overline{A'B'}^2 - \overline{O'B'}^2) / (2R_o^2)$$

$$\sin(q_o/2 - \Delta q) = (\overline{A'B'}^2 - \overline{O'B'}^2) / [4R_o^2 \sin(q_o/2)]$$

$$q = q_o/2 - \arcsin\{[\overline{A'B'}^2 - \overline{O'B'}^2] / [4R_o^2 \sin(q_o/2)]\}$$

$$\Delta q = q = q_o/2 - \arcsin\{[\overline{A'B'}^2 - \overline{O'B'}^2] / [4R_o^2 \sin(q_o/2)]\} \quad (3\text{-}56)$$

From eq. (3-53) we have:

$$Z_o = [\overline{O'B'}^2 - 2 R_o^2 (1 - \cos q)]^{0.5} \quad (3\text{-}57)$$

$$\Delta Z_o = Z_o - Z_{oo} = [\overline{O'B'}^2 - 2 R_o^2 (1 - \cos q)]^{0.5} - Z_{oo} \quad (3\text{-}58)$$

Eqs. (3-56) and (3-58) show that vertical and diagonal P-LDT can measure shear strain g_{zq} and axial train e_z, respectively at the outer surface of the specimen.

Note that to calculate the average strains of the whole specimen, it is needed to use another triangular P-LDT system to measure strains at the inner surface of the specimen. As a result, we can obtain similar equations that will be referred in the next section with the prime sign to distinguish between two cases.

3.5.3.1 Average strains using both inner and outer triangular P-LDTs

When both inner and outer triangular P-LDTs are employed, four average strain components can be determined as follows.

$e_z = -\Delta Z / Z_{ini}$ (3-59)

$e_r = -(u_o - u_i) / (R_{oo} - R_{io})$ (3-60)

$e_q = -(u_o + u_i) / (R_{oo} + R_{io})$ (3-61)

$g_{zq} = (R_o + R_i)\Delta q /(2Z_{ini})$ (3-62)

$\Delta Z = (\Delta Z_i + \Delta Z_o)/2$ (3-63)

In which,

ΔZ_i : Inner axial displacement measured by inner triangular P-LDT system and evaluated from eq. (3-58)'

ΔZ_o : Outer axial displacement measured by outer triangular P-LDT system and evaluated from eq. (3-58)

$u_o = \Delta R_o$: measured by outer horizontal P-LDT and calculated from eq. (3-52)

$u_i = \Delta R_i$: measured by inner horizontal LDT and calculated from eq. (3-52)'

$Z_{ini} = (Z_{io} + Z_{oo})/2$ (3-64)

$\Delta q = (\Delta q_i + \Delta q_o)/2$ (3-65)

Δq_i : inner rotation angle obtained from eq. (3-56)'

Δq_o : outer rotation angle obtained from eq. (3-56)

R_i : Inner radius, obtained from eqn (3-51)'

R_o: Outer radius, obtained from eqn (3-51)

R_{io} : Initial inner radius

R_{oo}: Initial outer radius

3.5.3.2 Average strains using outer triangular P-LDTs and one inner horizontal P-LDT

When outer triangular P-LDTs and one inner horizontal P-LDT are employed, four average strain components can be determined by,

$$e_z = -\Delta Z_o / Z_{oo} \qquad (3\text{-}66)$$

$$e_r = -(u_o - u_i) / (R_{oo} - R_{io}) \qquad (3\text{-}67)$$

$$e_q = -(u_o + u_i) / (R_{oo} + R_{io}) \qquad (3\text{-}68)$$

$$g_{zq} = (R_o + R_i)\, \Delta q_o /(2Z_{oo}) \qquad (3\text{-}69)$$

3.5.3.3 Average strains with using outer triangular P-LDTs

When only outer triangular P-LDTs is employed, following average strains can be obtained by neglecting the change in the outer and inner radii of the specimen.

$$e_z = -\Delta Z_o / Z_{oo} \qquad (3\text{-}70)$$

$$g_{zq} = \Delta q_o\, (R_{oo} + R_{io}) / (2Z_{oo}) \qquad (3\text{-}71)$$

Note that, e_r and e_q cannot be measured directly with this system.

3.5.4 Modified version of PLDT system

Some problems were encountered when the original version of PLDT system was employed for measurement of local strains in specimens with outer diameter less than 20 cm. Increase in the curvature of the specimen makes it extremely difficult to set the horizontal PLDT without going over its measuring range. To overcome this problem, one solution is to use a horizontal PLDT with a smaller length (less than 5cm). But in that case the reaction force at the hinge becomes larger and connection between the hinge and the membrane could be damaged (note that one hinge supports two PLDTs). In addition, it is very difficult to set the diagonal PLDT at an angle of 45 degrees approximately to the horizontal plane. This condition is vital to optimize shear strain measurement. If the diagonal PLDT is set at an angle different from the value stated above, the diagonal PLDT may not work efficiently; it will detect only very small change in its length during torsional small cyclic loading. Therefore, to obtain noise free data, it is essential to calibrate the diagonal PLDT for a smaller range (about 1.2 mm). This is again

making it extremely difficult to set the diagonal PLDT without going over its range. Also note that the large curvature of the specimen restricted the use of long PLDTs. This will result in creating higher reaction forces at the hinges.

The above-mentioned problems in the original version of PLDT system raised the importance of modifying it in order to use it for specimens with outer diameter less than 20 cm. Fig.3.6 illustrates the modified version of PLDT system that is used for the present study. In this system, each PLDT is attached to the specimen by using separate hinges. This gives more flexibility in setting the PLDTs and also the reaction forces at the connection between hinge and membrane is not significant. In addition, it became easy to set the diagonal PLDT at an angle of 45 degrees to the horizontal plane too.

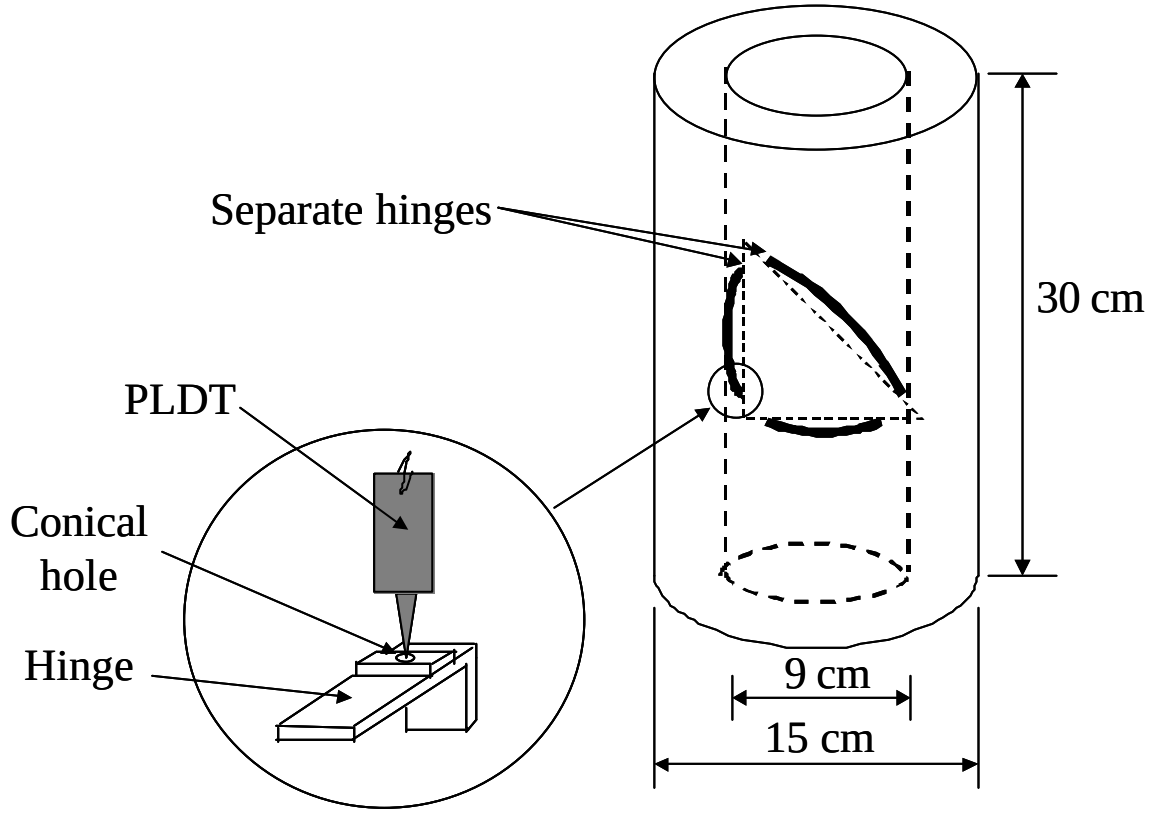

Fig. 3.6 Layout of PLDTs in the modified version of PLDT system

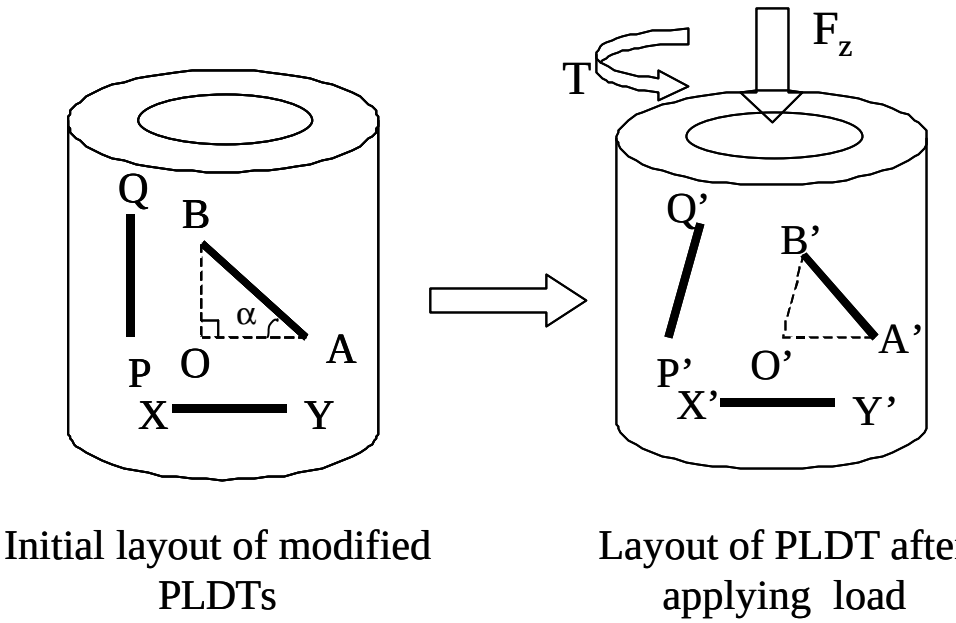

Fig.3.7. Coordinate system in the modified version of PLDT

3.5.4.1 Formulation of strains using the modified version of PLDT

At the initial stage, PLDTs PQ and XY are set vertically and horizontally, respectively.The diagonal PLDT AB makes an angle α to the horizontal plane. Usually α is set equal to 45^0 to optimize the shear strain measurement. At time *t*, points O, A, B, X, Y, P, Q are moved to new positions O', A', B', X', Y', P', Q', respectively. The two basic assumptions made in evaluating the strains using the original version of PLDT system are valid for the modified version of PLDT system too. In addition, it is assumed that the strain in PLDT P'Q' is equal to the strain of length O'B' and strain in PLDT X'Y' is equal to the strain of length O'A'. These assumptions are valid since all three PLDTs are arranged close to each other. Following equations can be derived from the above assumptions.

$$O'B' = P'Q' \times \frac{OB}{PQ} \qquad (3\text{-}72)$$

$$O'A' = X'Y' \times \frac{OA}{XY} \qquad (3\text{-}73)$$

Lengths P'Q', PQ, X'Y' and XY can be measured directly from the calibration curves of the respective PLDTs. Length OB and OA are the initial vertical and horizontal components of the diagonal PLDT, respectively. Then by assuming the same coordinate system as the original version of PLDT system and using equations (3-52), (3-56) and (3-58), three local deformations ΔR_o, $\Delta\theta$ and ΔZ_o can be evaluated.

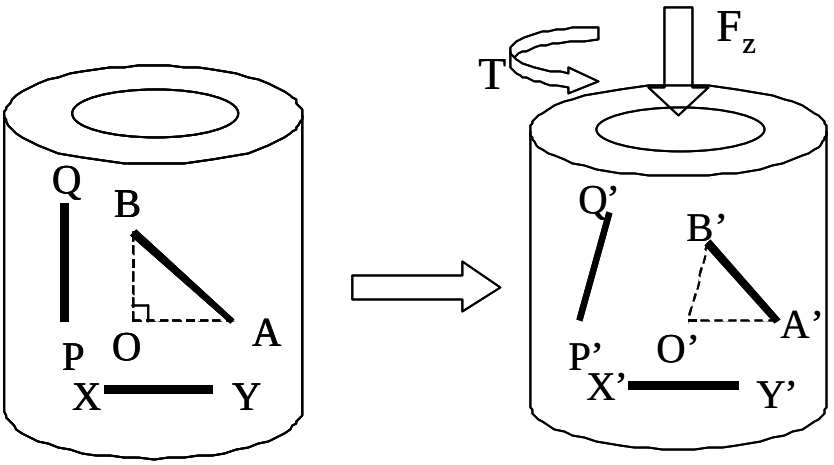

Initial layout of modified PLDTs

Layout of PLDT after applying load

3.5 SUMMARY

With the current setting of right triangular P-LDTs together with the assumptions regarding to the unchanged shape of hollow cylinders and unchanged central angle during shearing related to horizontal LDT, a number of points should be noted as follows.

- Horizontal P-LDTs can measure the change in the radii of the specimen; therefore, they can measure e_r and e_q. Vertical and diagonal P-LDTs can measure vertical displacement and rotation angle; thus, they can measure e_z and g_{zq} of the specimen. Using both inner and outer triangular LDTs is preferred to obtain full four average strain components e_r, e_z, e_q, g_{zq} of the specimen.

- However, due to a number of difficulties such as narrow working space in inner cylinder, in the present study, outer triangular P-LDTs and an inner horizontal P-LDT were used to obtain four strain components. In addition, in the extreme case with specimen size C having large curvature of outer surface (D_o = 10 cm), only outer vertical and diagonal P-LDTs can be employed.

CHAPTER 4: LOCALLY AND EXTERNALLY MEASURED DEFORMATION PROPERTIES OF TOYOURA SAND AT VARIOUS DENSITIES

4.1 Experiment program

Air-dried Toyoura sand specimens were prepared by pluviating sand particles into the space between inner and outer moulds. The height of pluviation was varied between 0.1 m to 1.0 m to prepare specimens with various densities from 1.443 g/cm^3 to 1.612 g/cm^3. In terms of relative density, it was between 38.2% and 90.6%, covering medium dense to very dense range. Specimens for Tests LIN6 and LIN14 were prepared by pluviating sand particles in alternate clockwise and anti-clockwise directions while, all the other specimens were prepared by pluviating sand in radial direction (refer to Fig. 2.3 in chapter 2). All the sand specimens have outer diameter of 15 cm, inner diameter of 9 cm and a height of 30 cm.

First, some preliminary tests (Tests LIN1-5) were conducted on the newly assembled medium-sized hollow cylinder apparatus to check its working condition. After solving some minor problems in the apparatus, Tests LIN4 and LIN5 were conducted by employing the original version of PLDT system (Hong Nam and Koseki, 2003) as the local strain measurement technique. Then the original version of PLDT system was modified as described in Chapter 3 and the rest of the tests were conducted by employing the modified version of PLDT system as the local measurement technique. Following paragraph describes the tests that were conducted by employing the modified version of PLDT system.

All the tests were conducted under drained condition. Specimens of the Tests LIN6, 7, 8 and 10 were loaded isotropically from $\sigma'_z = \sigma'_\theta$ = 30 kPa to 400 kPa and unloaded down to 50 kPa. Specimens of the Test LIN9 and 14 were isotropically loaded from $\sigma'_z = \sigma'_\theta$ = 50 kPa to 400 kPa and unloaded down to 50 kPa. Then specimens of Tests LIN6, 7, 8, 9 were subjected to triaxial shearing up to σ'_z = 250 kPa while keeping σ'_θ = 50 kPa. During Isotropic Consolidation (IC), small cyclic loading in both vertical and torsional directions were applied at several stress states with increments of $\Delta\sigma'_\theta$ = 50 kPa to evaluate small-strain Young's and shear modulus. The same procedure was followed at increments of $\Delta\sigma'_z$ = 25 kPa during triaxial shearing.

Specimen for Test LIN10 was subject to a shear stress of about 90 kPa while keeping $\sigma'_z = \sigma'_\theta$ = 150 kPa. Then it was triaxially sheared until σ'_z = 400 kPa while applying small cyclic loading at several stress states.

In order to investigate the effects of shear stress on Young's and shear moduli of Toyoura sand, specimen for Test LIN14 was subject to a shear stress of about 70 kPa while keeping $\sigma'_\theta = \sigma'_z$ =150 kPa. Small vertical and torsional cyclic loading were applied at each increment of $\Delta\tau_{z\theta}$ = 10 kPa.

A detailed description of employed stress paths is given in Chapter 2. Table 4.1 summarized the tests on Toyoura sand and Tables 4.2 and 4.3 illustrates the stress state dependency parameters (m and n) of all the tests.

4.2 Results and discussion

Discussion on the results of Toyoura sand is broadly categorized into eight major sections. Section 4.2.1 describes the variation of Young's modulus of Toyoura sand measured at different stress levels with the density and the consistency between the results by using local and external transducers in measuring the Young's modulus at isotropic stress state. Similar aspects of the shear modulus at isotropic stress state are discussed in section 4.2.2. The effects of large stress ratios for the locally and externally measured Young's and shear moduli are discussed in sections 4.2.3 and 4.2.4, respectively. The effect of large shear stress for the locally and externally measured Young's and shear moduli is discussed in sections 4.2.5. Section 4.2.6 discussed the results of Poisson's ratio. Comparison of the results from different transducers in the measurement of both quasi-elastic and global strains is discussed in the section 4.2.7. Finally, the effects of different pluviation techniques are discussed in the section 4.2.8. Note that, in this study, the variation of void ratio during isotropic and triaxial loading was assumed to be very small and neglected.

As described in chapter 2, data obtained by applying the original version of PLDT system (Hong Nam and Koseki, 2004) into specimens with outer diameter less than 20 cm, are showing very large noise in the evaluation of shear modulus as shown in Fig. 4.1. On the other hand, results from the Gap sensor at the same stress level, as shown in Fig. 4.2 are showing highly reversible stress strain behavior ($\gamma_{z\theta} < 0.002$ %) and noise free data.

Fig. 4.3 illustrates a typical record of vertical small cyclic loading measured by using the modified version of PLDT system. Eleven small cycles were applied at each stress level and the 10^{th} was used to evaluate the Young's modulus. Fig. 4.4 and Fig. 4.5 show a typical evaluation of E_z using the modified version of PLDT system and Gap sensors, respectively. A typical record of torsional small cyclic loading measured using the modified version of PLDT system is shown in Fig. 4.6. As similar to vertical small cyclic loading, the 10^{th} cycle was used for the evaluation of shear modulus. Fig. 4.7 and Fig. 4.8 show a typical evaluation of shear moduli using the modified version of PLDT system and Gap sensors, respectively. A typical evaluation of Poisson's ratio is shown in Fig. 4.9.

4.2.1 Vertical Young's modulus (E_z) at isotropic stress state

Fig. 4.10 illustrates the relationship between E_z and σ'_z measured using different transducers for a typical test. It could be seen that all the transducers, both local and external are giving similar E_z values at different stress levels.

Variations of the Young's modulus at different densities measured using different transducers are presented in Fig. 4.11 through Fig. 4.14. It is clear that E_z increases with the dry density at a particular stress state. This tendency is visible in the results from all the transducers.

In order to compare the Young's moduli of Toyoura sand specimens among different densities, the applicability of different void ratio functions was checked as shown in Fig. 4.15. E_z value at the initial void ratio (e_{ref}) equal to 0.654 and $\sigma'_z = \sigma'_\theta$ = 400 kPa is taken as the reference E_z ($E_{z(ref)}$). Then using the equation, $E_z = E_{z(ref)} / f(e_{ref}) \times f(e)$, relationships between E_z vs e proposed by different void ratio functions (refer to 3.2.1) was plotted. It can be seen that the void ratio function proposed by Hardin and Richart (1963) ($f(e) = (2.17 - e)^2 / (1 + e)$) is the most appropriate for Toyoura sand. As shown in the same figure, this void ratio function works well for E_z values at $\sigma'_z = \sigma'_\theta$ = 200 and 100 kPa as well. Both local and external transducers show similar tendency. Fig. 4.16 shows the relationships of E_z, and E_z /f(e) vs e_0 at a typical stress level measured using local and external transducers. This verifies that E_z/f(e) gives similar values against different void ratios when $f(e) = (2.17 - e)^2 / (1 + e)$ is used. Therefore this void ratio function is employed throughout the present study to compare Young's moduli of Toyoura sand specimens with different relative densities.

Fig. 4.17 to Fig. 4.20 shows E_z /f (e) vs σ'_z obtained from different transducers. After normalized by the void ratio function, E_z values from all the tests measured by different transducers show a rather unique relationship and E_z/ f (e) can be expressed as a function of σ'^m_z. More detailed verification will be given in section 4.2.3. This verifies the finding of Hardin (1978). As shown in Table 4.2, averaged m values from different transducers are similar to each other irrespective of local or external measurement.

4.2.2 Shear modulus (G_{zq}) at isotropic stress state

Fig. 4.7 shows a typical evaluation of $G_{z\theta}$ using the modified version of PLDT system. This suggests that the modified version PLDT system can be effectively used to evaluate shear modulus locally. Fig. 4.21 shows $G_{z\theta}$ measured using different transducers in a typical test. Unlike E_z, $G_{z\theta}$ measured externally are about 20% greater than that of measured locally using the modified version of PLDT system. One possible reason for this difference is explained in Appendix 4.1. On the other hand, variation of $G_{z\theta}$ with the density, as shown in Fig. 4.22 through Fig. 4.25, is similar to the variation of E_z.

In order to compare the shear moduli of Toyoura sand specimens among different densities, the applicability of different void ratio functions was checked as shown in Fig. 4.25a. $G_{z\theta}$ value at the initial void ratio (e_{ref}) equal to 0.654 and $\sigma'_z = \sigma'_\theta$ = 400 kPa is taken as the reference $G_{z\theta}$ ($G_{z\theta(ref)}$). Then using the equation, $G_{zq} = G_{zq\,(ref)} / f(e_{ref}) \times f(e)$, relationships between $G_{z\theta}$ vs e proposed by different void ratio functions (refer to 3.2.1) was plotted. It can be verified that the void ratio function proposed by Hardin and Richart (1963) ($f(e) = (2.17 - e)^2 / (1 + e)$) is the most appropriate for Toyoura sand. As shown in the same figure, this void ratio function works well for $G_{z\theta}$ values at $\sigma'_z = \sigma'_\theta$ = 200 and 100 kPa as well. Both local and external transducers show similar tendency. Fig. 4.25b shows the relationships of $G_{z\theta}$, and $G_{z\theta}$ /f(e) vs e, at a typical stress level measured using local and external transducers. This verifies that $G_{z\theta}$/f(e) gives similar values against different void ratios when $f(e) = (2.17 - e)^2 / (1 + e)$ is used. Therefore this void ratio function is employed throughout the present study to compare shear moduli of Toyoura sand specimens with different relative densities.

Fig 4.26 through Fig. 4.29 shows the relationship of $G_{z\theta}$/f(e) against $(\sigma'_z * \sigma'_\theta)^{0.5}$ measured using different transducers. It could be seen that $G_{z\theta}$/f(e) can be expressed as a function of $(\sigma'_z * \sigma'_\theta)^{0.5n}$. More detailed verification will be given in section 4.2.4. Table 4.3 illustrates the n values obtained from different transducers. According to the table both local and external transducers show similar n values.

4.2.3 E_z during triaxial compression (TC)

Comparison of E_z/f(e) values during IC and TC that are plotted versus σ'_z , $(\sigma'_z + \sigma'_\theta)/2$, and $(\sigma'_z + 2\sigma'_\theta)/3$ for a typical test measured by local and external transducers are presented in Fig. 4.30, Fig. 4.31 and Fig. 4.32, respectively. It can be clearly seen that E_z/ f (e) can be expressed as a function of σ'^{m}_z. At low stress levels, a slight difference of E_z/f(e) values between IC and TC could be observed in Fig. 4.30 while the difference seems to disappear with the increase of stress level. Both local and external transducers show similar trends.

Fig. 4.33 through Fig. 4.36 illustrates the relationship between E_z/f(e) and σ'_z measured using different transducers. All the transducers show an increasing trend of E_z/f(e) with σ'_z . In addition, E_z/f(e) of all the tests that are sheared at σ'_θ = 50 kPa show a rather unique relationship. Note that Test LIN10 was sheared at σ'_θ = 150 kPa and $\tau_{z\theta}$ = 92 kPa. Therefore it shows slightly smaller E_z/f(e) values at a particular stress level compared to those sheared at σ'_θ = 50 kPa at the initial stage and approaching the original line with the increase of stress level.

Fig. 4.37 and Fig. 4.38 show the relationship between E_z/ $E_{z(ref)}$ and principal stress ratio. $E_{(ref)}$ is calculated using the equation proposed by Hardin(1978)($E_{ref} = E_0 \times f(e_0) / f(e) \times (s_z / s_0)^m$). E_o is taken as the Young's modulus at $\sigma'_\theta = \sigma'_z$ = 100 kPa. m is obtained from the plots of E_z/f(e) vs σ'_z for each transducer during IC. σ'_0 = 100 kPa is assumed. Under the present test conditions, no significant effect of damage to the structure at large stress ratio is observed. Note that the initial value of E_z/ $E_{z(ref)}$ for the Test LIN10 does not start from unity as shown in Fig. 4.37 and Fig. 4.38. This is because of the large shear stress applied to the specimen before applying triaxial compression. But it can be seen clearly that, with the increase of stress level it is approaching unity.

4.2.4 G_{zq} during triaxial compression (TC)

$G_{z\theta}$/f(e) during IC and TC measured using local and external transducers and plotted against $(\sigma'_z * \sigma'_\theta)^{0.5}$, $(\sigma'_z + \sigma'_\theta)/2$, and $(\sigma'_z + 2\sigma'_\theta)/3$ are illustrated in Fig. 4.39, Fig. 4.40 and Fig.

4.41, respectively. All three plots show a sudden degradation of shear modulus at large stress levels. But it seems $G_{z\theta}/f(e)$ vs $(\sigma'_z * \sigma'_\theta)^{0.5}$ is the most appropriate among the three relationships. Fig. 4.42 through Fig. 4.44 show the relationship of $G_{z\theta}/f(e)$ versus $(\sigma'_z * \sigma'_\theta)^{0.5}$. Unlike Young's modulus, shear modulus shows a sudden degradation after the stress states of σ'_z = 150 kPa and σ'_θ = 50 kPa (i.e., the principal stress ratio, R exceeds three) as shown by an arrow in each figure. This confirms the previous observations by Hong Nam et al (2004). This behavior may be due to the damage to soil structure at principal stress ratios greater than three. But the reason why it could be observed significantly in shear modulus and not in Young's modulus is still unknown to the author. A similar degradation could be seen from the results of all the transducers. As shown in Fig. 4.45 and Fig. 4.46, $G_{z\theta}/G_{z\theta\,(ref)}$ shows a slight increase from unity until R = 3 and then degraded suddenly. $G_{z\theta\,(ref)}$ was evaluated by using the equation $G_{ref} = G_0 \times f(e_0)/f(e) \times \left(\sqrt{s_z s_q}\ / s_0\right)^n$ proposed by Hong Nam and Koseki (2004), taking G_0 as the shear modulus at $\sigma'_\theta = \sigma'_z$ = 100 kPa. n is obtained from the plots of $G_{zq}/f(e)$ vs $(\sigma'_z * \sigma'_\theta)^{0.5}$ for each transducer during IC and σ'_0 = 100 kPa is assumed.

4.2.5 E_z and G_{zq} during TSI

Relationship between $E_z/f(e)$ and shear stress level ($\tau_{z\theta}$) measured by different transducers is illustrated in Fig. 4.47. It can be seen that $E_z/f(e)$ values remain almost unchanged until $\tau_{z\theta}$ = 50 kPa. After that a degradation of E_z occurred. This may be representing the damage of the soil structure occurred at large shear stress ratios. Also note that both local and external transducers are showing a similar trend. Comparison of $E_z/E_{z\,(ref)}$ vs $\tau_{z\theta}/\sigma'_\theta$ and $E_z/E_{z\,(ref)}$ vs principal stress ratio R ($= \sigma_1/\sigma_3$) between Hong Nam (2004) and present study is illustrated in Fig. 4.48 and Fig. 4.49, respectively. Fig. 4.49a shows the comparison of $E_z/E_{z\,(ref)}$ vs R during TC, ATL and TSI. It can be observed in TSI that $E_z/E_{z\,(ref)}$ remains almost unchanged until R = 2.2 and then started degrading.

The effect of $\tau_{z\theta}$ on locally and externally measured shear modulus is shown in Fig. 4.50. A slight but gradual degradation of shear modulus was observed from both local and external measurements. Similar to the behavior of Young's modulus, shear modulus after $\tau_{z\theta}$ = 50 kPa degraded rapidly giving signs of possible damage of the soil structure. Comparison of $G_{z\theta}/$

$G_{z\theta(ref)}$ vs $\tau_{z\theta}/\ \sigma'_{\theta}$ and $G_{z\theta}/\ G_{z\theta(ref)}$ vs R (= σ_1/σ_3) between Hong Nam (2004) and present study is illustrated in Fig. 4.51 and Fig. 4.52, respectively. Fig. 4.52a compares the $G_{z\theta}/\ G_{z\theta(ref)}$ vs R during TC, ALT and TSI. Unlike the cases TC and ALT, TSI shows a gradual degradation of $G_{z\theta}/\ G_{z\theta(ref)}$ vs R. Note that, the specimen subject to TSI was very loose (D_r = 38.2 %). Therefore, a small disturbance might cause a significant damage to the specimen. However, more verification is needed in this regard.

4.2.6 Poisson's ratio during IC and TC

Fig. 4.53 shows the comparison of $\nu_{z\theta}$ versus $\sigma'_z = \sigma'_{\theta}$ between Hong Nam (2004) and the present study. Although $\nu_{z\theta}$ values show some scatter, it can be noticed that $\nu_{z\theta}$ remains almost unchanged during isotropic consolidation with an average value of 0.137.

$\nu_{z\theta}$ vs R during triaxial compression is illustrated in Fig. 4.54. It can be noticed from the relationship that $\nu_{z\theta}$ can be expressed as a function of $(\sigma'_z / \sigma'_{\theta})^k$, where average *k* is 0.405. Table 4.4 illustrates the k values. This tendency is similar to that of Hong Nam (2004), as shown in Fig. 4.54a

4.2.7 Comparison of local and external measurements

Local strains are those measured from the modified version of PLDT system that are directly attached to the specimen and external strains refer to those measured from transducers attached to the top cap. Two such external transducers namely, Potentiometer and Gap sensor were used in this study to measure small and large strains. Potentiometer 2(POT2) was used to measure the rotation of specimen while two gap sensors (GS2 and GS3) were used to measure the vertical deformation of the specimen.

Fig. 4.55 and Fig. 4.58 show the comparison of average Young's modulus from external transducers (GS3 and GS3) and local transducers (PLDT Set1 and PLDT Set2) during IC and TC. The ratio E_z (GS_{ave})/ E_z ($PLDT_{ave}$) lies between 0.97 – 1.07 for all the tests in both IC and TC. As shown in the figure, the average values of E_z (GS_{ave})/ E_z ($PLDT_{ave}$) were almost close to 1.0. Fig. 4.56 compares the Young's modulus obtained from GS2 and GS3 during IC while Fig. 4.57 compares the same between PLDT Set1 and Set2. Fig. 4.59 and Fig. 4.60 compare

the same as above during TC. It could be seen that both local and external measurements are giving similar results within a range of 0.98 – 1.02 for their ratio.

Comparison of average $G_{z\theta}$ from two PLDT sets and GS1, during IC is shown in Fig. 4.61. Unlike in the case of Young's modulus, the ratio $G_{z\theta}$ (GS1)/$G_{z\theta}$ ($PLDT_{ave}$) lies between 1.10-1.25. This confirms the observation by HongNam (2004). A similar trend could be observed during triaxial compression in Fig. 4.64. On the other hand, $G_{z\theta}$ obtained from two external transducers (GS1 and POT2) are giving almost similar results as shown in Fig. 4.62 and Fig. 4.65 during IC and TC, respectively. Two local PLDT systems are also giving similar results between each other as shown in Fig. 4.63 and Fig. 4.66.

Comparison of externally and locally measured Young's and shear moduli during large torsional shear (TSI) is presented in Fig. 4.67 through Fig. 4.70. A relationship between external and local transducers that is similar to those observed during IC and TC could be observed during TSI too.

Global behavior of different specimens during IC, TC and TSI measured by various local and external transducers are presented in Fig. 4.71 through Fig. 4.82. It could be observed that during IC, external transducer is giving the largest vertical strain (ε_z) in most of the cases followed by PLDTs. But it should be noted that a clear separation of externally and locally measured global ε_z during IC is not visible. Fig. 4.76 and Fig. 4.77 show the effects of density on ε_z during IC. Both local and external transducers show a stiffer response with the increase of density. During TC, ε_z measured by PLDTs is giving the largest in all the cases, followed by external transducers and gap sensors, respectively. Shear strain measured by POT2, GS1 and PLDTs during IC and TC is small. Shear strain measured externally and locally during TSI is showing almost similar stress-strain curves while ε_z and ε_θ measured using local and external transducers is almost close to zero as shown in Fig. 4.82.

4.2.8 Effects of different pluviation techniques

Two different pluviation techniques, as shown in Fig. 2.3 in chapter 2, were used in preparing the specimens. The plots of σ_z vs ε_z and σ_z vs ε_θ for two different pluviation techniques are

shown in Fig. 4.83. It can be recognized that the effect of the pluviation technique on ε_z is very small while its effect on ε_θ is significant. It can be observed that ε_z and ε_θ of the specimen, which is prepared by pluviating sand in radial direction, are of the same order around 0.2 %.

Toyoura sand particles are sub-angular in shape. Therefore the orientation of the particles seems to be playing an important role in the isotropy of the specimen. Specimens prepared by pluviating sand particles in radial direction show more isotropic behavior during IC. But it should be noted that pluviation in radial direction cannot be applied to prepare very loose specimens because of the limited working space between inner and outer moulds of the specimen.

Table 4.1 Summary of the tests on Toyoura sand

Test	Dry density (g/cm^3)	Initial void ratio	Relative density (%)	Stress path (kPa)
LIN2	1.536	0.715	68.4	IC ($\sigma'_z = \sigma'_\theta$ = 30 ~ 450 ~ 200) TC (σ'_θ = 200, σ'_z = 200 ~ 400)
LIN3	1.532	0.720	67.2	IC ($\sigma'_z = \sigma'_\theta$ = 30 ~ 450 ~ 200) TC (σ'_θ = 200, σ'_z = 200 ~ 400)
LIN4	1.545	0.706	71.2	IC ($\sigma'_z = \sigma'_\theta$ = 30 ~ 450 ~ 200) TC (σ'_θ = 200, σ'_z = 200 ~ 400)
LIN5	1.610	0.635	90.6	IC ($\sigma'_z = \sigma'_\theta$ = 30 ~ 450 ~ 100) TC (σ'_θ = 100, σ'_z = 100 ~ 300)
LIN6	1.612	0.634	90.6	IC ($\sigma'_z = \sigma'_\theta$ = 30 ~ 400 ~ 50) TC (σ'_θ = 50, σ'_z = 50 ~ 250)
LIN7	1.557	0.692	74.8	IC ($\sigma'_z = \sigma'_\theta$ = 30 ~ 400 ~ 50) TC (σ'_θ = 50, σ'_z = 50 ~ 250)
LIN8	1.593	0.654	85.3	IC ($\sigma'_z = \sigma'_\theta$ = 30 ~ 400 ~ 50) TC (σ'_θ = 50, σ'_z = 50 ~ 250)
LIN9	1.551	0.699	72.8	IC ($\sigma'_z = \sigma'_\theta$ = 50 ~ 400 ~ 50) TC (σ'_θ = 50, σ'_z = 50 ~ 250)
LIN10	1.612	0.635	90.6	IC ($\sigma'_z = \sigma'_\theta$ = 30 ~ 400 ~ 150) TSI ($\sigma'_z = \sigma'_\theta$ = 150, $\tau_{z\theta}$ = 0 ~ 92) ALT (σ'_θ = 150, $\tau_{z\theta}$ = 92, σ'_z = 150 ~ 400)
LIN14	1.443	0.826	38.2	IC ($\sigma'_z = \sigma'_\theta$ = 60 ~ 400 ~ 150) TSI ($\sigma'_z = \sigma'_\theta$ = 150, $\tau_{z\theta}$ = 0 ~ 65)

Table 4.2 Averaged *m* values of Toyoura sand during IC and TC by different transducers

Test	***m* during IC**		***m* during TC**	
	PLDTs	**GSs**	**PLDTs**	**GSs**
LIN6	0.490	0.506	0.467	0.572
LIN7	0.484	0.481	0.450	0.478
LIN8	0.494	0.488	0.489	0.577
LIN9	0.512	0.500	0.572	0.602
LIN10	0.449	0.469	0.446	0.332
LIN14	0.491	0.452	-	-

Table 4.3 *n* values of Toyoura sand during IC by different transducers

Test	*n* during IC		
	PLDTs	**GS**	**POT**
LIN6	0.452	0.454	0.438
LIN7	0.511	0.494	0.475
LIN8	0.490	0.507	0.477
LIN9	0.474	0.530	0.496
LIN10	0.446	0.481	0.445
LIN14	0.502	0.479	-

Table 4.4 k values of Toyoura sand during TC

Test	k values from PLDTs
LIN8	0.368
LIN9	0.442

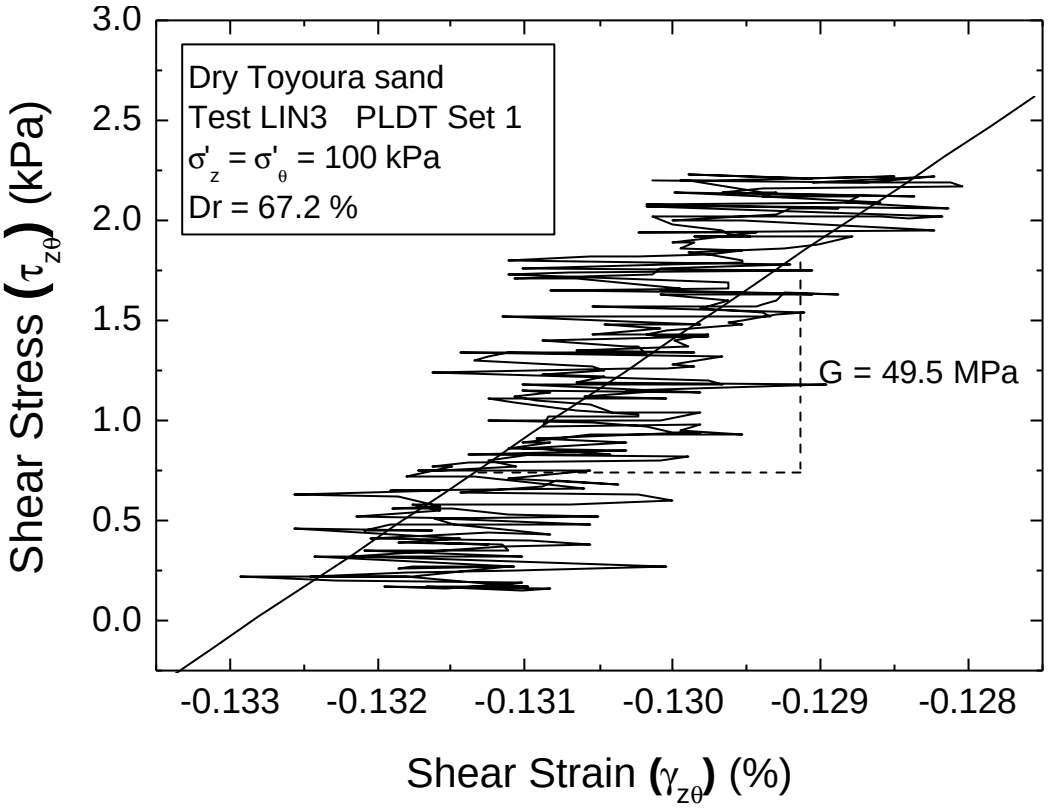

Fig. 4.1 Evaluation of G using the original version of PLDT

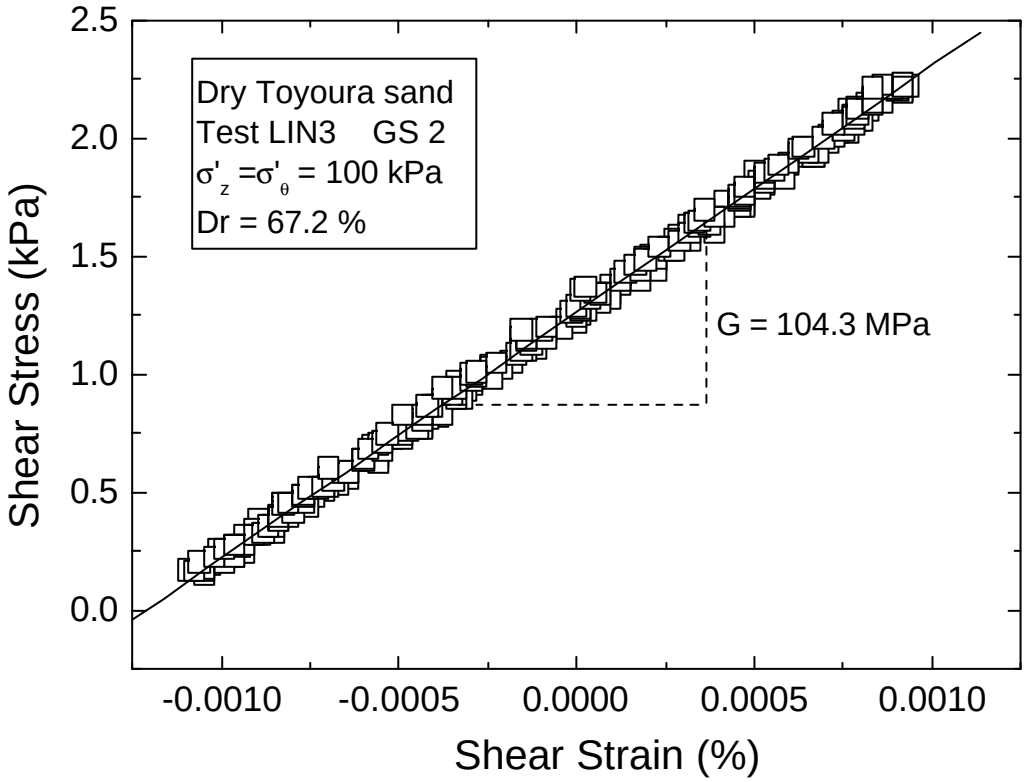

Fig. 4.2 Evaluation of G using proximity transducer (Gap sensor)

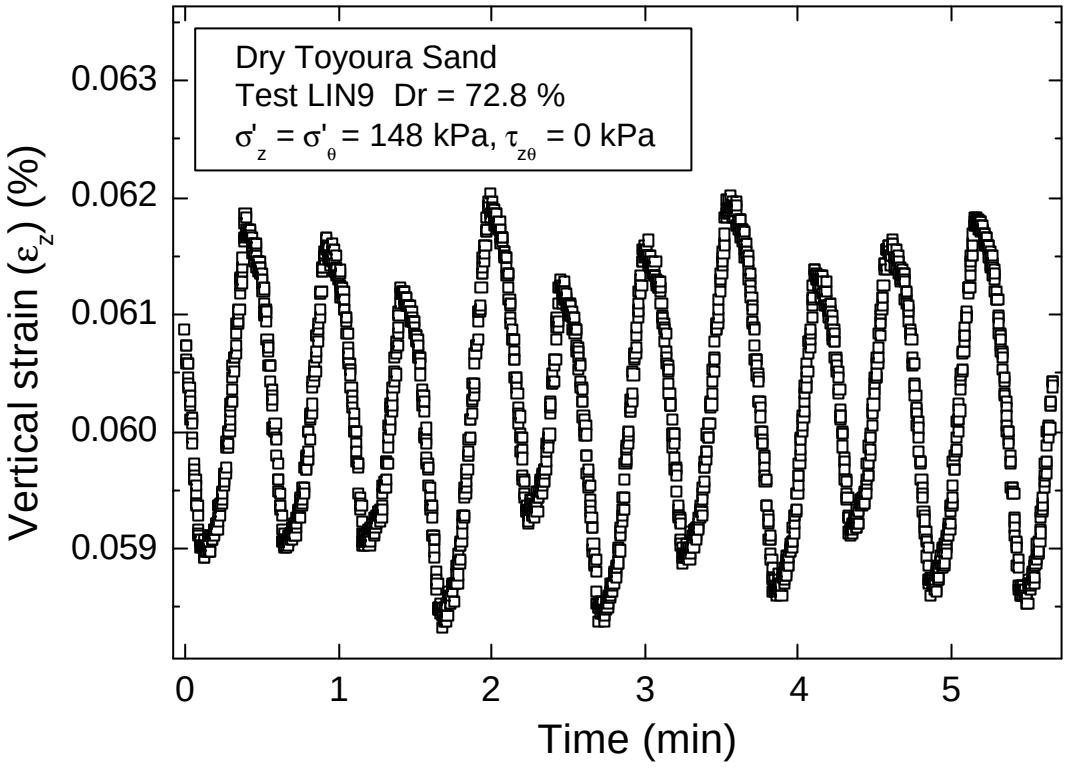

Fig. 4.3 Vertical small cyclic loading measured by modified version of PLDTs

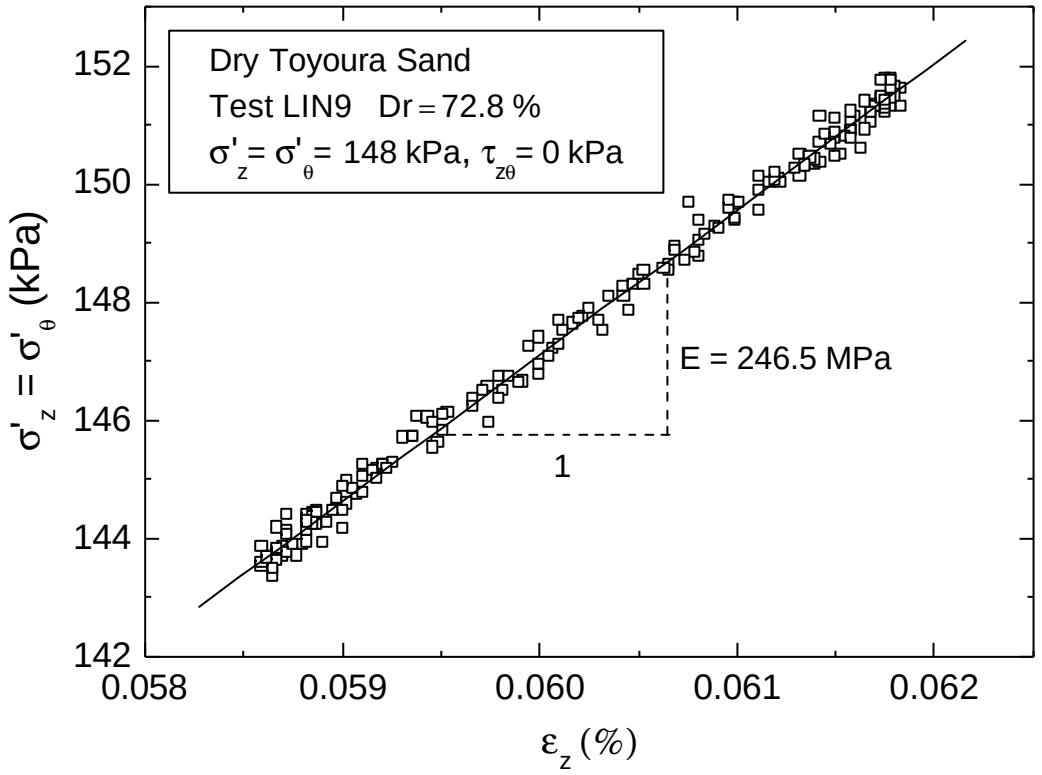

Fig. 4.4 Typical evaluation of E_Z using the modified version of PLDTs

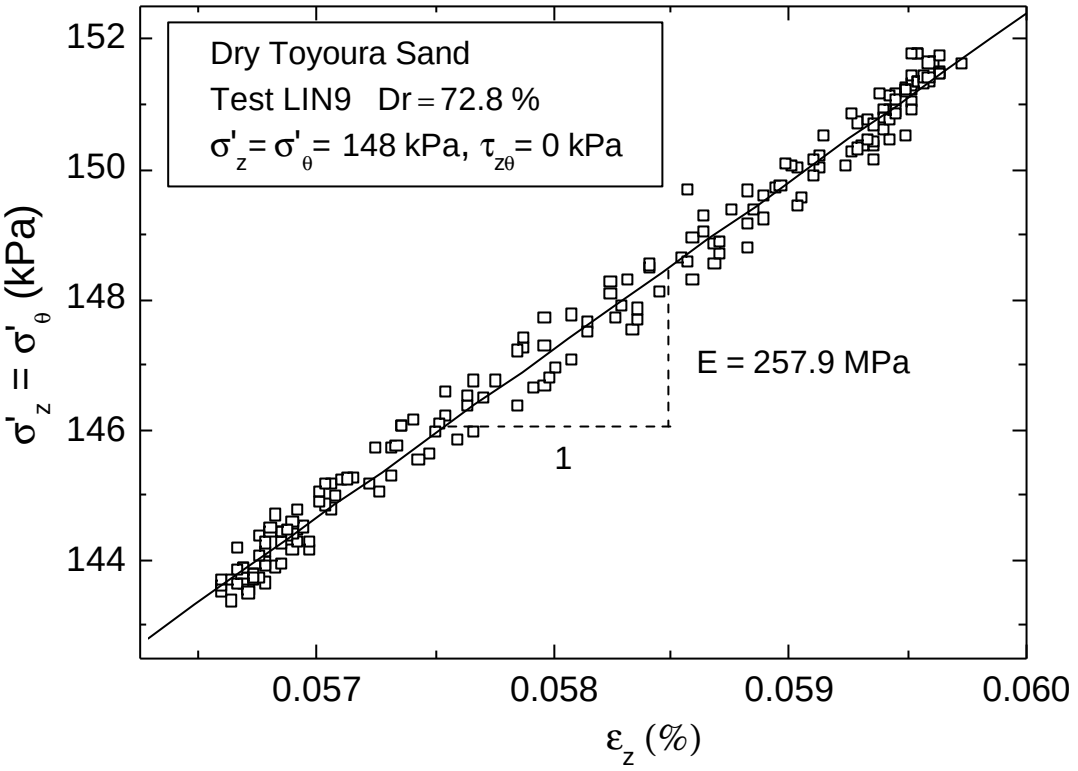

Fig. 4.5 Typical evaluation of E_Z using gap sensors

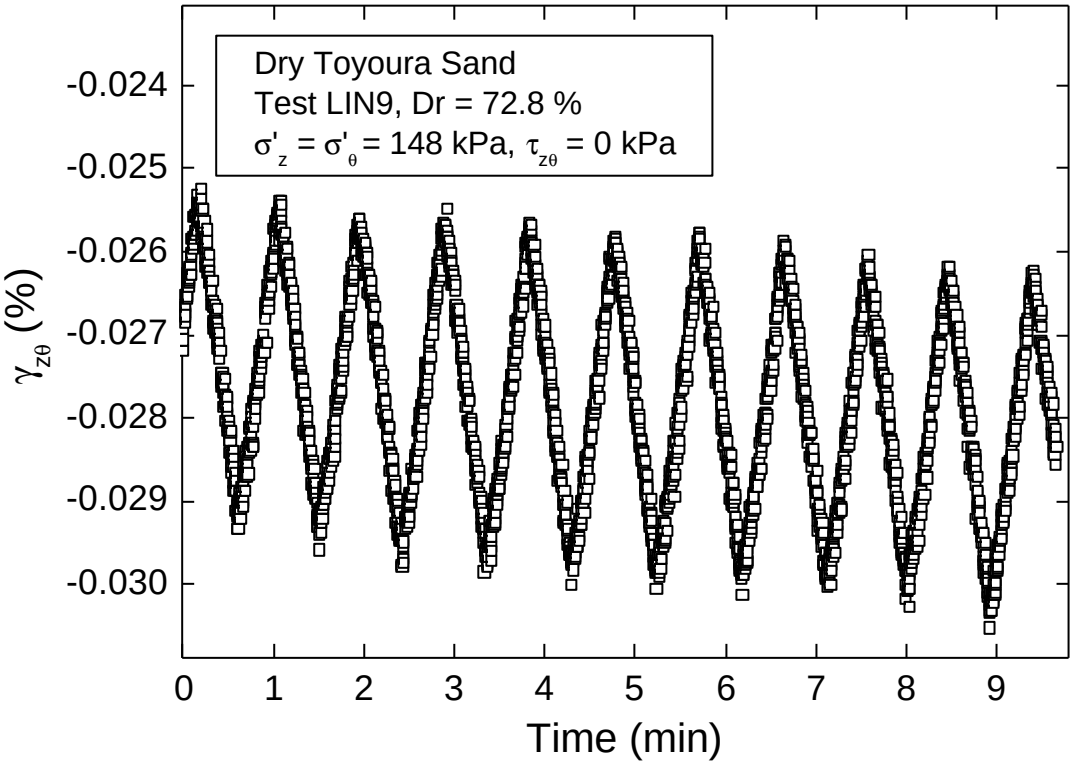

Fig. 4.6 Torsional small cyclic loading measured by modified version of PLDTs

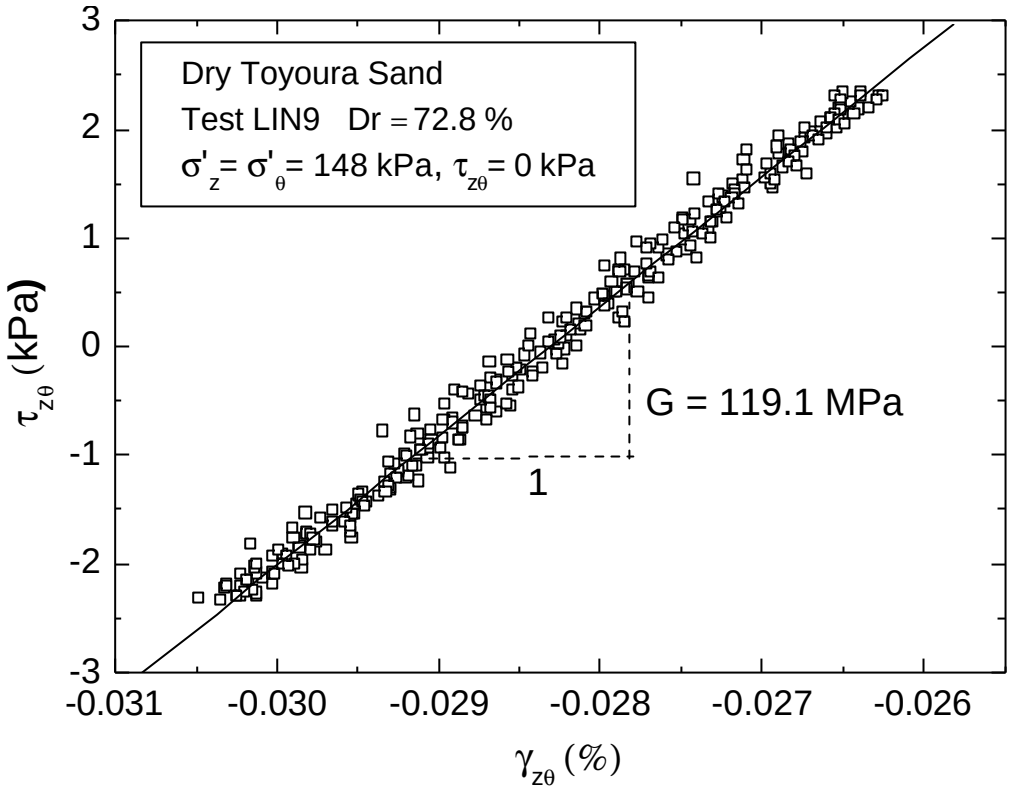

Fig. 4.7 Typical evaluation of $G_{z\theta}$ using the modified version of PLDTs

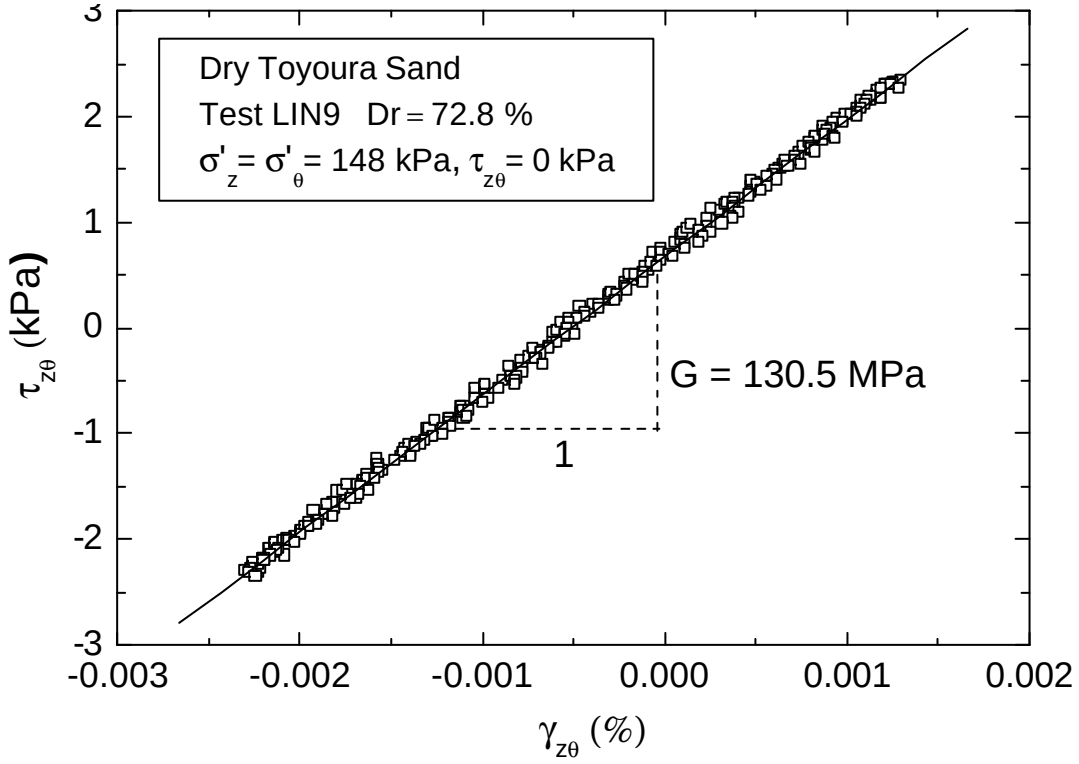

Fig. 4.8 Typical evaluation of $G_{z\theta}$ using gap sensors

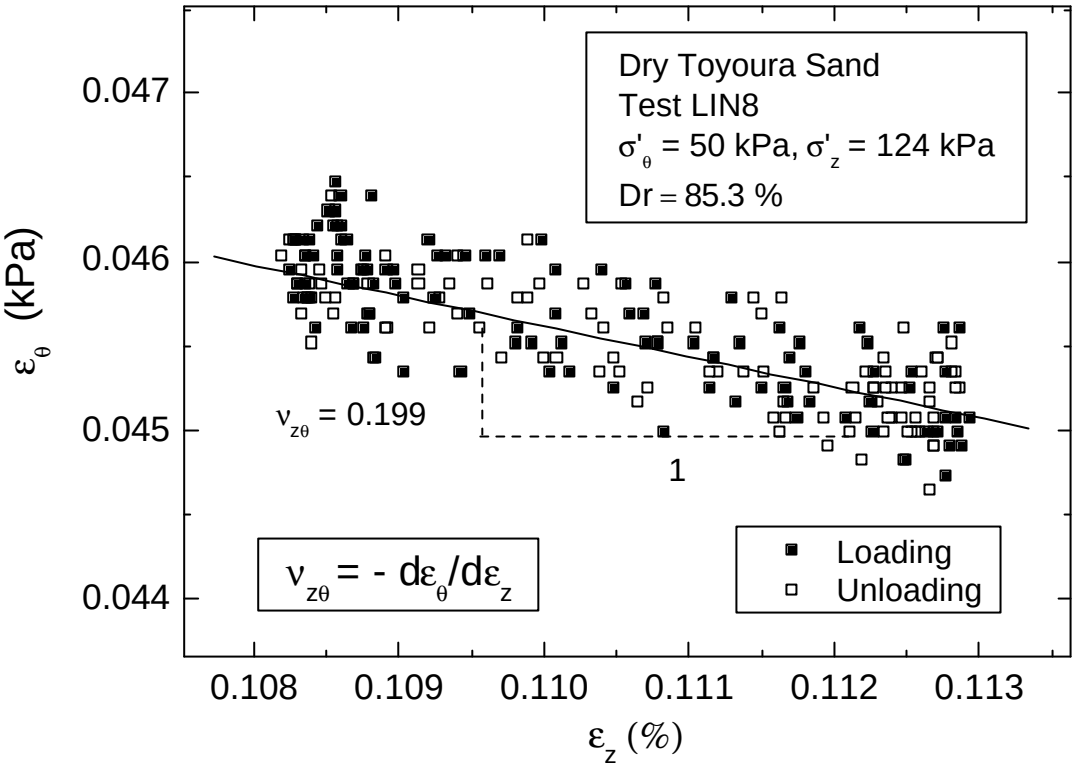

Fig. 4.9 Typical evaluation of $\nu_{z\theta}$ using the modified version of PLDTs

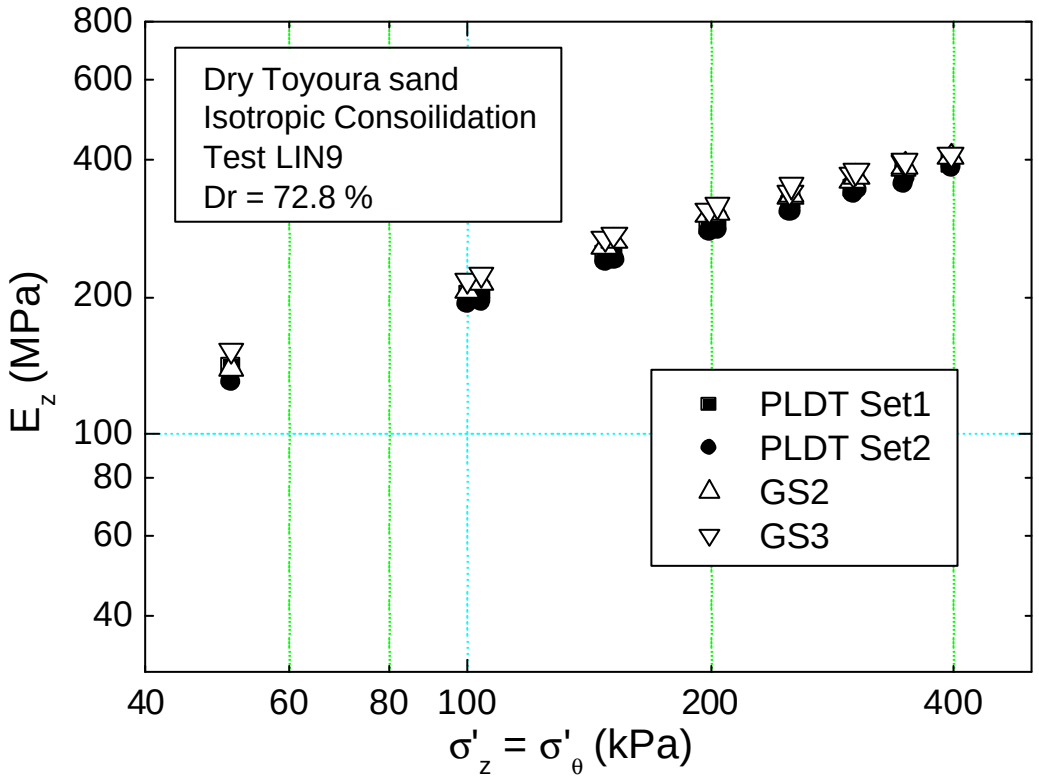

Fig. 4.10 E_z values measured using different transducers

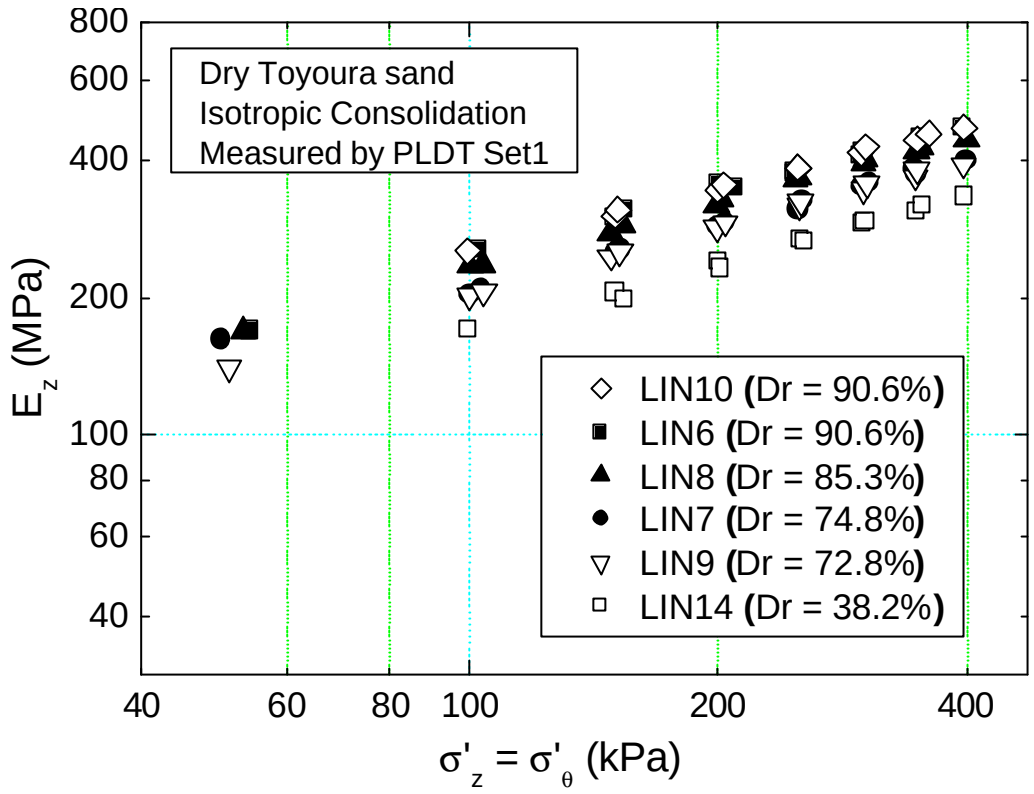

Fig. 4.11 E_z during IC measured using the modified version of PLDT Set1

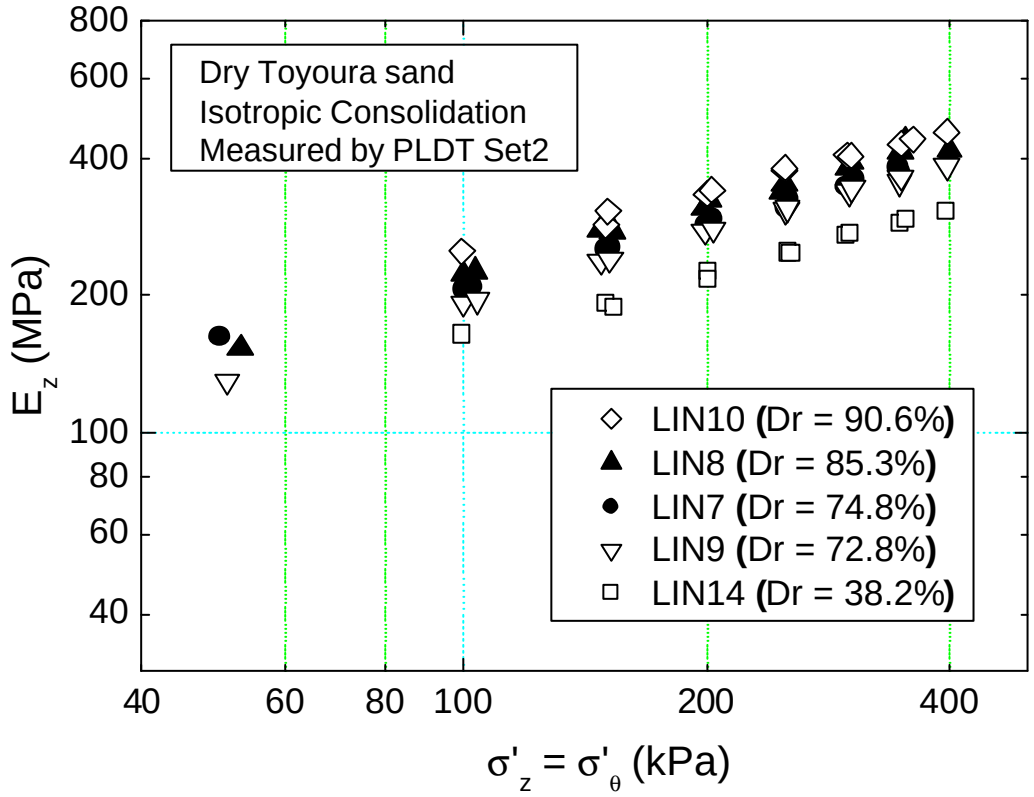

Fig. 4.12 E_z during IC measured using the modified version of PLDT Set2

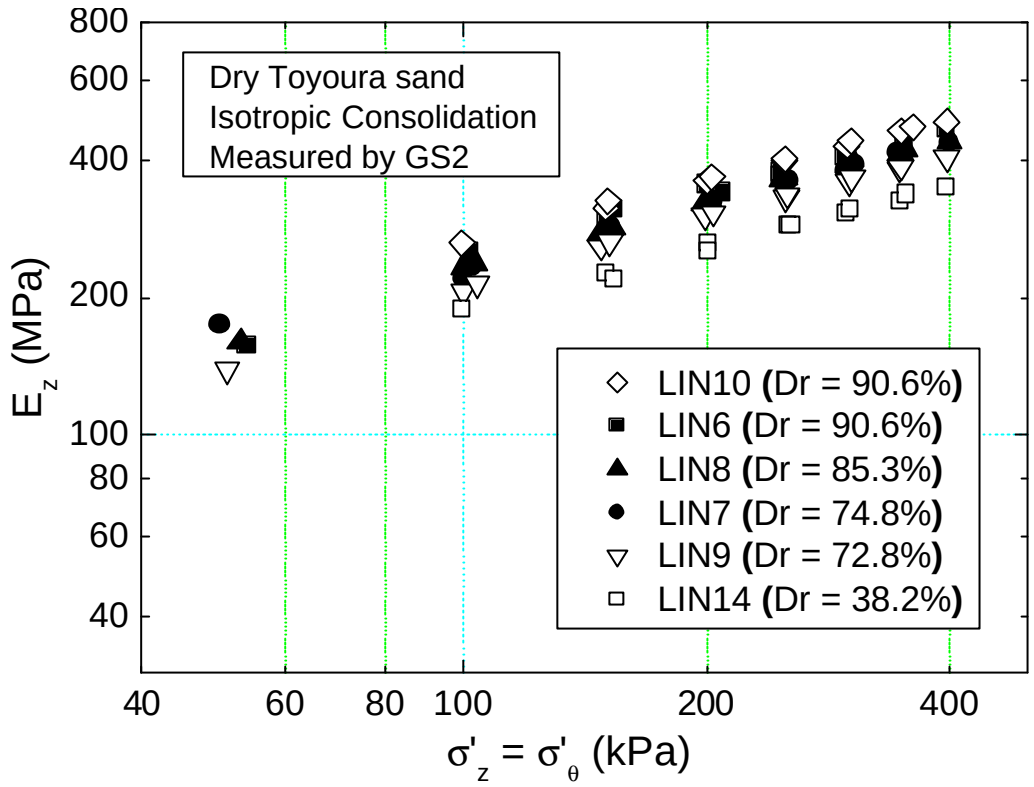

Fig. 4.13 E_z during IC measured using gap sensor 2 (GS2)

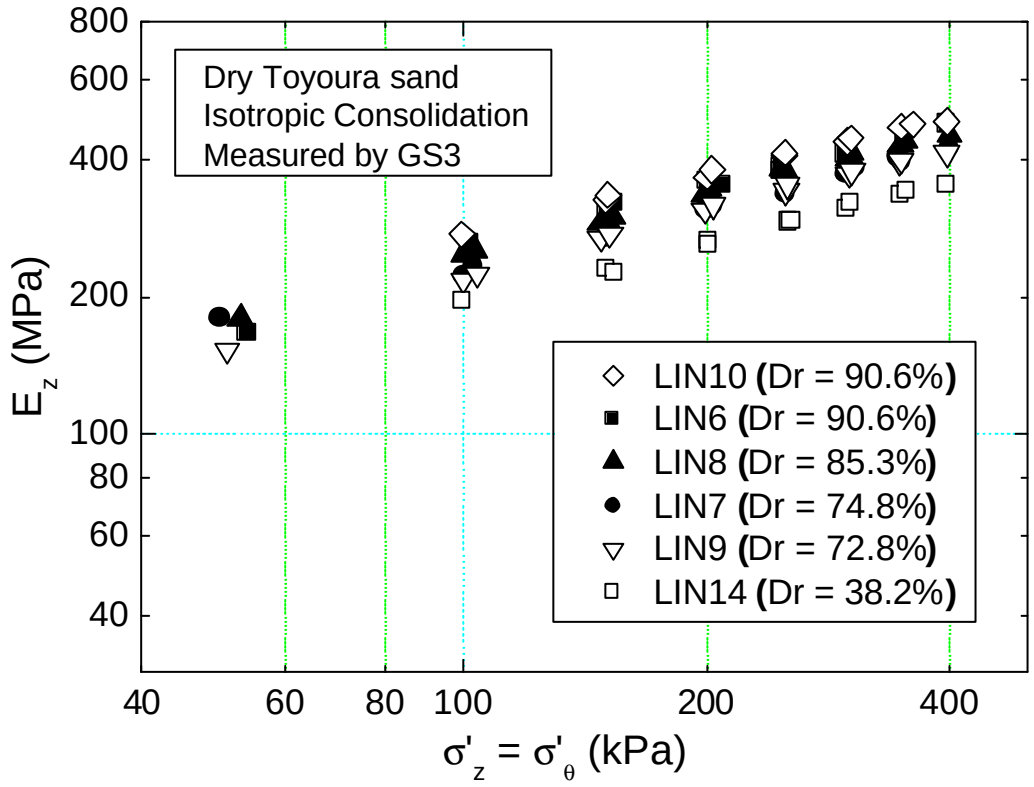

Fig. 4.14 E_z during IC measured using gap sensor 3 (GS3)

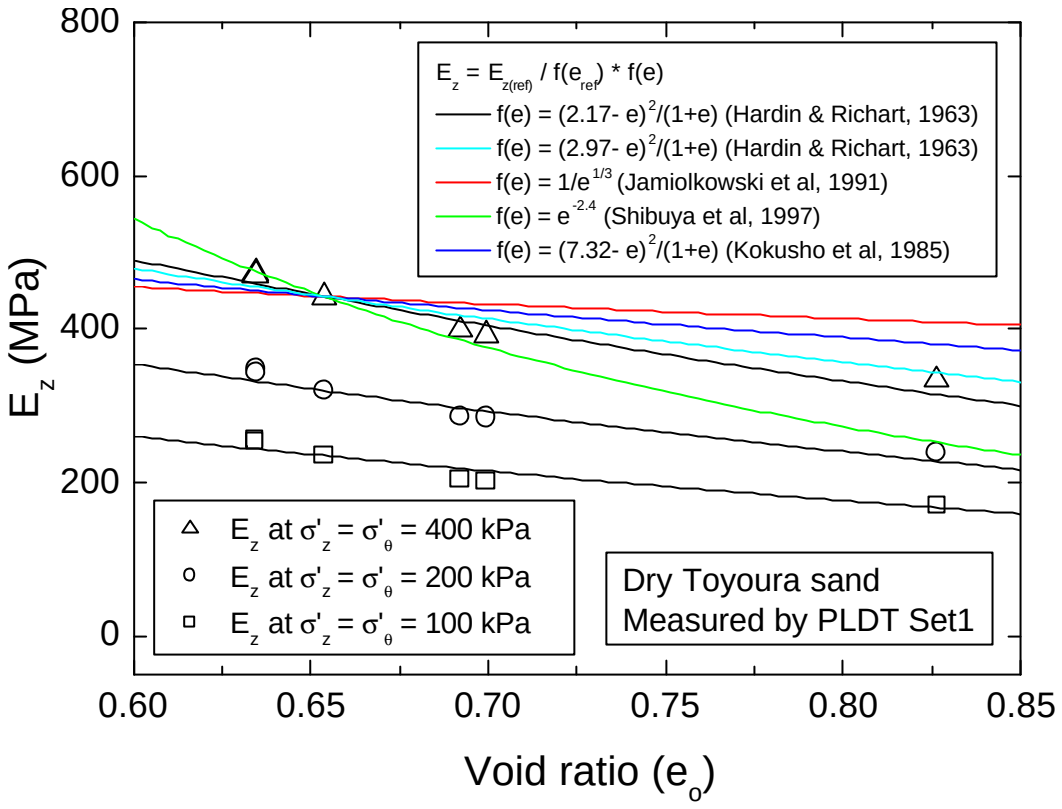

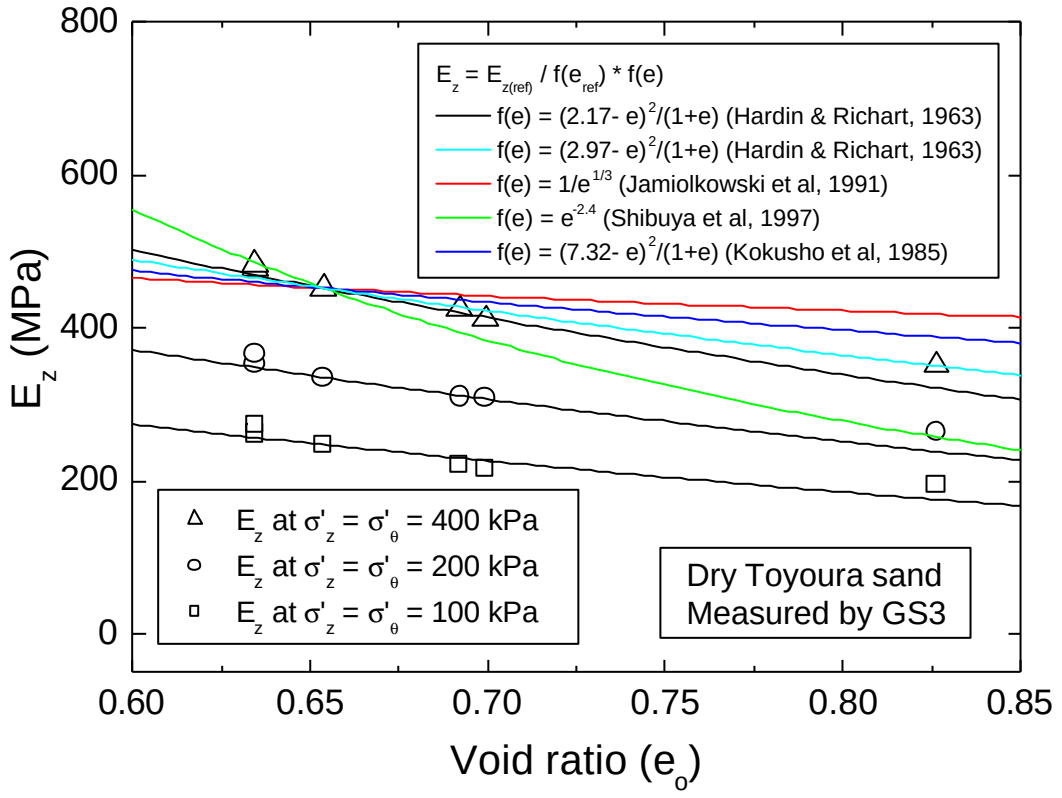

Fig. 4.15 Applicability of different void ratio functions

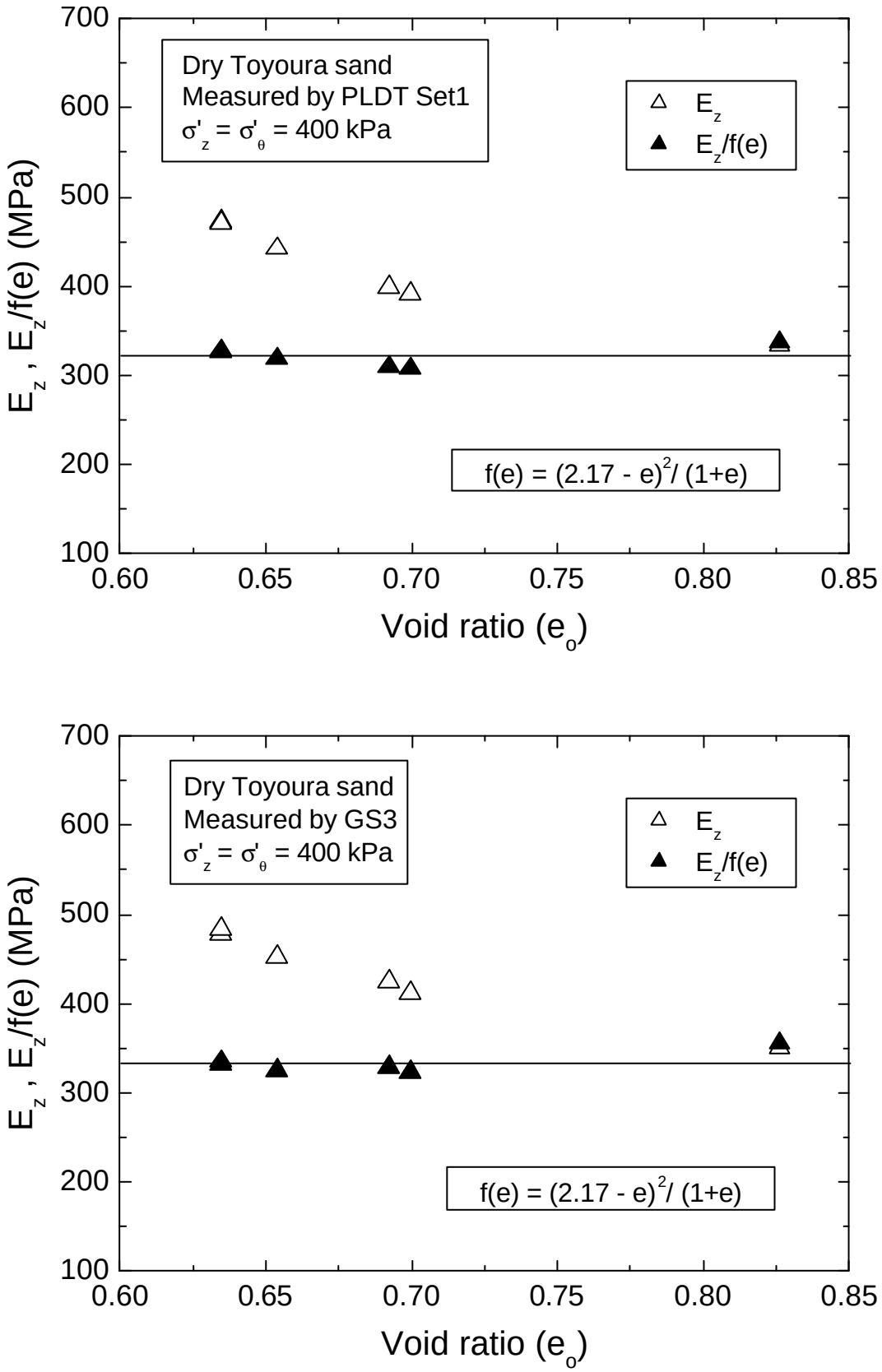

Fig. 4.16 E_z, $E_z/f(e)$ vs initial void ratio (e_o) at a typical stress state

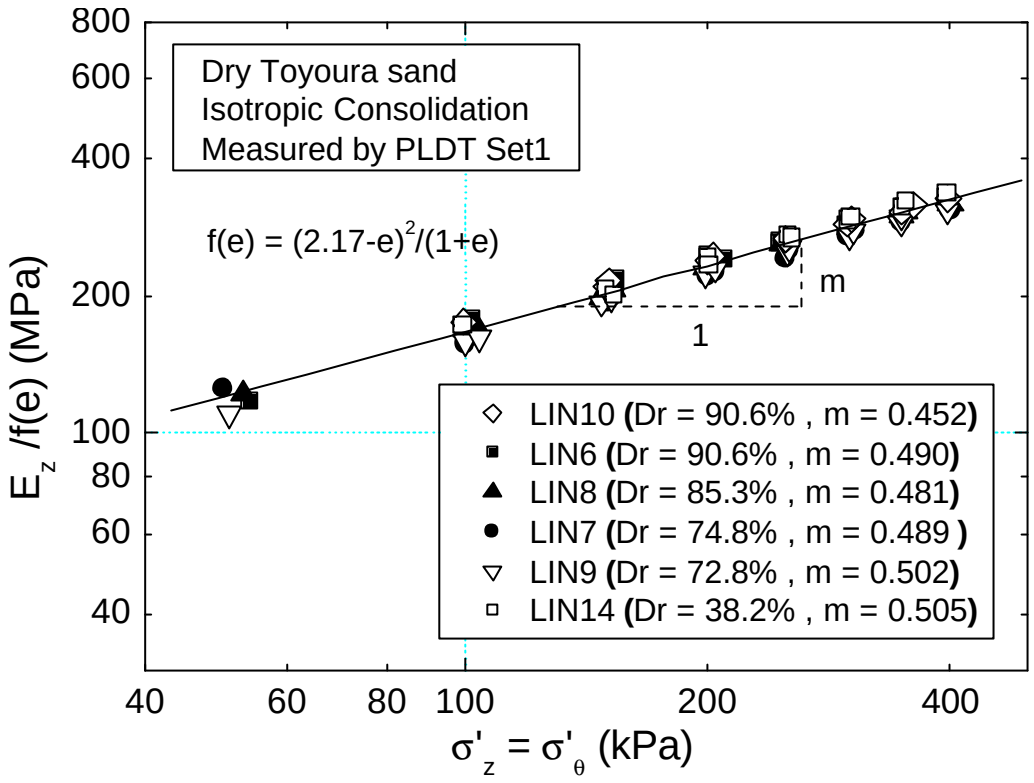

Fig. 4.17 $E_z/f(e)$ during IC measured using PLDT Set1

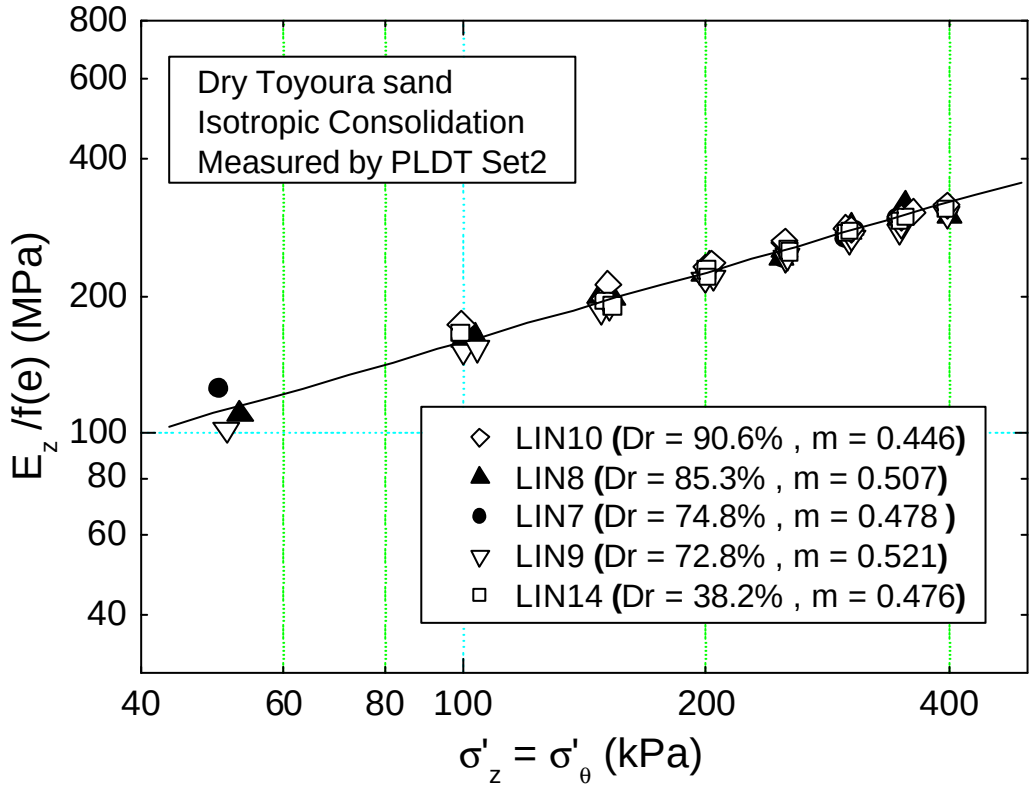

Fig. 4.18 $E_z/f(e)$ during IC measured using PLDT Set2

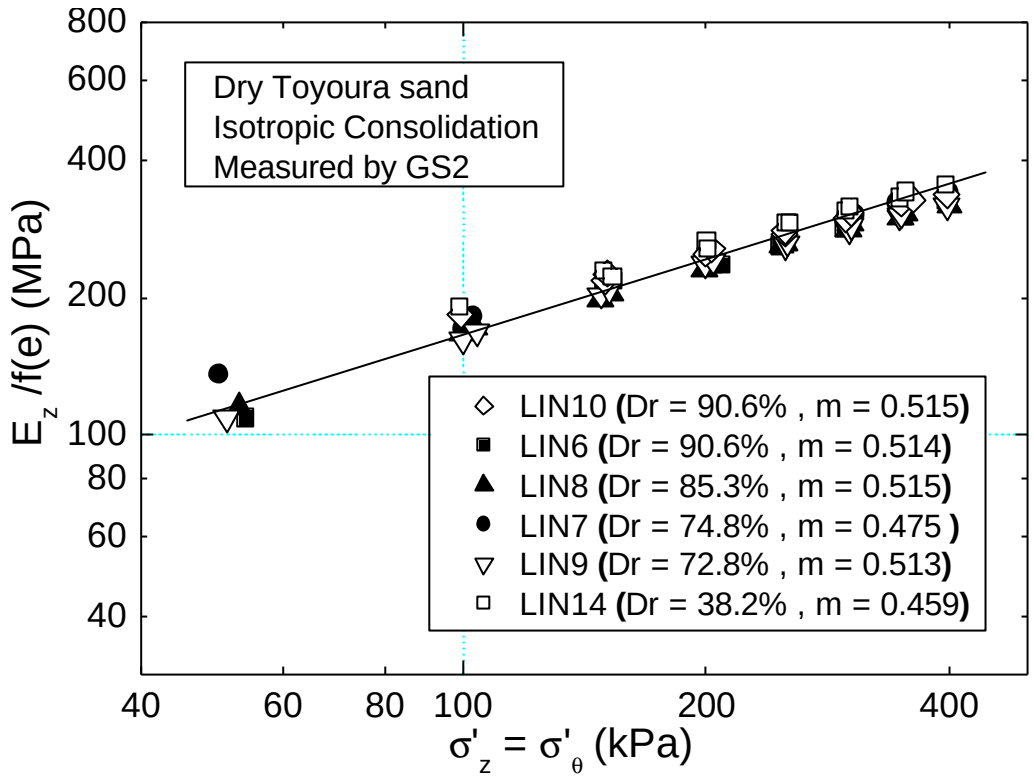

Fig. 4.19 $E_z/f(e)$ during IC measured using GS2

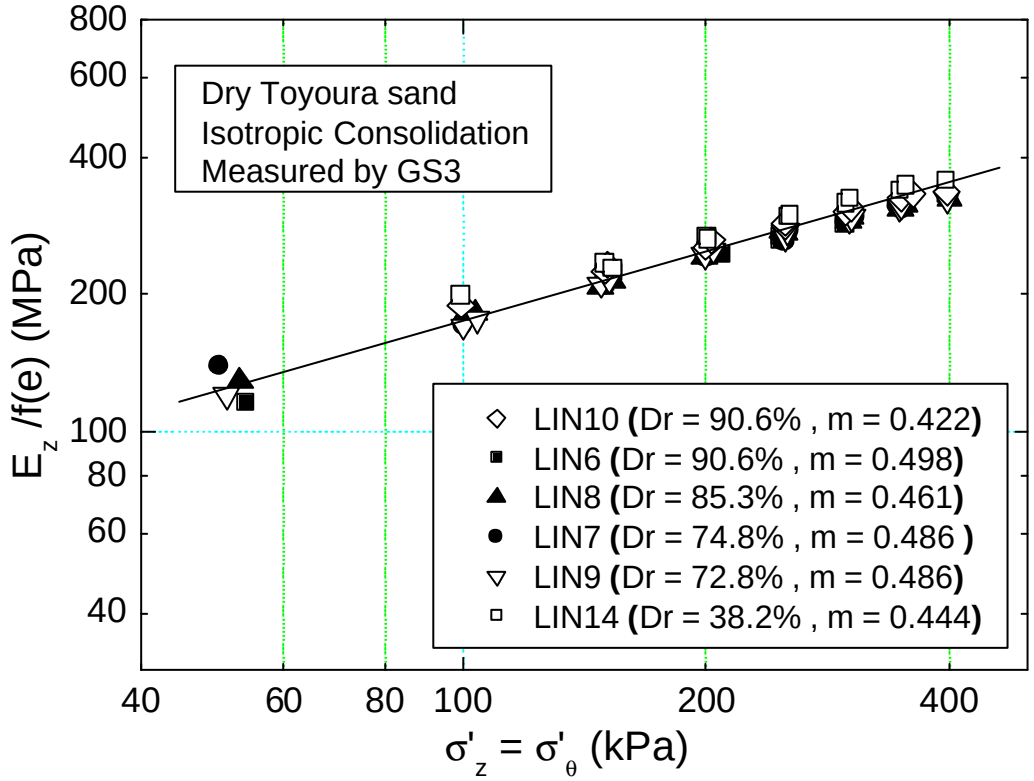

Fig. 4.20 $E_z/f(e)$ during IC measured using GS3

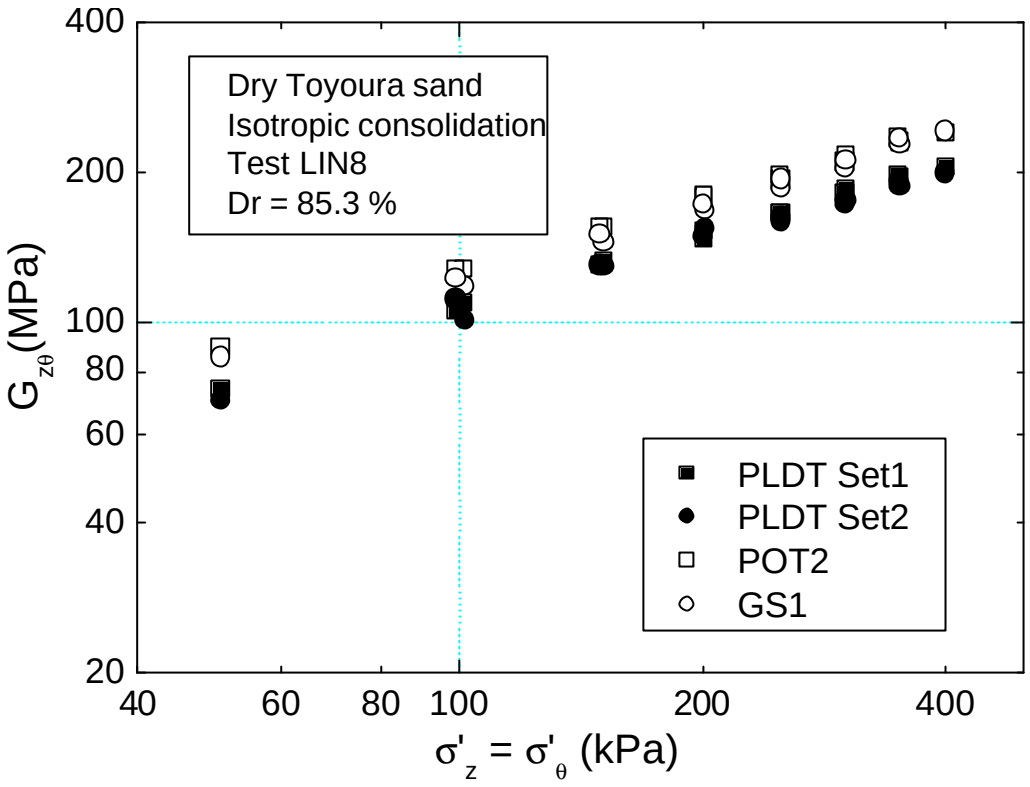

Fig. 4.21 $G_{z\theta}$ values measured using diferent transducers

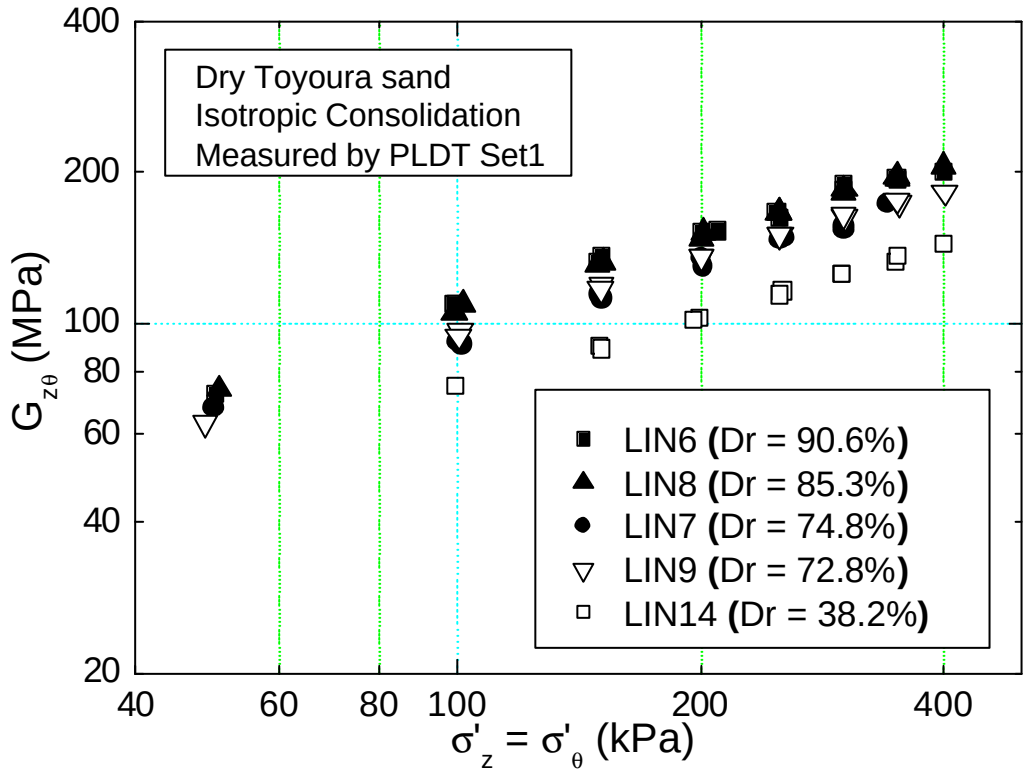

Fig. 4.22 $G_{z\theta}$ values measured using PLDT Set1

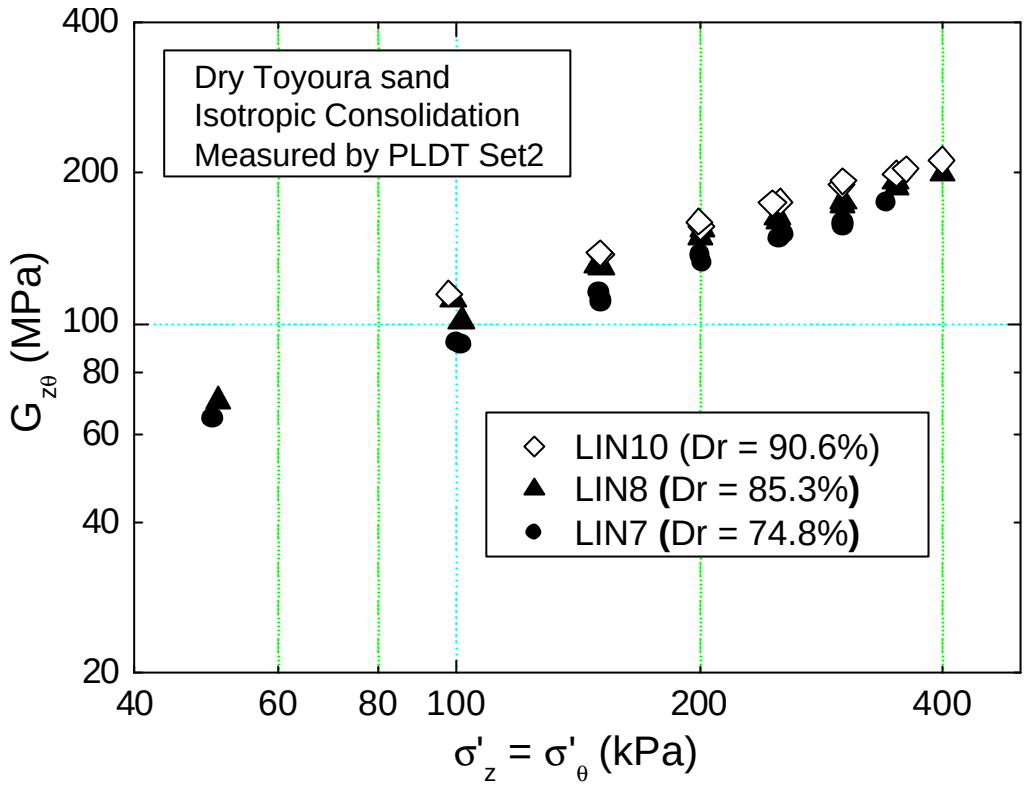

Fig. 4.23 $G_{z\theta}$ values measured using PLDT Set2

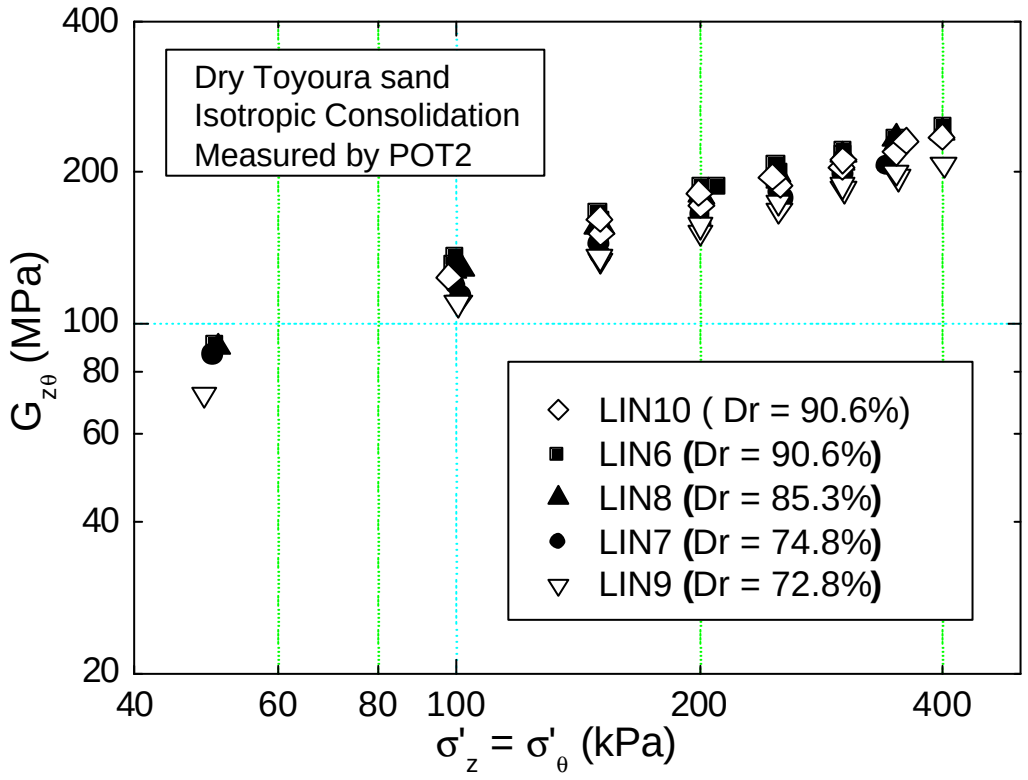

Fig. 4.24 $G_{z\theta}$ values measured using POT2

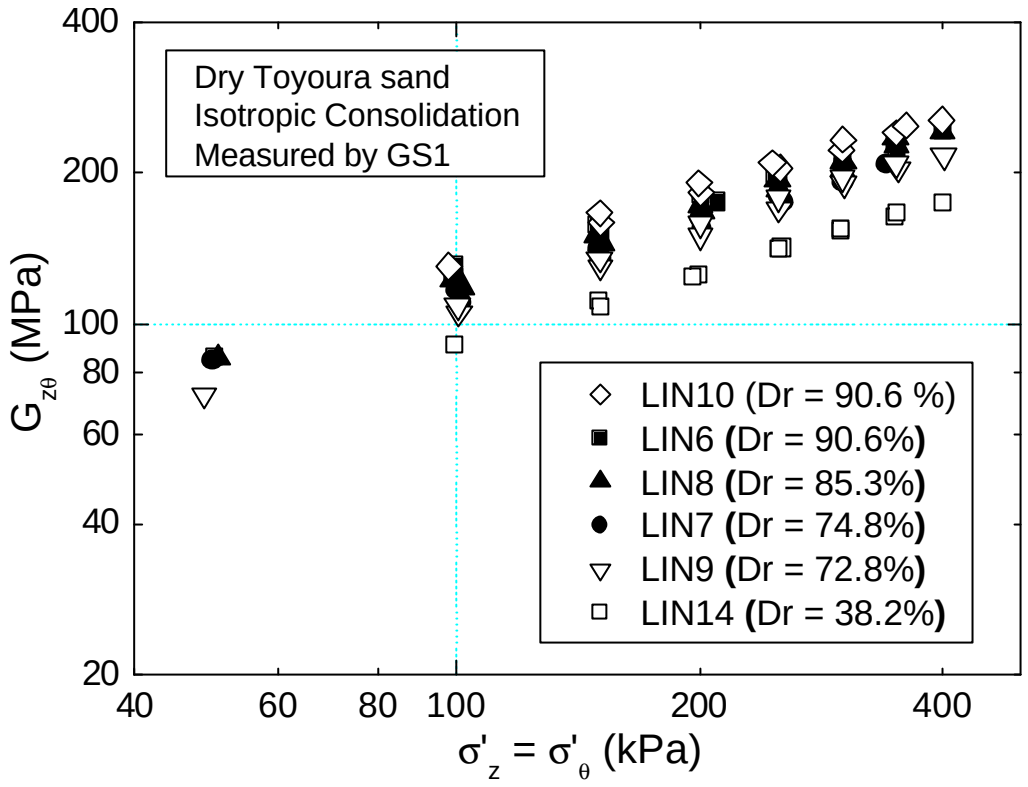

Fig. 4.25 $G_{z\theta}$ values measured using GS1

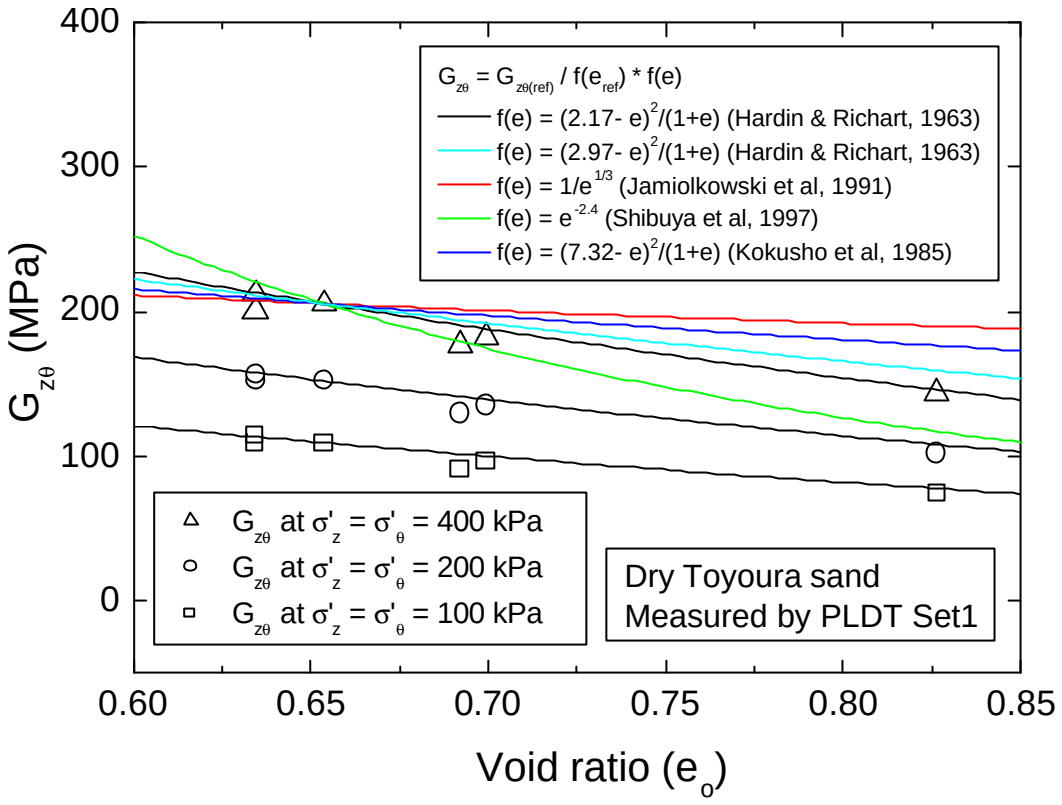

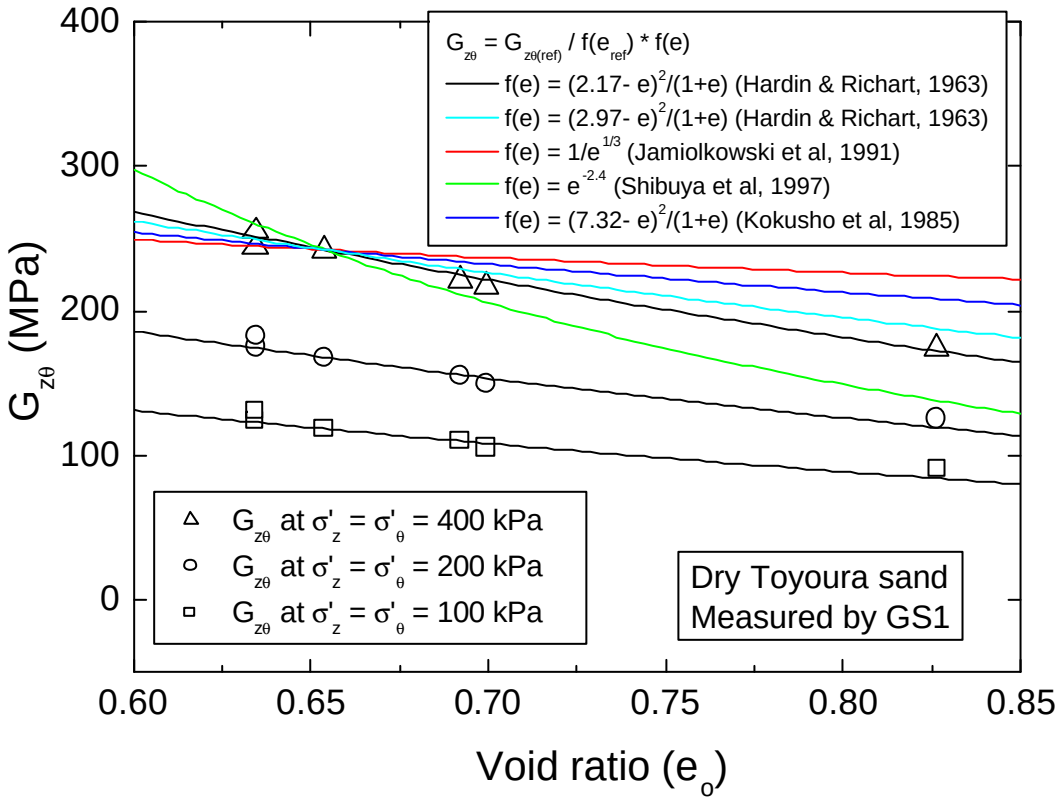

Fig. 4.25a Applicability of different void ratio functions for $G_{z\theta}$

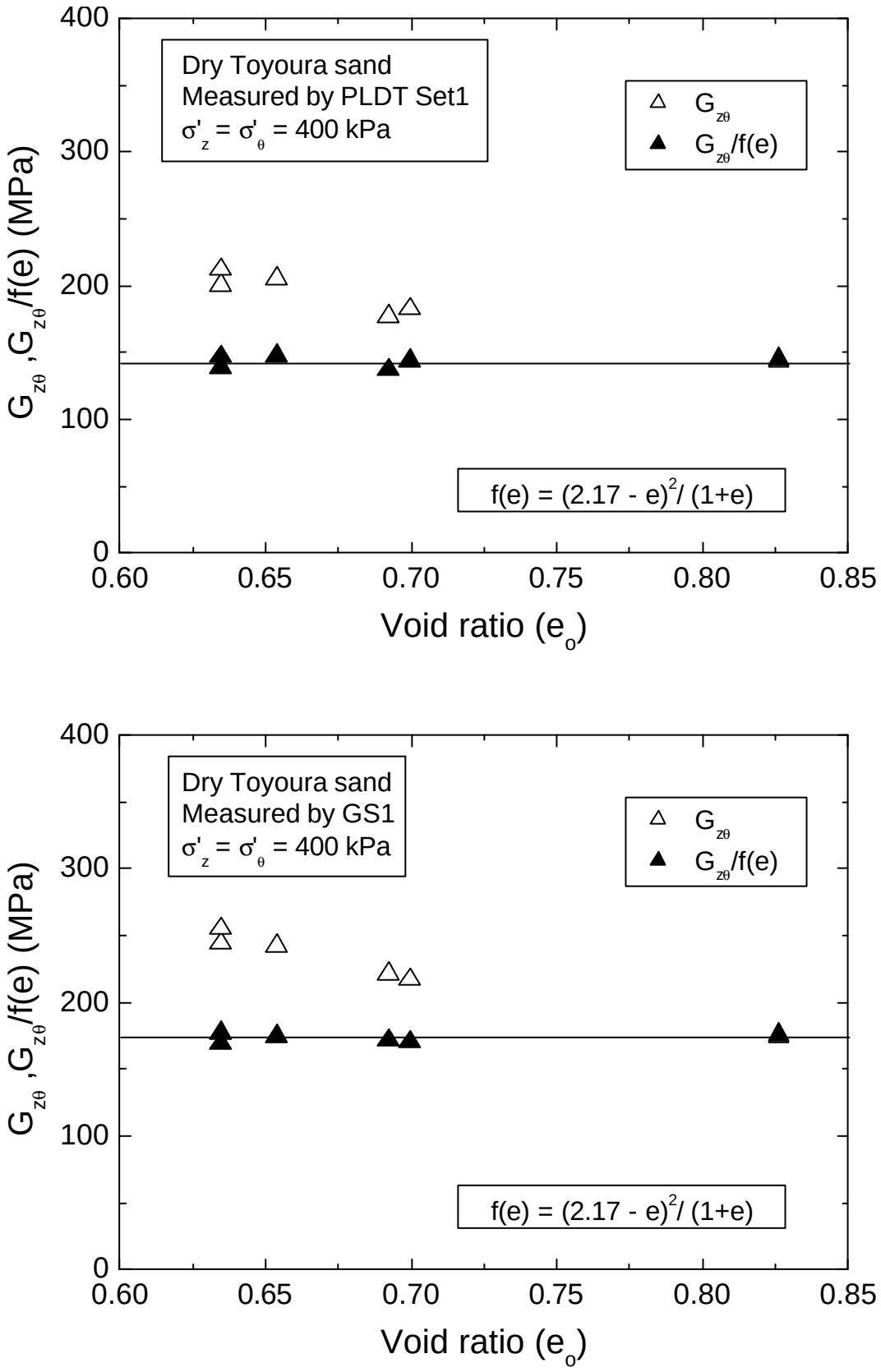

Fig. 4.25b $G_{z\theta}$, $G_{z\theta}/f(e)$ vs initial void ratio (e_o) at a typical stress state

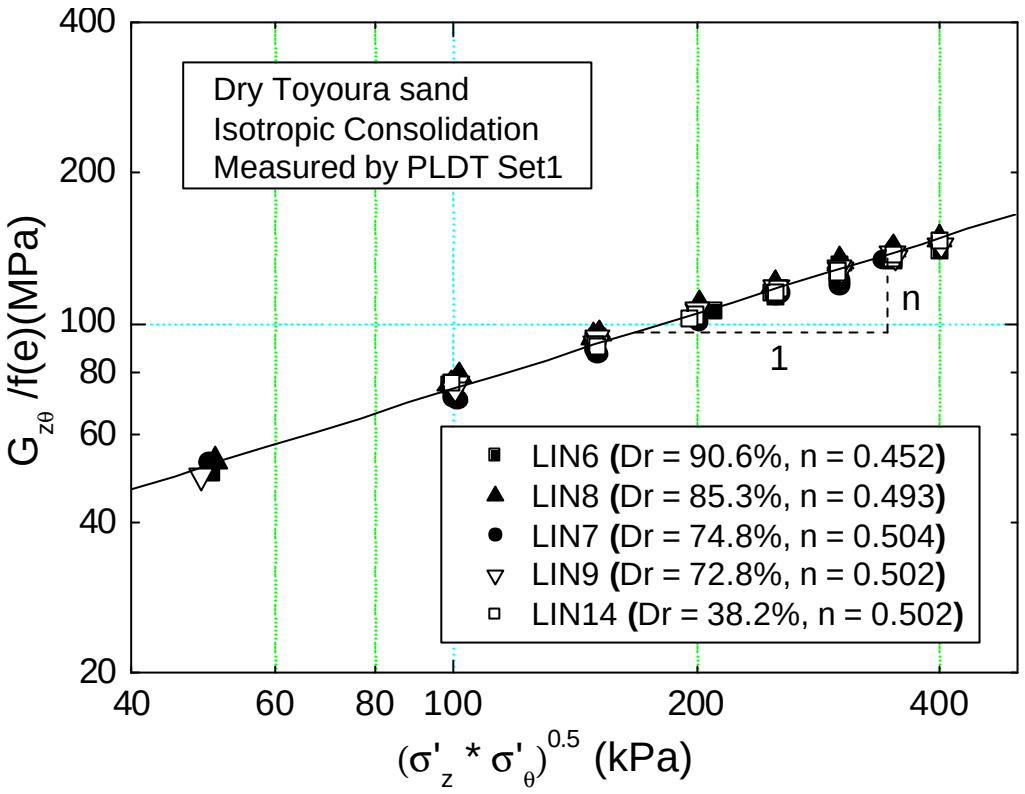

Fig. 4.26 $G_{z\theta}$/f(e) values measured using PLDT Set1

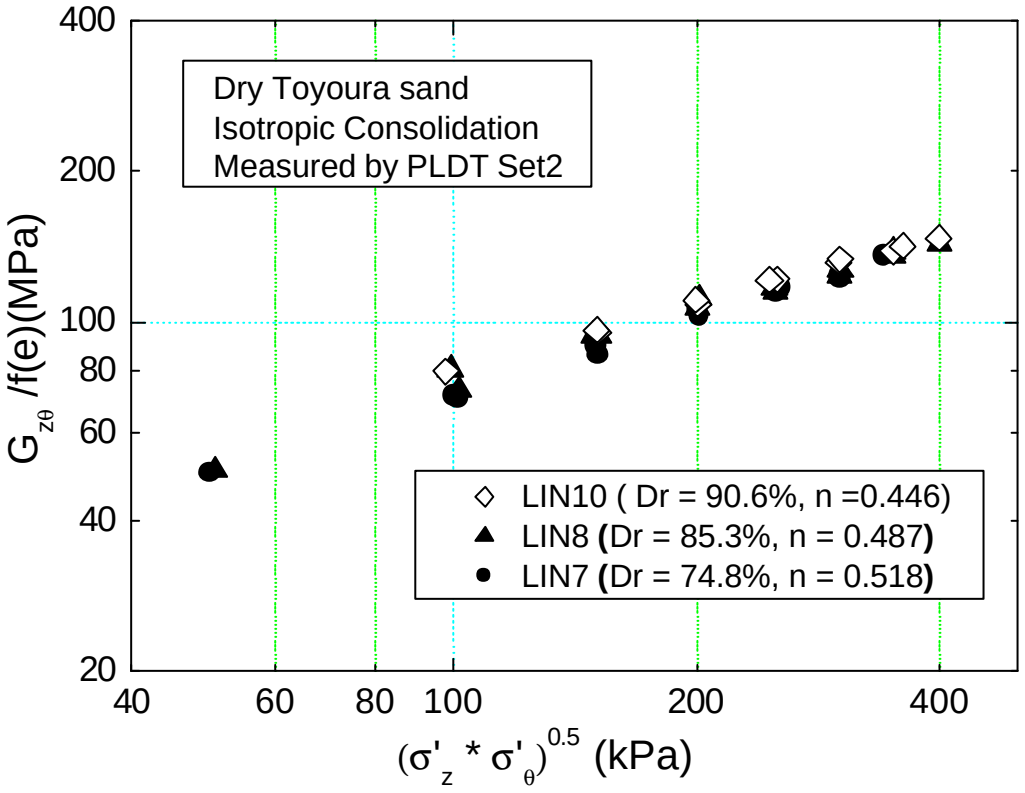

Fig. 4.27 $G_{z\theta}$/f(e) values measured using PLDT Set2

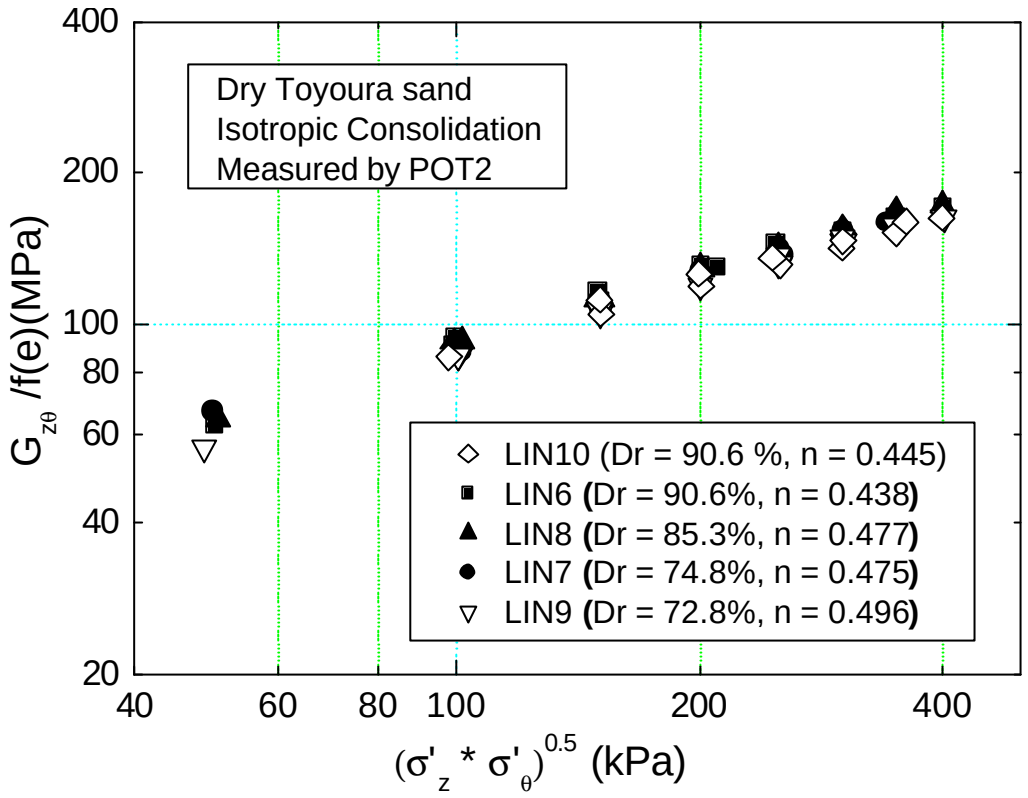

Fig. 4.28 $G_{z\theta}$/f(e) values measured using POT2

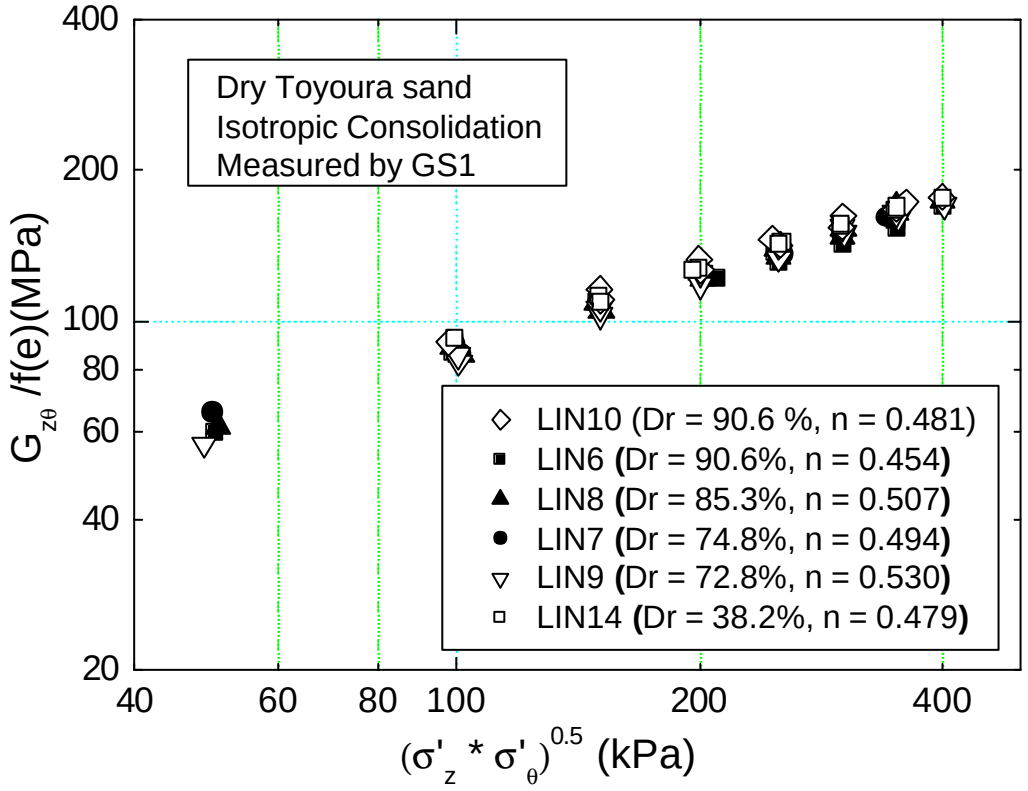

Fig. 4.29 $G_{z\theta}$/f(e) values measured using GS1

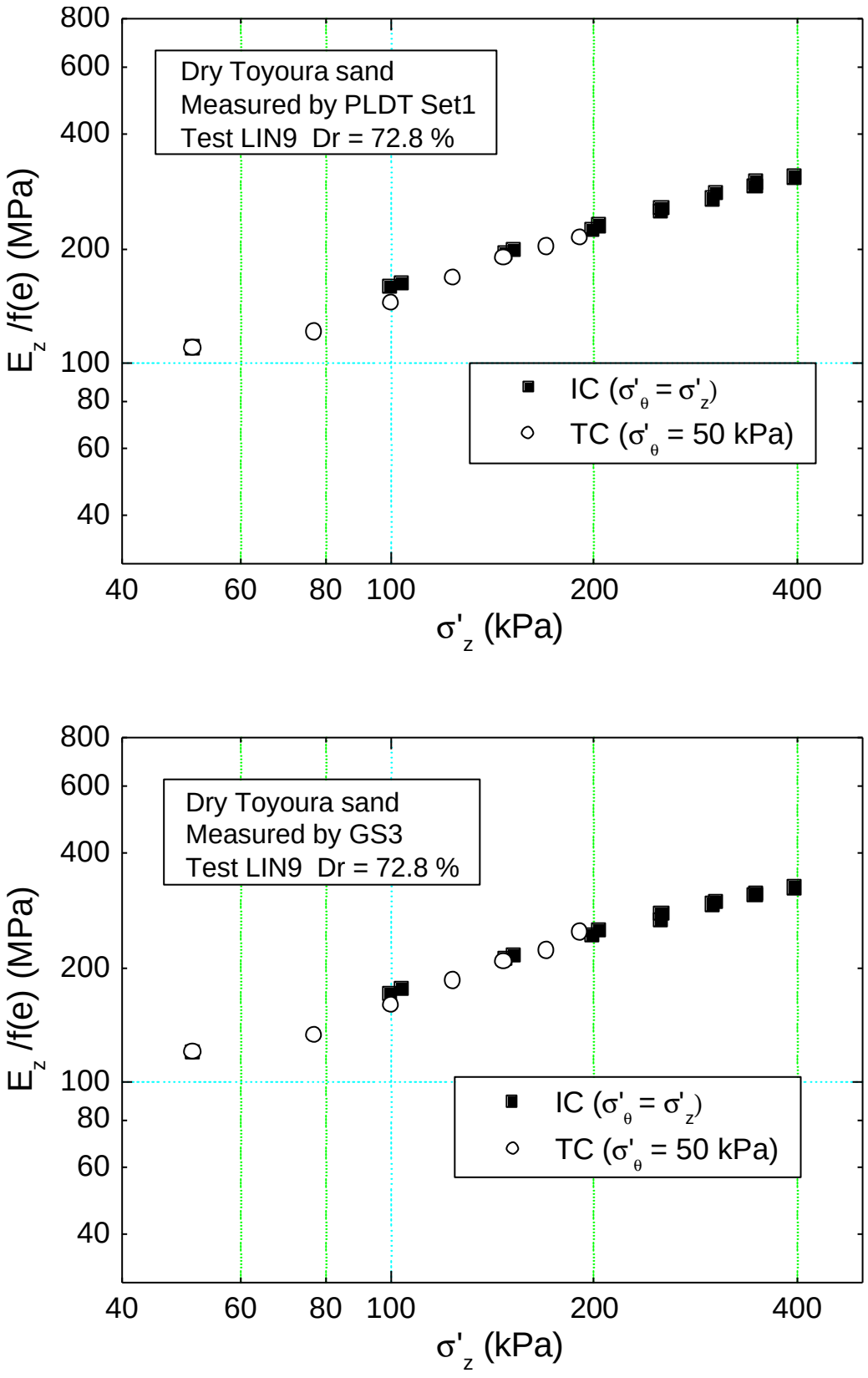

Fig. 4.30 $E_z/f(e)$ vs σ'_z during IC and TC

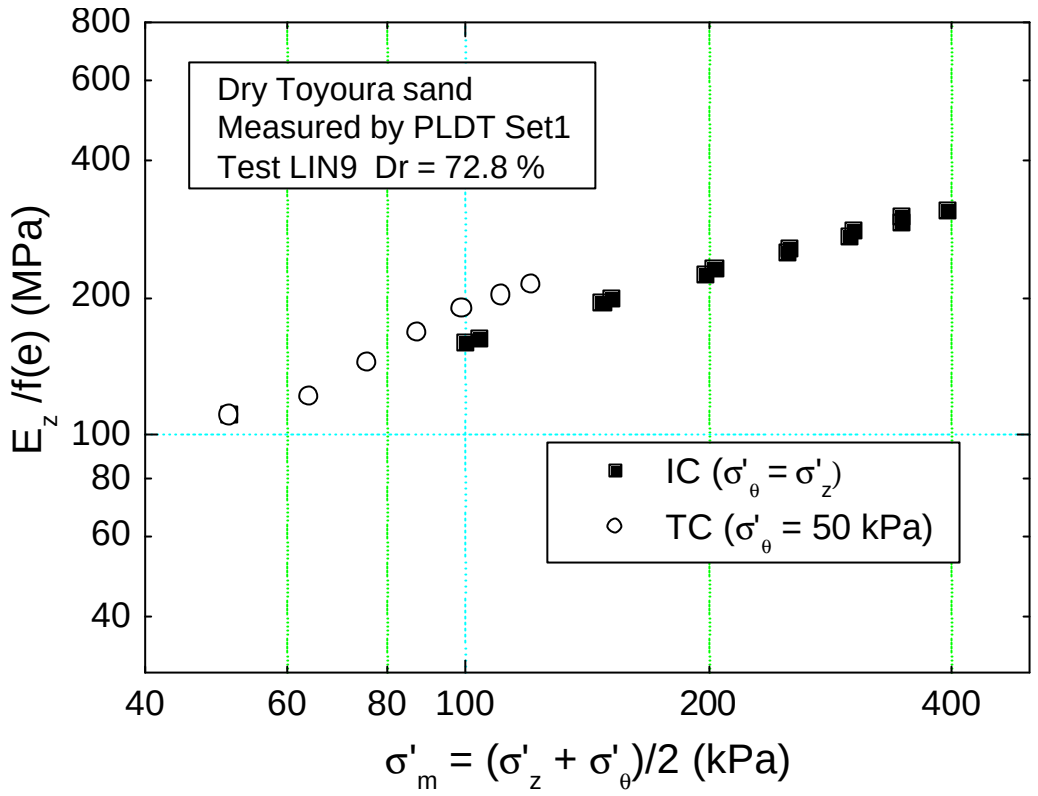

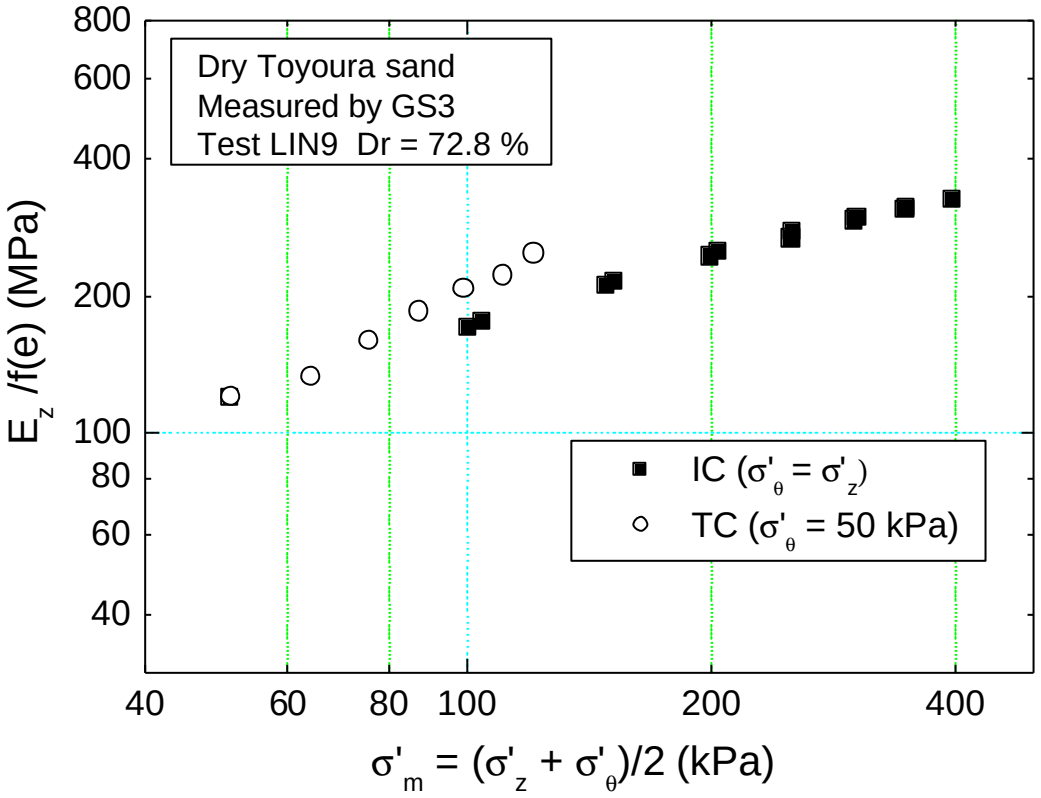

Fig. 4.31 $E_z/f(e)$ vs σ'_m during IC and TC

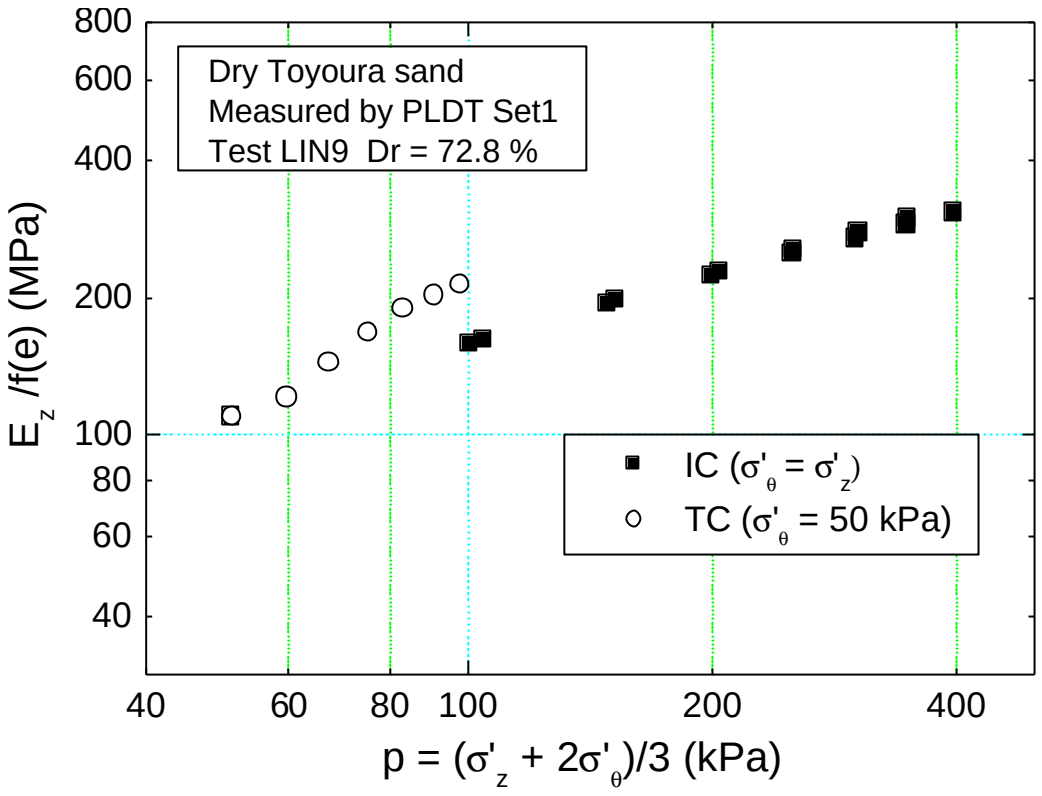

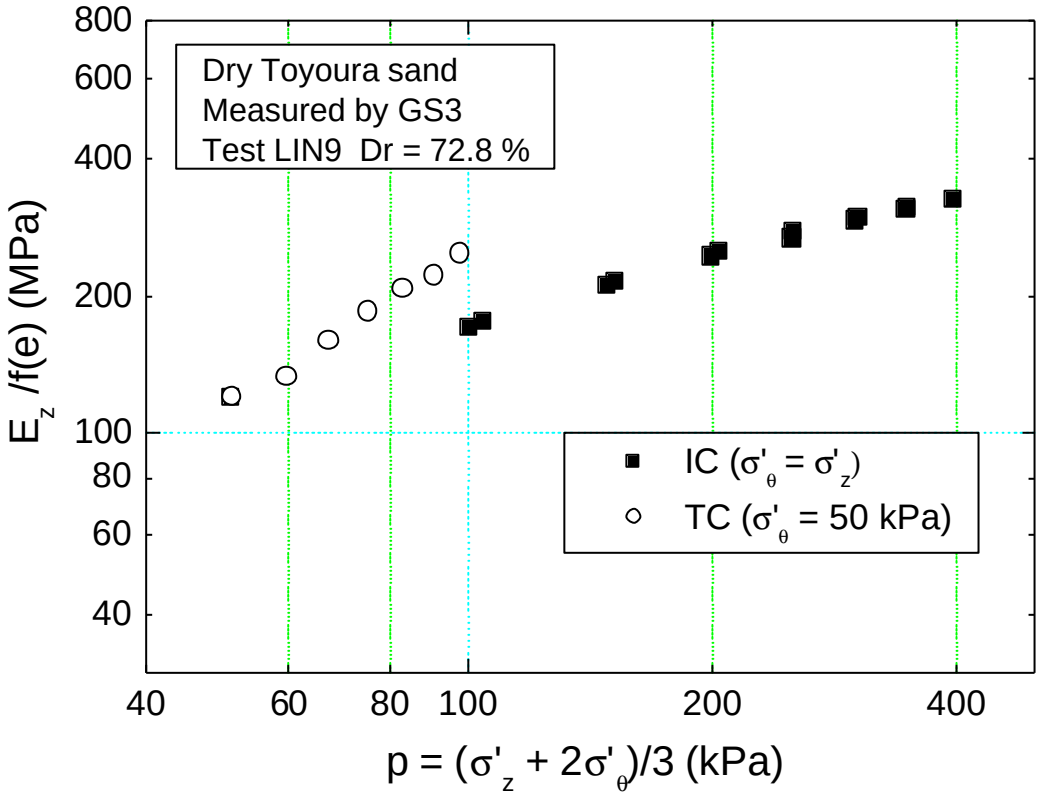

Fig. 4.32 $E_z/f(e)$ vs p during IC and TC

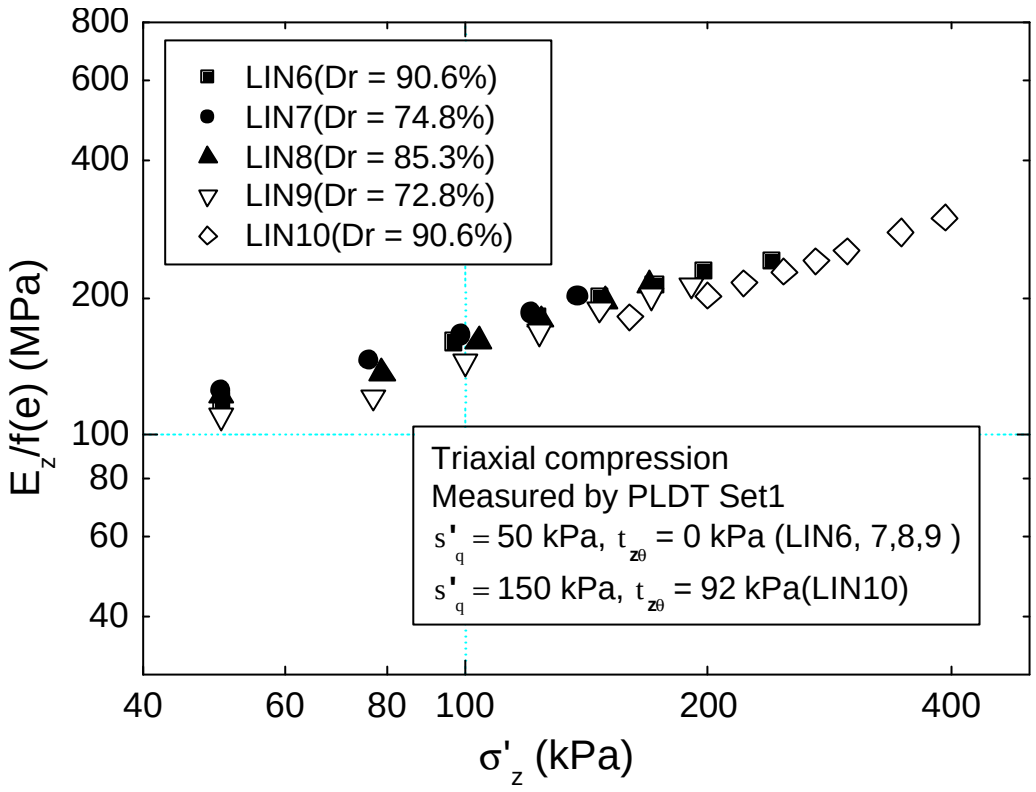

Fig. 4.33 $E_z/f(e)$ vs σ'_z during TC measured by PLDT Set1

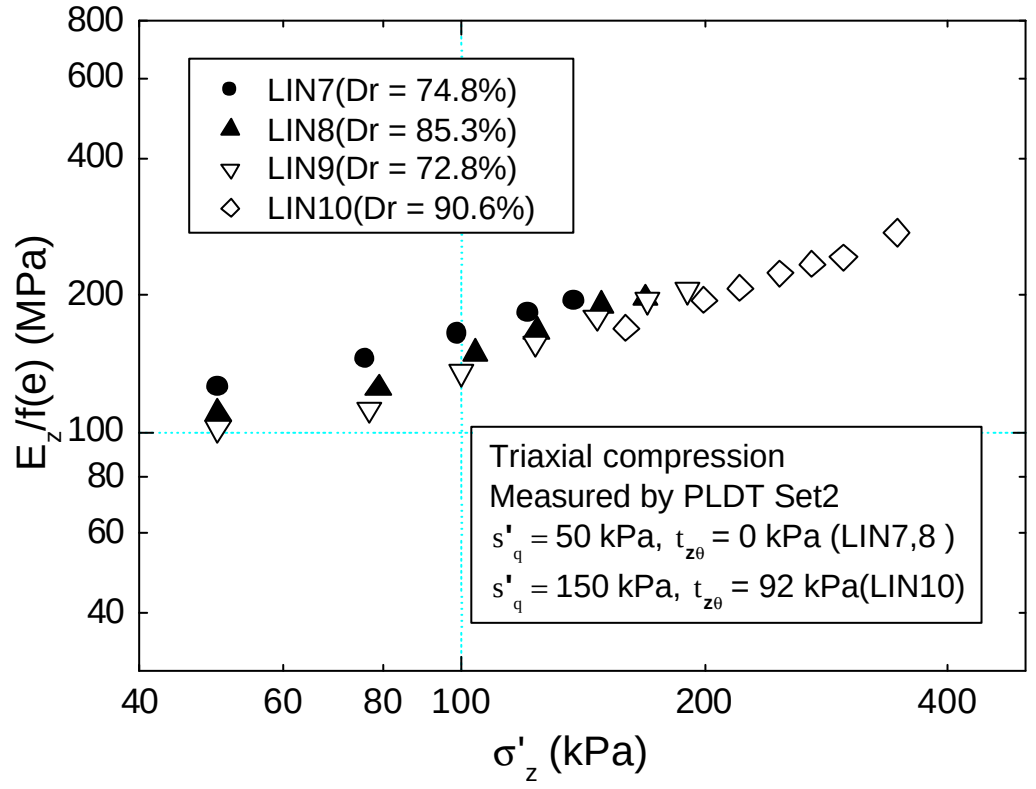

Fig. 4.34 $E_z/f(e)$ vs σ'_z during TC measured by PLDT Set2

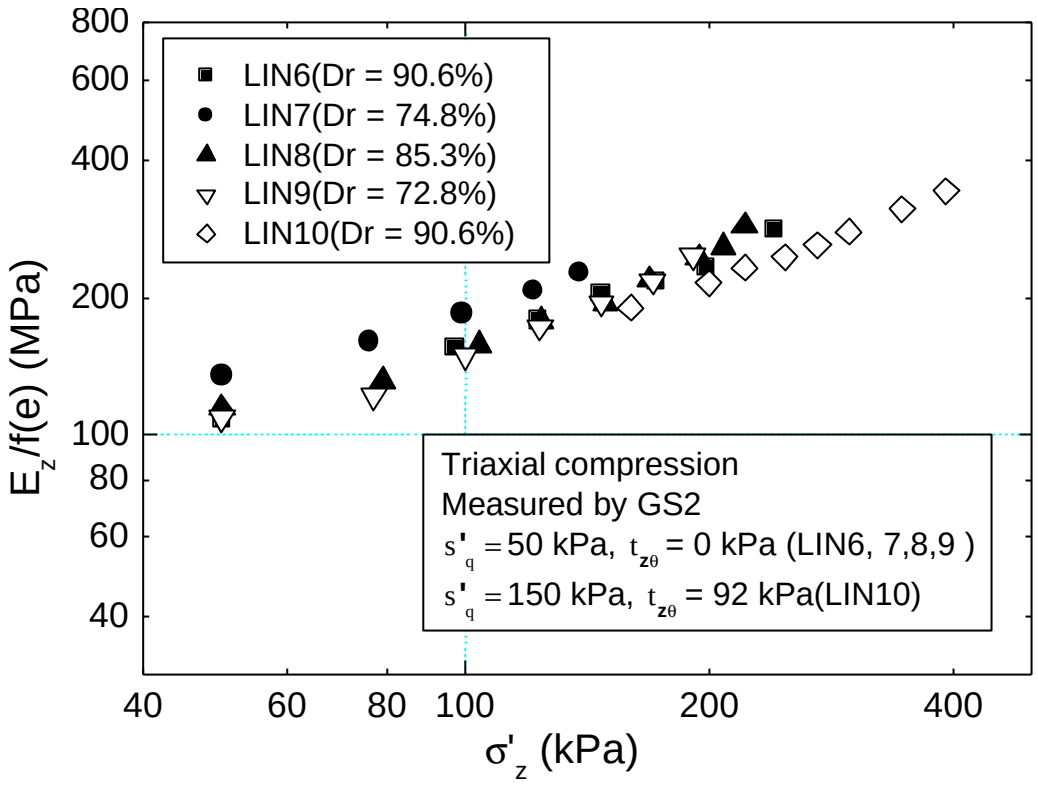

Fig. 4.35 $E_z/f(e)$ vs σ'_z during TC measured by GS2

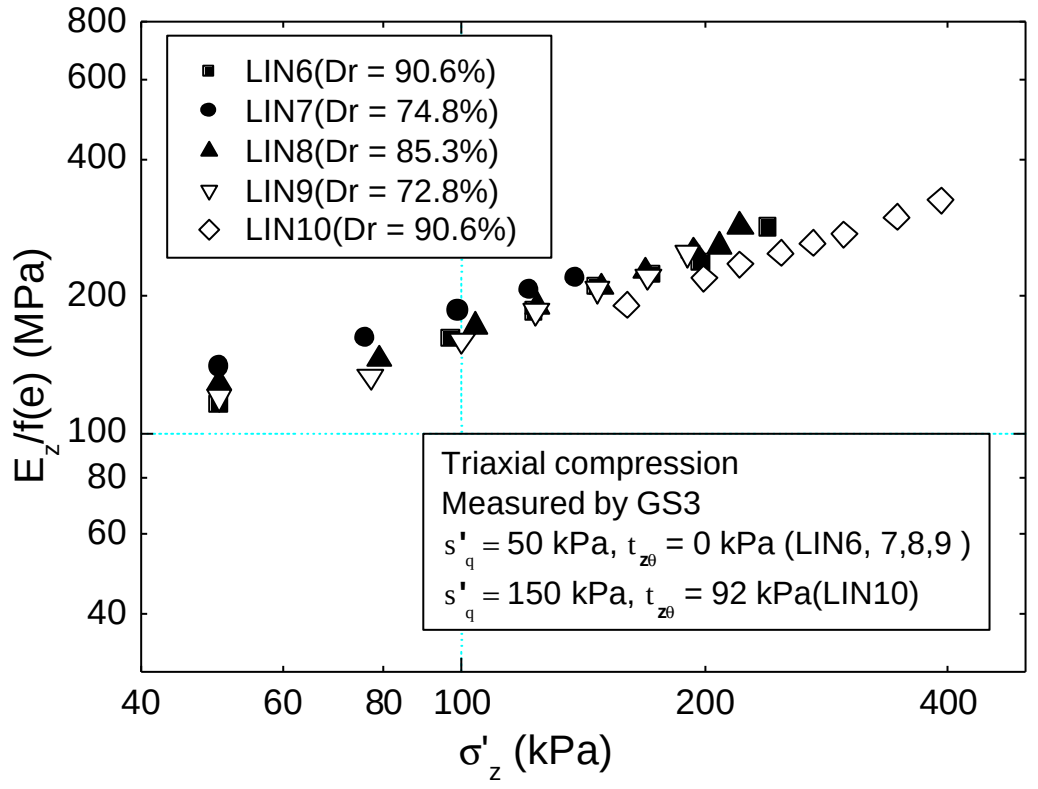

Fig. 4.36 $E_z/f(e)$ vs σ'_z during TC measured by GS3

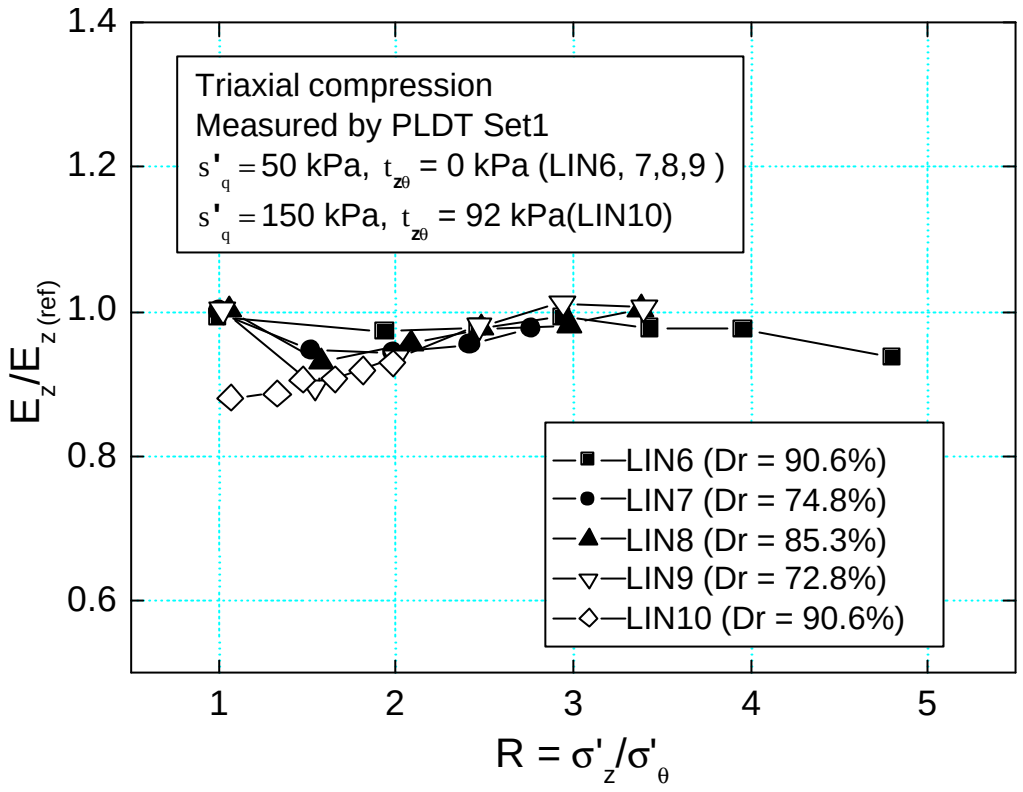

Fig. 4.37 $E_z/ E_{z\ (ref)}$ vs R during TC measured by PLDT1

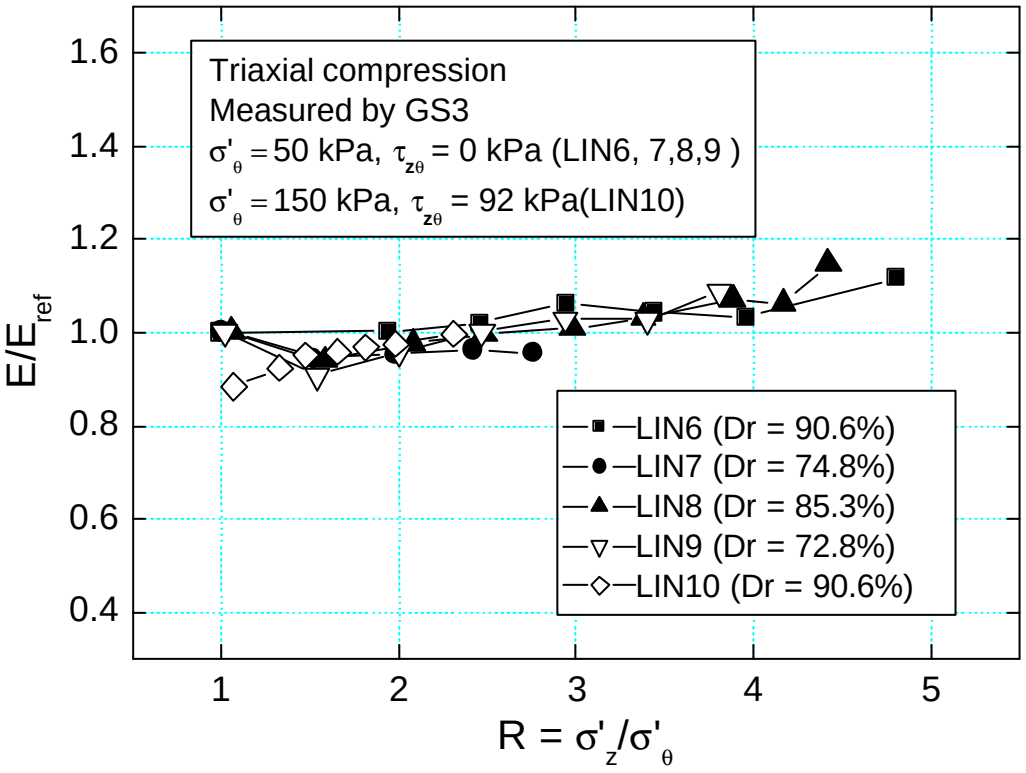

Fig. 4.38 $E_z/ E_{z\ (ref)}$ vs R during TC measured by GS3

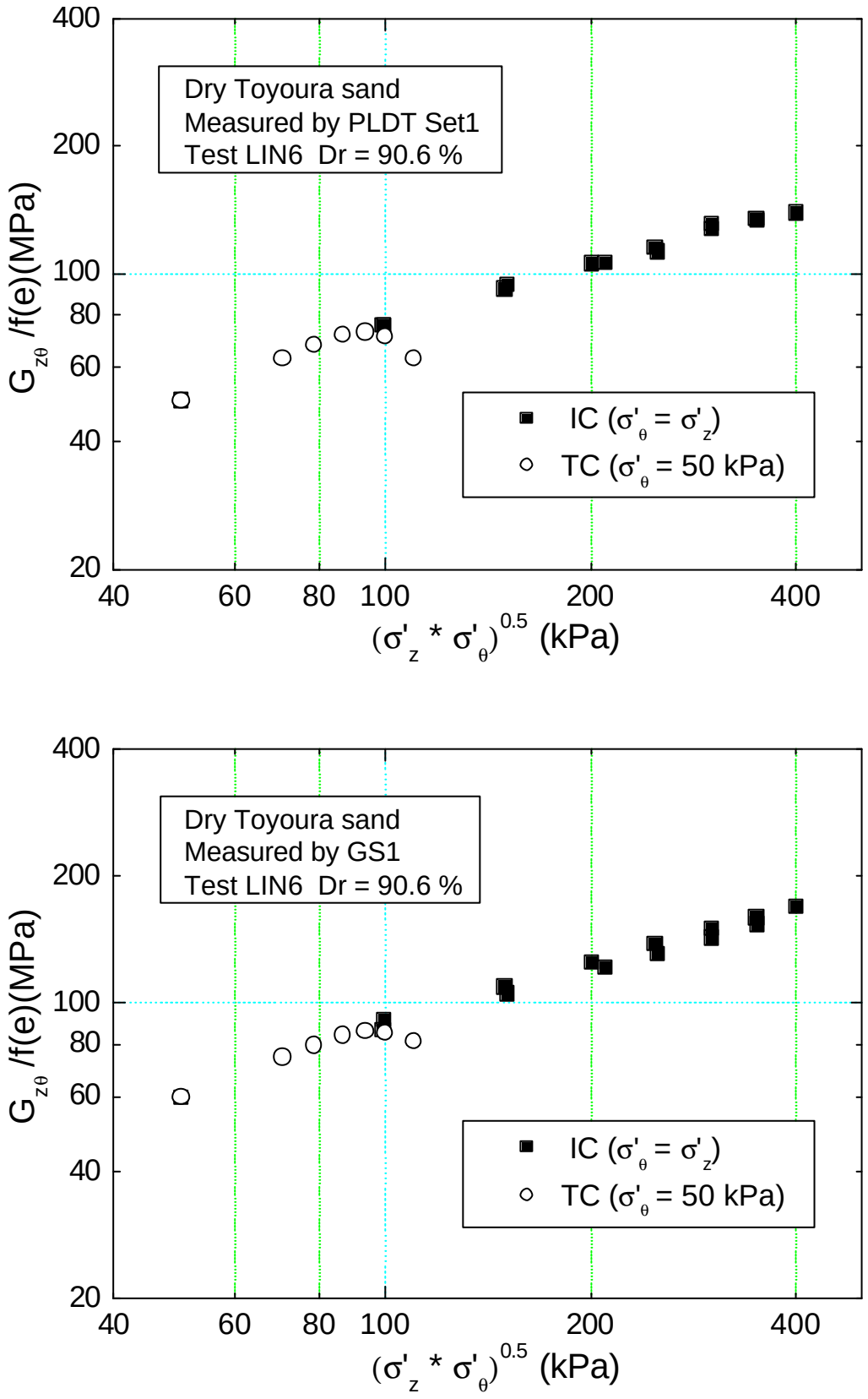

Fig. 4.39 $G_{z\theta}/f(e)$ vs $(\sigma'_z * \sigma'_\theta)^{0.5}$ during IC and TC

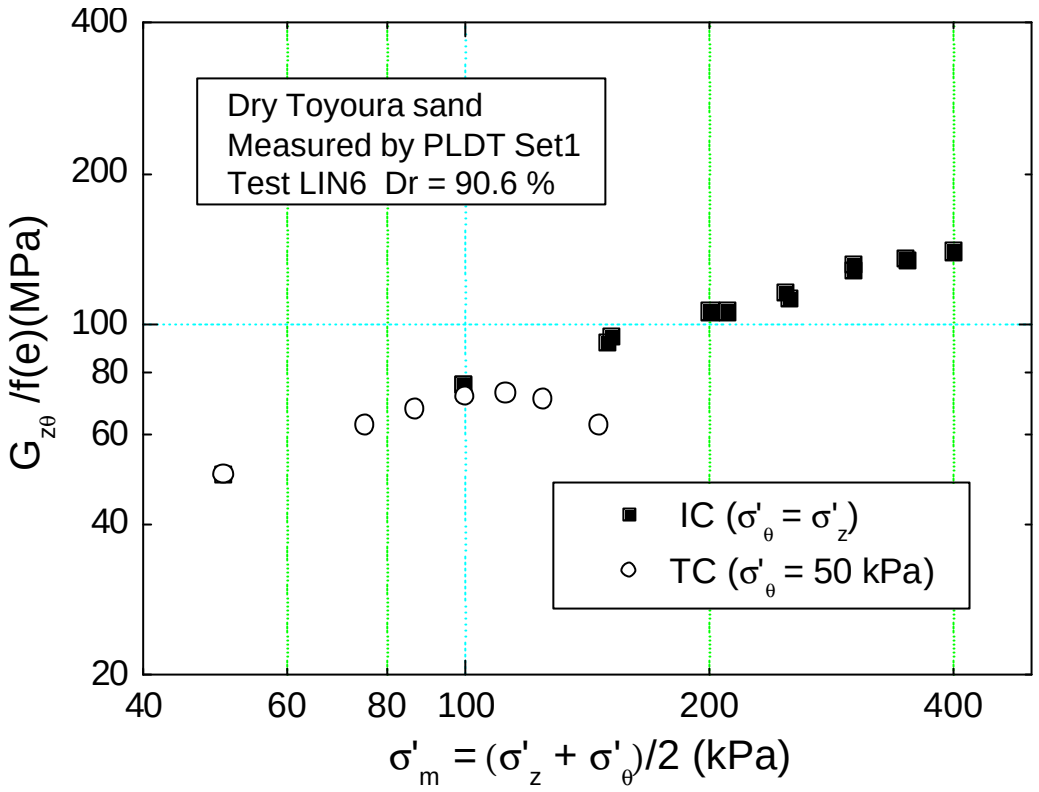

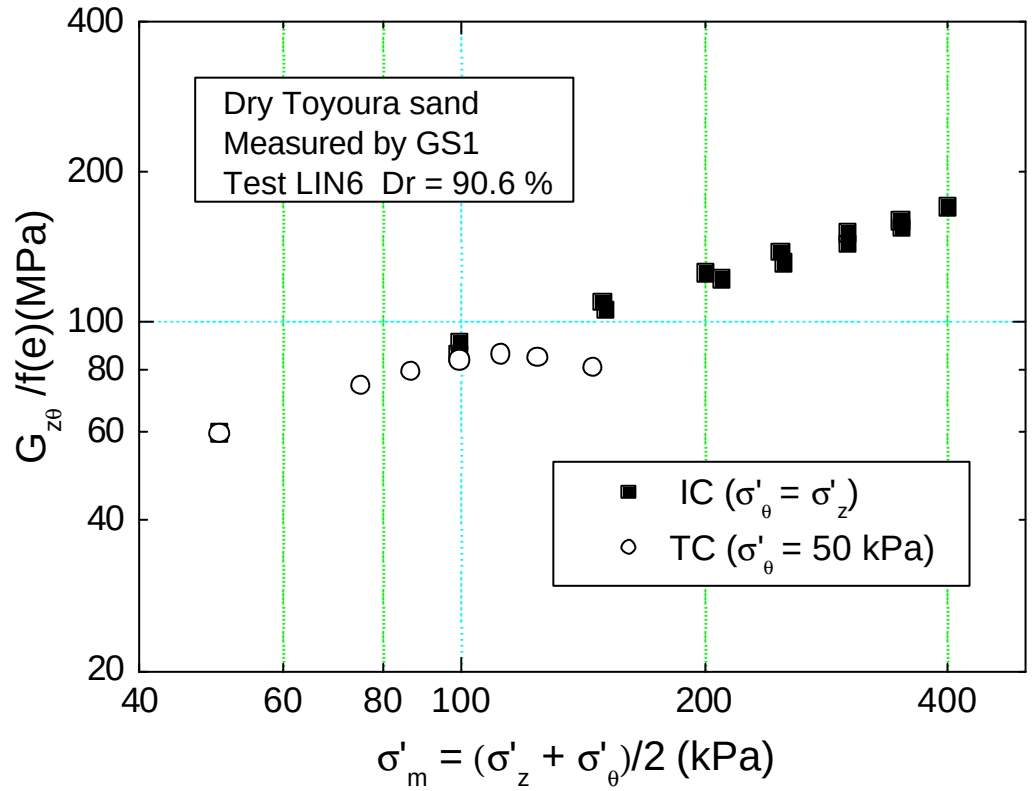

Fig. 4.40 $G_{z\theta}/f(e)$ vs $\sigma'_m = (\sigma'_z + \sigma'_\theta)/2$ during IC and TC

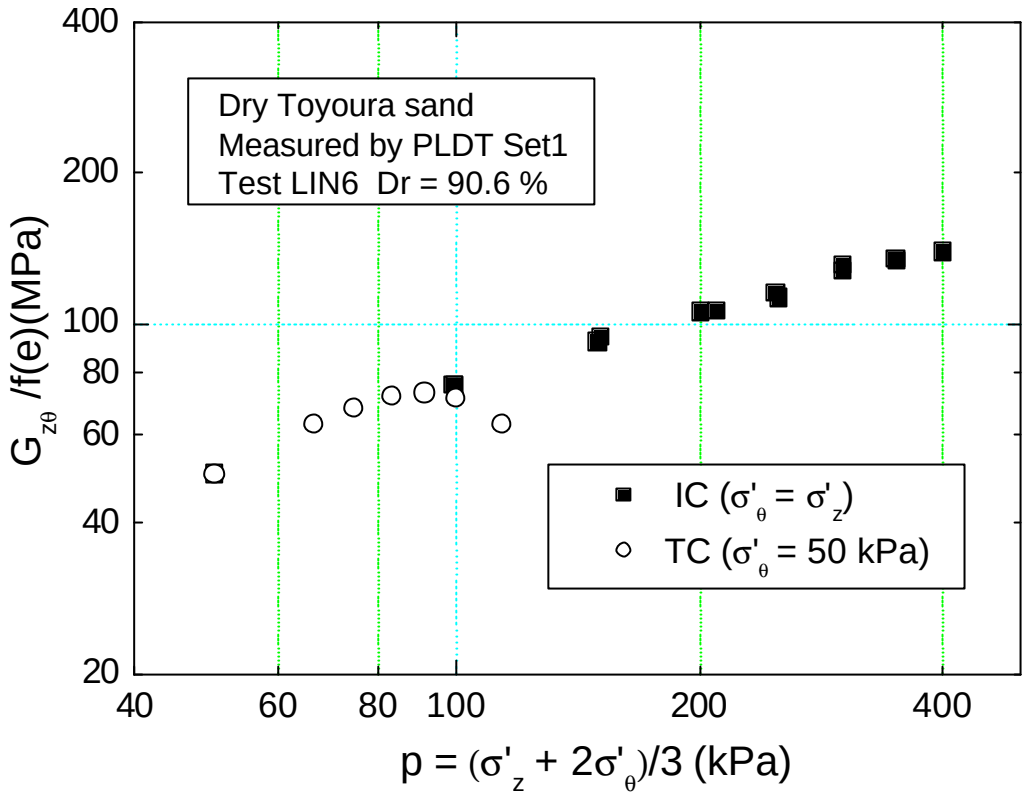

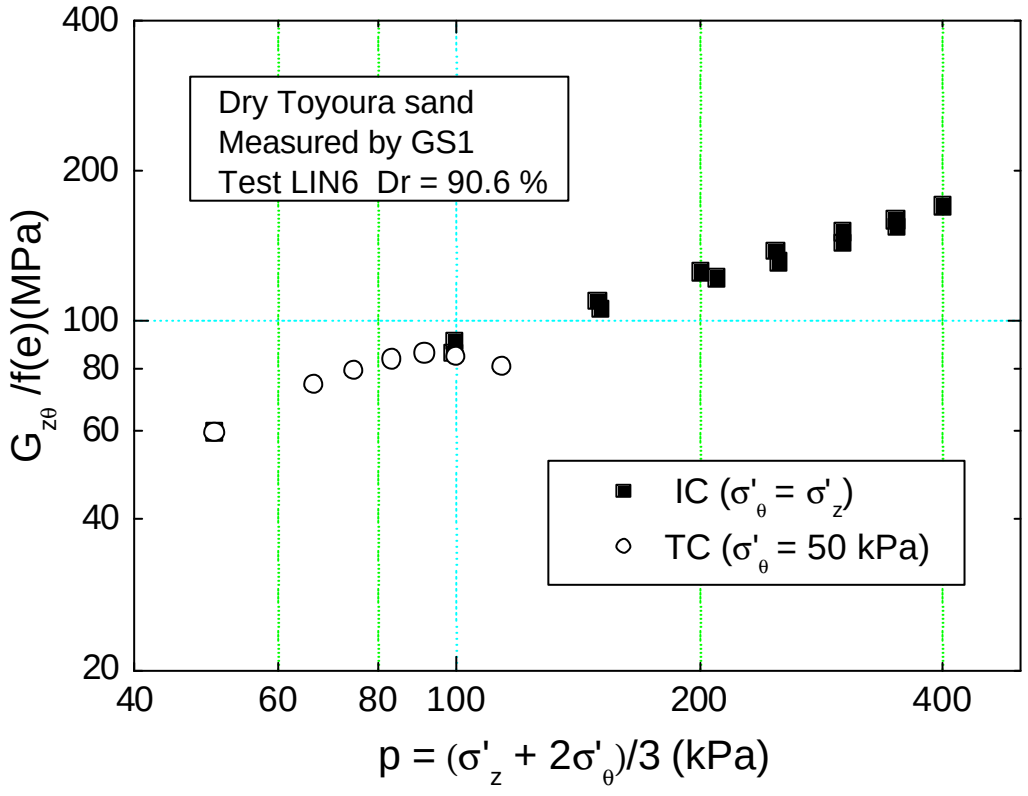

Fig. 4.41 $G_{z\theta}/f(e)$ vs $p = (\sigma'_z + 2\sigma'_\theta)/3$ during IC and TC

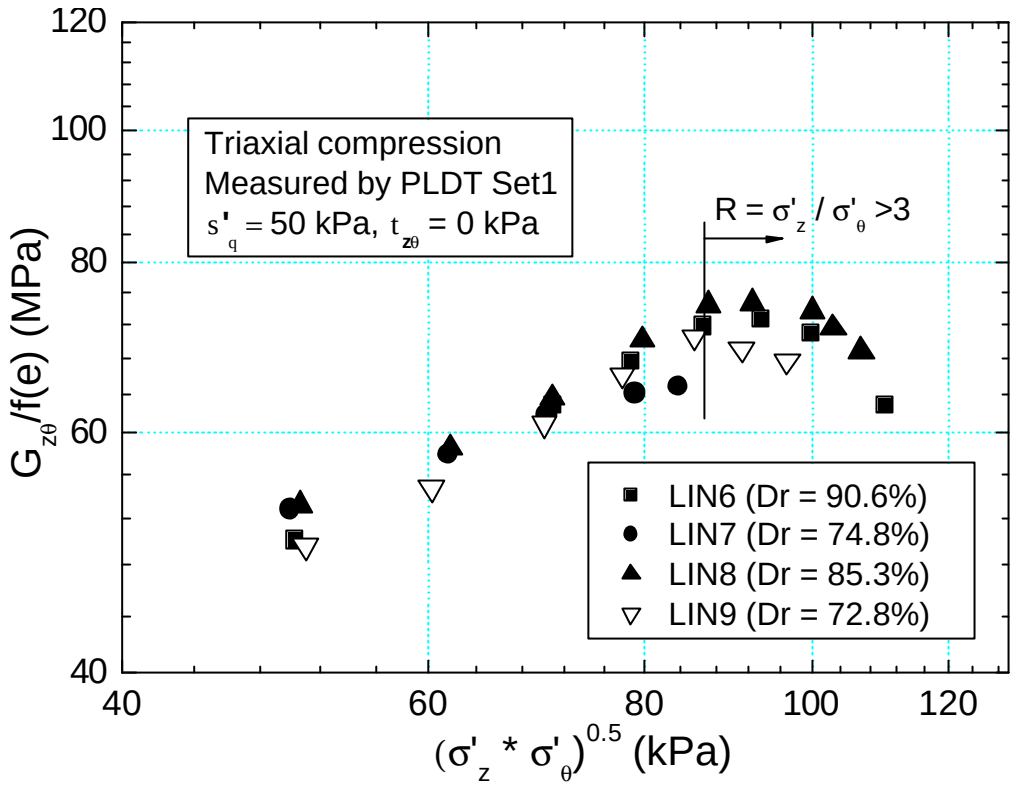

Fig. 4.42 $G_{z\theta}/f(e)$ vs $(\sigma'_z * \sigma'_\theta)^{0.5}$ during TC measured by PLDT Set1

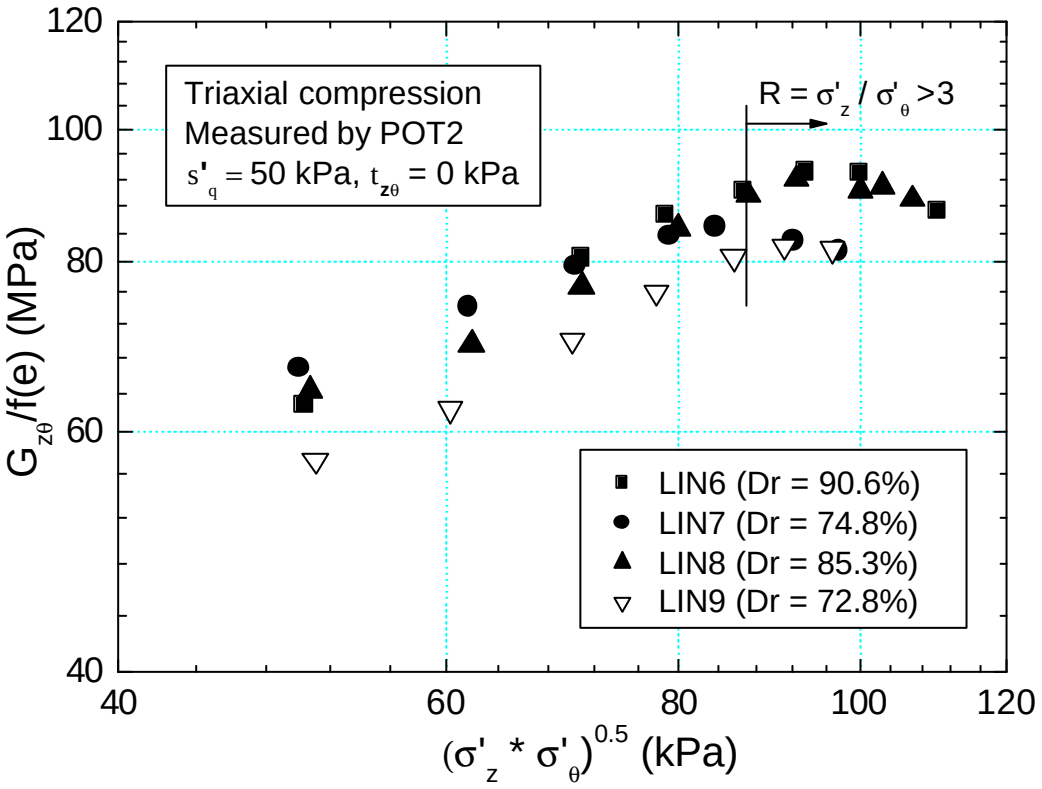

Fig. 4.43 $G_{z\theta}/f(e)$ vs $(\sigma'_z * \sigma'_\theta)^{0.5}$ during TC measured by POT2

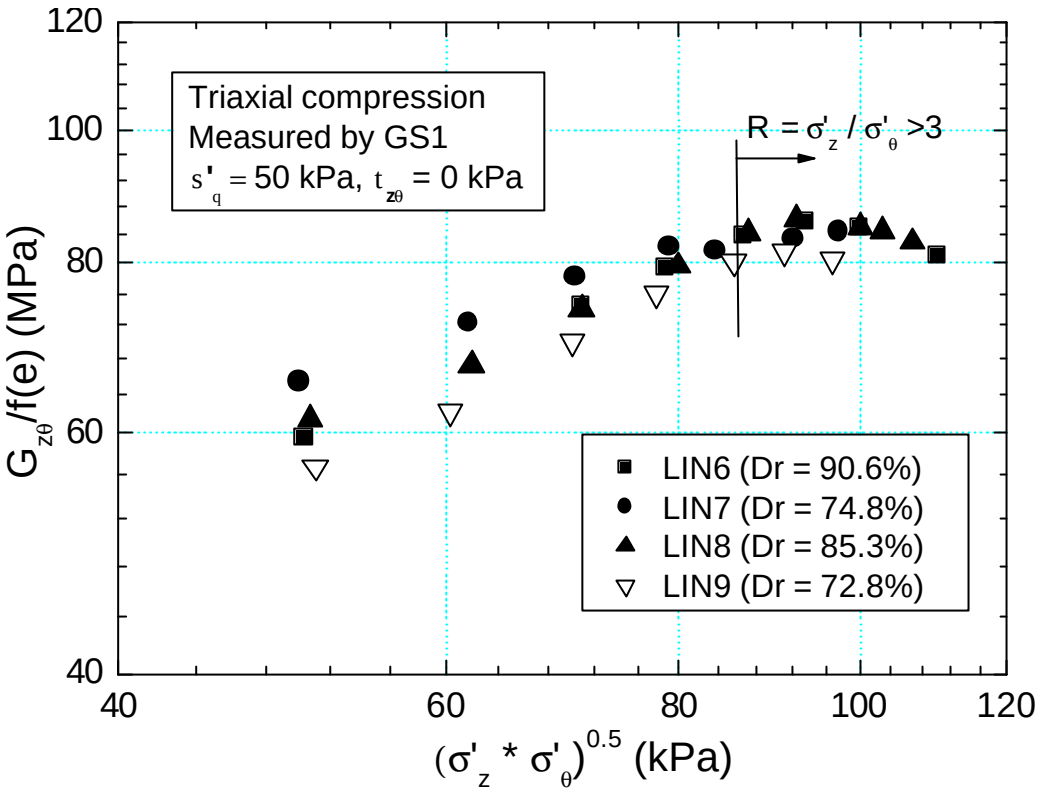

Fig. 4.44 $G_{z\theta}/f(e)$ vs $(\sigma'_z * \sigma'_\theta)^{0.5}$ during TC measured by GS1

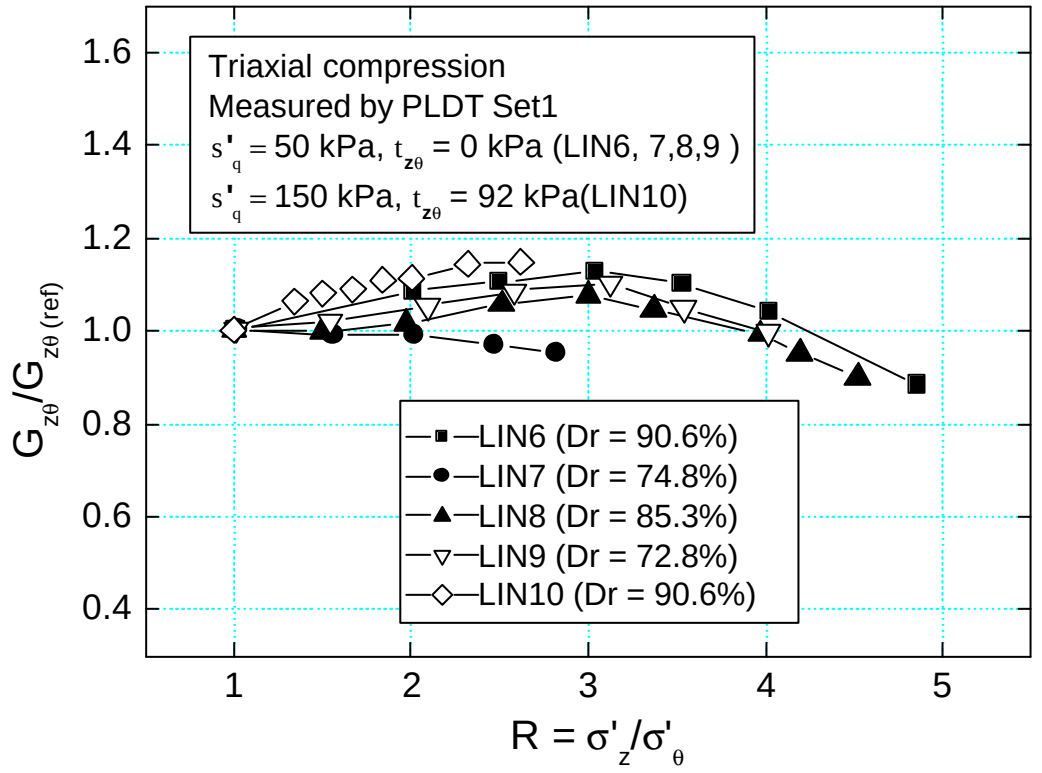

Fig. 4.45 $G_{z\theta}/ G_{z\theta(ref)}$ vs R during TC measured by PLDT Set1

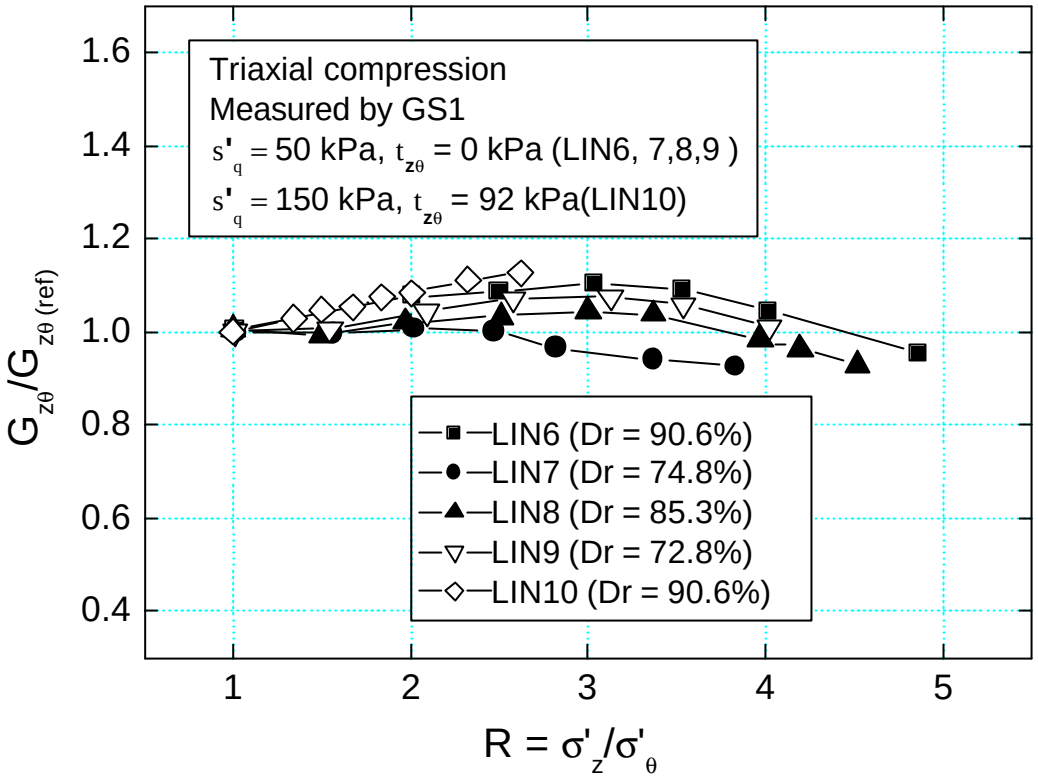

Fig. 4.46 $G_{z\theta}/ G_{z\theta(ref)}$ vs R during TC measured by GS1

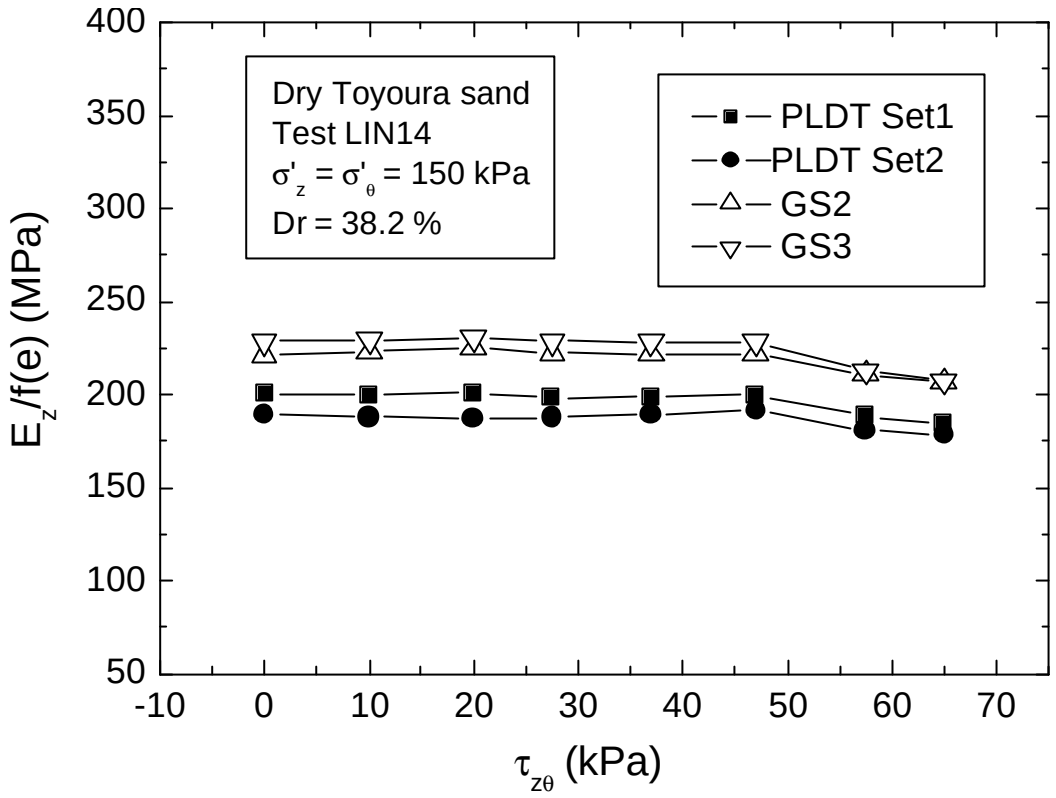

Fig. 4.47 $E_z/f(e)$ vs $\tau_{z\theta}$ measured by different transducers

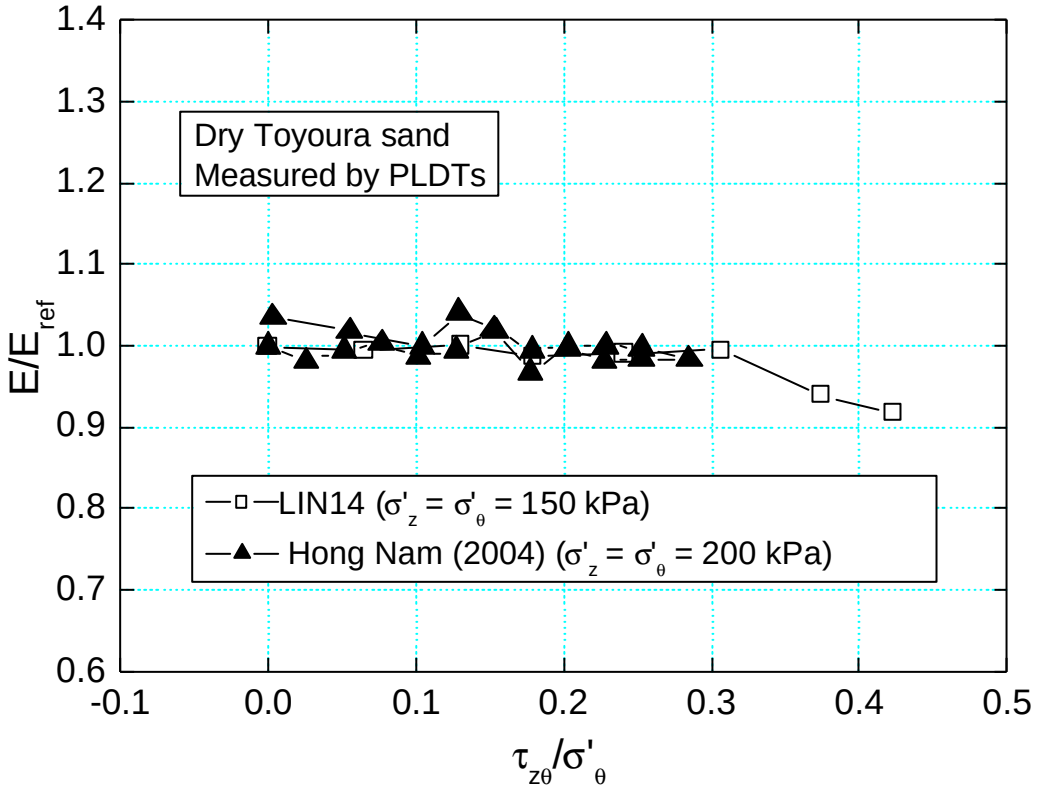

Fig. 4.48 $E_z/ E_{z(ref)}$ vs $\tau_{z\theta}/\sigma'_{\theta}$ during TSI

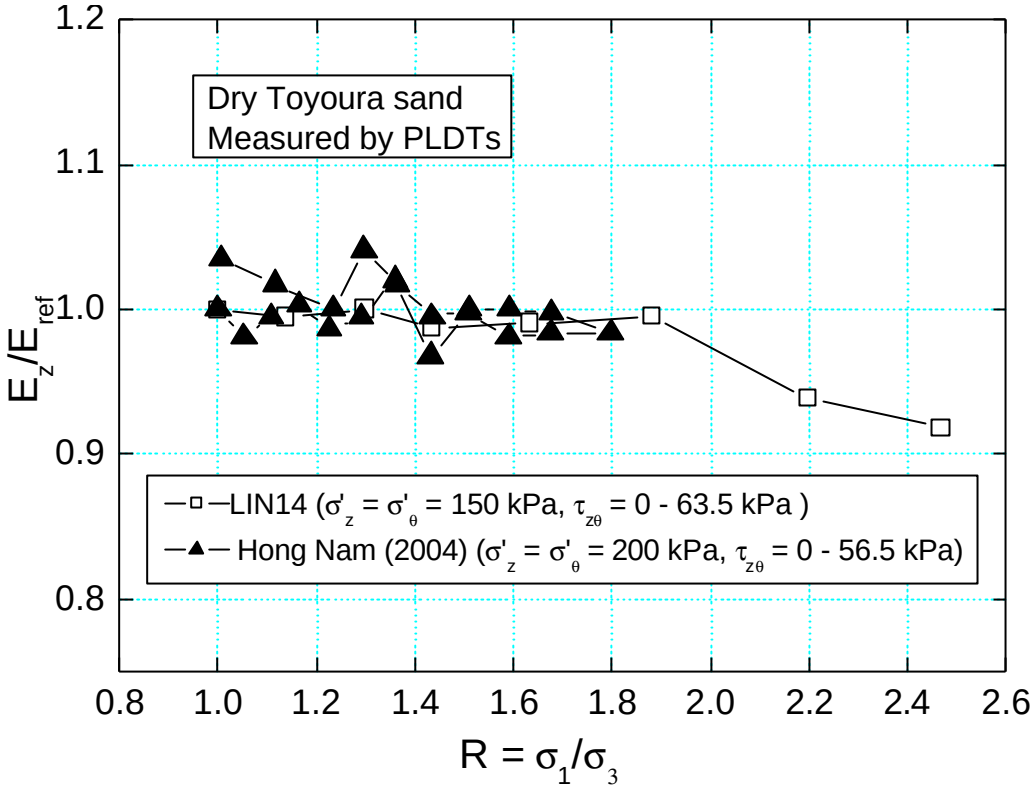

Fig. 4.49 $E_z/ E_{z(ref)}$ vs R during TSI

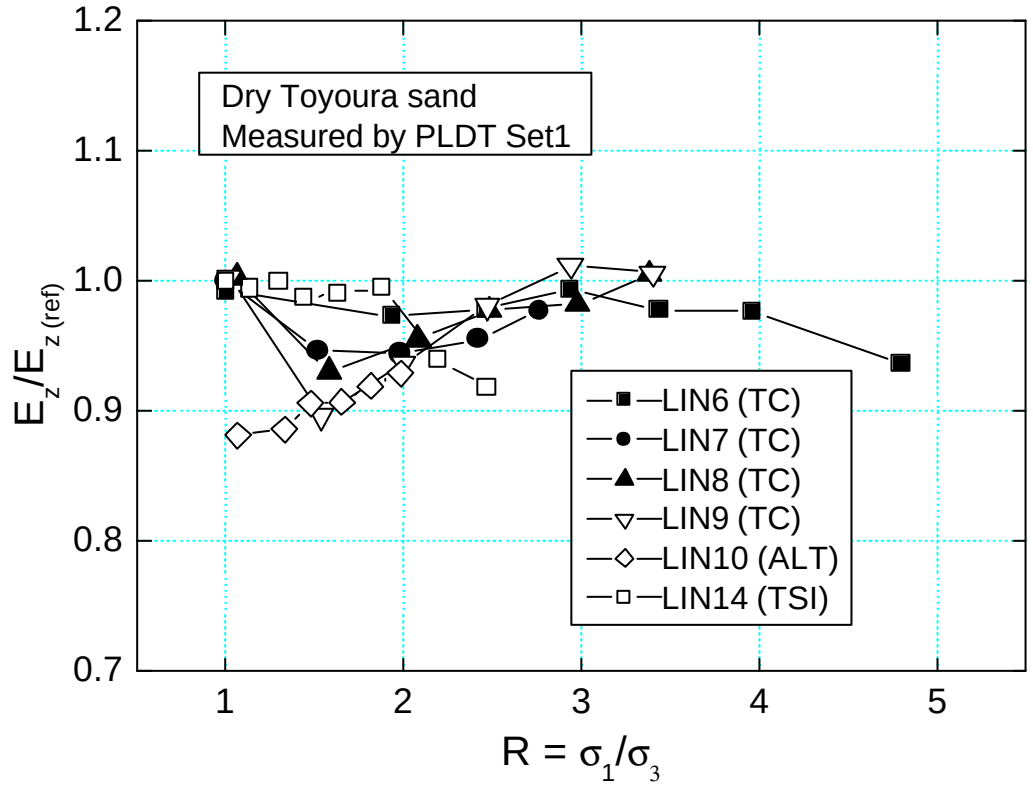

Fig. 4.49a Comparison of $E_z/ E_{z(ref)}$ vs R during TC, ALT and TSI

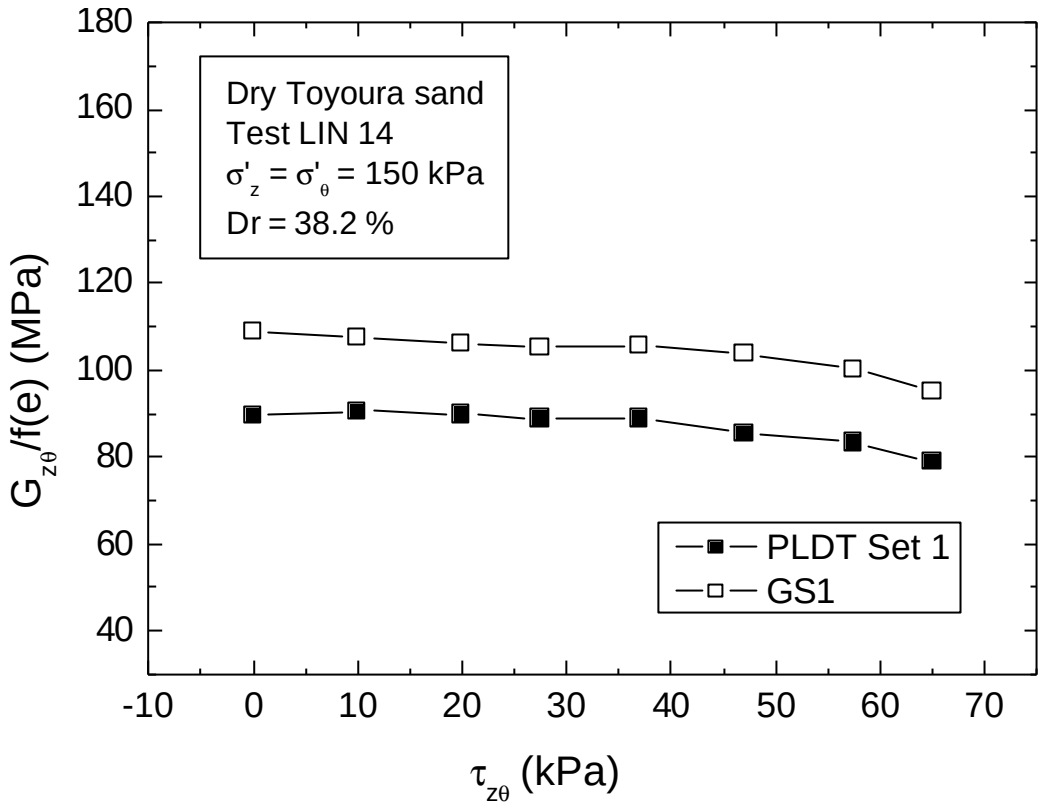

Fig. 4.50 $G_{z\theta}/f(e)$ vs $\tau_{z\theta}$ measured by different transducers

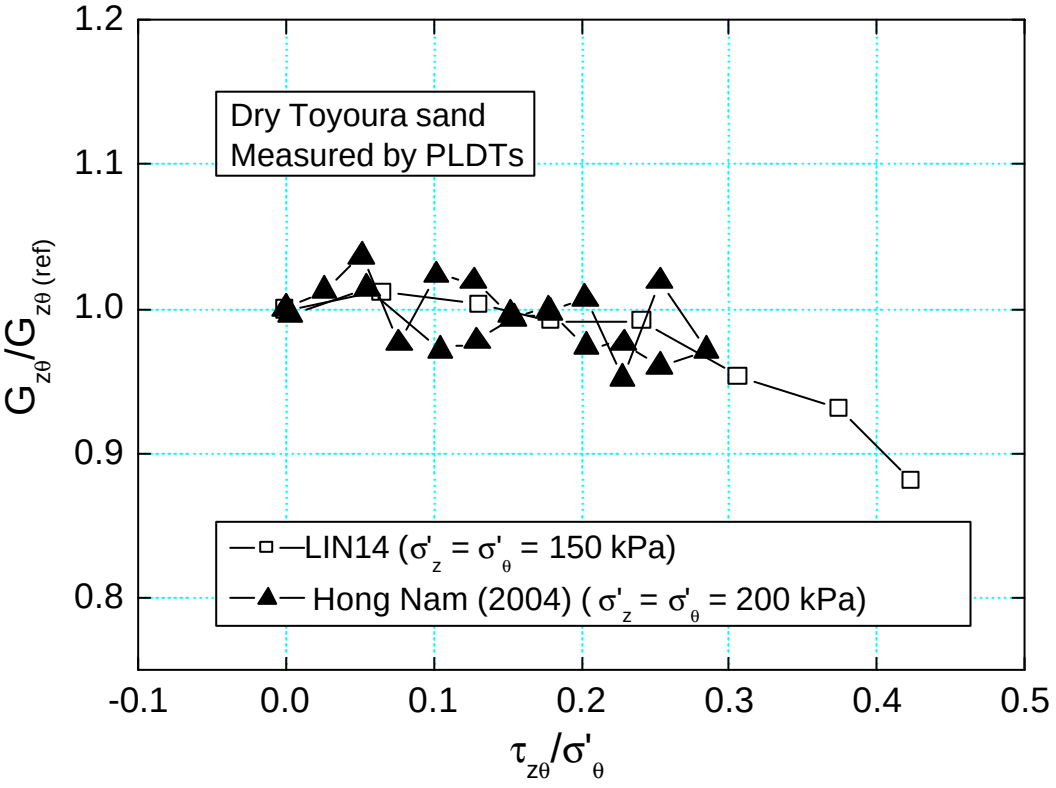

Fig. 4.51 $G_{z\theta}/ G_{z\theta(ref)}$ vs $\tau_{z\theta}/\sigma'_{\theta}$ during TSI

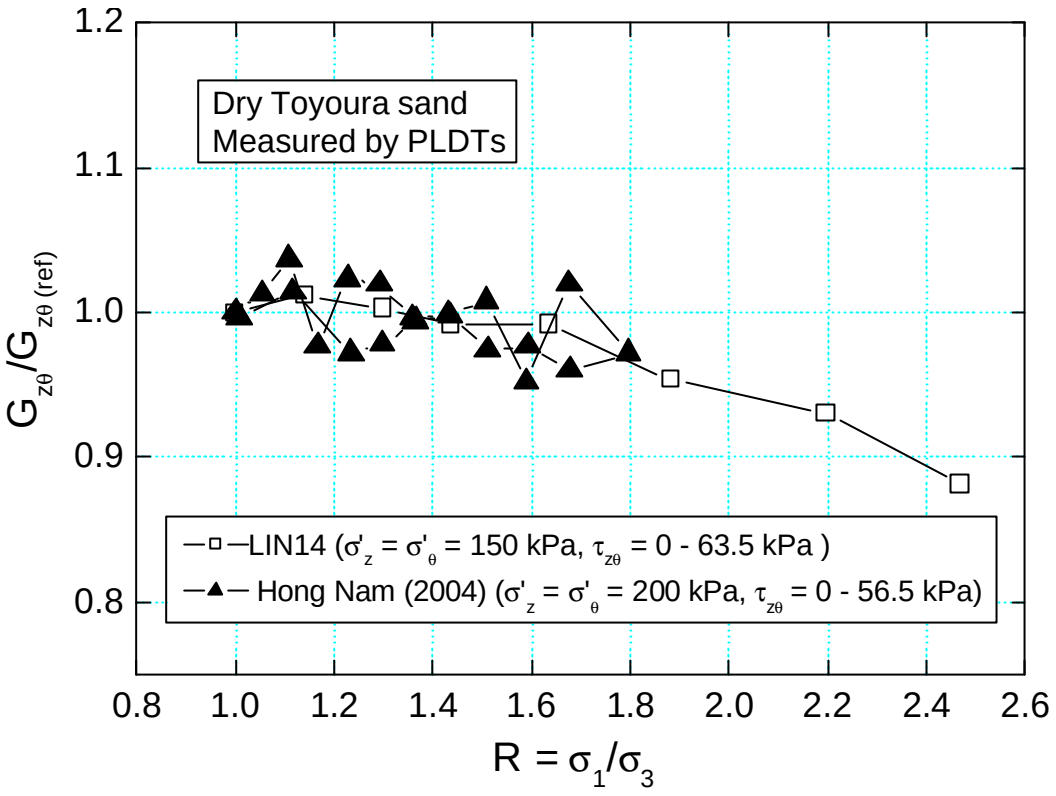

Fig. 4.52 $G_{z\theta}/ G_{z\theta(ref)}$ vs R during TSI

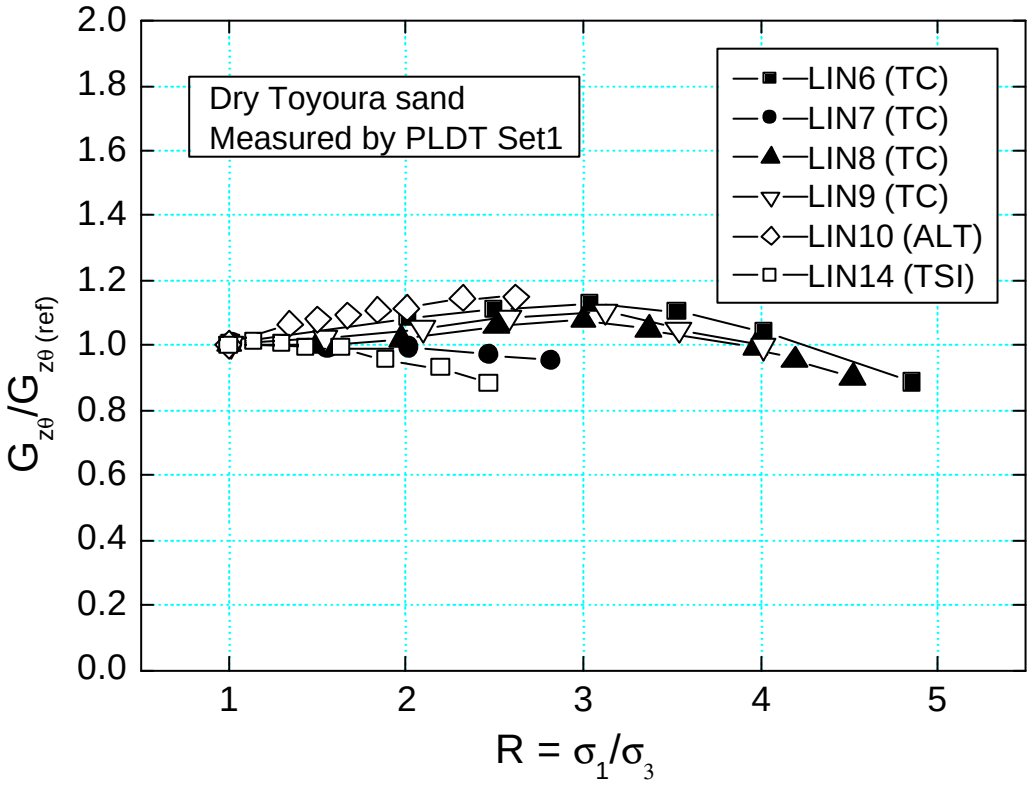

Fig. 4.52a Comparison of $G_{z\theta}/ G_{z\theta(ref)}$ vs R during TC, ALT and TSI

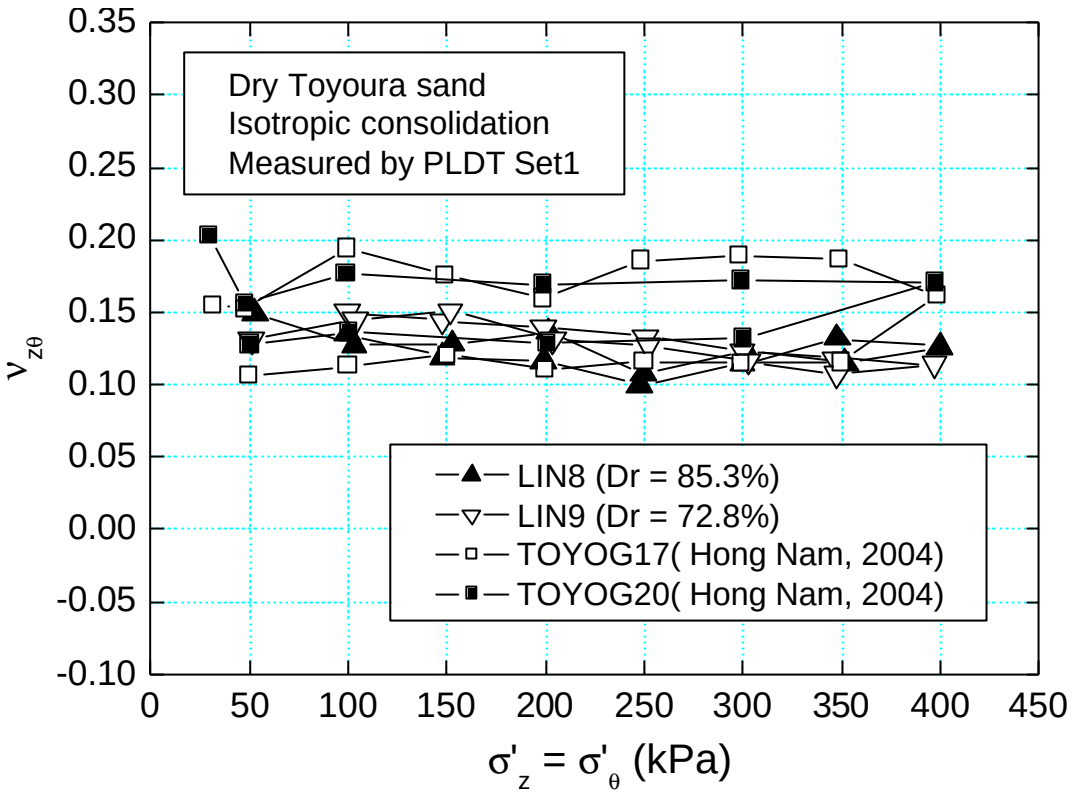

Fig. 4.53 $\nu_{z\theta}$ during IC measured by PLDT Set1

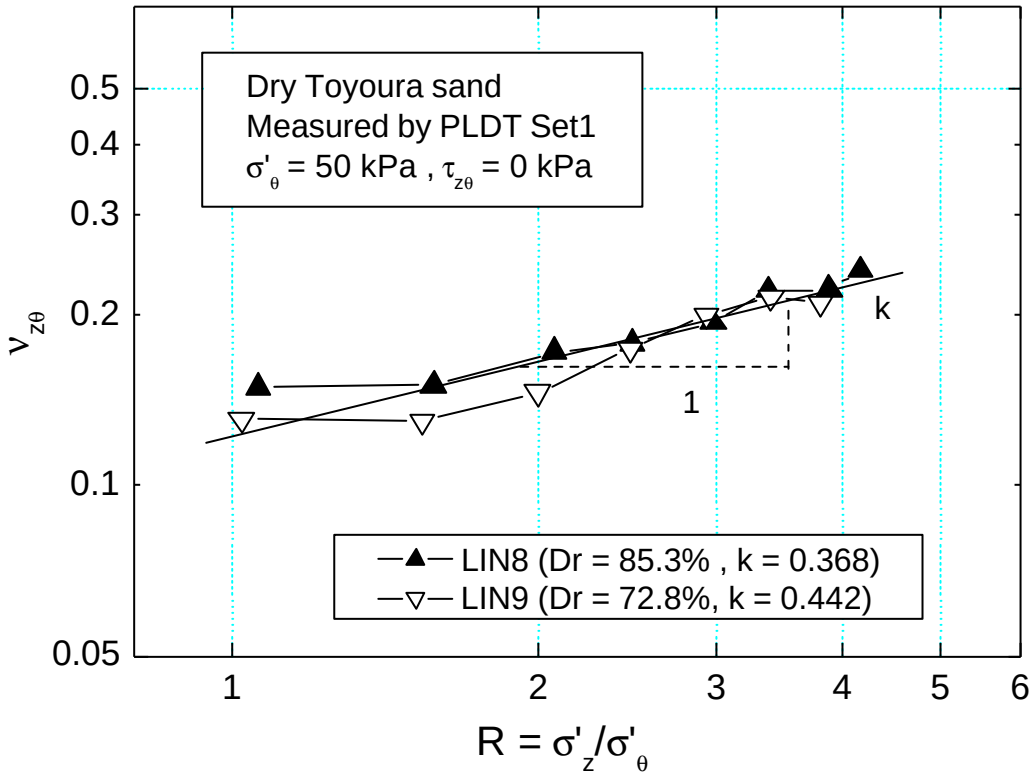

Fig. 4.54 $\nu_{z\theta}$ during TC measured by PLDT Set1

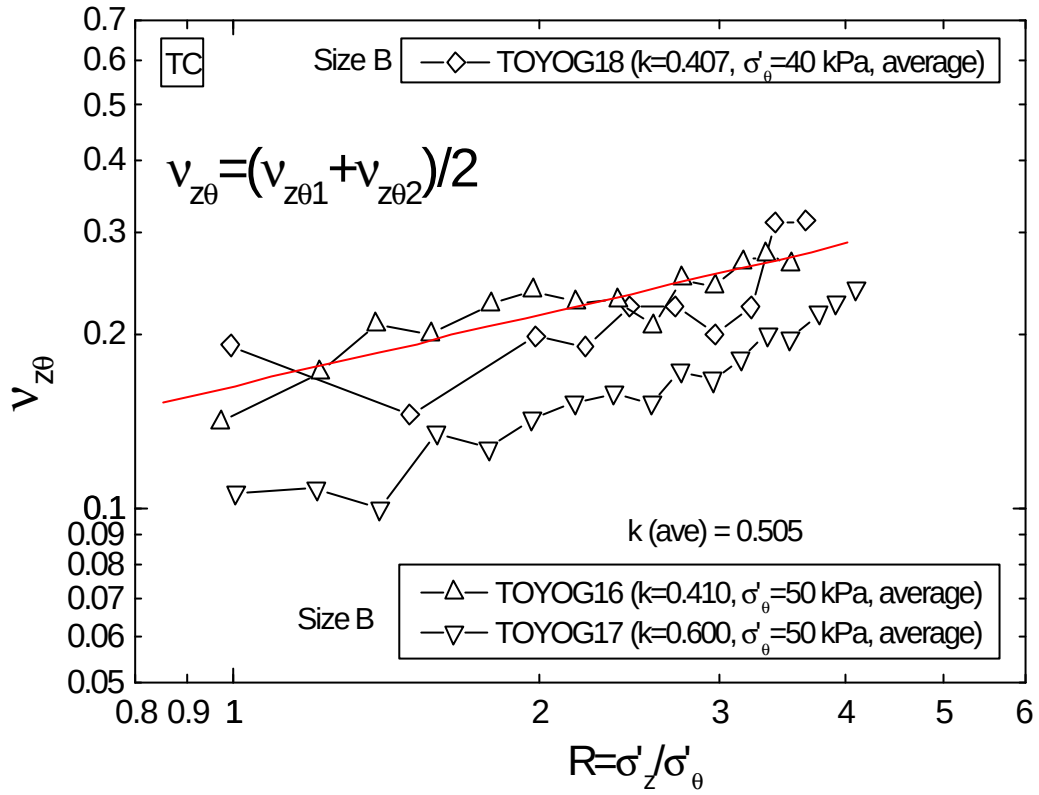

Fig. 4.54a $\nu_{z\theta}$ during TC (Hong Nam, 2004)

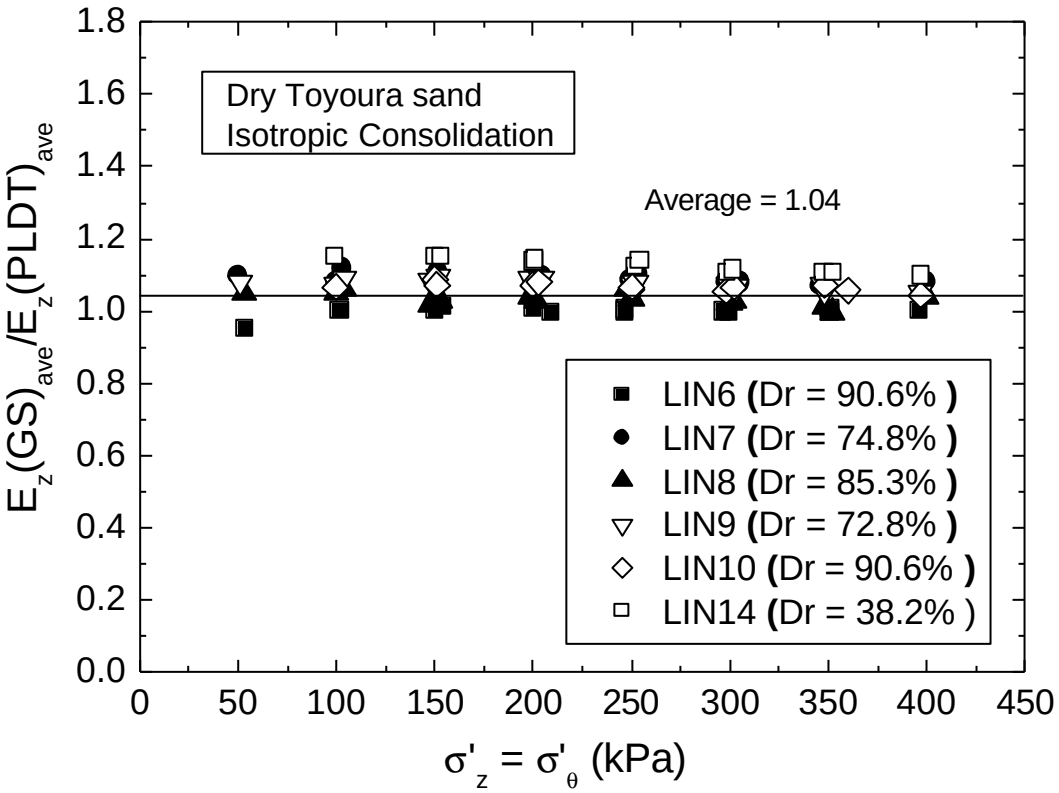

Fig. 4.55 E_z (GS_{ave})/ E_z ($PLDT_{ave}$) during IC

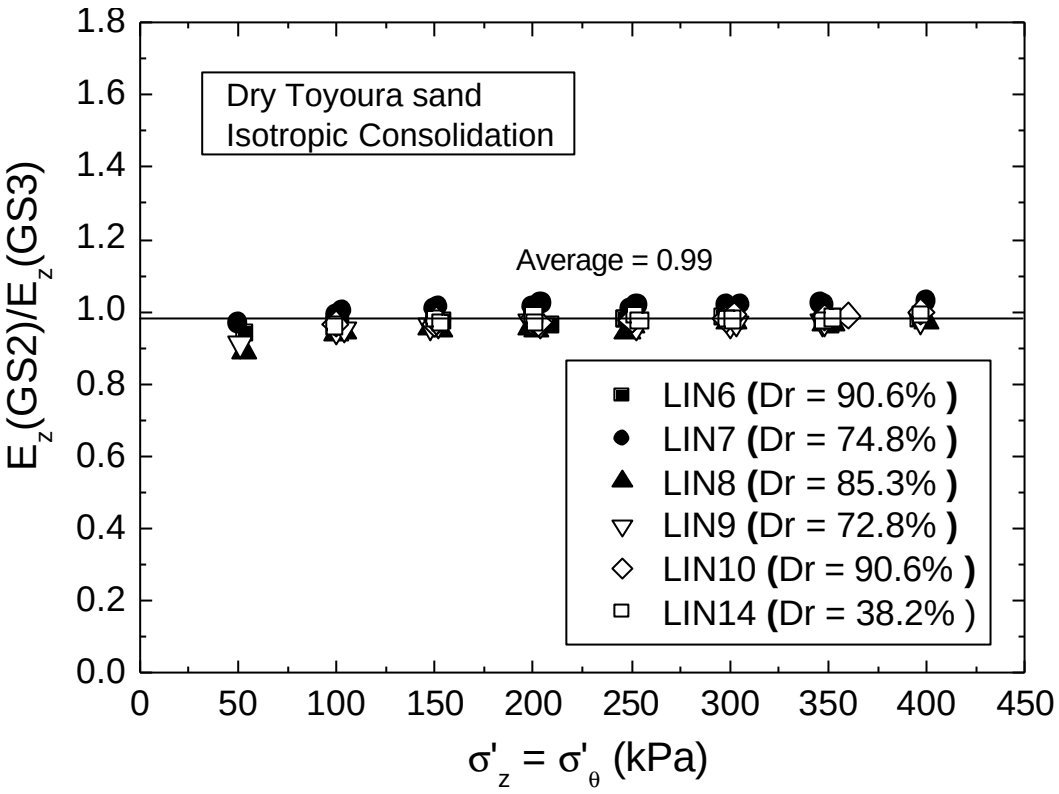

Fig. 4.56 E_z (GS2)/ E_z (GS3) during IC

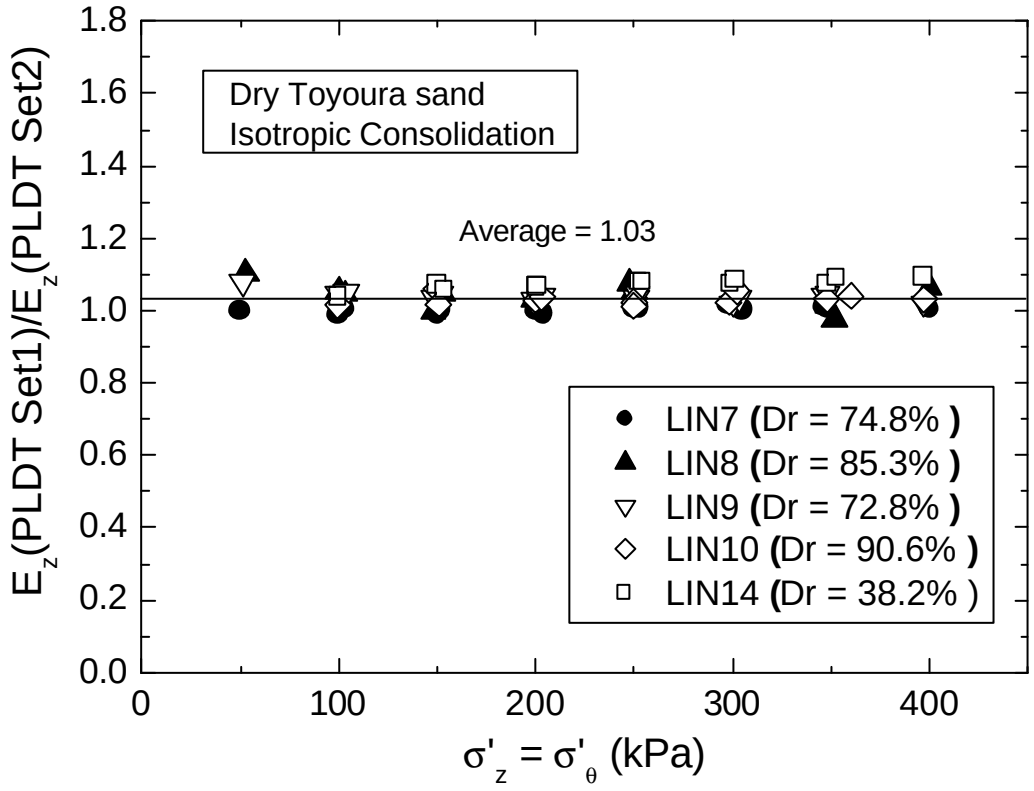

Fig. 4.57 E_z (PLDT Set1)/ E_z (PLDT Set2) during IC

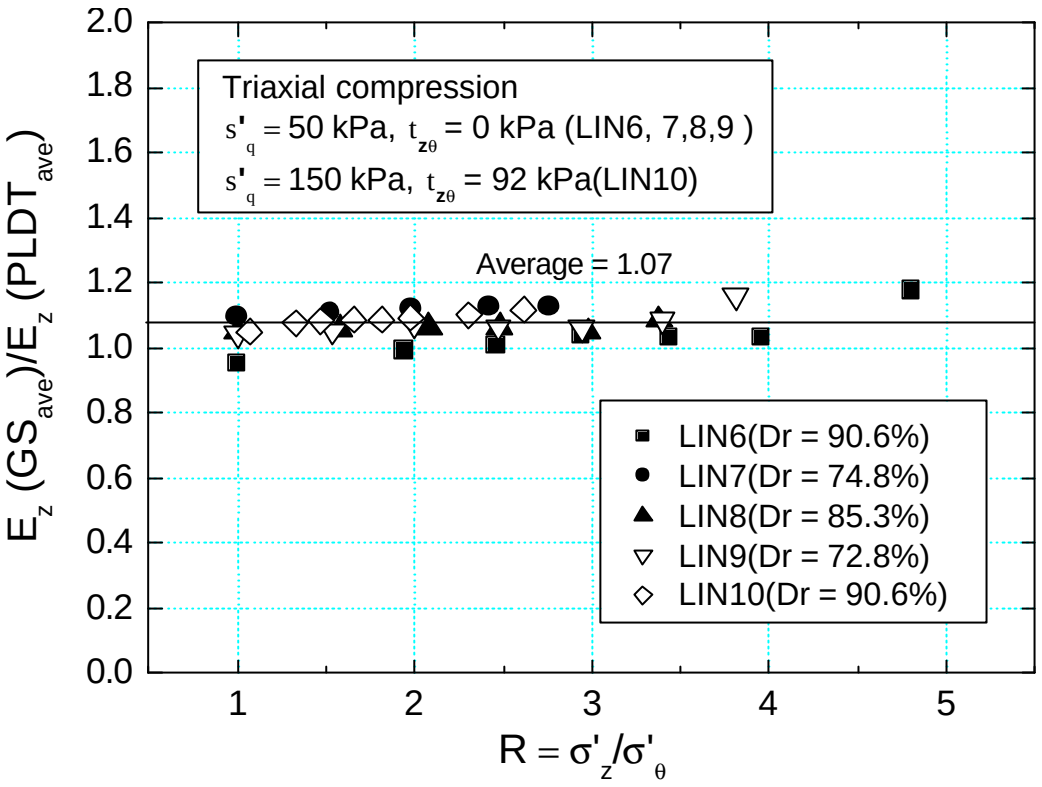

Fig. 4.58 E_z (GS_{ave})/ E_z ($PLDT_{ave}$) during TC

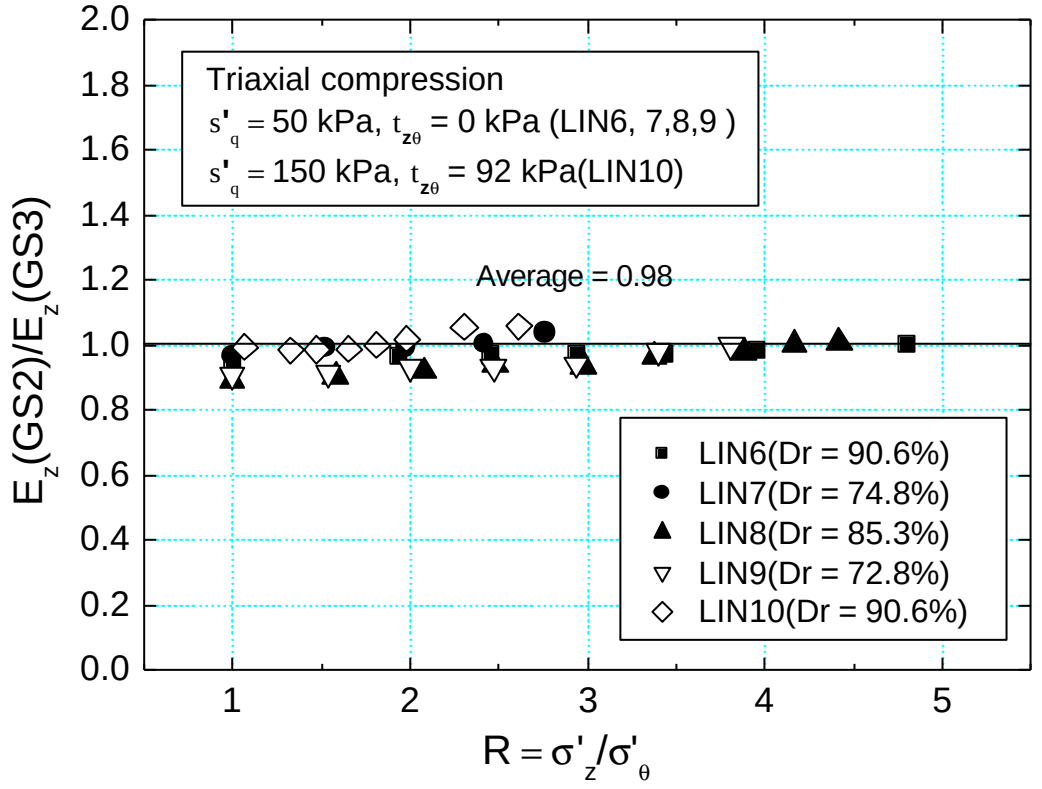

Fig. 4.59 E_z (GS2)/ E_z (GS3) during TC

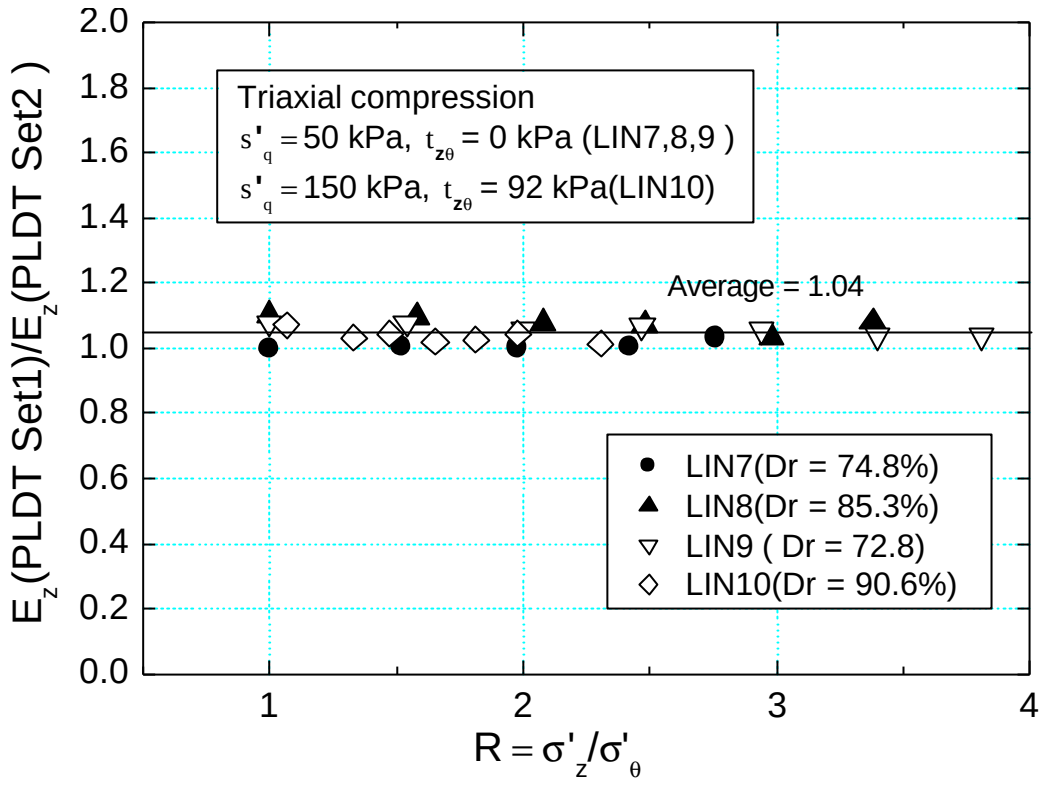

Fig. 4.60 E_z (PLDT Set1)/ E_z (PLDT Set2) during TC

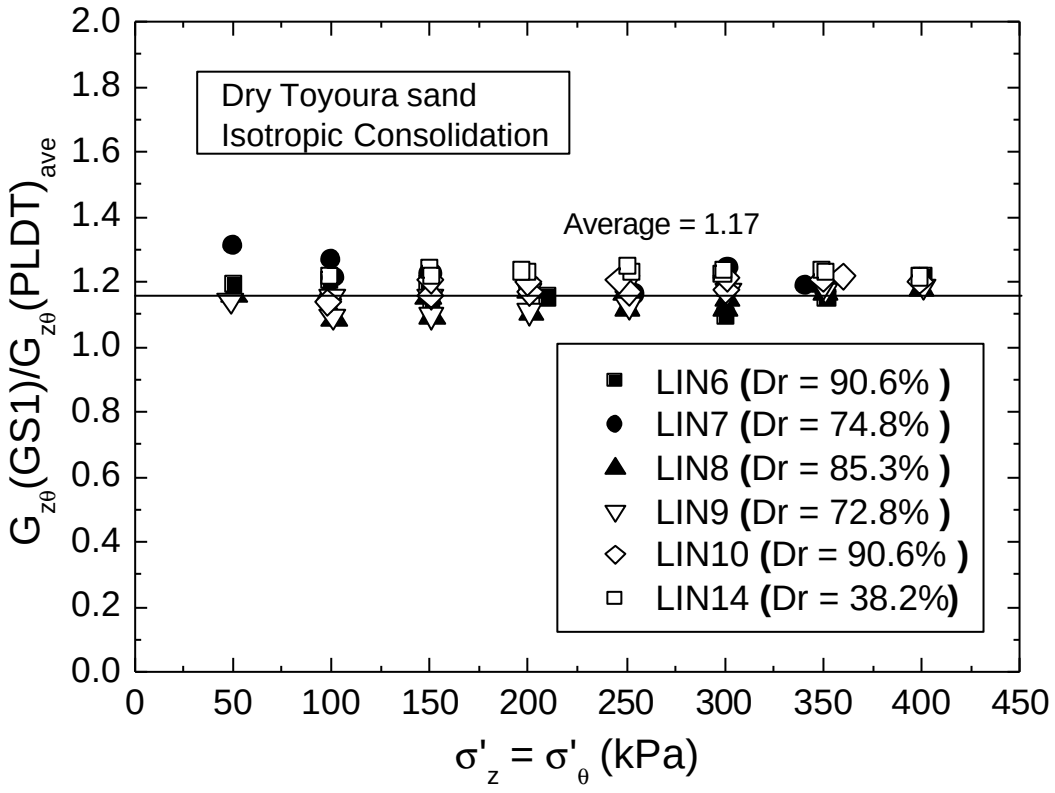

Fig. 4.61 $G_{z\theta}$ (GS1)/ $G_{z\theta}$ ($PLDT_{ave}$) during IC

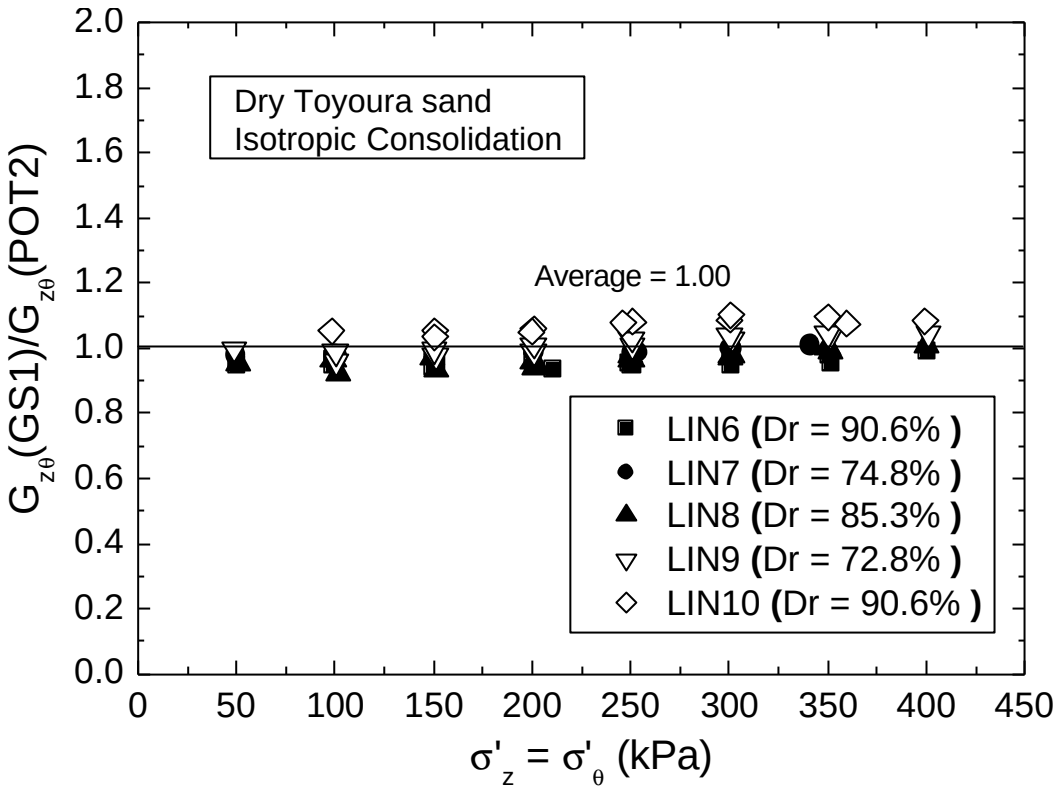

Fig. 4.62 $G_{z\theta}$ (GS1)/ $G_{z\theta}$ (POT2) during IC

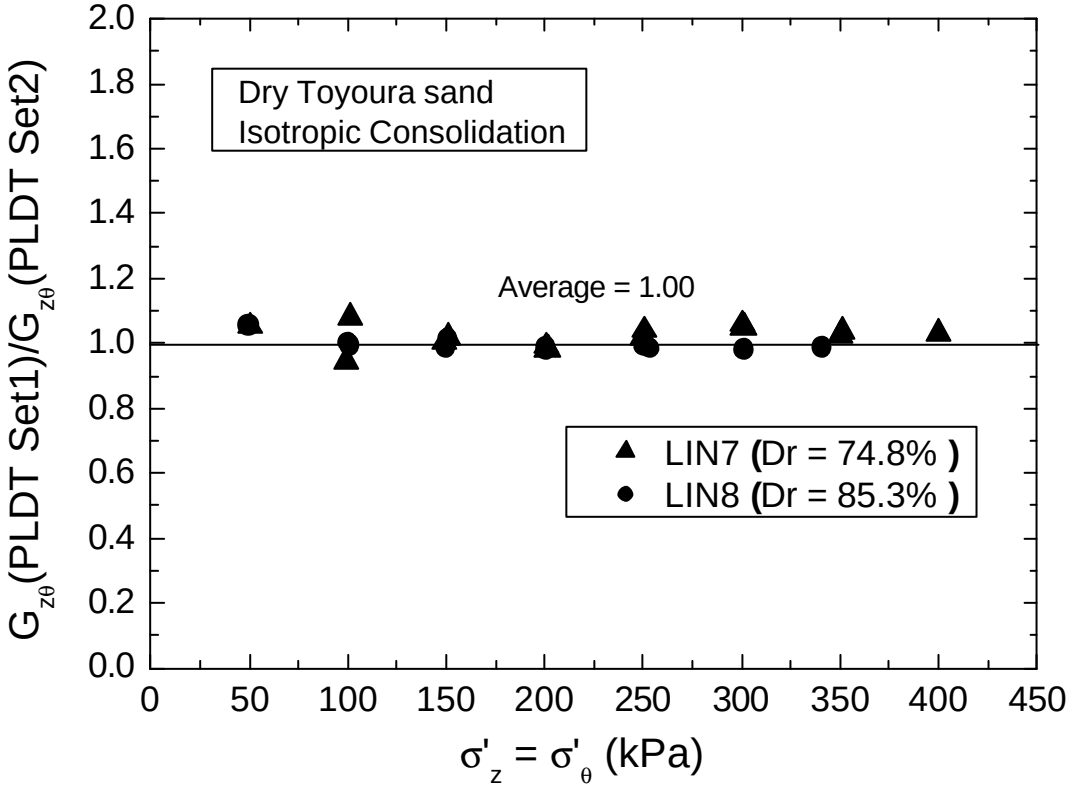

Fig. 4.63 $G_{z\theta}$ (PLDT Set1)/ $G_{z\theta}$ (PLDT Set2) during IC

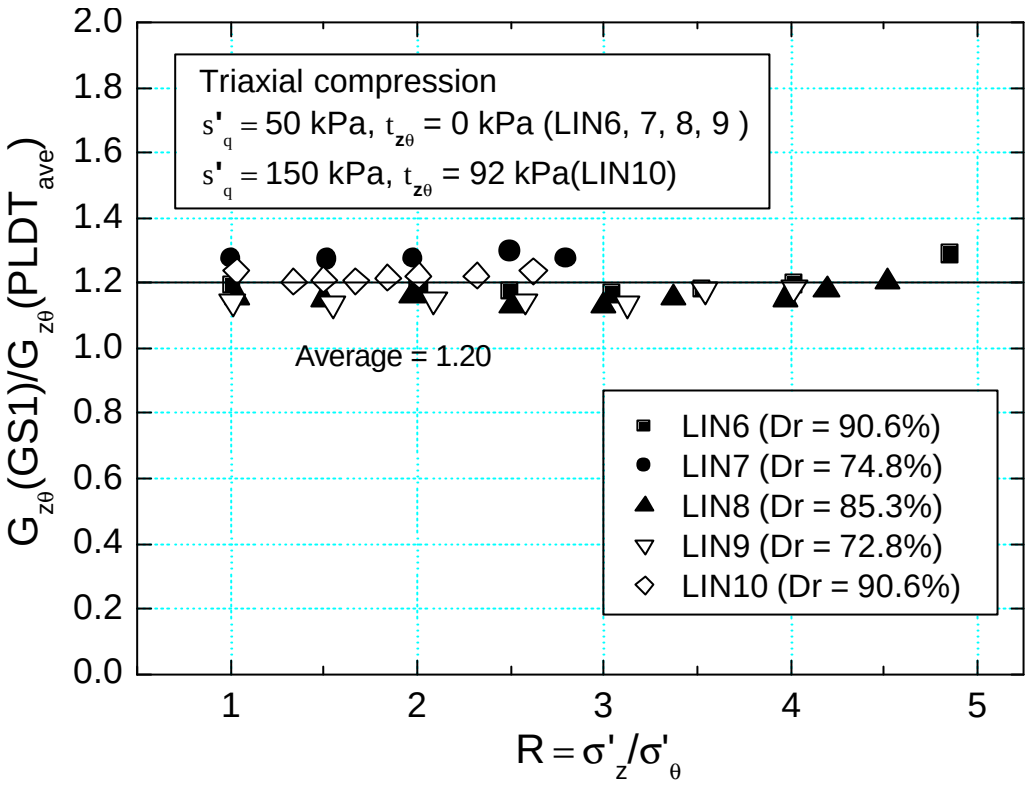

Fig. 4.64 $G_{z\theta}$ (GS1)/ $G_{z\theta}$ ($PLDT_{ave}$) during TC

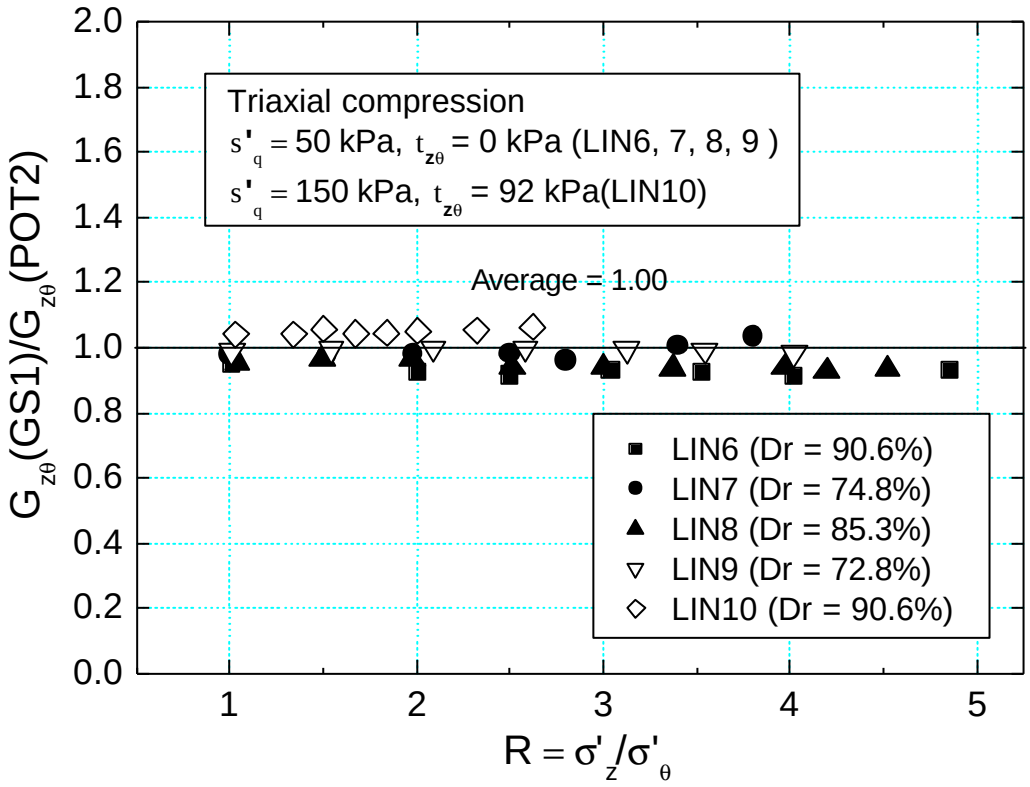

Fig. 4.65 $G_{z\theta}$ (GS1)/ $G_{z\theta}$ (POT2) during TC

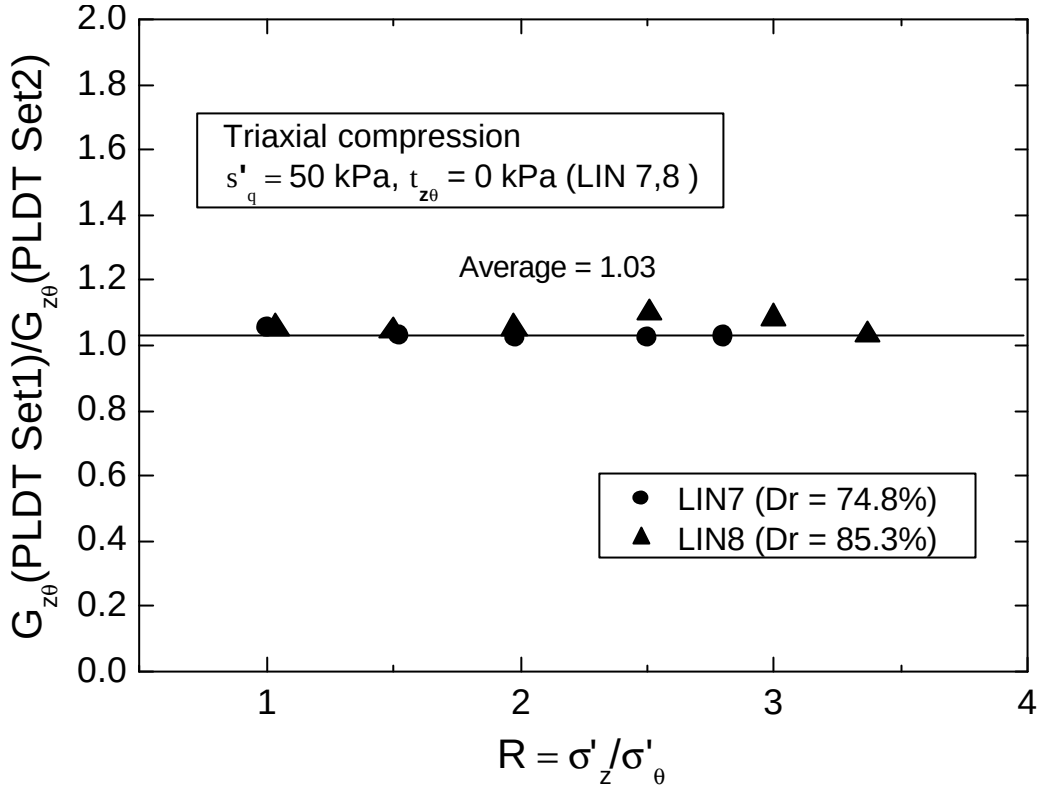

Fig. 4.66 $G_{z\theta}$ (PLDT Set1)/ $G_{z\theta}$ (PLDT Set2) during TC

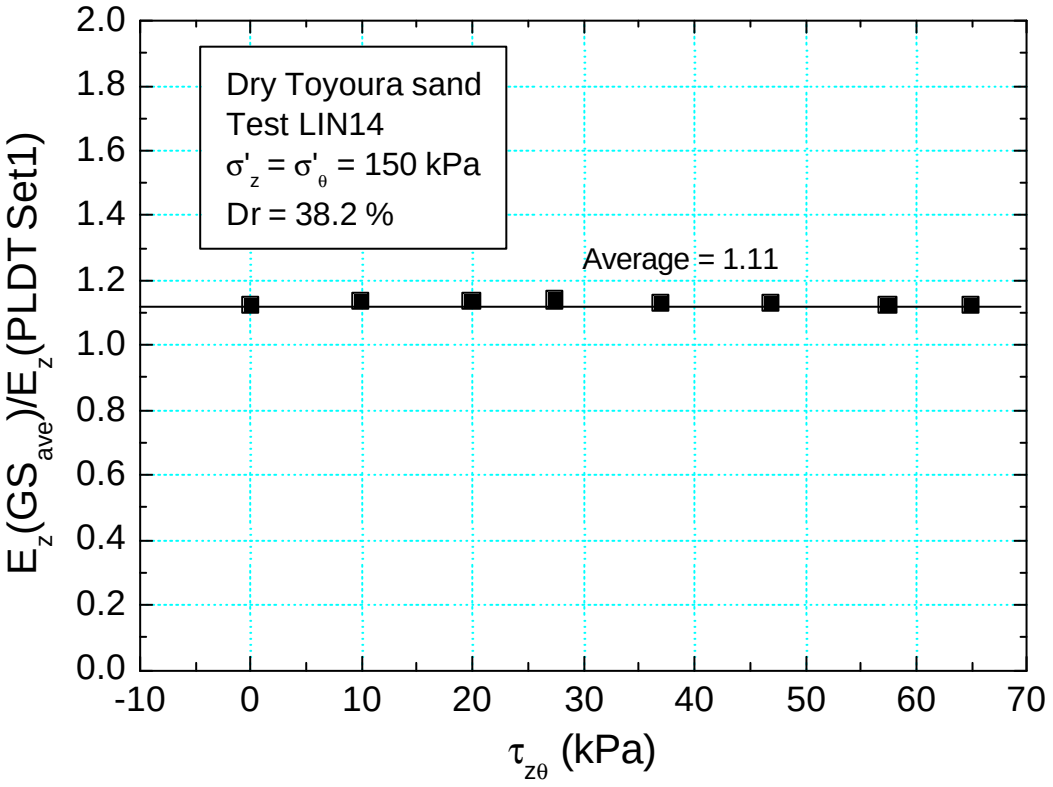

Fig. 4.67 E_z (GS_{ave})/ E_z (PLDT Set1) during TS

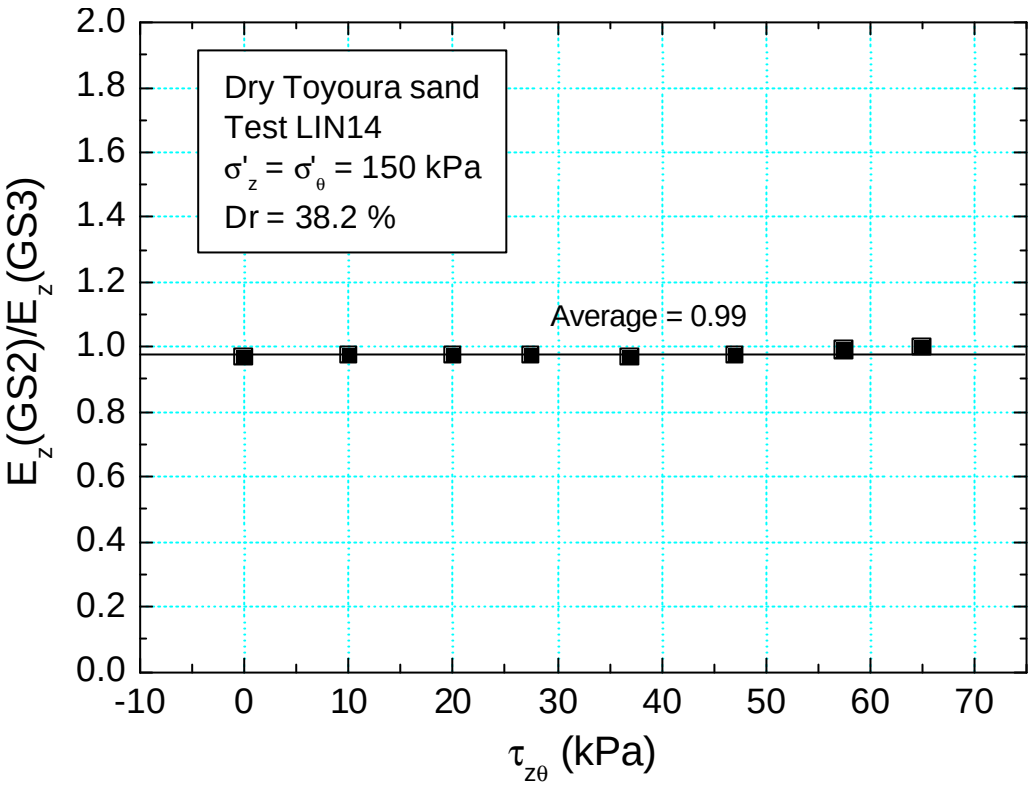

Fig. 4.68 E_z (GS2)/ E_z (GS3) during TSI

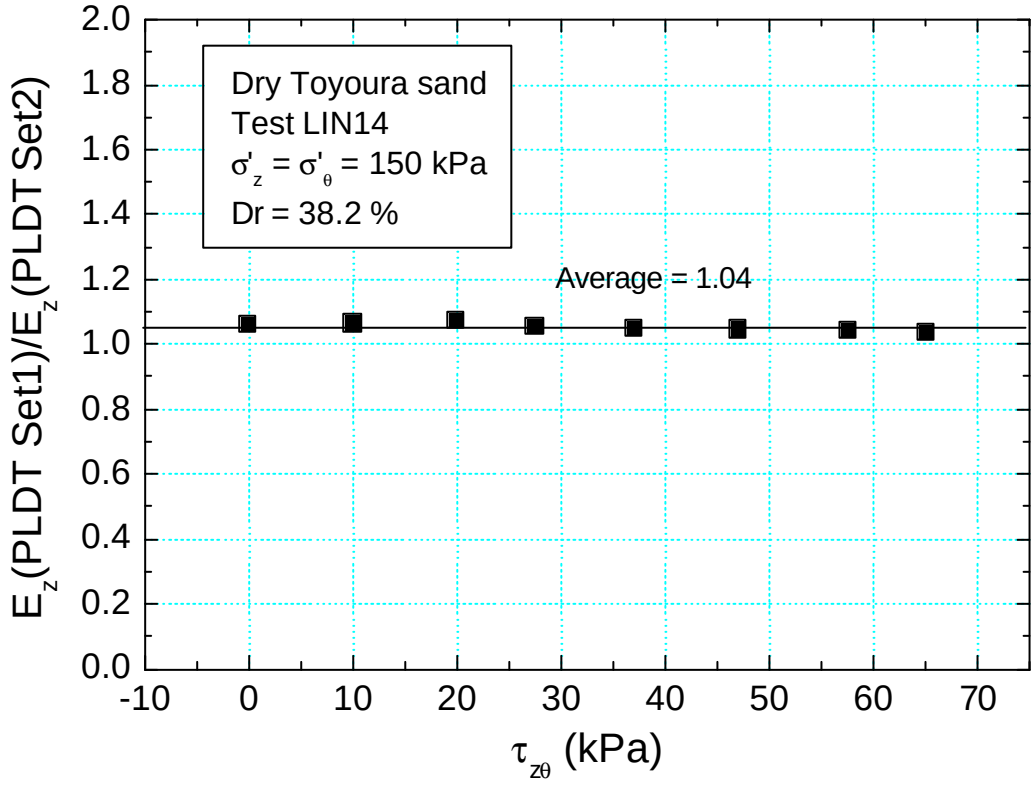

Fig. 4.69 E_z (PLDT Set1)/ E_z (PLDT Set2) during TSI

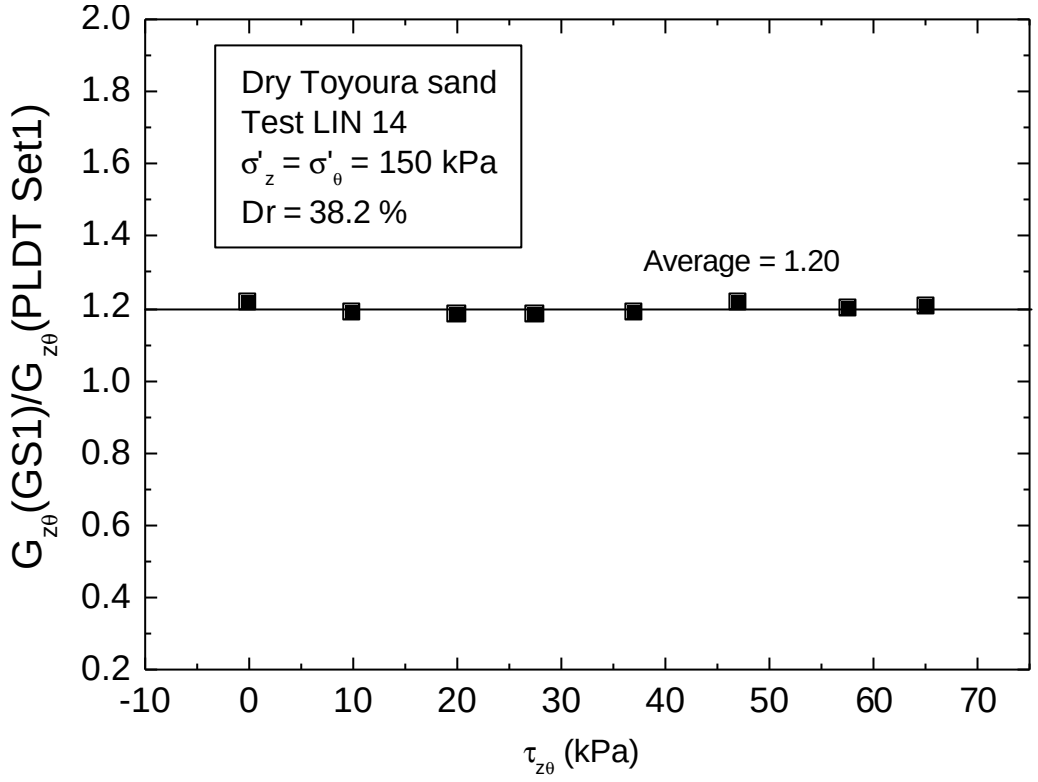

Fig. 4.70 $G_{z\theta}$ (GS1)/ $G_{z\theta}$ (PLDT Set1) during TSI

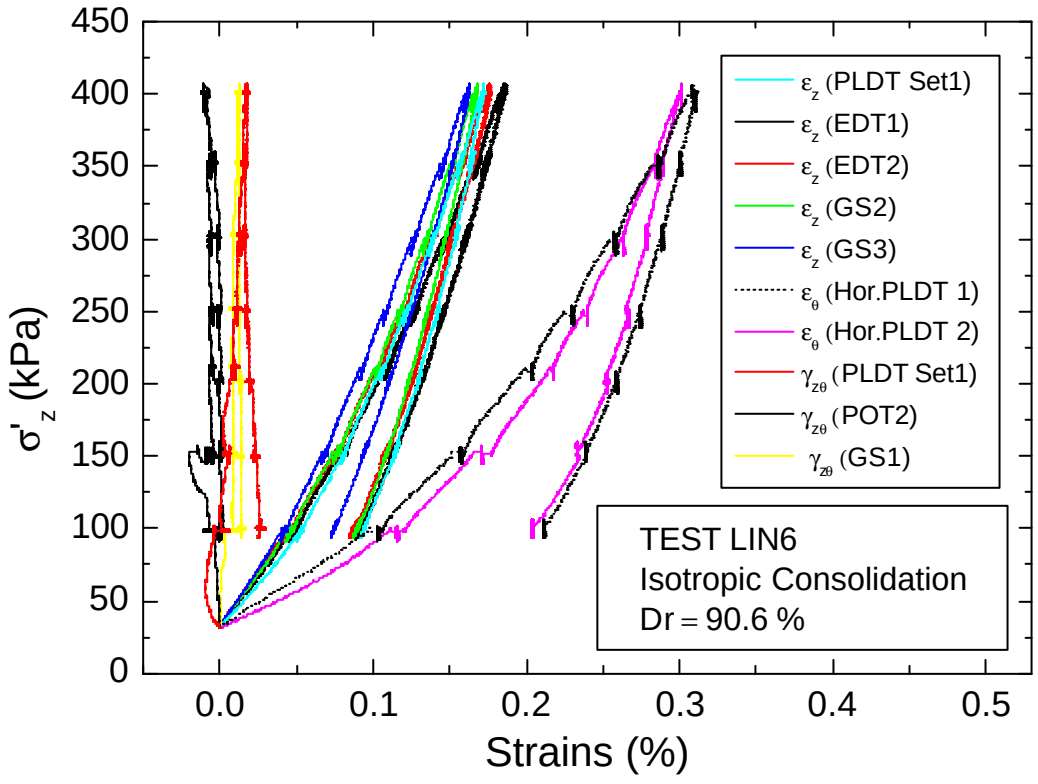

Fig. 4.71 Global strains of test LIN6 during IC

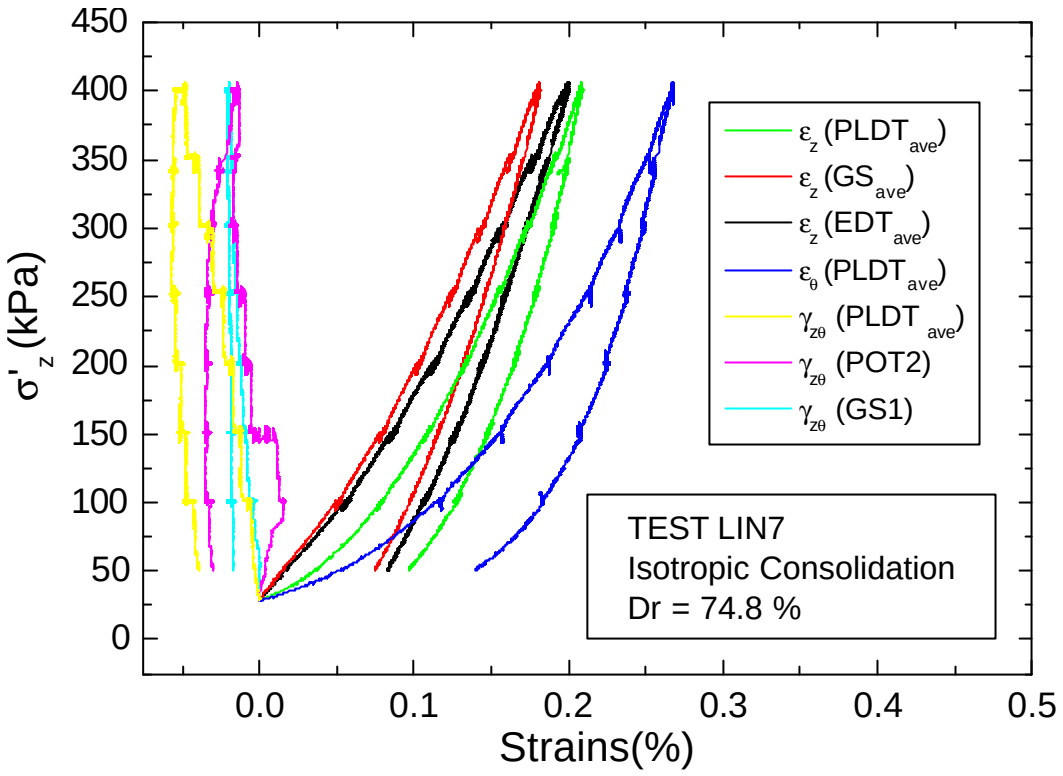

Fig. 4.72 Global strains of test LIN7 during IC

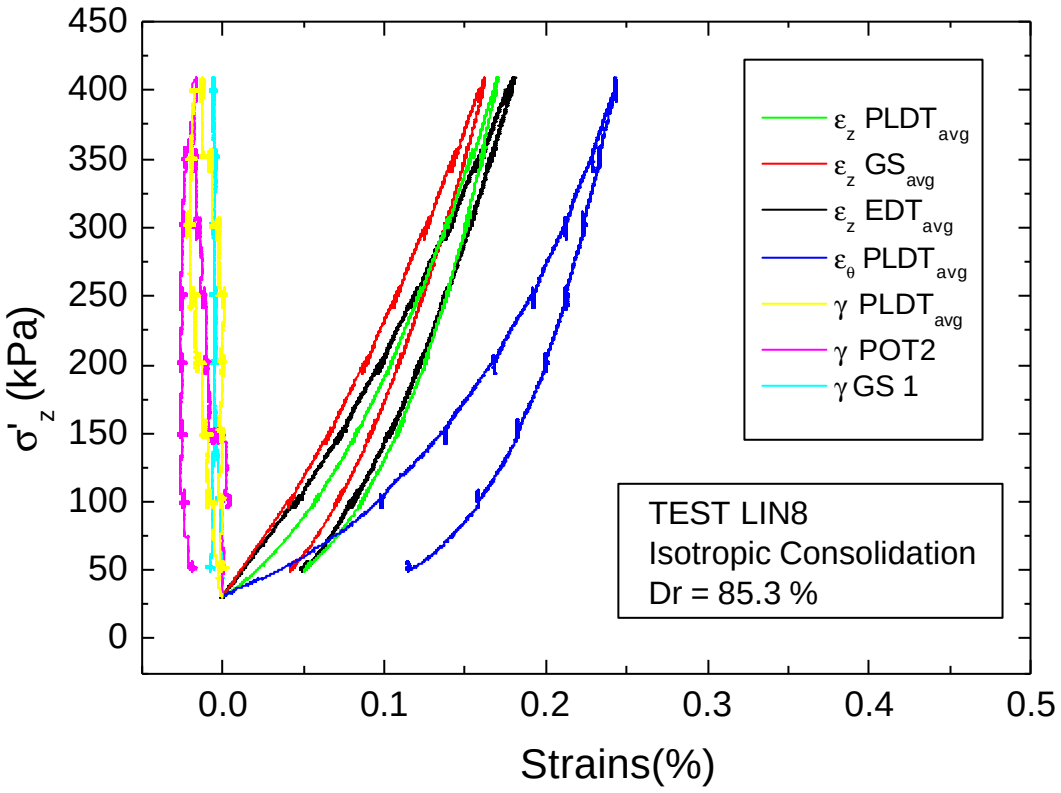

Fig. 4.73 Global strains of test LIN8 during IC

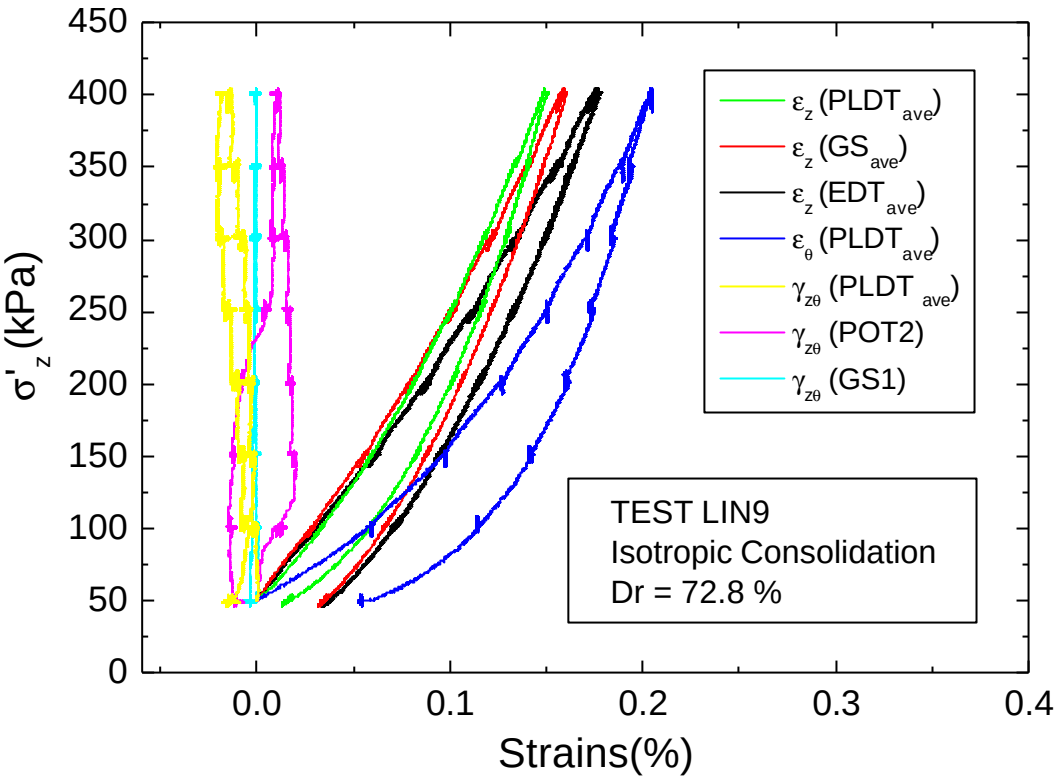

Fig. 4.74 Global strains of test LIN9 during IC

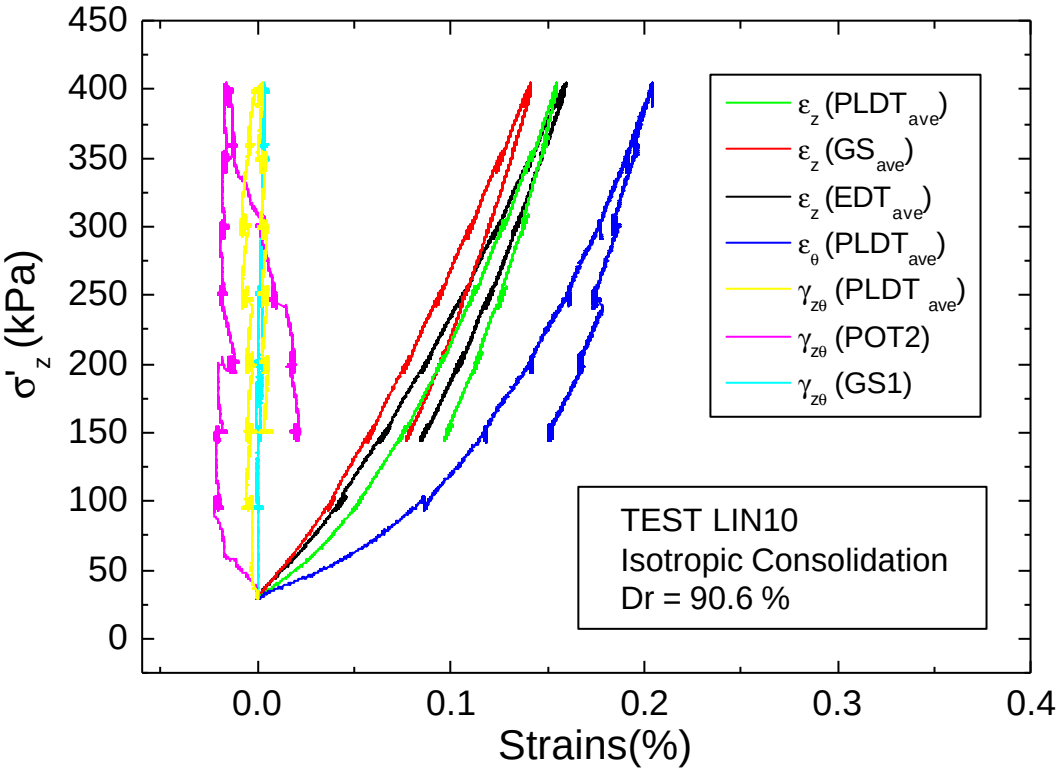

Fig. 4.75 Global strains of test LIN10 during IC

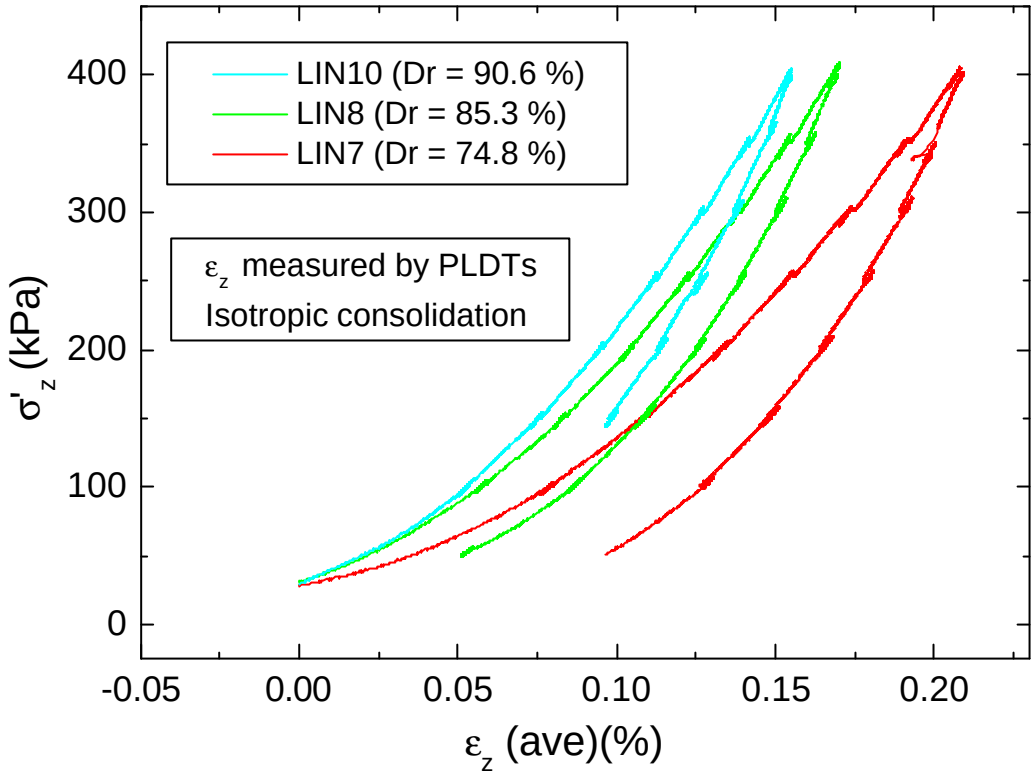

Fig. 4.76 Comparison of σ'_z vs ε_z during IC measured by PLDTs

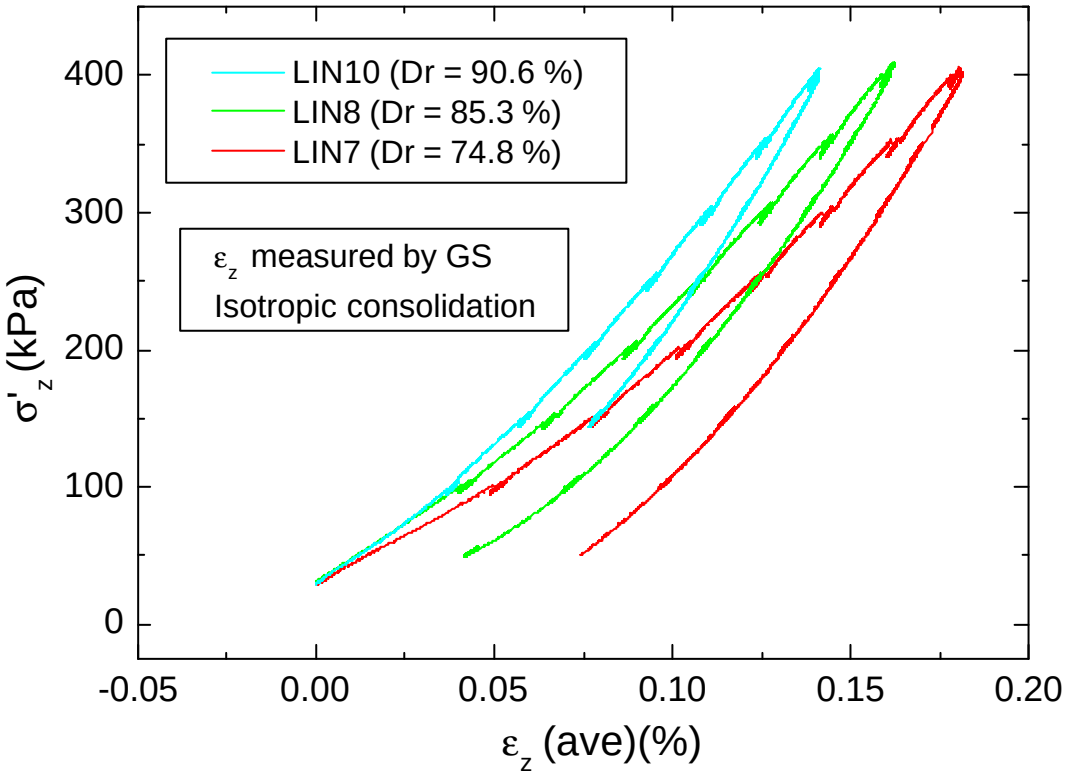

Fig. 4.77 Comparison of σ'_z vs ε_z during IC measured by GS

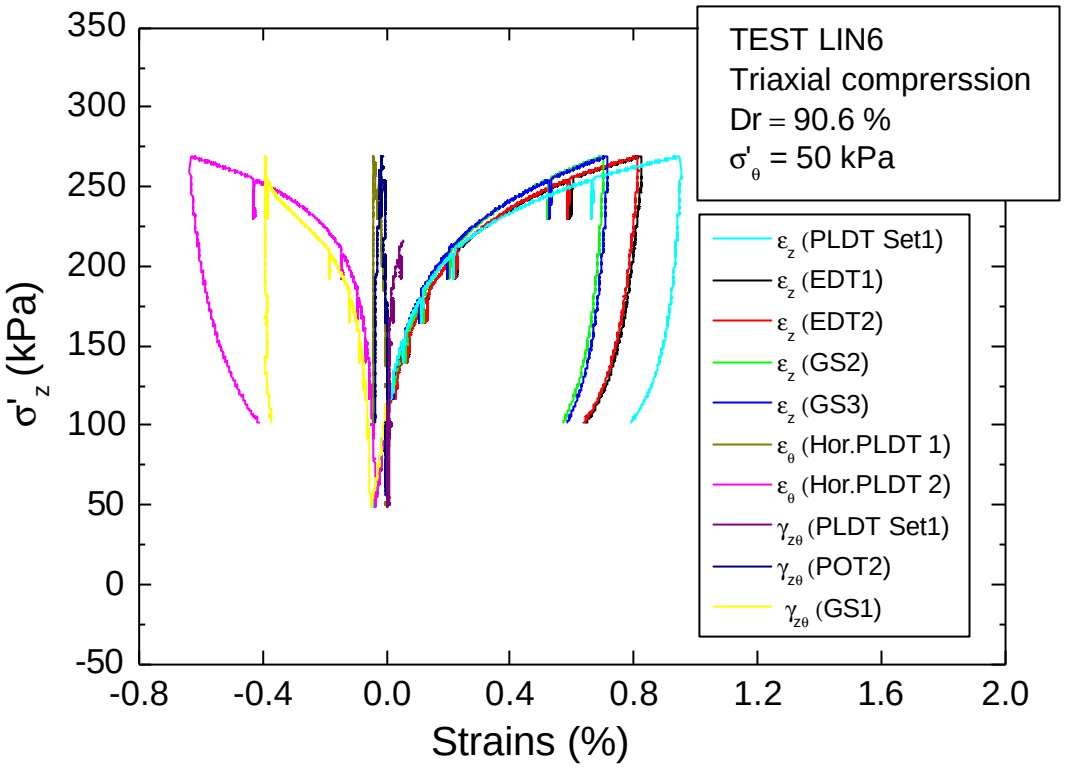

Fig. 4.78 Global strains of test LIN6 during TC

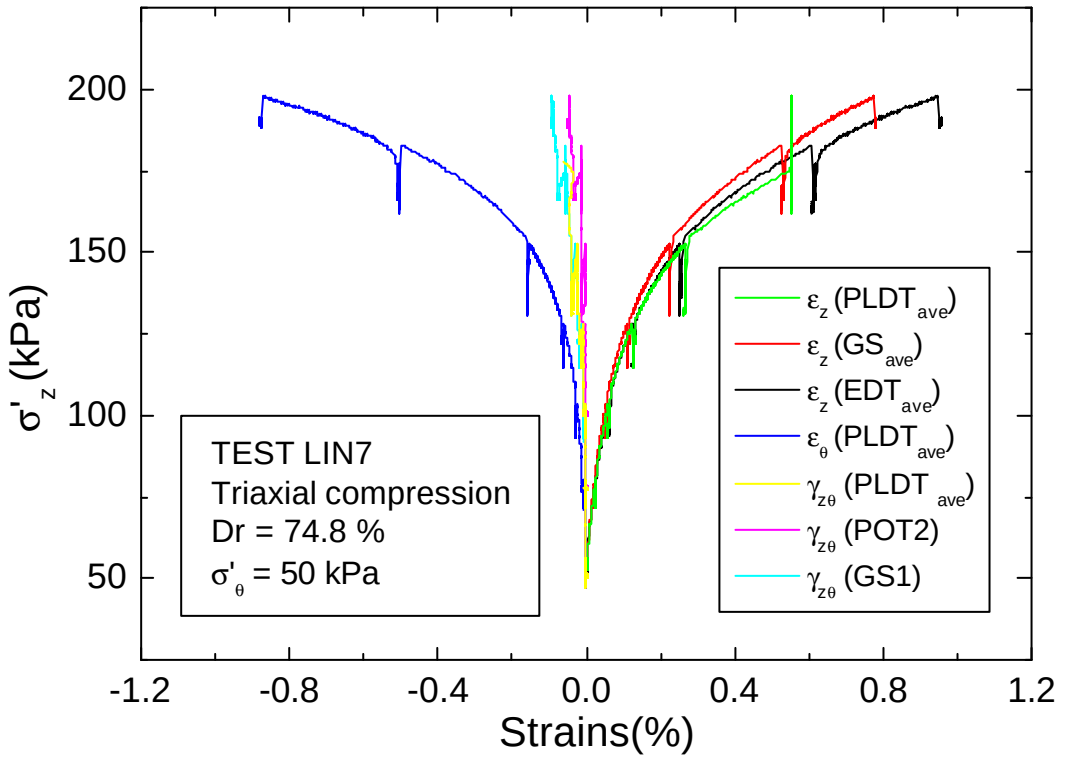

Fig. 4.79 Global strains of test LIN7 during TC

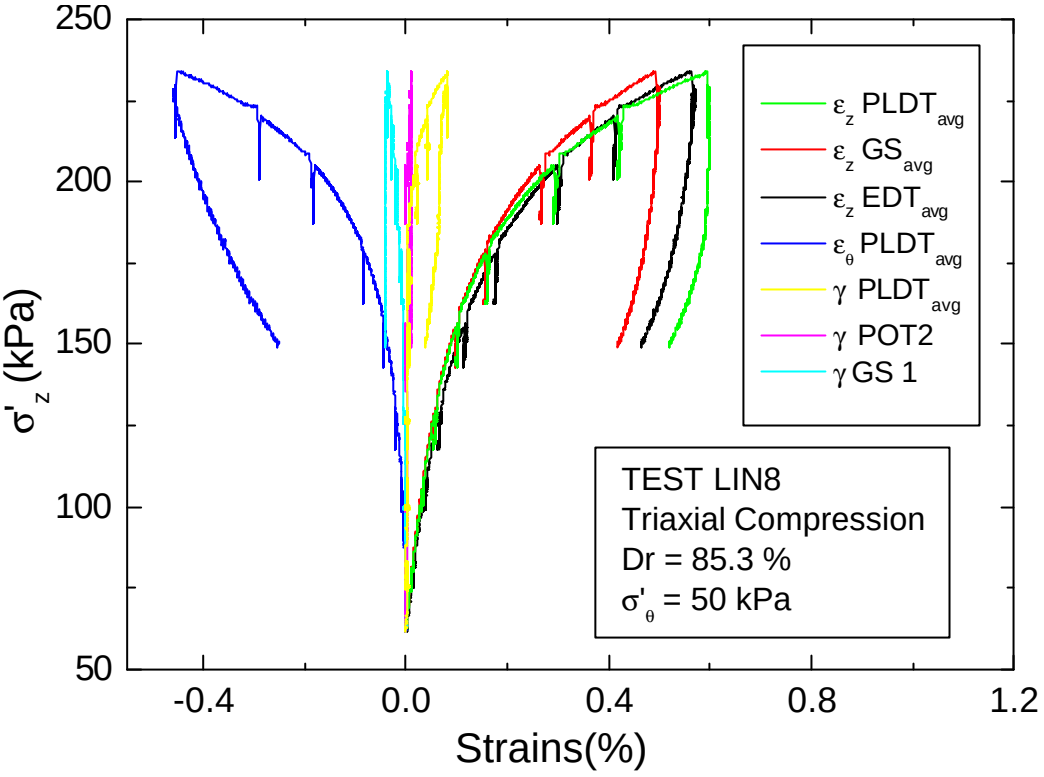

Fig. 4.80 Global strains of test LIN8 during TC

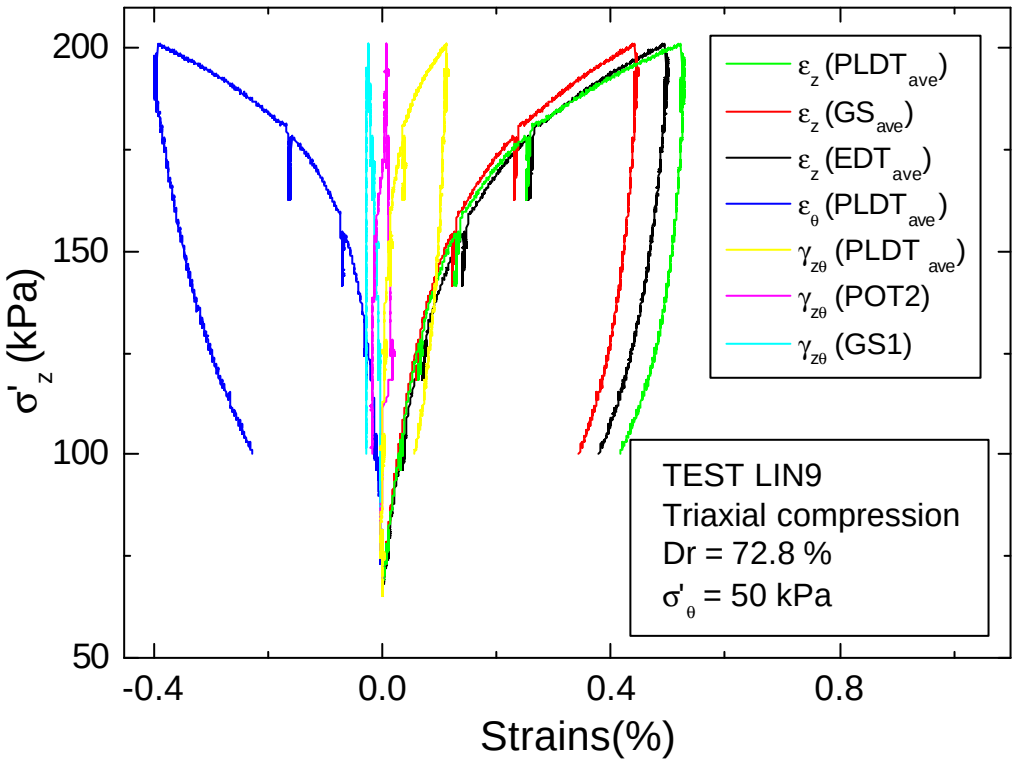

Fig. 4.81 Global strains of test LIN9 during TC

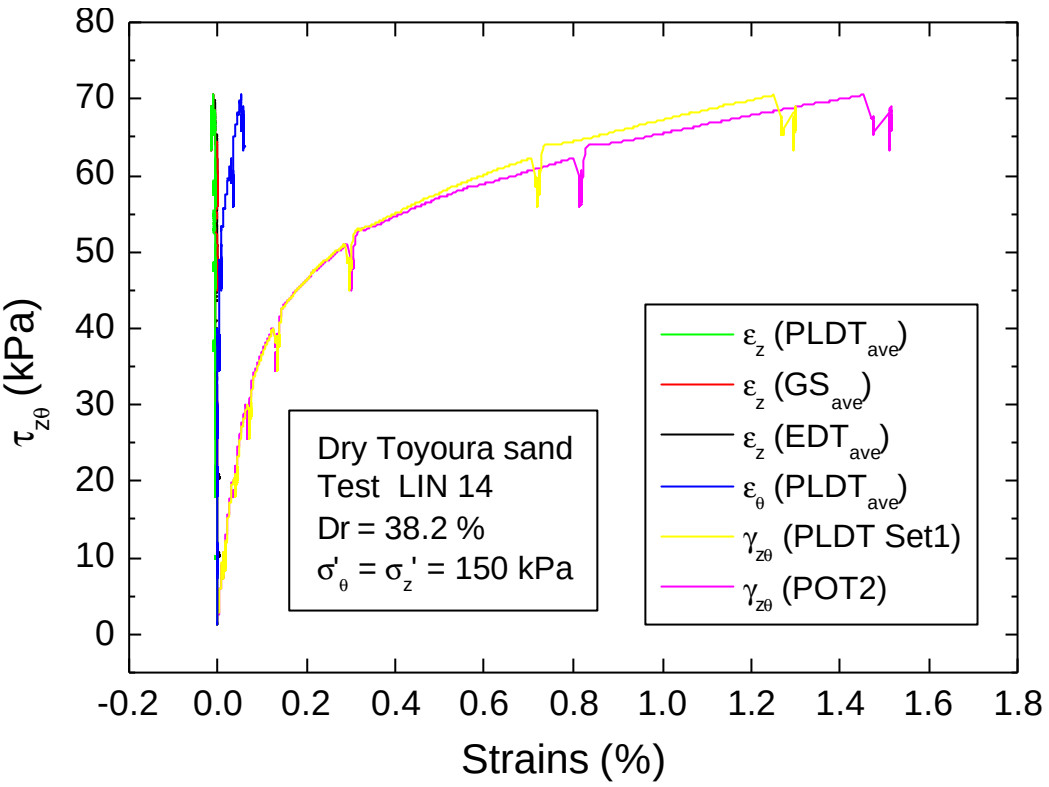

Fig. 4.82 Global strains during TSI

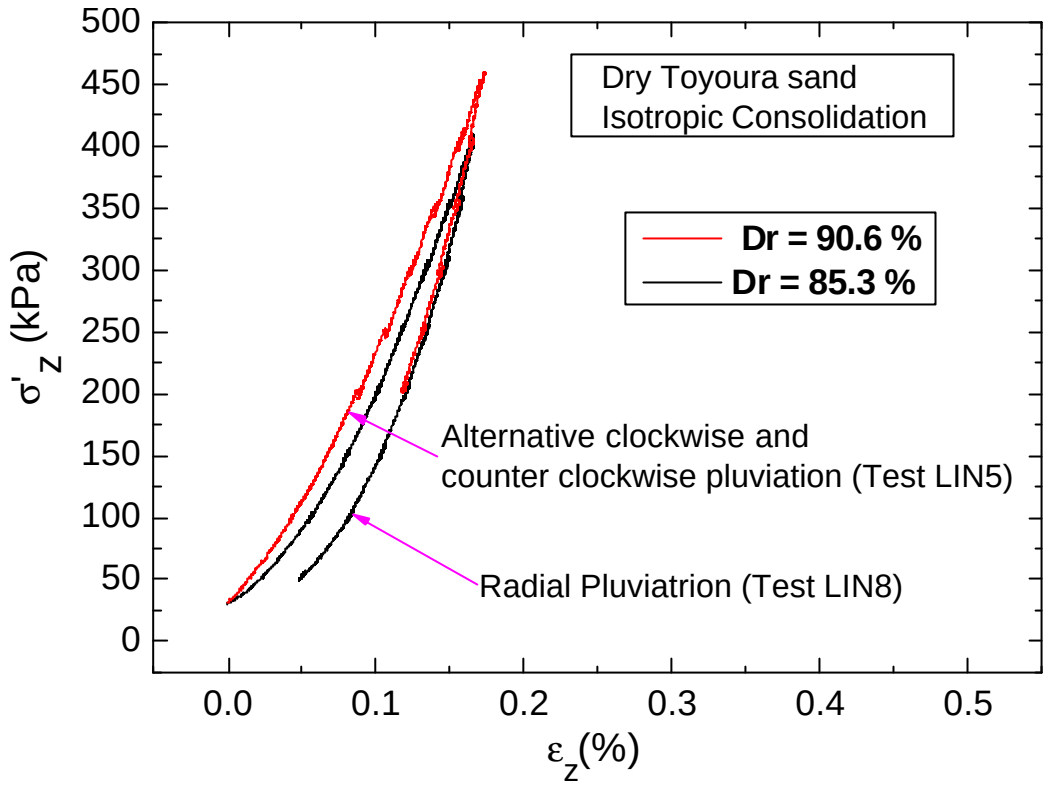

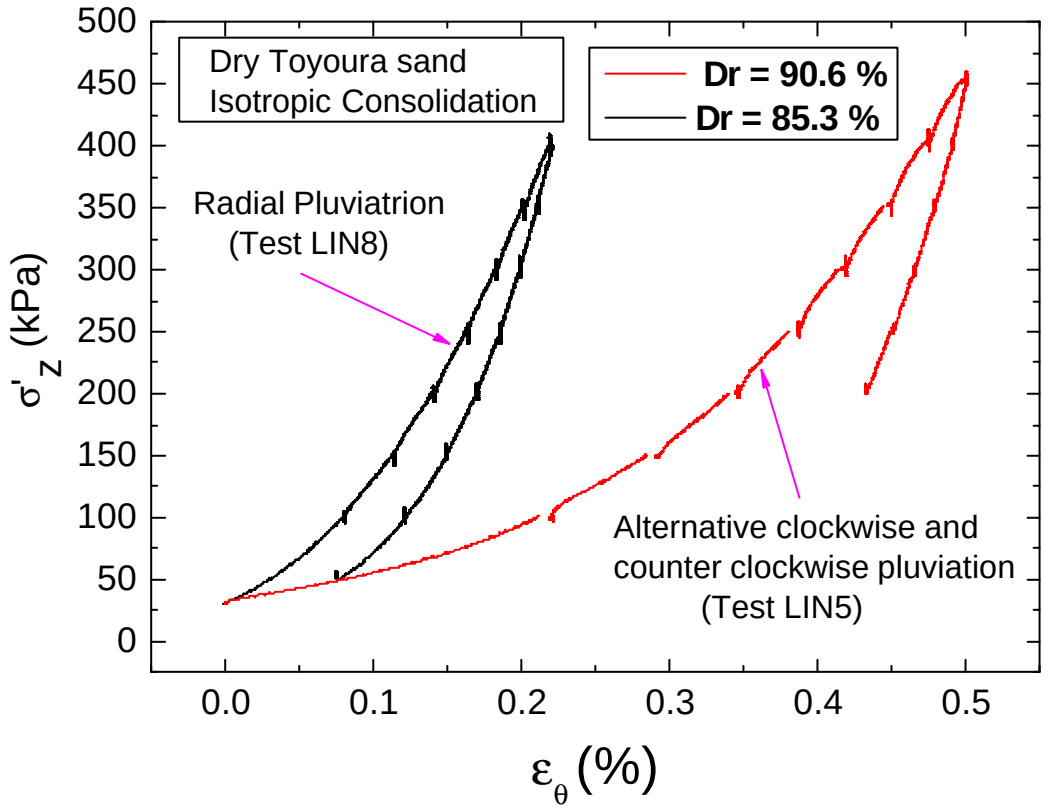

Fig. 4.83 Effects of different pluviation techniques on ε_θ

Appendix 4.1 Possible reason for the difference in locally and externally measured G_{zq}

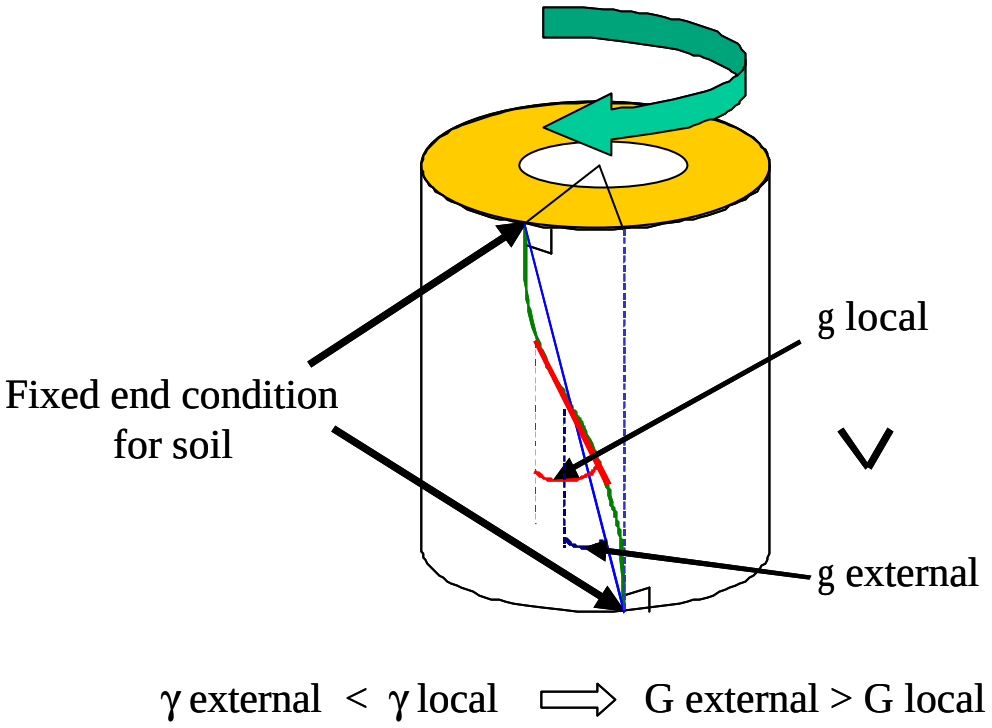

Fig. A.4.1 Possible mode of deformation

Fig.A.4.1 explains a possible reason for the difference in externally and locally measured shear modulus inferred by assuming no slippage between the top cap, pedestal and the specimen. The friction blades of the top cap and pedestal restrains the free movement of top and bottom layers of soils, which has a thickness at least equal to the height of the blades. This is creating a non-uniform distribution of shear strains along the specimen height, as shown in the figure. Therefore shear strain ($\gamma_{z\theta}$) measured externally is smaller than that measured locally, which yields higher shear modulus from external measurements than that from local measurements. Theoretically, the difference between external and local measurements should reduce with the increase of the specimen height.

Appendix 4.2: $E_z/f(e)$ and $G_{zq}/f(e)$ vs principal stress ratio, R

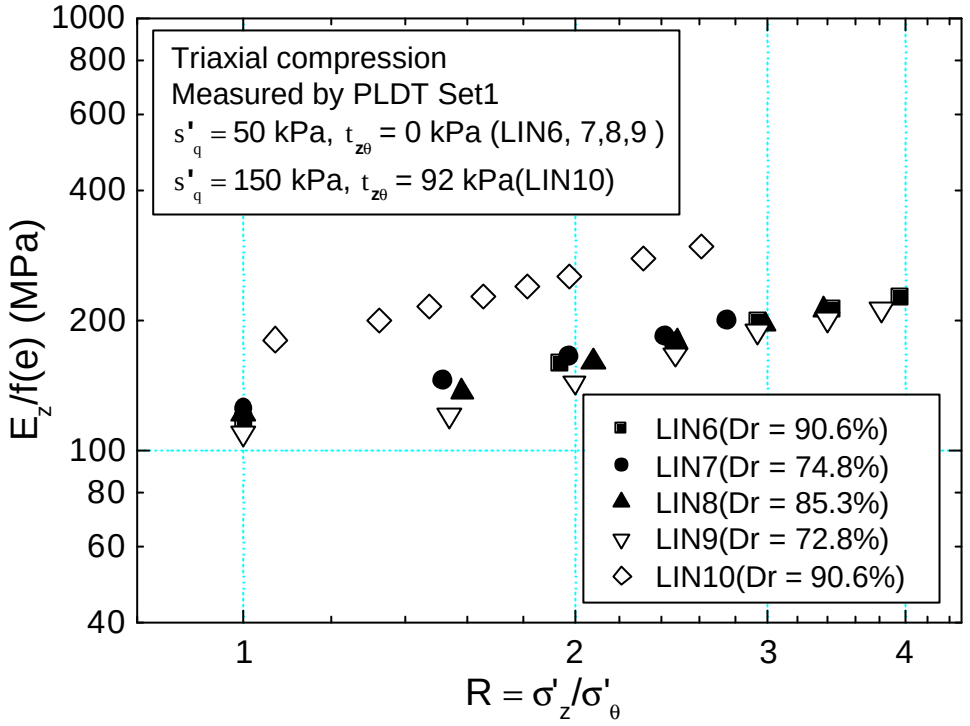

Fig. A.4.2 $E_z/f(e)$ vs R during TC measured by PLDT Set1

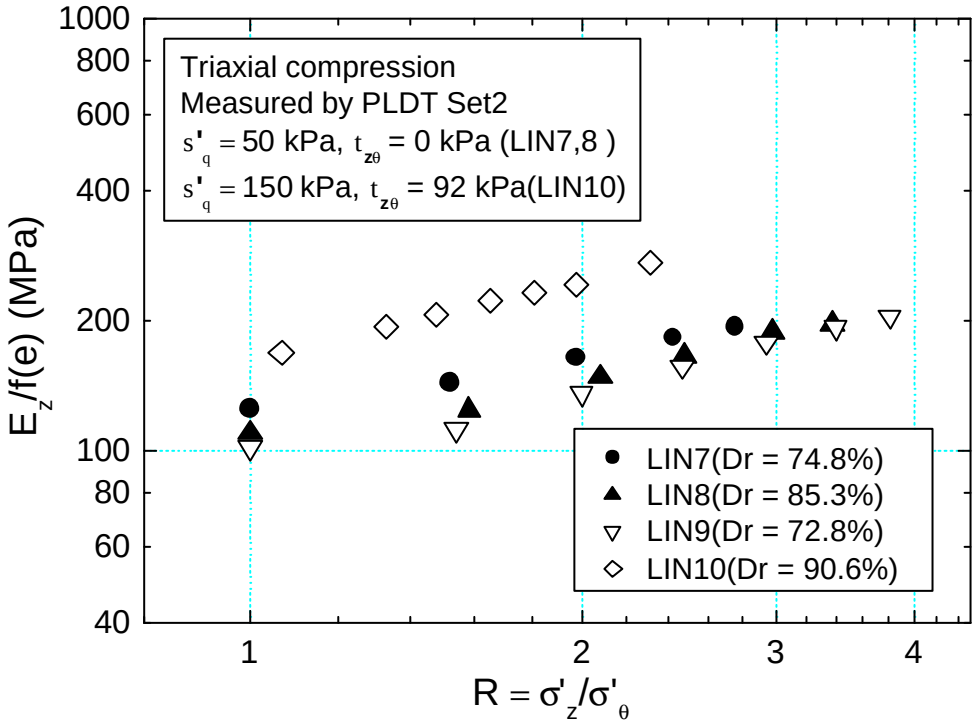

Fig. A.4.3 $E_z/f(e)$ vs R during TC measured by PLDT Set2

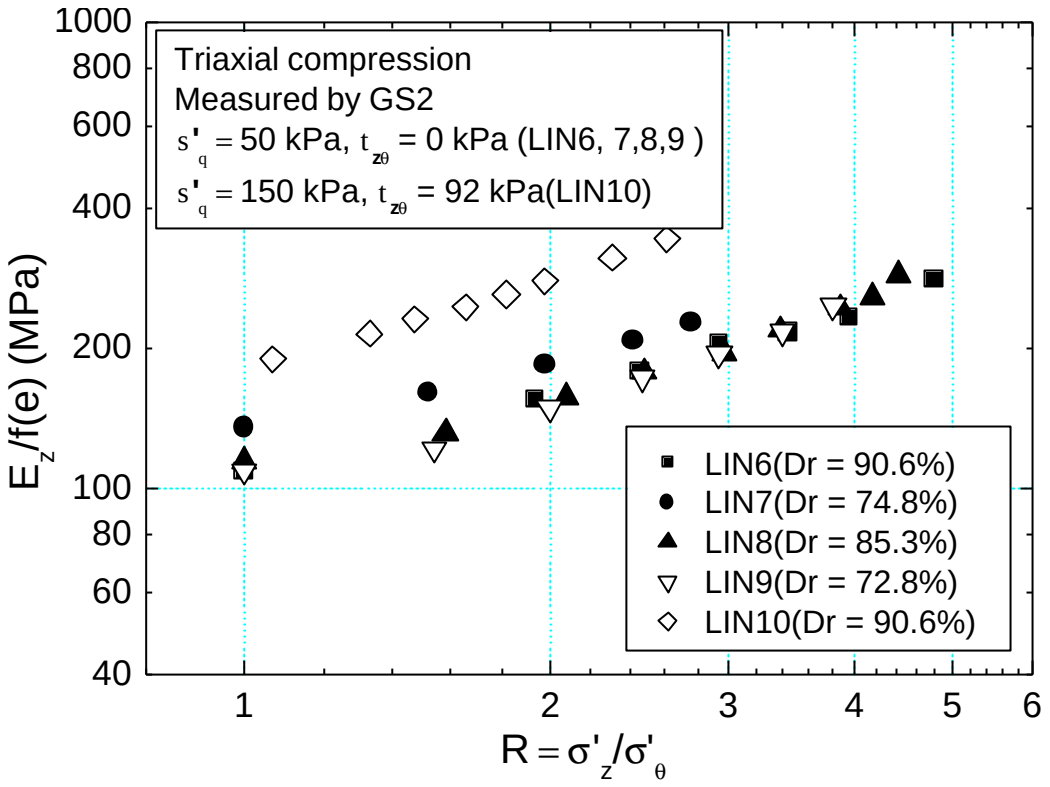

Fig. A.4.4 $E_z/f(e)$ vs R during TC measured by GS2

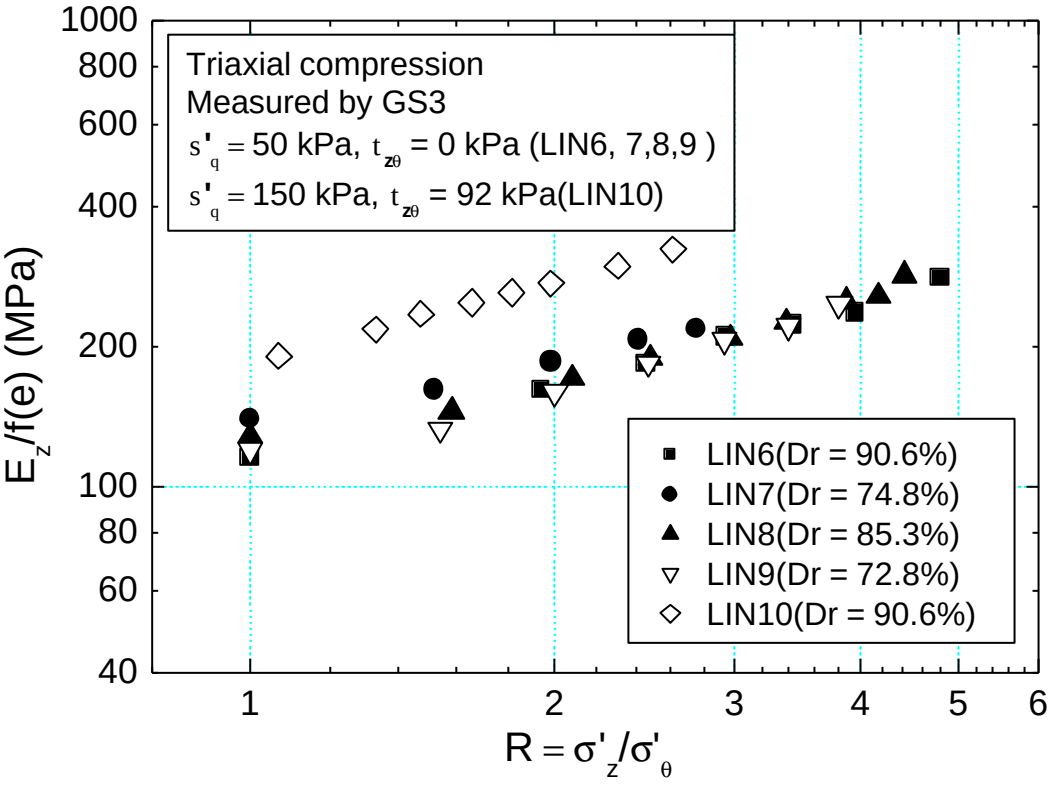

Fig. A.4.5 $E_z/f(e)$ vs R during TC measured by GS3

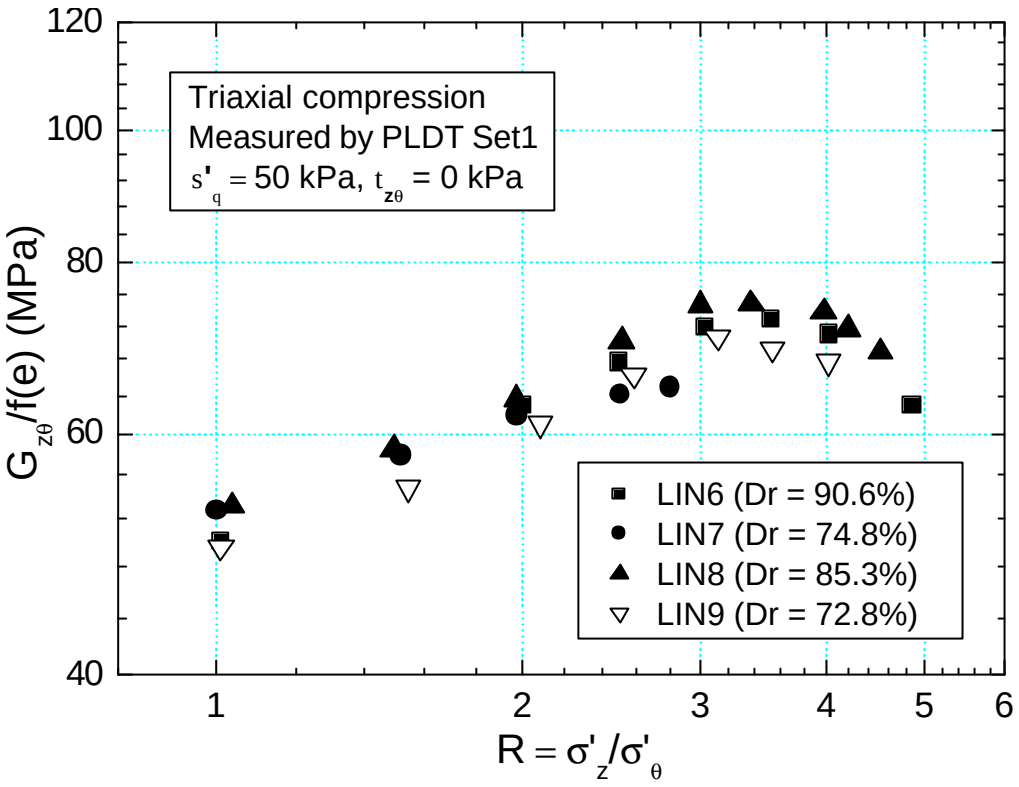

Fig. A.4.6 $G_{z\theta}/f(e)$ vs R during TC measured by PLDT Set1

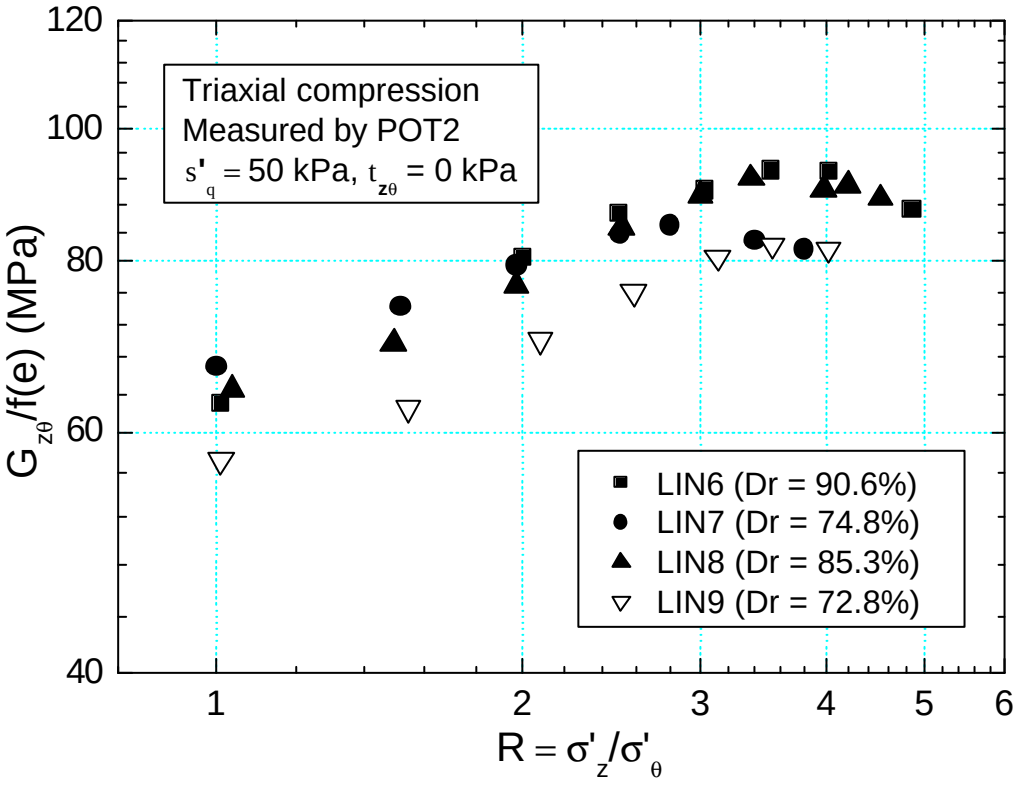

Fig. A.4.7 $G_{z\theta}/f(e)$ vs R during TC measured by POT2

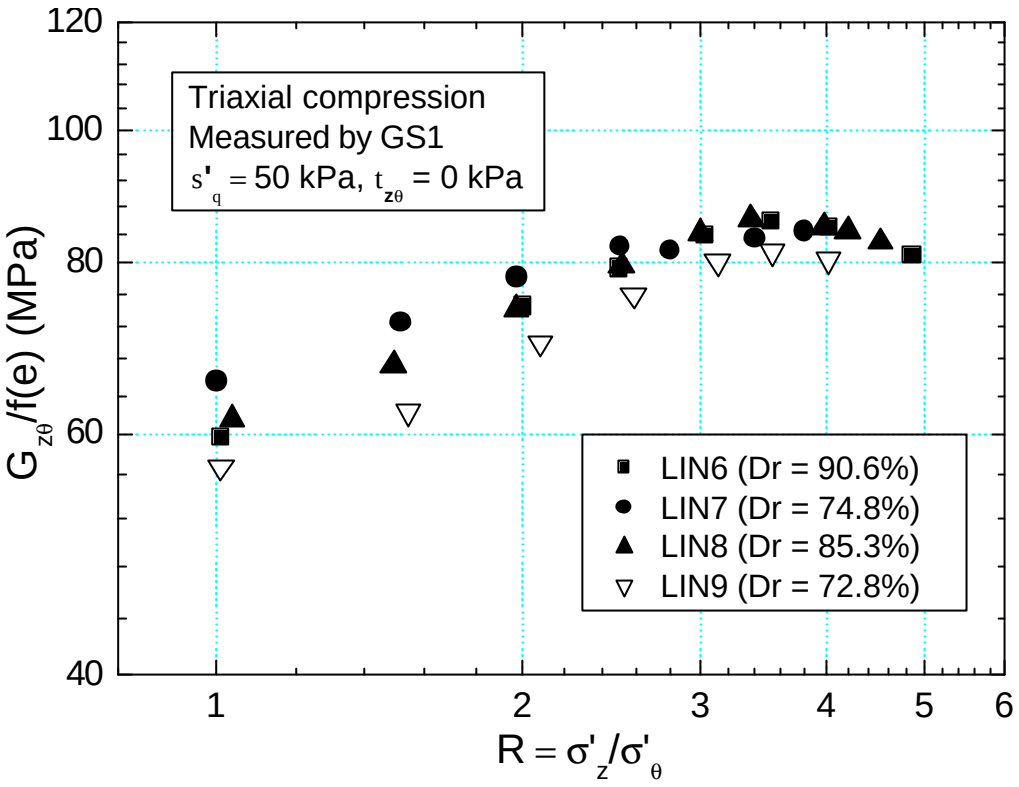

Fig. A.4.8 $G_{z\theta}/f(e)$ vs R during TC measured by GS1

Appendix 4.3: Applicability of $f(e) = (2.17-e)^2/(1+e)$ (Hardin & Richart, 1963) at different stress levels

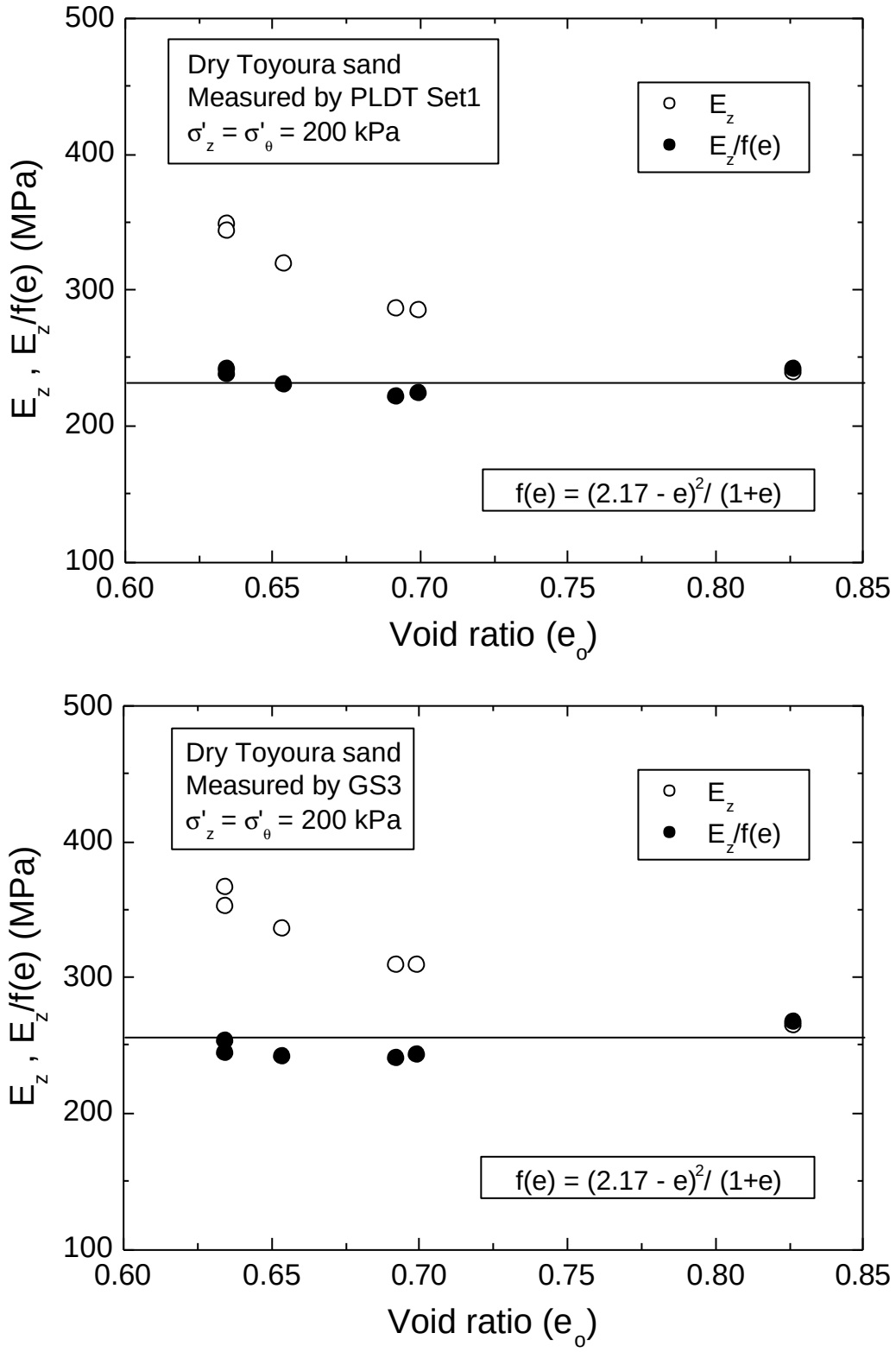

Fig. A.4.9 E_z, $E_z/f(e)$ vs initial void ratio (e_o) at $\sigma'_z = \sigma'_\theta = 200$ kPa

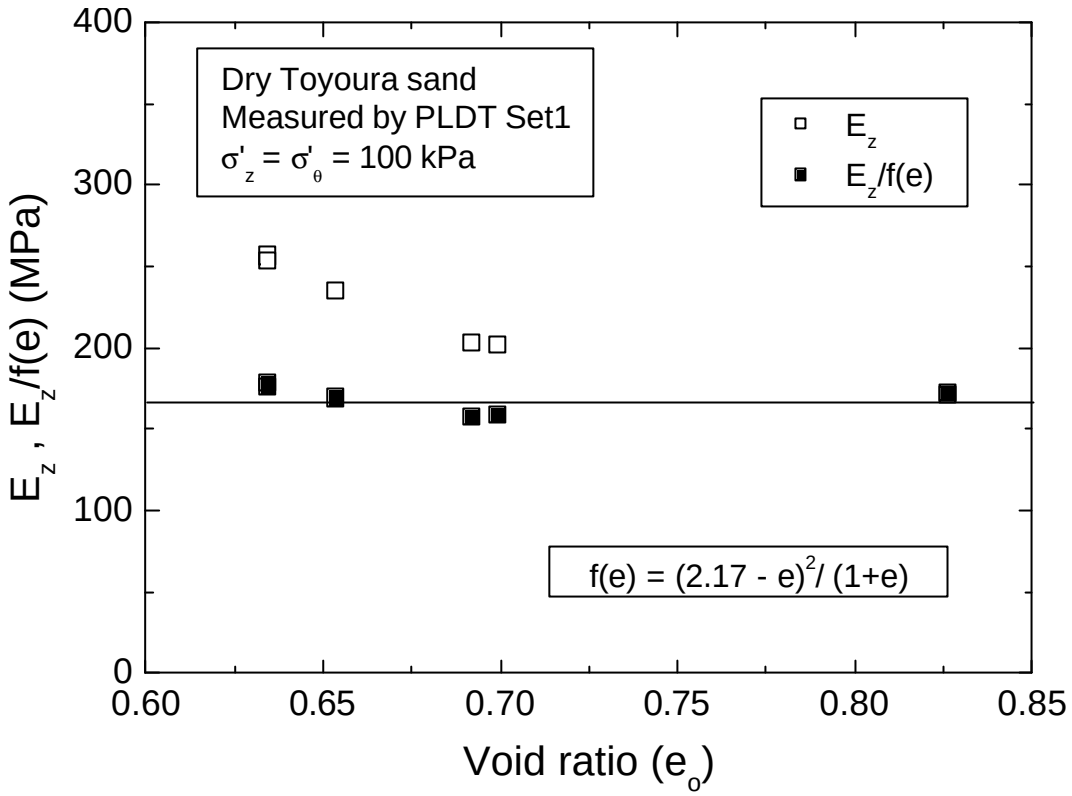

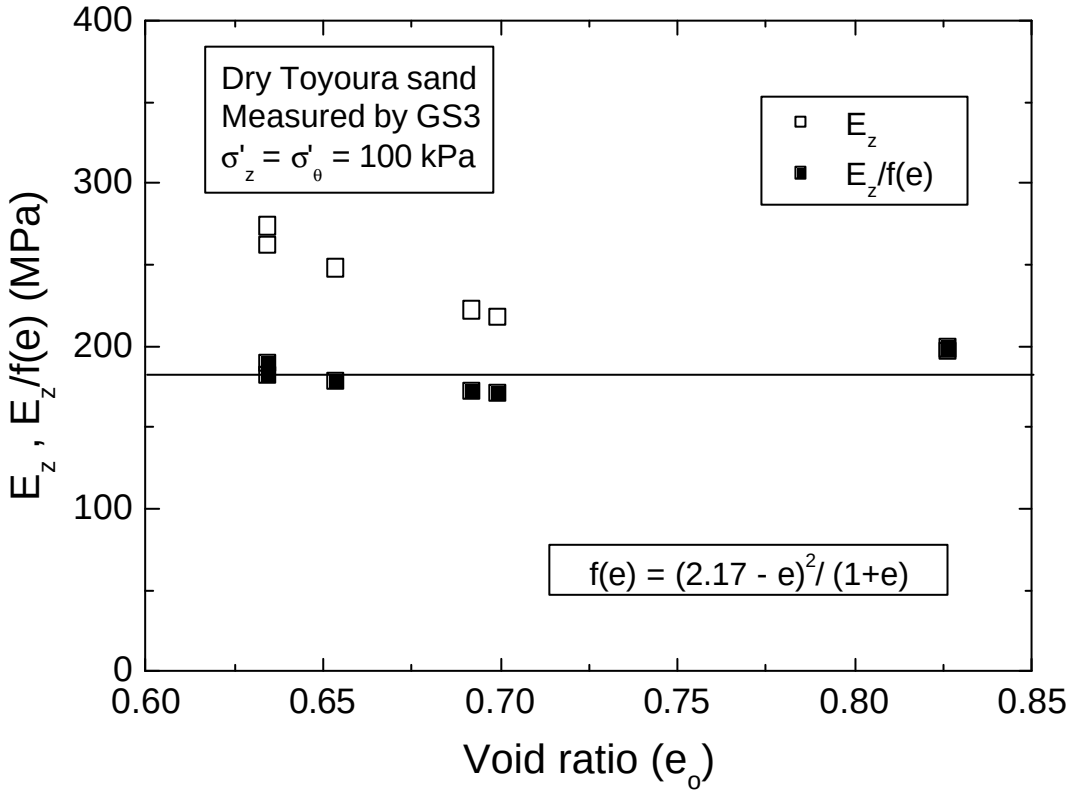

Fig. A.4.10 E_z, $E_z/f(e)$ vs initial void ratio (e_o) at $\sigma'_z = \sigma'_\theta = 100$ kPa

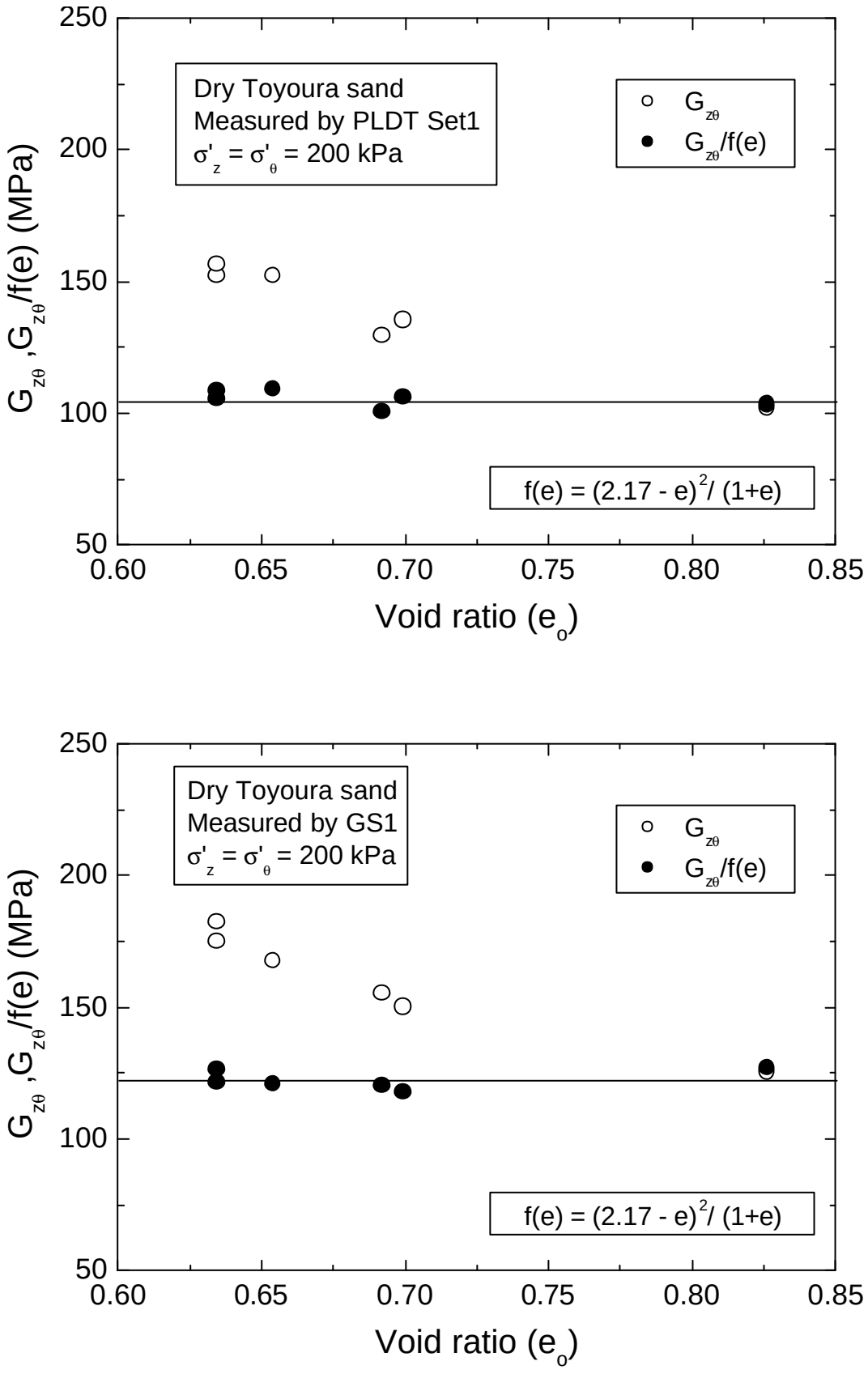

Fig. A.4.11 $G_{z\theta}$, $G_{z\theta}$ /f(e) vs initial void ratio (e_o) at $\sigma'_z = \sigma'_\theta$ = 200 kPa

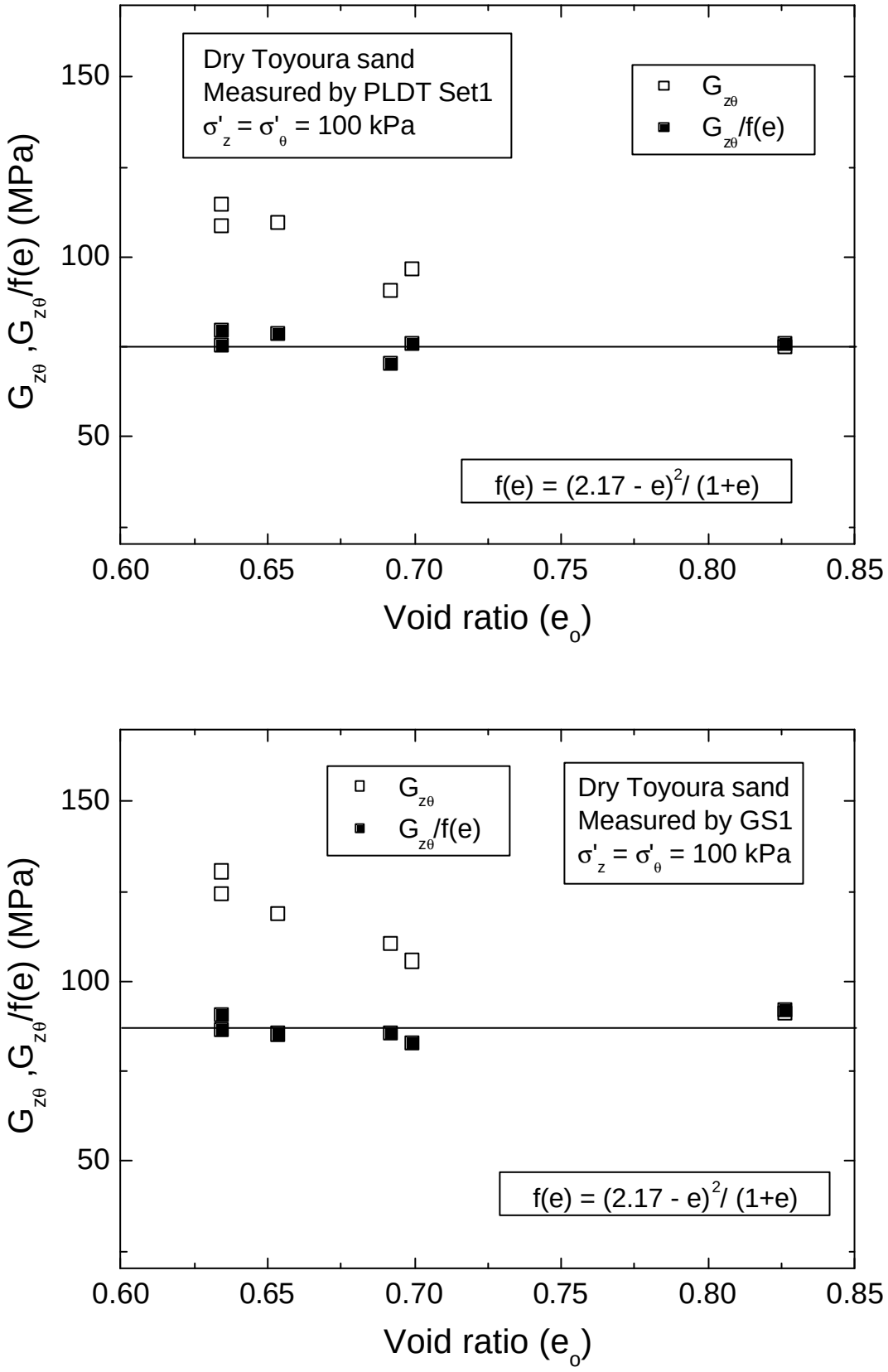

Fig. A.4.12 $G_{z\theta}$, $G_{z\theta}$ /f(e) vs initial void ratio (e_o) at $\sigma'_z = \sigma'_\theta$ = 100 kPa

Appendix 4.4: $-De_q/De_z$ vs principal stress ratio, $R = s'_z/s'_q$

As shown Fig. A.4.13 through Fig. A.4.17, $-\Delta\varepsilon_\theta/\Delta\varepsilon_z$ vs principal stress ratio ($R = \sigma'_z/\sigma'_\theta$) for each test was plotted to understand the possible reason for the sudden degradation of shear modulus after principal stress ratio becomes greater than three. $-\Delta\varepsilon_\theta/\Delta\varepsilon_z$ can be considered as a measure of the amount of dilation occurs during triaxial compression. Note that, during small cyclic loading very large values of $-\Delta\varepsilon_\theta/\Delta\varepsilon_z$ can be observed. But a general trend of dilation pattern could be observed during isotropic consolidation. According to the results shown in Fig. A.4.13 through Fig. A.4.17, all the Toyoura sand specimens show a gradual dilation with principal stress ratio, where there is no clear change of the dilation pattern after principal stress ratios become greater than three was observed. Therefore, it seems that the sudden degradation of shear modulus is not caused by a sudden dilation of the specimen after principal stress ratio become greater than three. Further investigation is needed to understand the possible reason for this phenomenon.

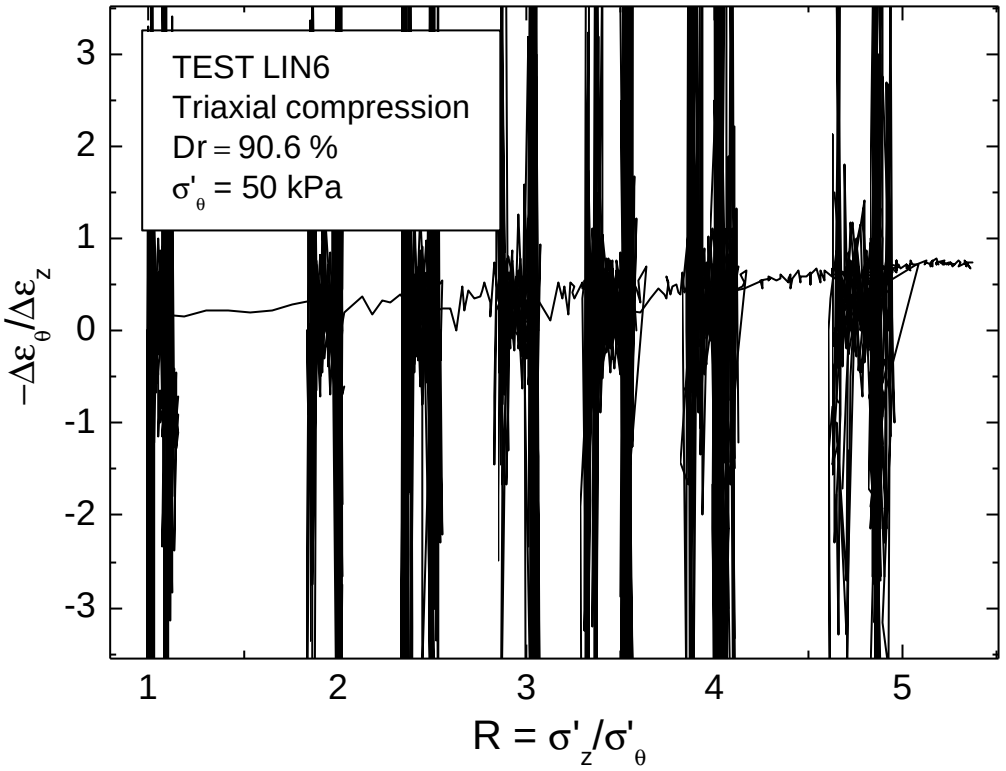

Fig. A.4.13 $-\Delta\varepsilon_\theta/\Delta\varepsilon_z$ vs $R = \sigma'_z/\sigma'_\theta$ for Test LIN6

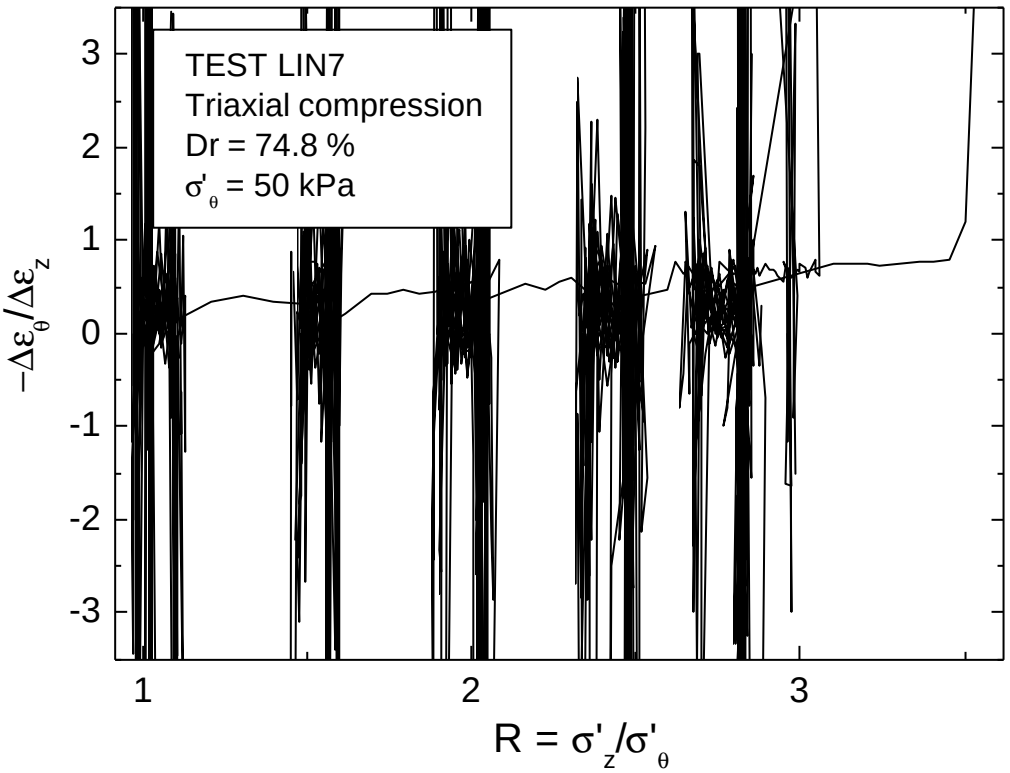

Fig. A.4.14 $-\Delta\varepsilon_\theta/\Delta\varepsilon_z$ vs $R = \sigma'_z/\sigma'_\theta$ for Test LIN7

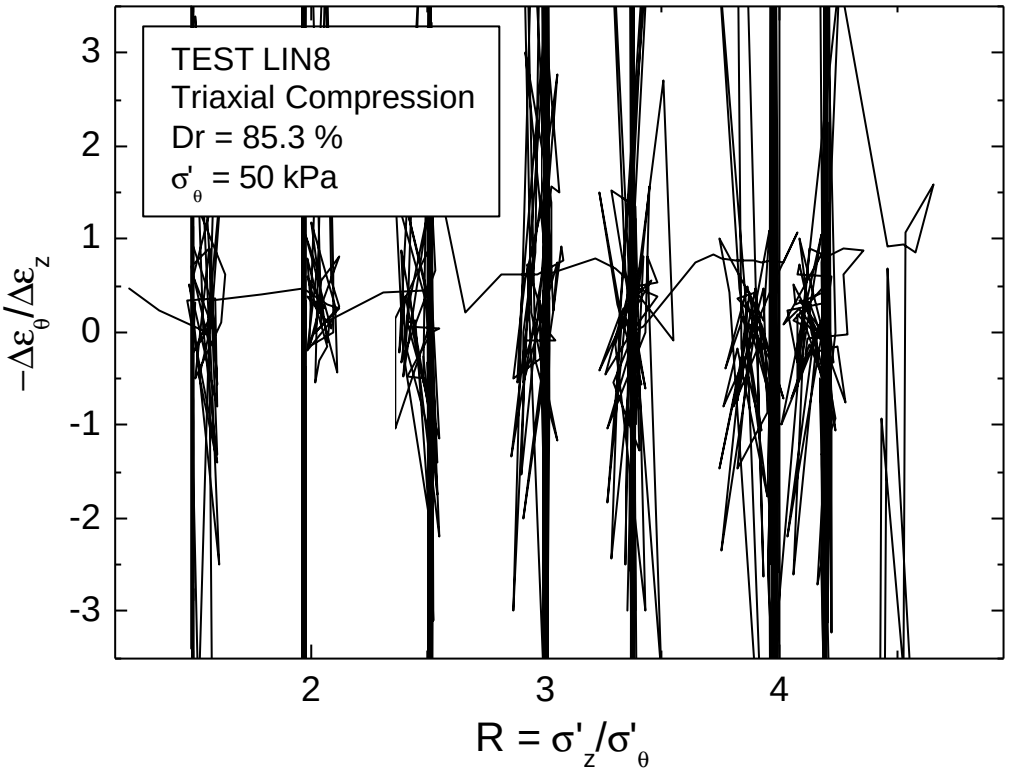

Fig. A.4.15 $-\Delta\varepsilon_\theta/\Delta\varepsilon_z$ vs $R = \sigma'_z/\sigma'_\theta$ for Test LIN8

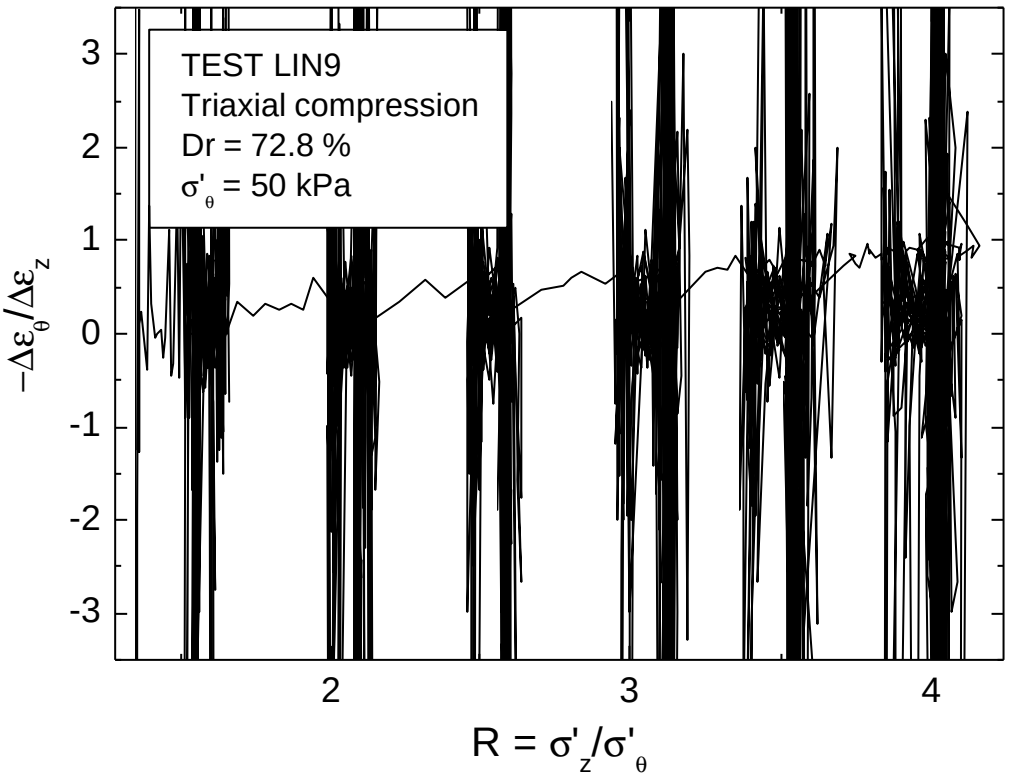

Fig. A.4.16 $-\Delta\varepsilon_\theta/\Delta\varepsilon_z$ vs $R = \sigma'_z/\sigma'_\theta$ for Test LIN9

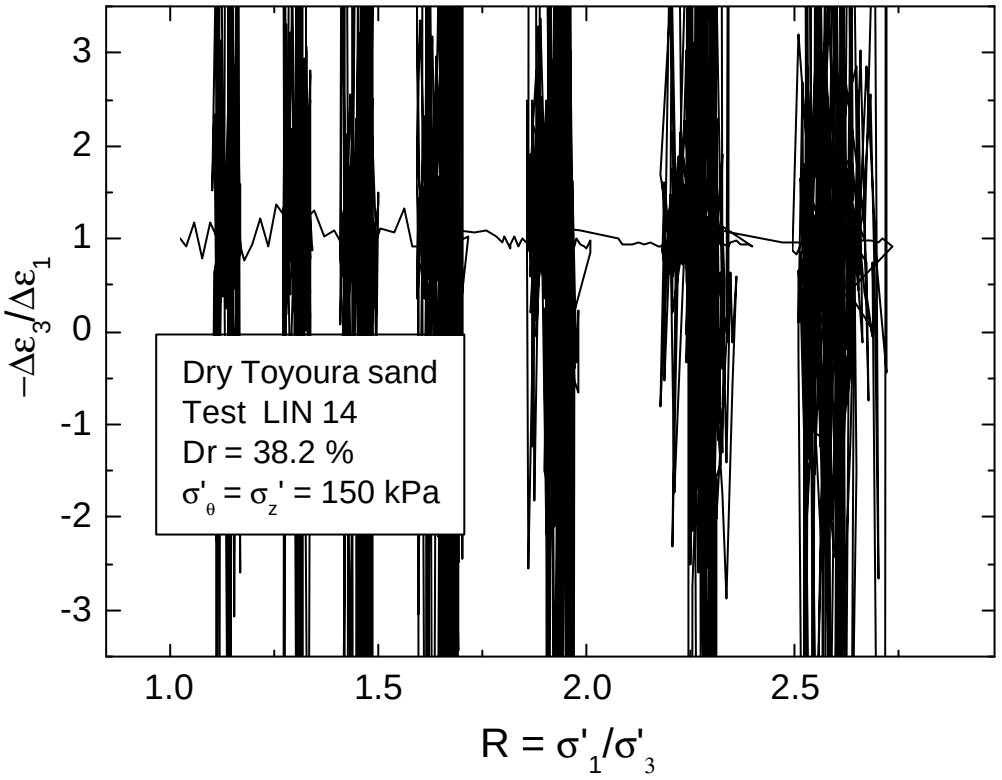

Fig. A.4.17 -$\Delta\varepsilon_\theta/\Delta\varepsilon_z$ vs $R = \sigma'_z/\sigma'_\theta$ for Test LIN14

CHAPTER 5: LOCALLY AND EXTERNALLY MEASURED DEFORMATION PROPERTIES OF HIME GRAVEL AT VARIOUS DENSITIES

5.1 Experiment program

The medium-sized hollow cylinder apparatus is capable of testing specimens that has dimensions varying from 15 cm in outer diameter, 12 cm in inner diameter and 30 cm in height to 20 cm in outer diameter, 12 cm in inner diameter and 30 cm in height. In addition, the loading system has a higher loading capacity also. Internal load cell is capable of measuring up to 15 kN of axial load and 0.3 kNm of torque. Taking the advantage of those two factors, Hime gravel (D_{50} = 1.73 mm) was tested under the same stress paths as Toyoura sand.

Table 5.1 describes the details of the tests. Dimensions of all Hime gravel specimens were 20 cm in outer diameter, 12 cm in inner diameter and 30 cm in height. Specimens were prepared by pluviating gravel particles in alternative clockwise and anti-clockwise directions. Pluviation height was varied between 0.1 m to 0.8 m to obtain specimens with dry densities varying from 1.725 g/cm^3 to 1.761 g/cm^3. In terms of relative density, it was between 75.5 % and 89.2 %. The modified version of PLDT system was employed for local strain measurement, while a base plate was introduced into the specimens (photo 14, Appendix) from the Test LIN12 onwards to attach the hinge to membrane because the effects of membrane penetration seemed to be predominant due to the large size of particles.

All the tests were conducted under drained condition. Specimens of the Tests LIN11 and LIN12 were isotropically consolidated from $\sigma'_\theta = \sigma'_z = 50$ kPa to $\sigma'_\theta = \sigma'_z = 400$ kPa and unloaded down to $\sigma'_\theta = \sigma'_z = 40$ and 50 kPa, respectively. Specimens of the Tests LIN13 and LIN15 were isotropically consolidated from $\sigma'_\theta = \sigma'_z = 60$ kPa to $\sigma'_\theta = \sigma'_z = 400$ kPa and unloaded down to $\sigma'_\theta = \sigma'_z = 50$ kPa. Eleven small unload-reload cycles were applied in both vertical and torsional directions after each increment of $\sigma'_\theta = \sigma'_z = 50$ kPa. Then Test LIN11 was subjected to triaxial compression while keeping $\sigma'_\theta = 40$ kPa. Rest of the tests were triaxially sheared at $\sigma'_\theta = 50$ kPa. Again, eleven small unload-reload cycles were applied in both vertical and torsional directions after each increment of $\sigma'_z = 25$ kPa. Data of the 10^{th} cycle was used to evaluate Young's and shear modulus.

5.2 Results and discussion

Although falling height was varied between 0.1m - 0.8m, the variation in relative density of the different specimens used in this study was about 15% (75.5 % - 89.2 %). This is because the diameter of the funnel is not sufficient to store a column of particles and release some particles at the end. Large amount of gravel particles trapped at the beginning of the funnel tube and few were falling straight. So the actual falling height was different from what we measured. To overcome this problem, it is necessary to modify the current pluviator and have a funnel with a larger diameter tube.

Discussion on the results of Hime gravel is categorized into three major sections. Section 5.2.1 discuss the results of locally and externally measured Young's and shear modulus of Hime gravel during isotropic consolidation (IC). Locally and externally measured Young's and shear modulus of Hime gravel during triaxial compression (TC) is discussed in section 5.2.2. Comparison of local and external measurements during IC and TC is discussed in section 5.2.3.

Fig. 5.1 illustrates a typical record of vertical strain vs time measured using the modified version of PLDTs during vertical small cyclic loading. Data of the 10^{th} cycle was used for the evaluation of vertical Young's modulus. A typical evaluation of Young's modulus using the modified vertion of PLDTs and Gap sensors is presented in Fig. 5.2 and Fig. 5.3, respectively.

Fig. 5.4 shows a typical record of shear strain vs time measured using the modified version of PLDTs during torsional small cyclic loading. As similar to the evaluation of Young's modulus, data of the 10th cycle was used in the evaluation of shear modulus. Fig. 5.5 and Fig. 5.6 show a typical evaluation of shear modulus using the modified version of PLDTs and Gap sensors, respectively. A typical evaluation of Poisson's ratio is shown in Fig. 5.7.

5.2.1 E_z and G_{zq} during isotropic consolidation

Relationship of E_z vs isotropic stress level measured by different transducers for a typical test is shown in Fig.5.8. Both external and local transducers at the same side (i.e., PLDT Set1 & GS3, and PLDT Set2 & GS2, respectively) give similar E_z values at different stress levels. On the other hand, both pairs of external or local transducers at the opposite sides of the specimen (i.e., PLDT Set 1 & 2, and GS2 & GS3, respectively) give slightly different values to each other, respectively. It may be due to the occurrence of local disturbance to different extents during specimen preparation. It was also observed that the specimen top surface and the top cap bottom face are not exactly parallel to each other, which might cause local disturbance when preparing the specimens.

Comparison of E_z of different tests measured by different transducers is shown in Fig. 5.9 through Fig. 5.12. It can be observed that both local and external transducers give similar E_z values and E_z at a particular stress state increases with the relative density of the specimens. However, the latter tendency is not very clear because the variation of the relative density is not so significant. In particular, results of Test LIN15 seem to be over-estimated for its lower relative density.

In order to compare the Young's moduli of Hime gravel specimens among different densities, the applicability of different void ratio functions (refer to 3.2.1) was checked as shown in Fig. 5.13. E_z value at the initial void ratio (e_{ref}) equal to 0.536 and $\sigma'_z = \sigma'_\theta = 400$ kPa is taken as the reference E_z ($E_{z(ref)}$). Then using the equation, $E_z = E_{z(ref)} / f(e_{ref}) \times f(e)$, relationships between E_z vs e proposed by different void ratio functions was plotted. It can be seen that the void ratio function proposed by Hardin and Richart (1963) ($f(e) = (2.17 - e)^2 / (1 + e)$) is the most appropriate for Hime gravel as well. As shown in the

same figure, this void ratio function works well for E_z values at $\sigma'_z = \sigma'_\theta$ = 200 and 100 kPa as well. Both local and external transducers show similar tendency. Fig 5.14 shows the relationships of E_z, and E_z /f(e) vs e_0 at a typical stress level measured using local and external transducers. This verifies that E_z/f(e) gives similar values against different void ratios when $f(e) = (2.17 - e)^2 / (1 + e)$ is used. Therefore this void ratio function is employed throughout the present study to compare Young's moduli of Hime gravel specimens with different relative densities.

After normalized by the void ratio function (Hardin and Richart, 1963), E_z/f(e) values show a rather unique relationship irrespective of the relative density as depicted in Fig. 5.15 through Fig. 5.18. *m* values that are averaged for the same type of transducers vary between 0.478 and 0.582 as shown in Table 5.2. Compared to that of Toyoura sand, however, the relationship of E_z/f(e) vs stress level is not so unique. Although both materials are uniformly graded, there may be an effect of particle shape on such relationships. Toyoura sand particles are sub-angular among geomaterials with different particle shapes while Hime gravel particles are sub-round. Therefore the use of same void ratio function may not be so relevant.

Fig. 5.19 shows $G_{z\theta}$ vs isotropic stress state measured by different transducers for a typical test. It can be seen that all the transducers give similar results. This observation is different from that of Toyoura sand. In the case of Toyoura sand, externally measured shear moduli are about 15 % greater than the locally measured ones. It seems that the effect of end restraint is not predominant in the results of shear modulus of Hime gravel. Height of the friction blades at the top cap and pedestal is about 2 mm and D_{50} of Hime gravel is 1.73 mm. Therefore, friction blade height is almost equal to a diameter of one Hime gravel particle, while it is about 15 times of the diameter of Toyoura sand particles. This may be the reason why Toyoura sand shows a significant effect of end restraint in the evaluation of shear modulus.

$G_{z\theta}$ vs isotropic stress level at different relative densities are shown in Fig. 5.20 through Fig.5.23. In a manner that is similar to E_z, $G_{z\theta}$ at a particular stress level increase with the relative density. All the transducers except PLDT Set2 show a similar tendency. As shown in Fig. 5.21, PLDT Set2 gives highly scattered data in some tests and hence the results were omitted. It seems that the diagonal PLDT in PLDT Set2 was not working well. This may be due to some unusual hinge movement.

In order to compare the shear moduli of Hime gravel specimens among different densities, the applicability of different void ratio functions was checked as shown in Fig. 4.23a. $G_{z\theta}$ value at the initial void ratio (e_{ref}) equal to 0.536 and $\sigma'_z = \sigma'_\theta$ = 400 kPa is taken as the reference $G_{z\theta}$ ($G_{z\theta(ref)}$). Then using the equation, $G_{zq} = G_{zq\,(ref)} / f(e_{ref}) \times f(e)$, relationships between $G_{z\theta}$ vs e proposed by different void ratio functions was plotted. It can be verified that the void ratio function proposed by Hardin and Richart (1963) ($f(e) = (2.17 - e)^2 / (1 + e)$) is the most appropriate for Hime gravel as well. As shown in the same figure, this void ratio function works well for $G_{z\theta}$ values at $\sigma'_z = \sigma'_\theta$ = 200 and 100 kPa as well. Both local and external transducers show similar tendency. Fig. 4.23b shows the relationships of $G_{z\theta}$, and $G_{z\theta}$ /f(e) vs e_0 at a typical stress level measured using local and external transducers. This verifies that $G_{z\theta}$/f(e) gives similar values against different void ratios when $f(e) = (2.17 - e)^2 / (1 + e)$ is used. Therefore this void ratio function is employed throughout the present study to compare shear moduli of Hime gravel specimens with different relative densities.

As shown in Fig. 5.24 through Fig. 5.26, after normalized by f(e), $G_{z\theta}$ during IC show a unique relationship against the stress level, $(\sigma'_\theta * \sigma'_z)^{0.5}$. *n* values from different transducers vary between 0.511 – 0.574 as shown in Table 5.3.

5.2.2 E_z and G_{zq} during triaxial compression

Fig. 5.27 through Fig. 5.29 show E_z/f(e) during IC and TC vs σ'_z, σ'_m, and p, respectively for a typical test measured using both local and external transducers. It was verified from those relationships that E_z/f(e) can be expressed as a function of σ'^{m}_z. E_z/f(e) vs σ'_z for all the tests is depicted in Fig.5.30 through Fig.5.33. It can be seen that both local and external transducers show an increasing trend of E_z/f(e) against σ'_z.

Fig. 5.34 and Fig. 5.35 show the relationship between $E_z/E_{z(ref)}$ and principal stress ratio, R. $E_{z(ref)}$ was evaluated using the same equation ($E_{ref} = E_0 \times f(e_0) / f(e) \times (s_z / s_0)^m$) as described in chapter 4. Both local and external transducers show that $E_z/E_{z(ref)}$ values remain

unchanged (close to unity) during triaxial compression. As typically shown in Fig. 5.36, both Toyoura sand and Hime gravel show a similar tendency of $E_z/E_{z(ref)}$ against the principal stress ratio.

Fig.5.37 through Fig.5.39 show the relationships of $G_{z\theta}/f(e)$ vs $(\sigma'_\theta * \sigma'_z)^{0.5}$, σ'_m and p ,respectively. $G_{z\theta}/f(e)$ can be best expressed as a function of $(\sigma'_\theta * \sigma'_z)^{0.5n}$ as found by Hong Nam (2004). It should be noted that all the relationships show a gradual degradation of $G_{z\theta}/f(e)$ after a particular stress level, showing evidences of possible damage to the specimen.

Fig.5.40 through Fig. 5.42 show the relationship of $G_{z\theta}/f(e)$ vs $(\sigma'_\theta * \sigma'_z)^{0.5}$ measured using different transducers. All the plots show a gradual degradation of shear modulus after principal stress ratio becomes greater than three. In addition, $G_{z\theta}/G_{z\theta(ref)}$ vs principal stress ratio, as shown in Fig. 5.43 and Fig. 5.44, show a gradual degradation of $G_{z\theta}/G_{z\theta(ref)}$ after principal stress ratio becomes greater than three. $G_{z\theta(ref)}$ was evaluated using the equation, $G_{ref} = G_0 \times f(e_0)/\ f(e) \times \left(\sqrt{s_z s_q}\ / s_0\right)^n$, as described in chapter 4. Although the degradation is visible in both Toyoura sand and Hime gravel, as typically shown in Fig. 5.45, the degradation of Toyoura sand after principal stress ratio becomes greater than three seemed to be sudden, while that of Hime gravel seemed to be gradual.

Poisson's ratio ($\nu_{z\theta}$) during IC and TC is shown in Fig. 5.46 and Fig. 5.47. During IC, Poisson's ratio remains almost unchanged against the stress level with an average value of 0.165. On the other hand, as shown in Fig. 5.47, $\nu_{z\theta}$ during TC can be expressed as a function of $(\sigma'_z/\sigma'_\theta)^k$. k varies between 0.377 and 0.692. Table 5.4 shows the k values.

5.2.3 Comparison of local and external measurements

Fig. 5.48 through Fig. 5.57 shows the comparison of E_z measured by different transducers. It can be observed from Fig. 5.48 and Fig. 5.53 that the ratio of externally and locally measured average Young's modulus in both IC and TC is almost unity. As shown in Fig. 5.51, Fig. 5.52, Fig. 5.56 and Fig. 5.57, however, ratio of E_z measured using different external transducers and local transducers are not always close to unity. But, as shown in Fig. 5.49, Fig. 5.50, Fig. 5.54

and Fig. 5.55, the ratio of E_z measured using local and external transducers attached at the same side of the specimen (PLDT Set1 & GS3, and PLDT Set2 & GS2) is close to unity during IC and TC. During the specimen preparation, it was observed that the specimen top surface is not perfectly parallel to the top cap. As a result, a small force had to be applied to connect the top cap to the loading shaft. There is a possibility of having a local disturbance due to this force. This may cause some non-uniformity of the specimen.

Comparison of locally and externally measured $G_{z\theta}$ during IC and TC is shown in Fig. 5.58 through Fig. 5.61. Fig. 5.58 and Fig. 5.60 shows the comparison of $G_{z\theta}$ measured by GS1 and PLDT Set1 during IC and TC, respectively. It can be observed that the ratio between externally and locally measured $G_{z\theta}$ lie between 0.98 and 1.15. In the case of Toyoura sand it is between 1.10 and 1.20. It seems that the effects of end restraint is not predominant in Hime gravel specimens as described in detail in section 5.2.1. Comparison of $G_{z\theta}$ measured using two external transducers GS1 and POT2 during IC and TC is shown in Fig. 5.59 and Fig. 5.61. Its ratio varies between 1.00 and 1.12. In the case of Toyoura sand, it is almost close to unity. This is again showing some evidences of local disturbance.

Global behavior of Hime gravel specimens during IC and TC is shown in Fig. 5.62 through Fig. 5.69. It can be noted that Hime gravel shows a stiffer response in the vertical direction compared to Toyoura sand (Fig. 4.76). It is interesting to note that ε_θ is of the same order as ε_z. Unlike Toyoura sand, the direction of pluviation seems immaterial to Hime gravel. The shape of the Hime gravel particle is sub-round while that of Toyoura sand is sub-angular. Therefore the orientation of particles may not be a concern in Hime gravel specimens, while the uniformity and isotropy of Toyoura sand specimens is largely affected by the orientation of particles. This may be the possible reason for getting similar values of ε_z and ε_θ. However more verifications are needed in this regard. Note that, $\gamma_{z\theta}$ measured by using PLDT Set1 in the Test LIN11 is very large. No base plate was used in the Test LIN11, while they were used in all the other Hime gravel tests. Therefore this strange behavior of PLDT Set1 may be due to the unusual hinge movement caused by membrane penetration. Note that, the area of a hinge base is just 5 mm * 5 mm, which is sufficient only to cover about eight Hime gravel particles. After introducing base plates in Tests LIN12, 13 and 15, it can be observed that $\gamma_{z\theta}$ measured both locally and externally remains almost close to zero during IC and TC.

Table 5.1 Details of Hime gravel specimens

Test	Dry density (g/cm^3)	Initial void ratio	Relative density (%)	Stress path (kPa)
LIN11	1.761	0.505	89.2	IC ($\sigma'_z = \sigma'_\theta$ = 50 ~ 400 ~ 40) TC (σ'_θ = 40, σ'_z = 40 ~ 200)
LIN12	1.735	0.527	79.4	IC ($\sigma'_z = \sigma'_\theta$ = 50 ~ 400 ~ 50) TC (σ'_θ = 50, σ'_z = 50 ~ 250)
LIN13	1.737	0.525	80.3	IC ($\sigma'_z = \sigma'_\theta$ = 60 ~ 400 ~ 50) TC (σ'_θ = 50, σ'_z = 50 ~ 250)
LIN15	1.725	0.536	75.5	IC ($\sigma'_z = \sigma'_\theta$ = 60 ~ 400 ~ 50) TC (σ'_θ = 50, σ'_z = 50 ~ 250)

Table 5.2 Averaged *m* values of Hime gravel during IC and TC

Test	***m* during IC**		***m* during TC**	
	PLDTs	**GSs**	**PLDTs**	**GSs**
LIN11	0.478	0.532	0.402	0.593
LIN12	0.582	0.559	0.678	0.726
LIN13	0.579	0.546	0.600	0.675
LIN15	0.509	0.542	0.534	0.634

Table 5.3 *n* values of Hime gravel during IC and TC

Test	***n* during IC**		
	PLDT Set1	**GS1**	**POT2**
LIN11	0.511	0.569	-
LIN12	0.536	0.574	0.547
LIN13	0.536	0.561	0.532
LIN15	0.547	0.533	0.538

Table 5.4 k values of Hime gravel during TC

Test	k values from PLDTs
LIN12	0.692
LIN13	0.377

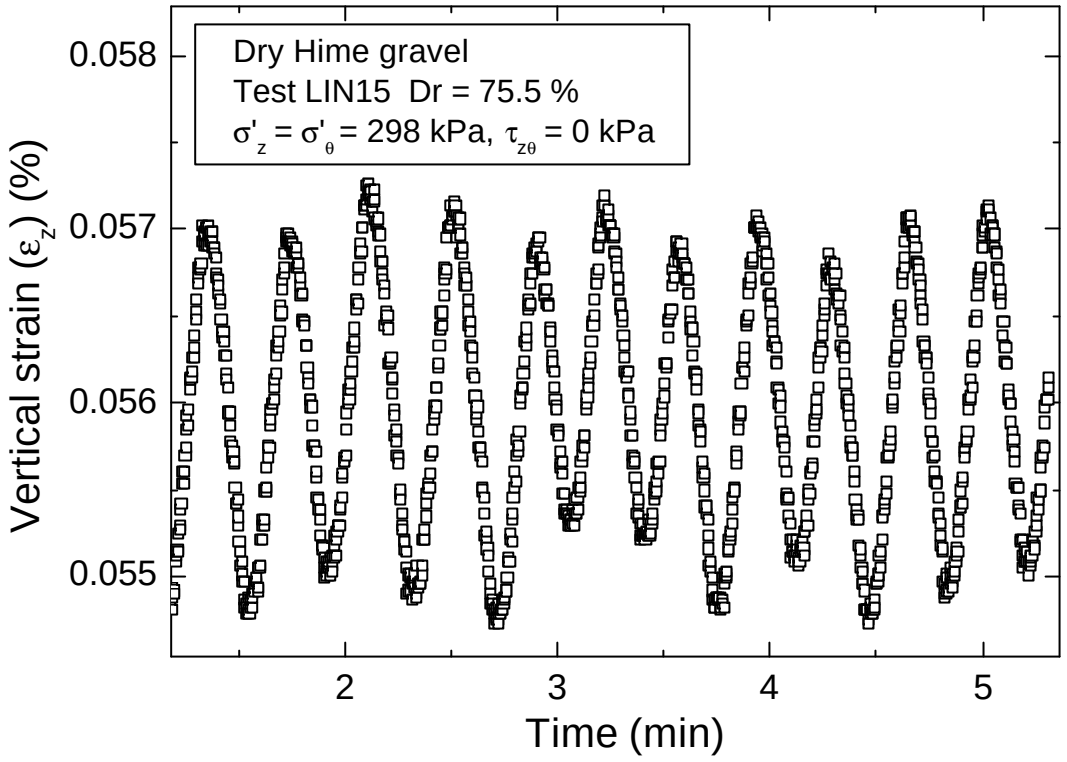

Fig. 5.1 Vertical small cyclic loading measured by modified version of PLDTs

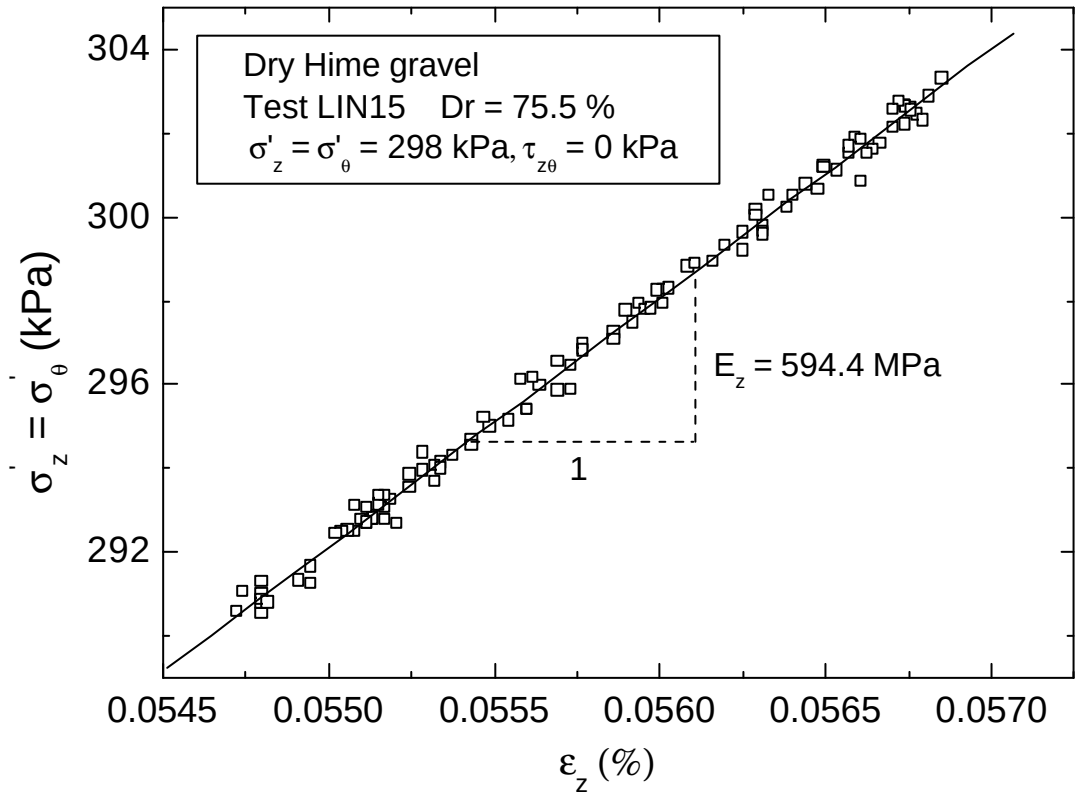

Fig. 5.2 Typical evaluation of E_z using modified version of PLDTs

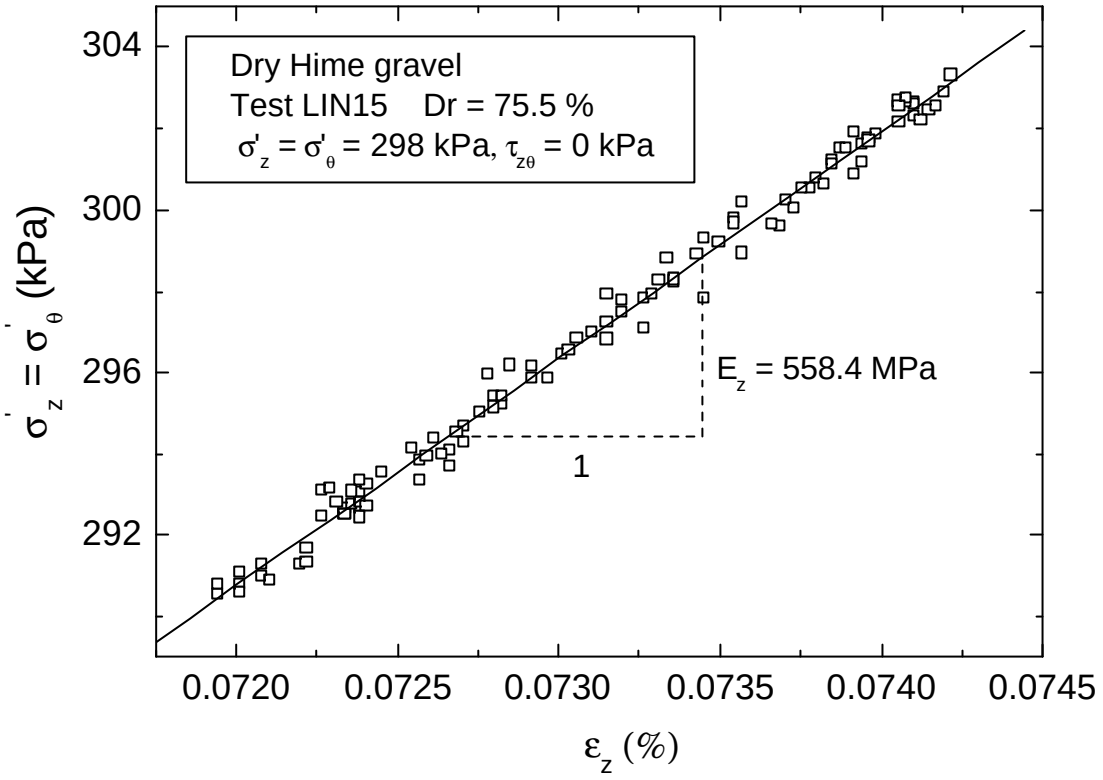

Fig. 5.3 Typical evaluation of E_z using gap sensors

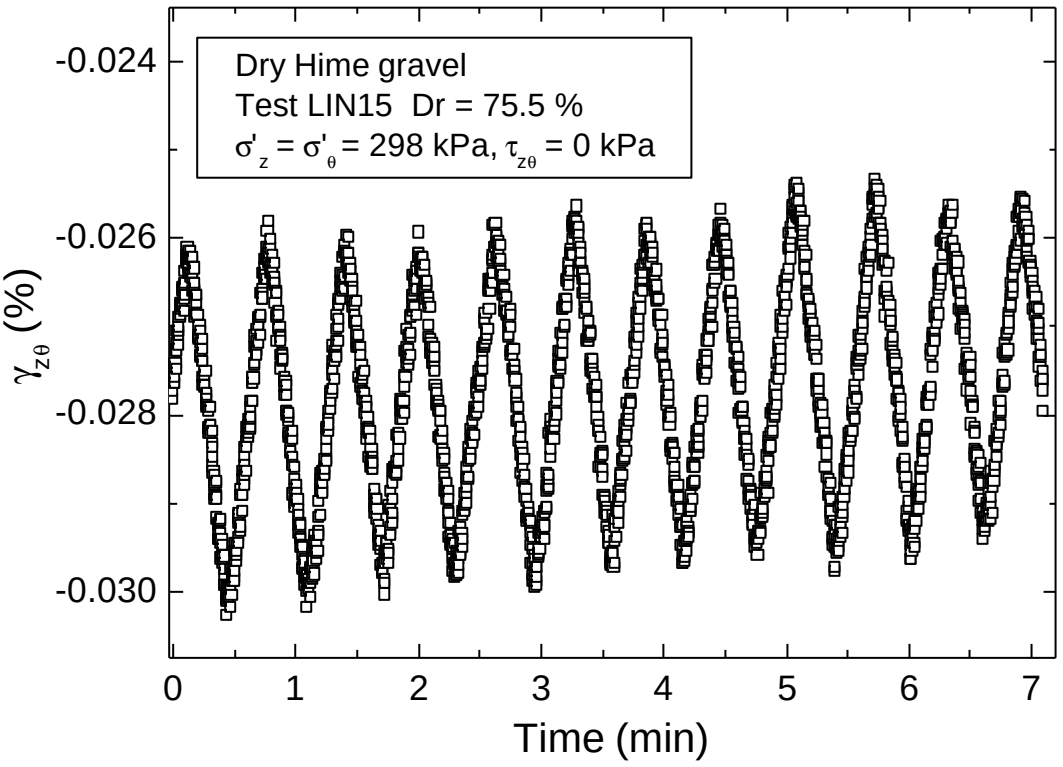

Fig. 5.4 Torsional small cyclic loading measured by modified version of PLDTs

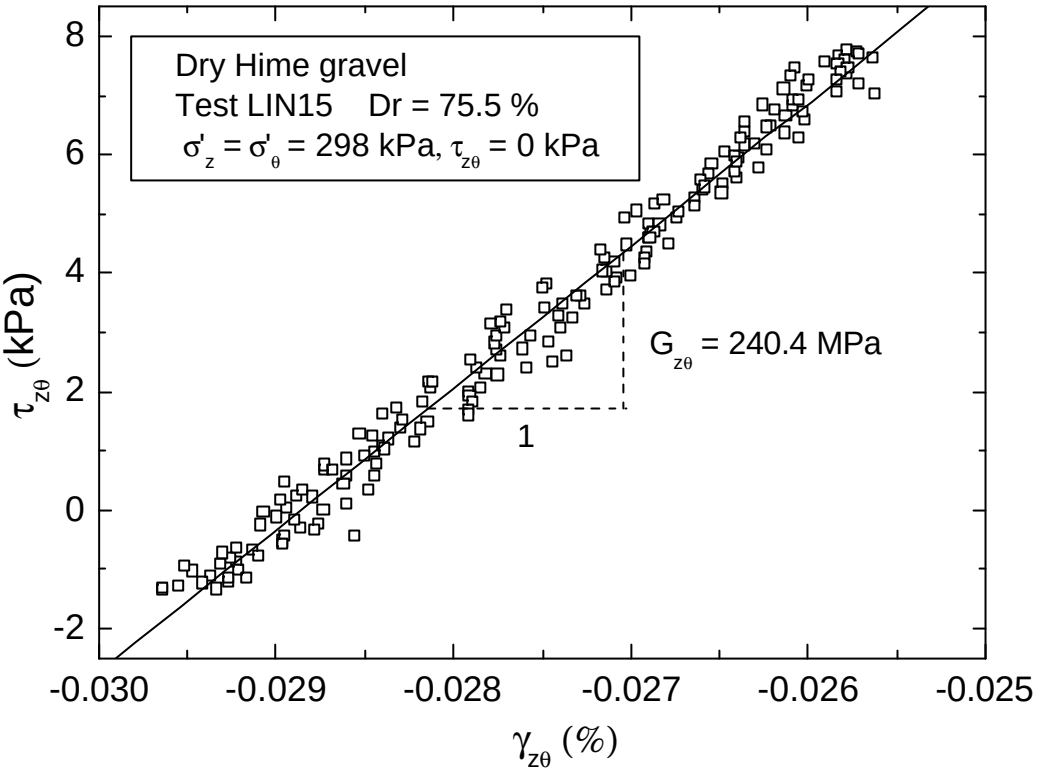

Fig. 5.5 Typical evaluation of $G_{z\theta}$ using modified version of PLDTs

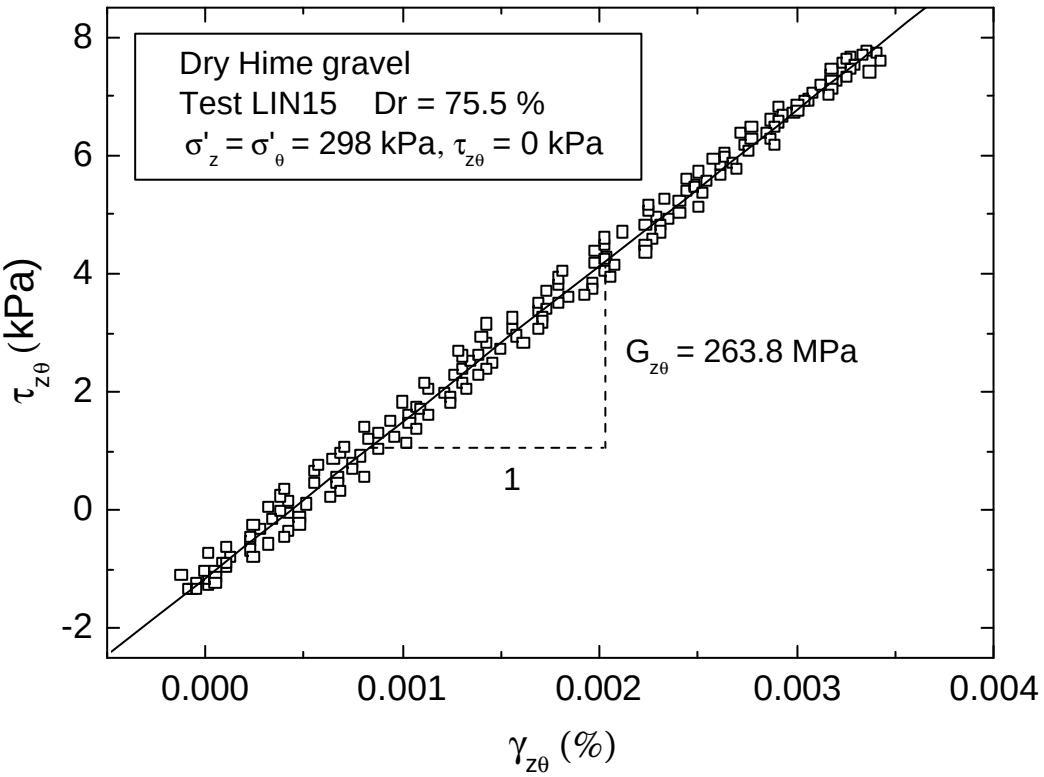

Fig. 5.6 Typical evaluation of $G_{z\theta}$ using gap sensors

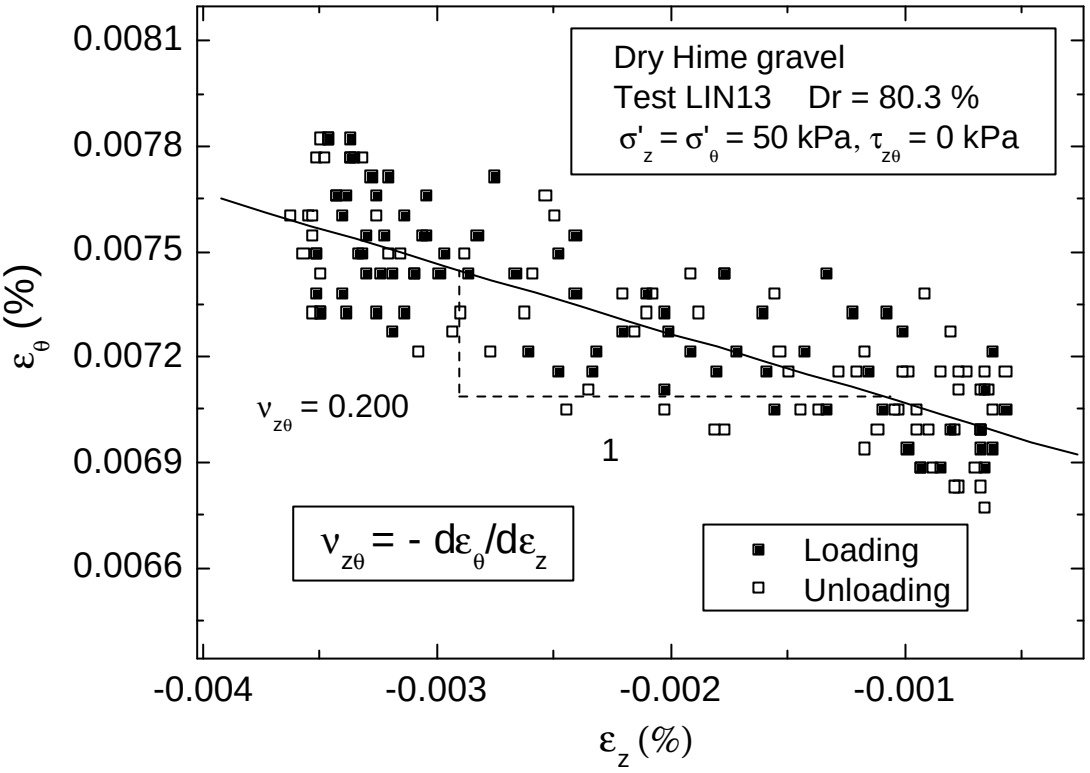

Fig. 5.7 Typical evaluation of $\nu_{z\theta}$ using modified version of PLDTs

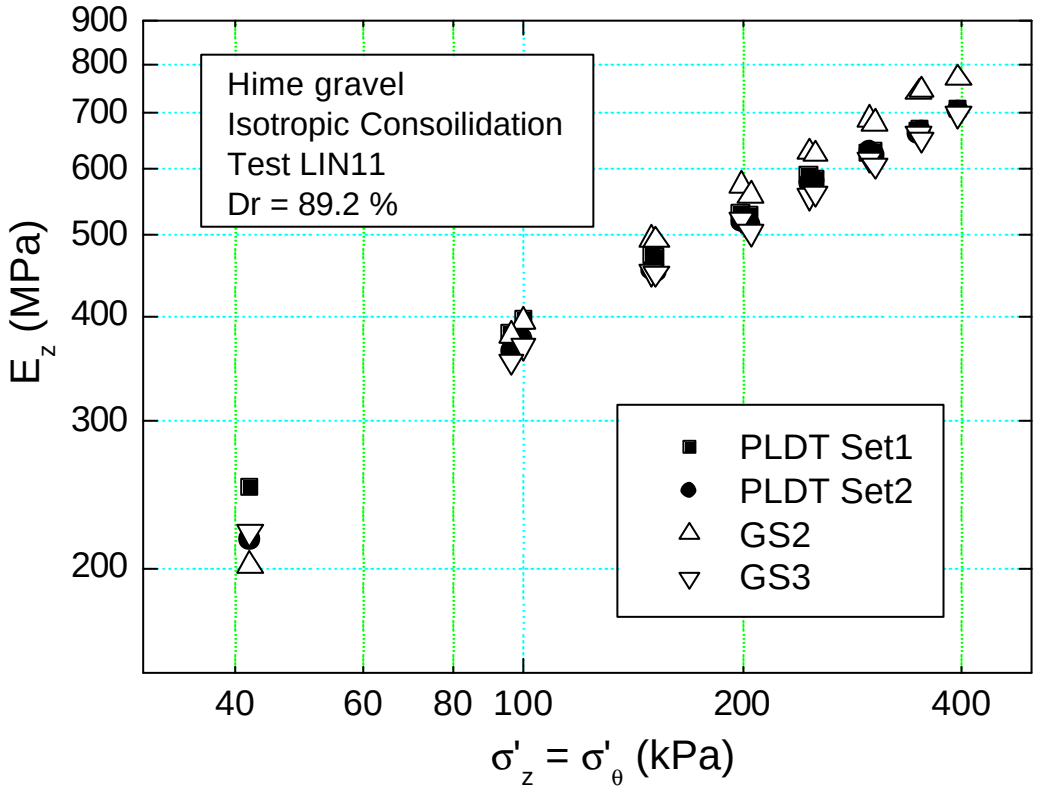

Fig. 5.8 E_z values measured using different transducers

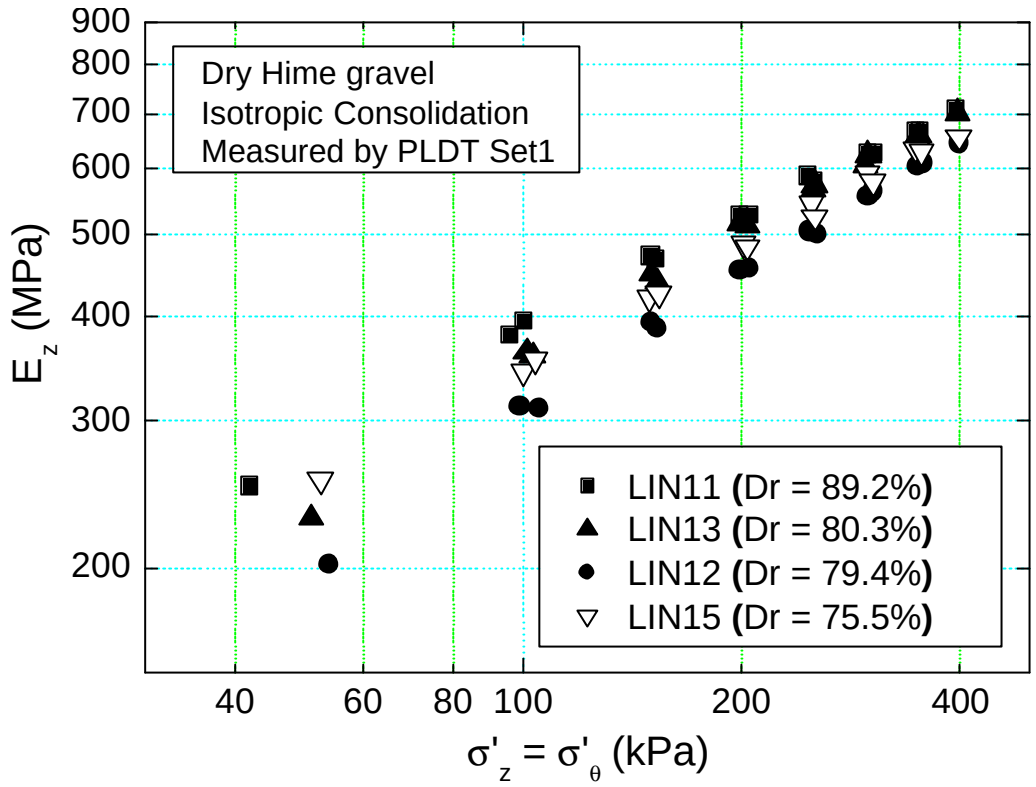

Fig. 5.9 E_z during IC measured using the modified version of PLDT Set1

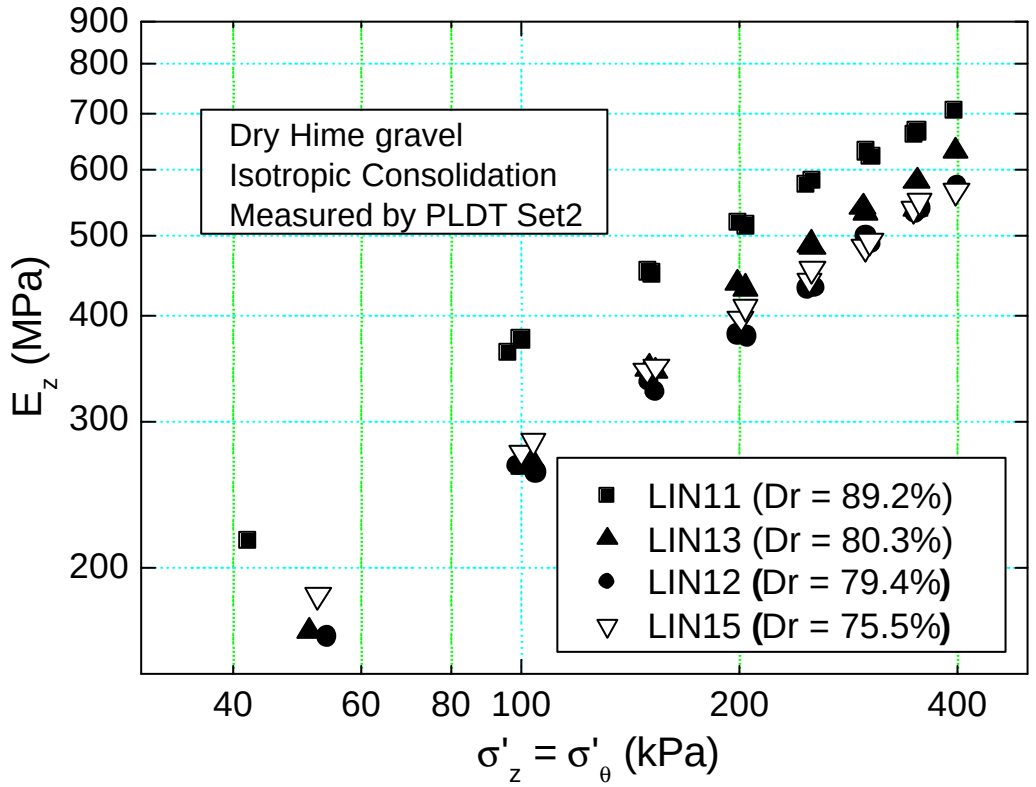

Fig. 5.10 E_z during IC measured using the modified version of PLDT Set2

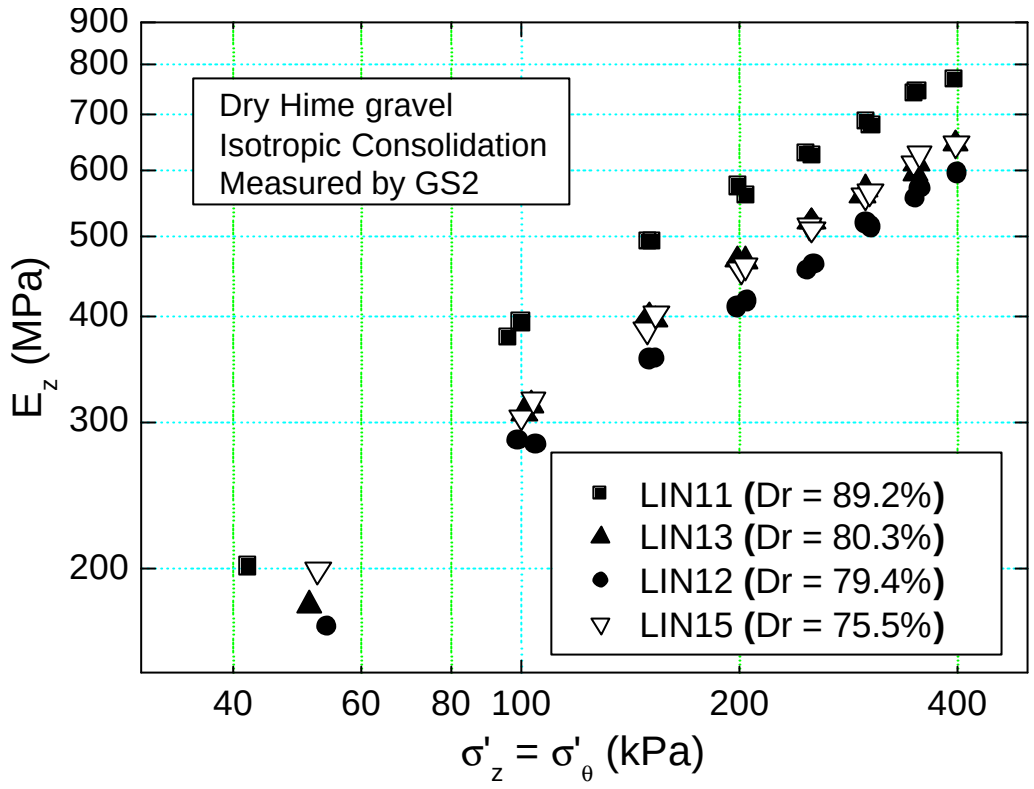

Fig. 5.11 E_z during IC measured using GS2

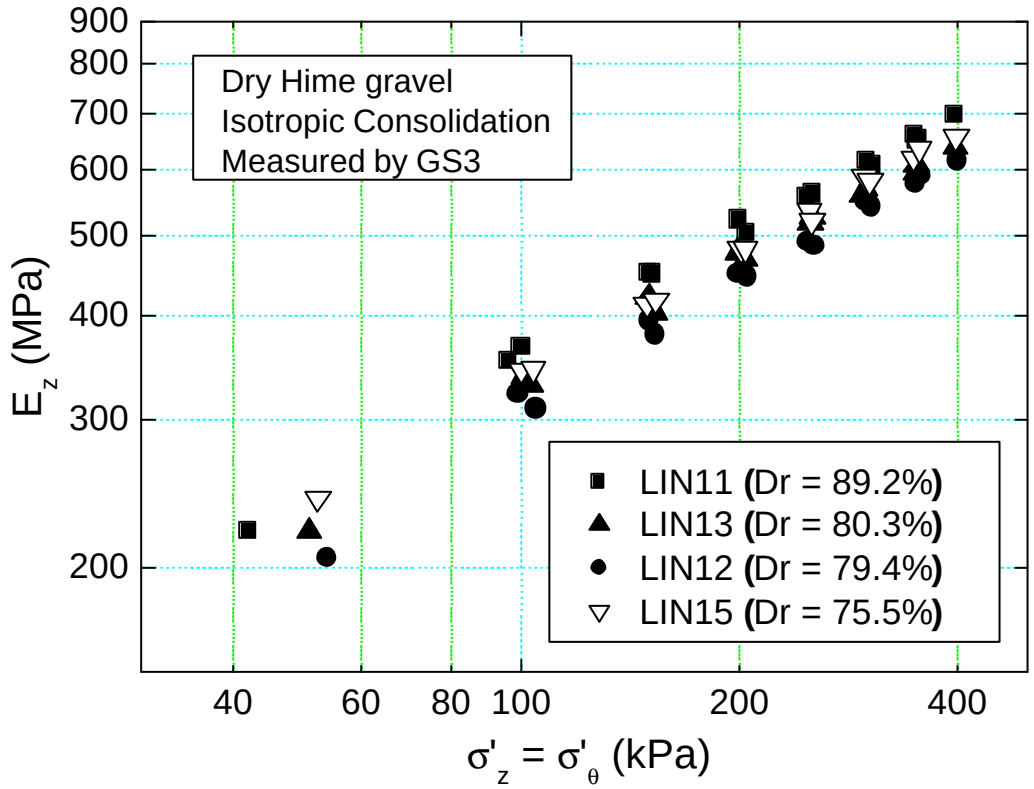

Fig. 5.12 E_z during IC measured using GS3

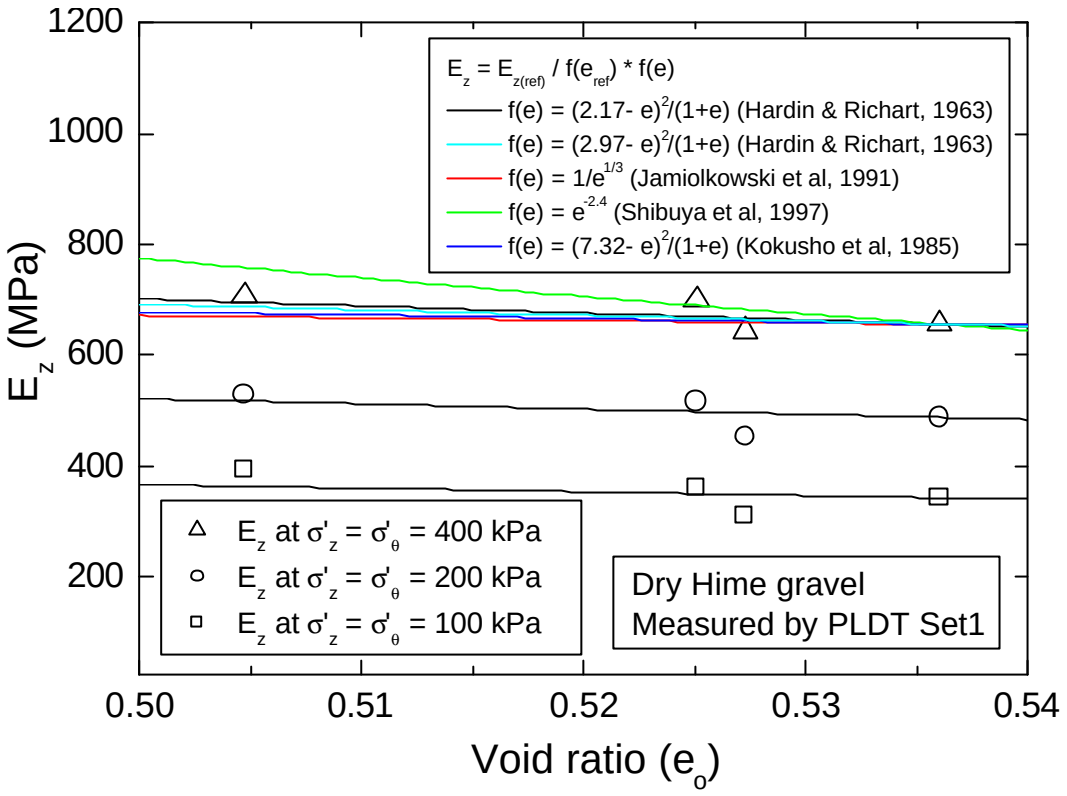

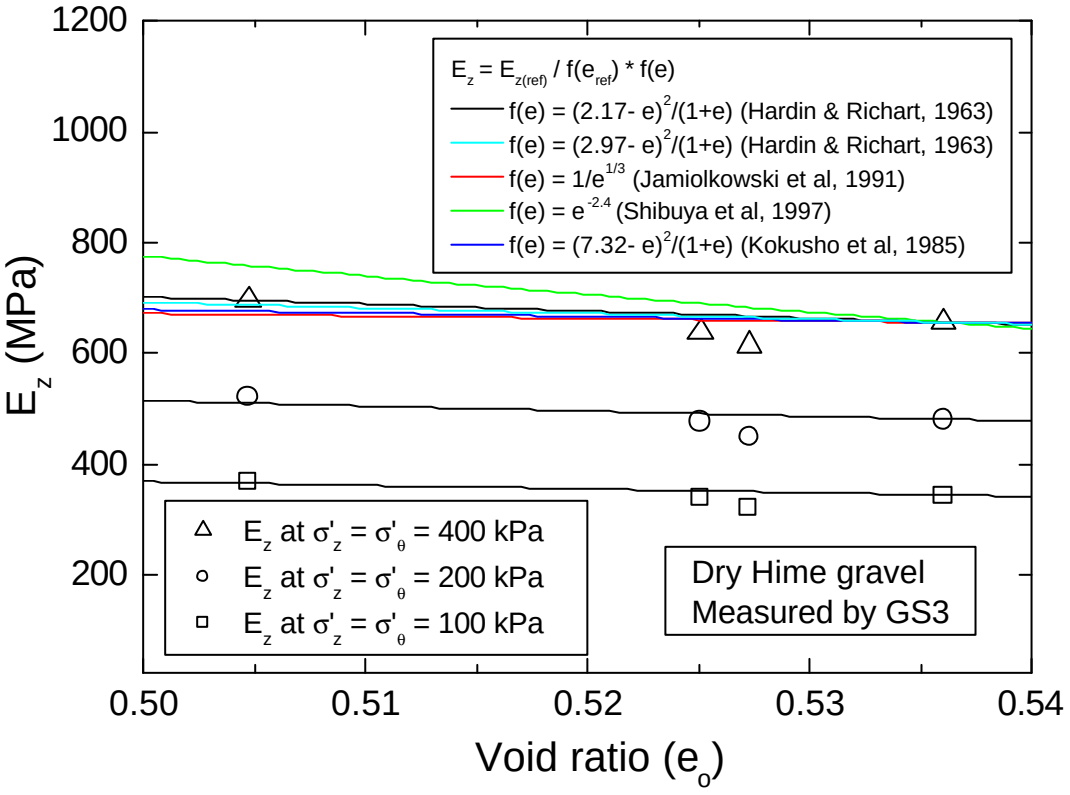

Fig. 5.13 Applicability of different void ratio functions for E_z

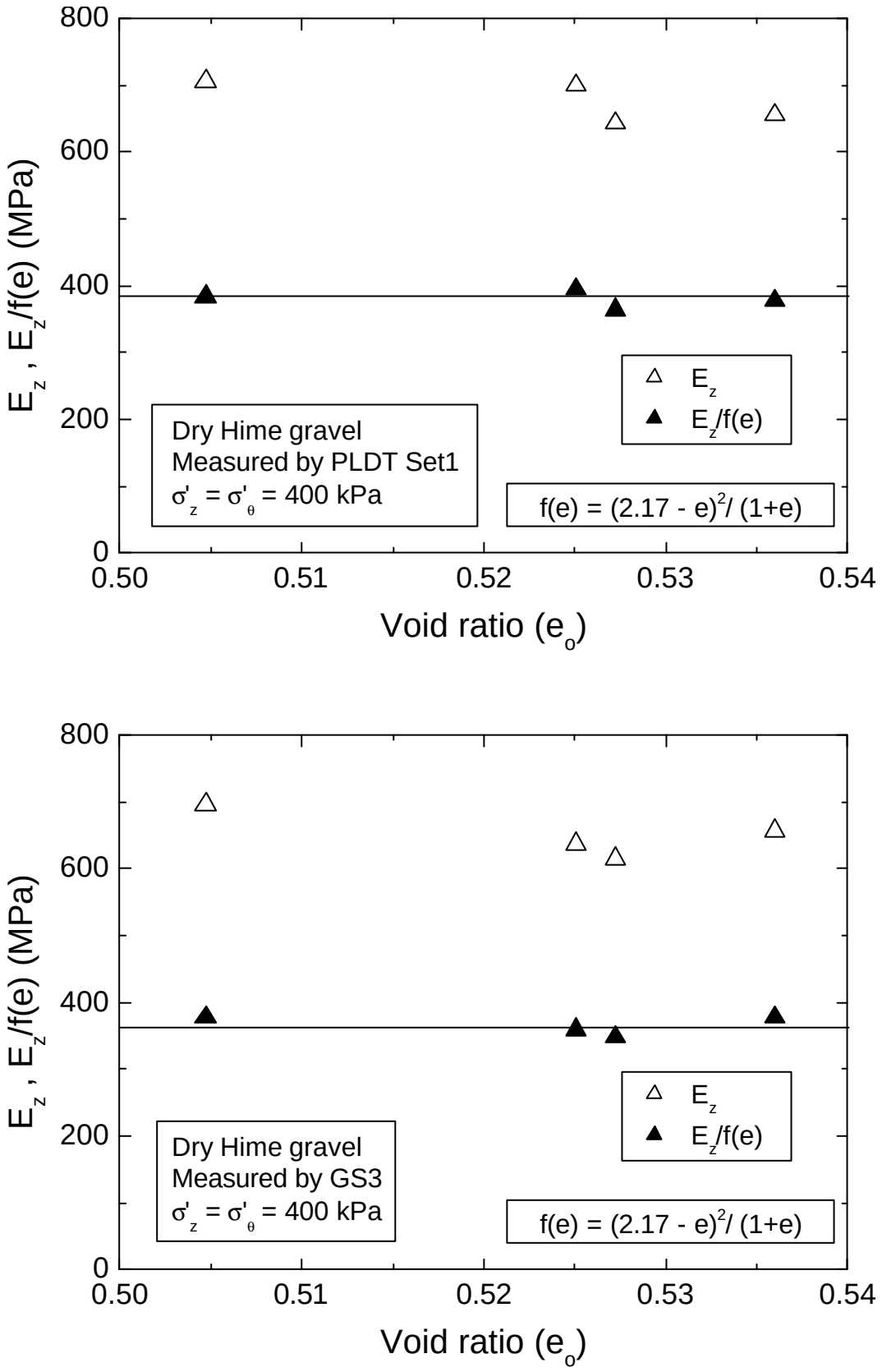

Fig. 5.14 E_z , E_z/f(e) vs initial void ratio (e_o) at a typical stress state

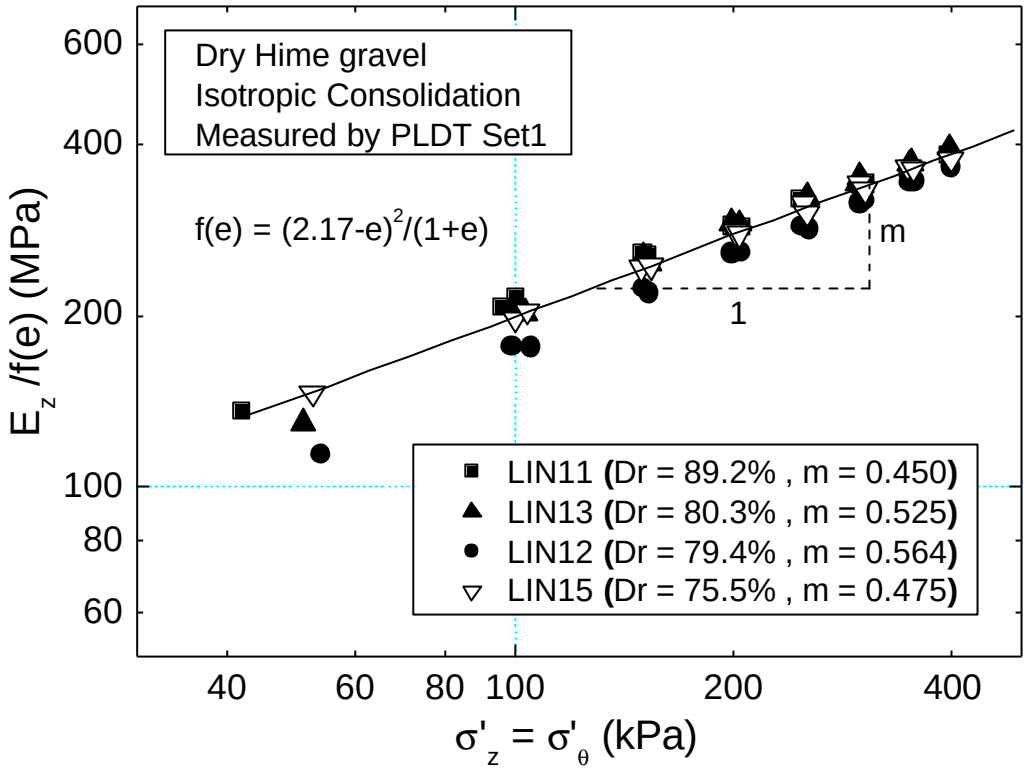

Fig. 5.15 E_z/f(e) during IC measured using PLDT Set1

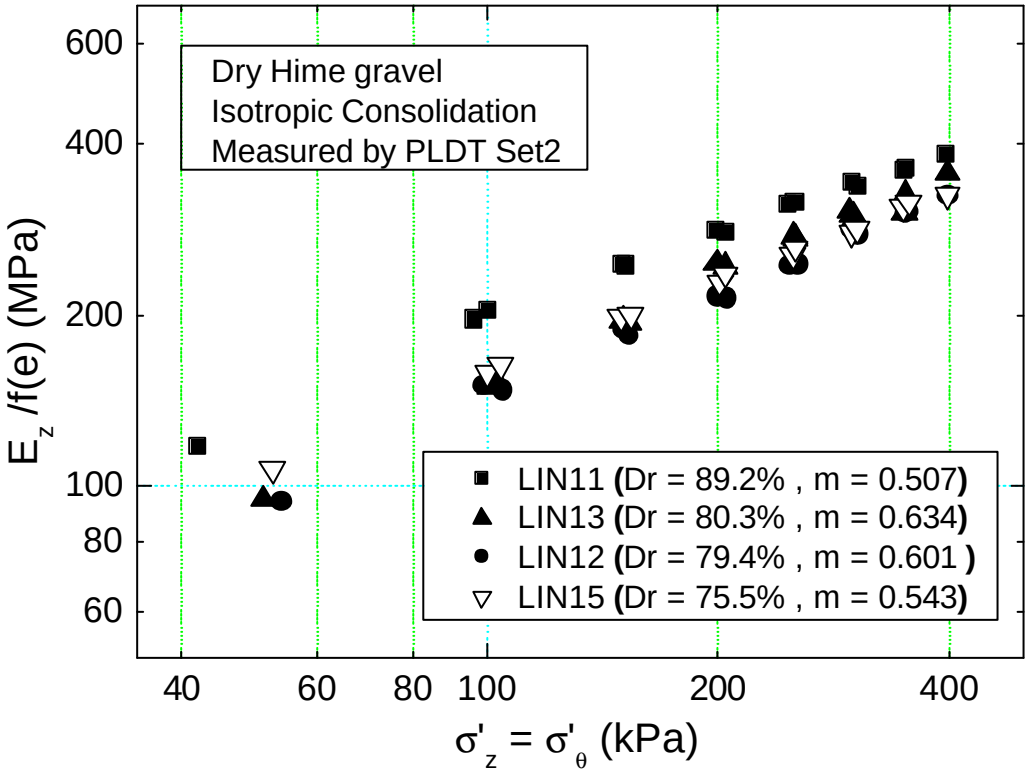

Fig. 5.16 E_z/f(e) during IC measured using PLDT Set2

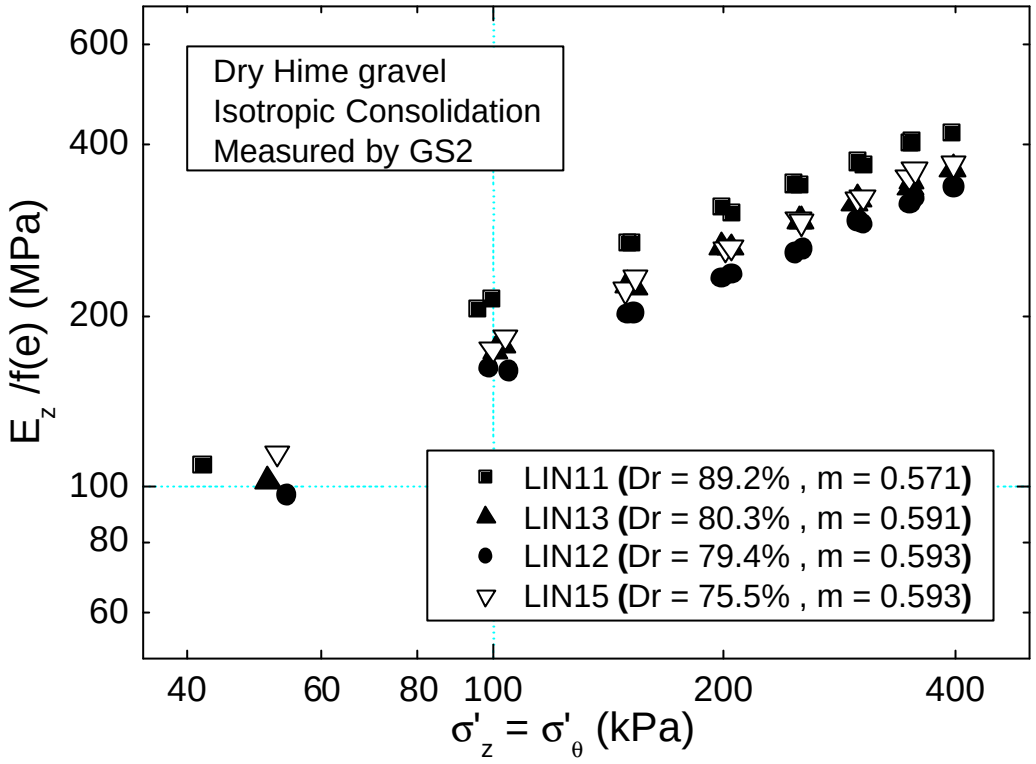

Fig. 5.17 $E_z/f(e)$ during IC measured using GS2

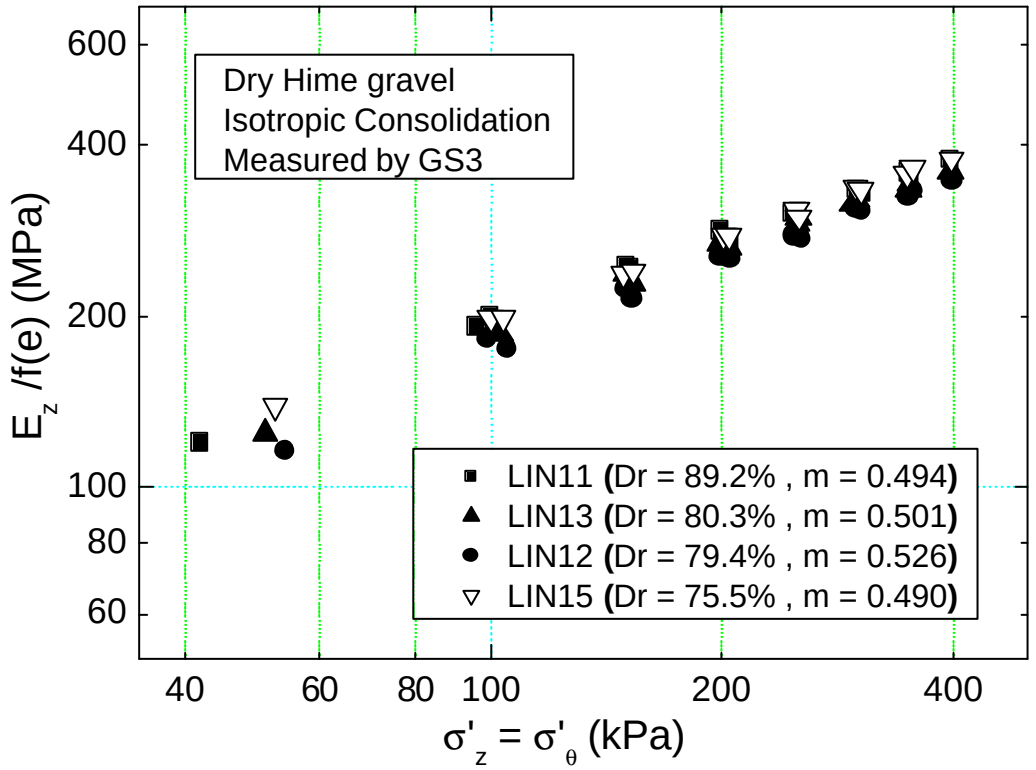

Fig. 5.18 $E_z/f(e)$ during IC measured using GS3

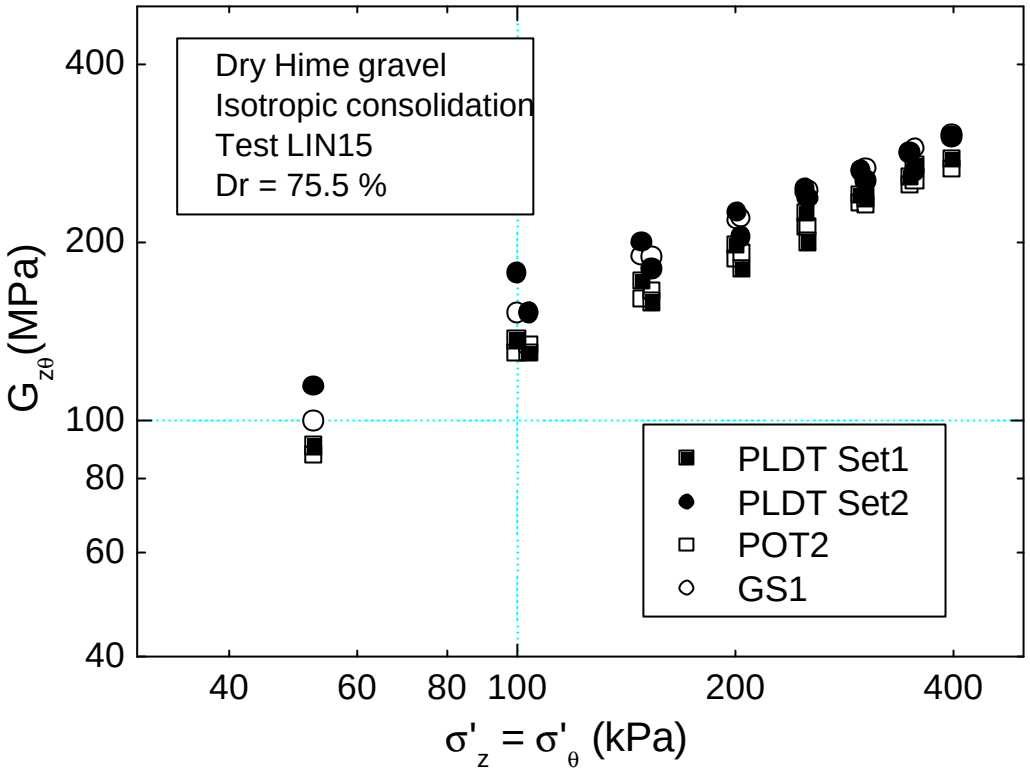

Fig. 5.19 $G_{z\theta}$ during IC measured using different transducers

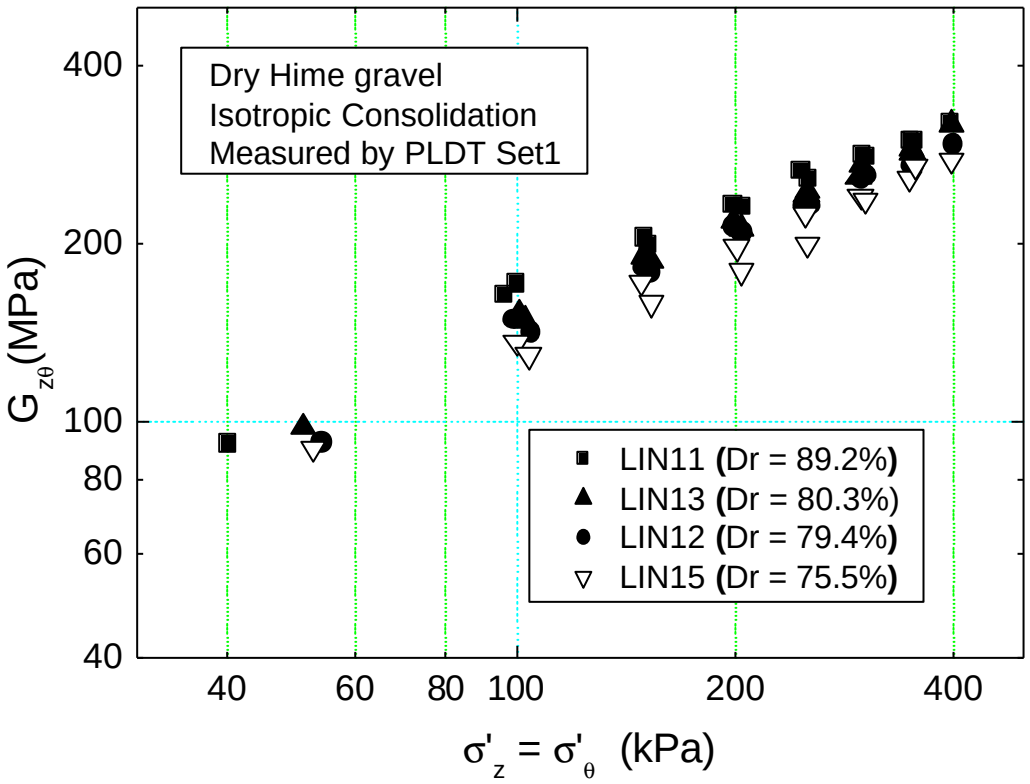

Fig. 5.20 $G_{z\theta}$ during IC measured using PLDT Set1

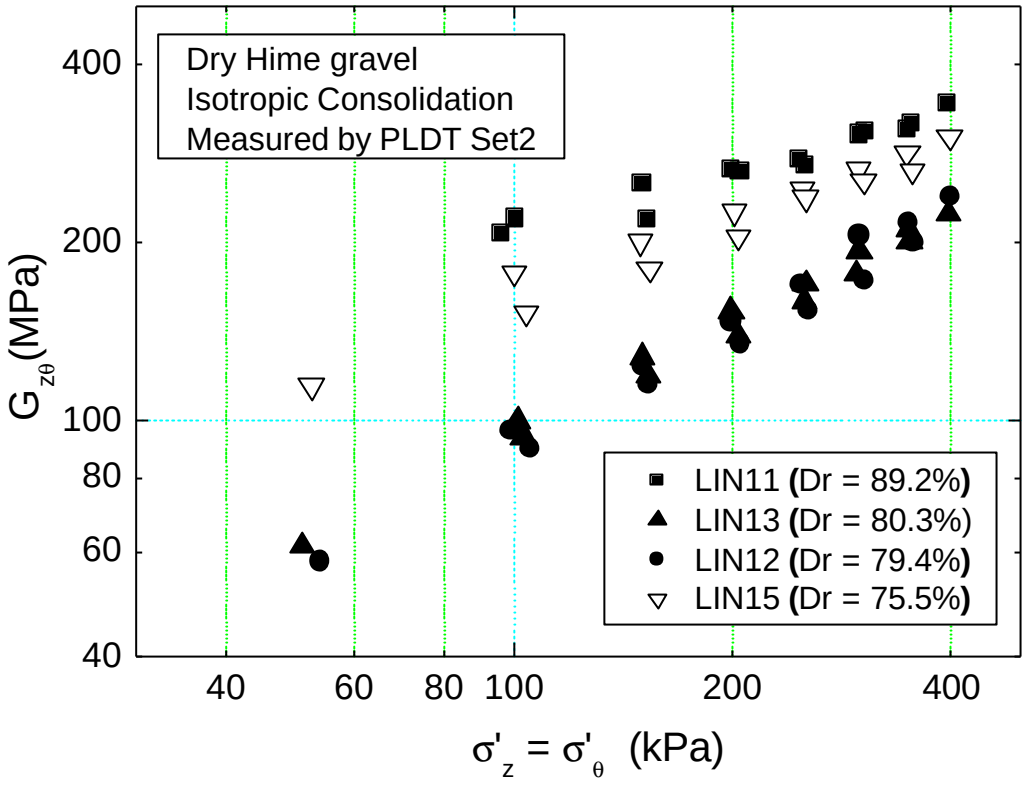

Fig. 5.21 $G_{z\theta}$ during IC measured using PLDT Set2

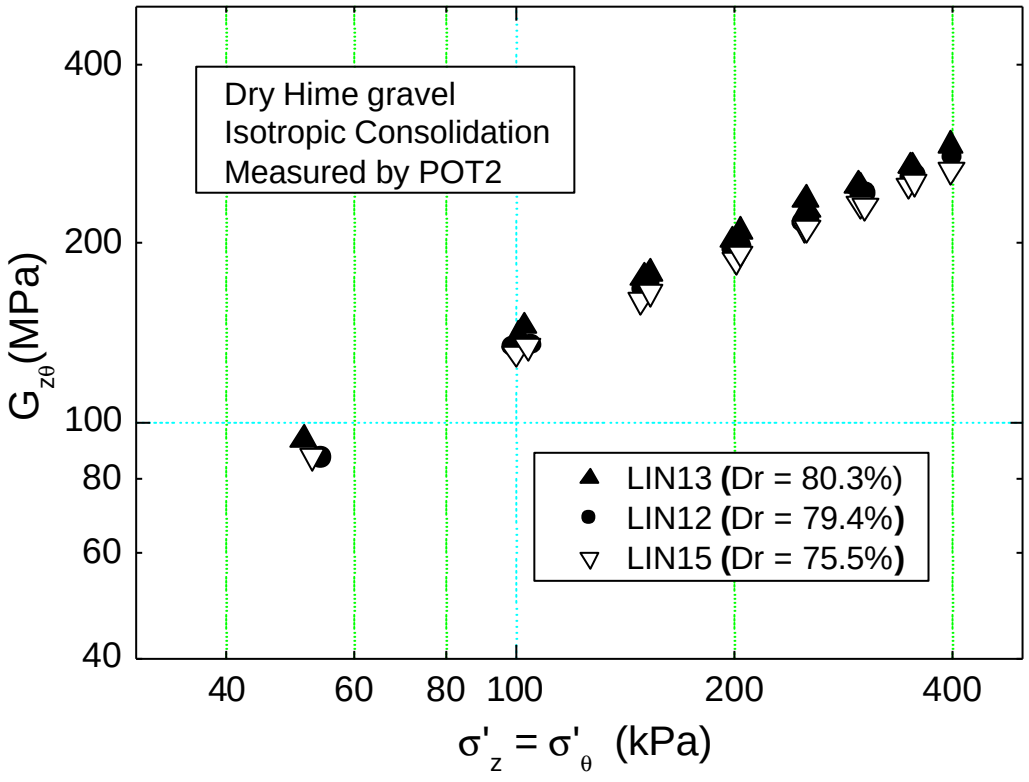

Fig. 5.22 $G_{z\theta}$ during IC measured using POT2

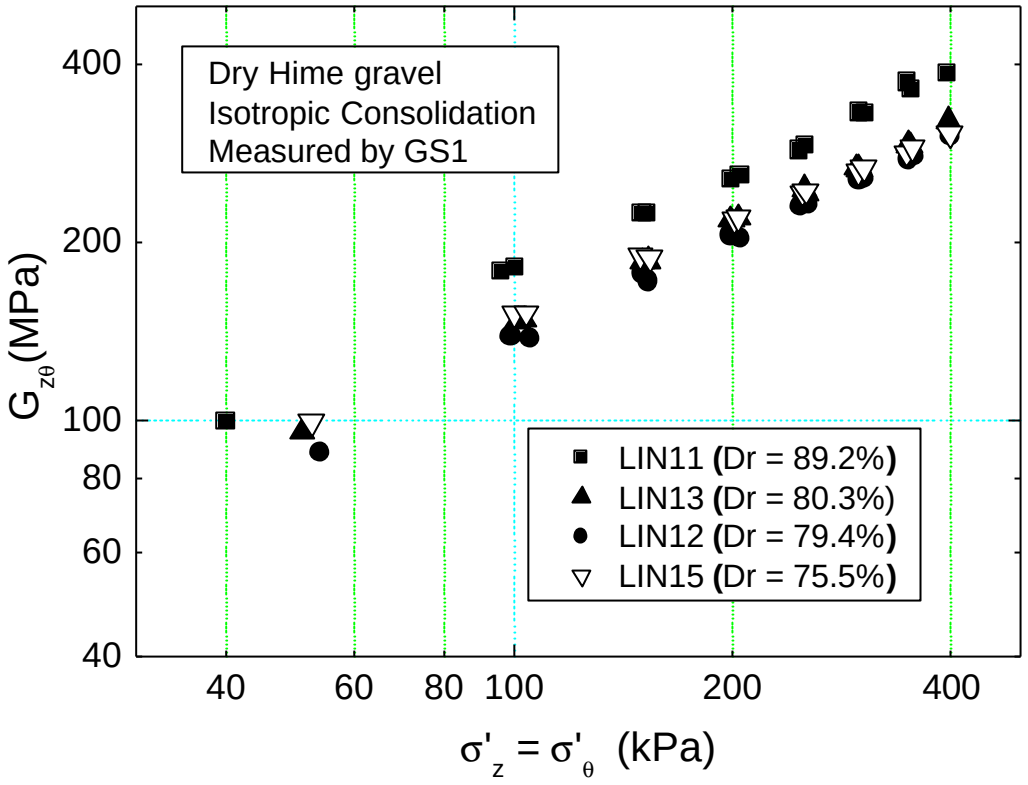

Fig. 5.23 $G_{z\theta}$ during IC measured using GS1

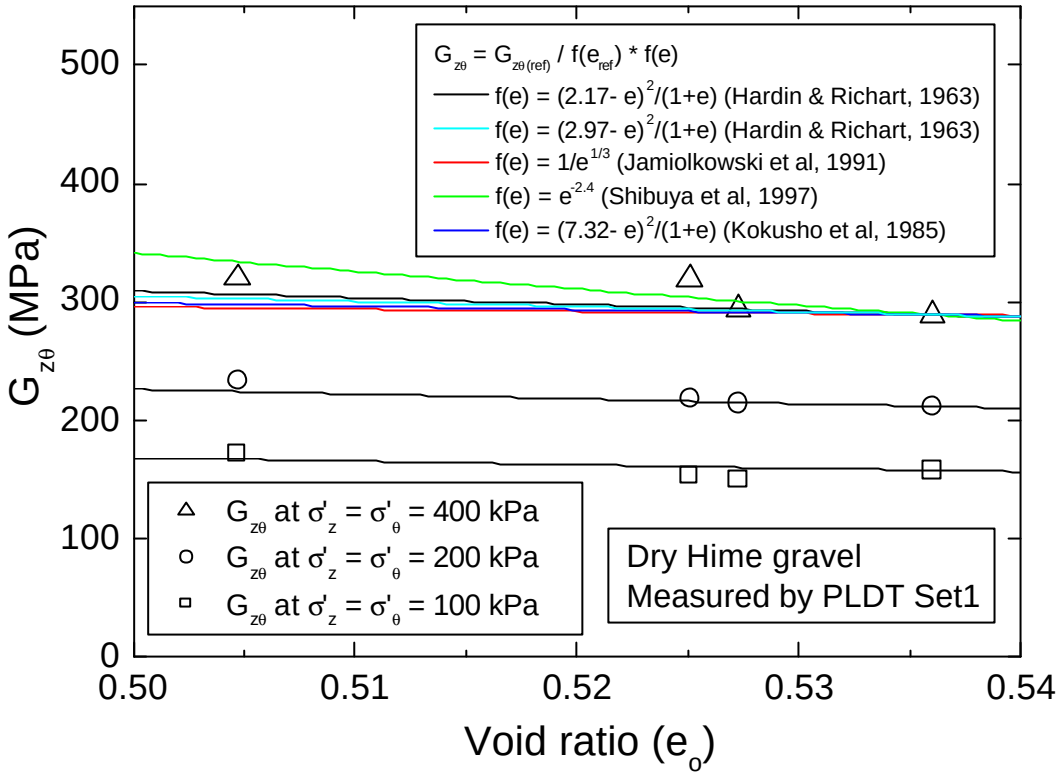

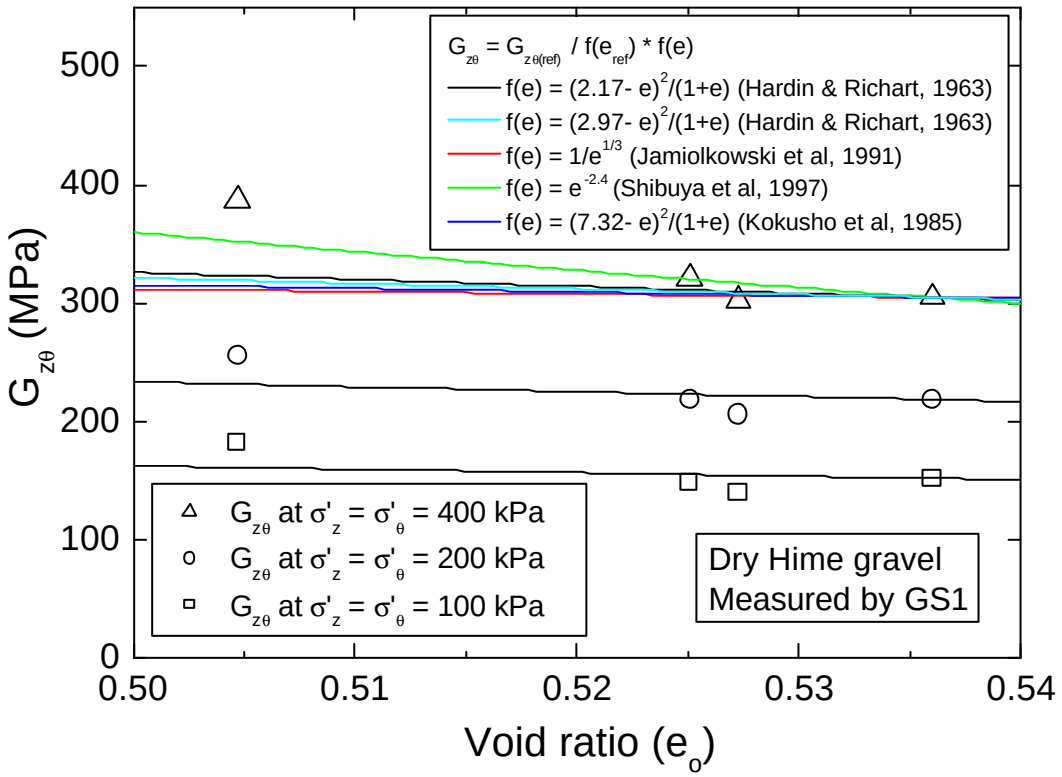

Fig. 5.23a Applicability of different void ratio functions for $G_{z\theta}$

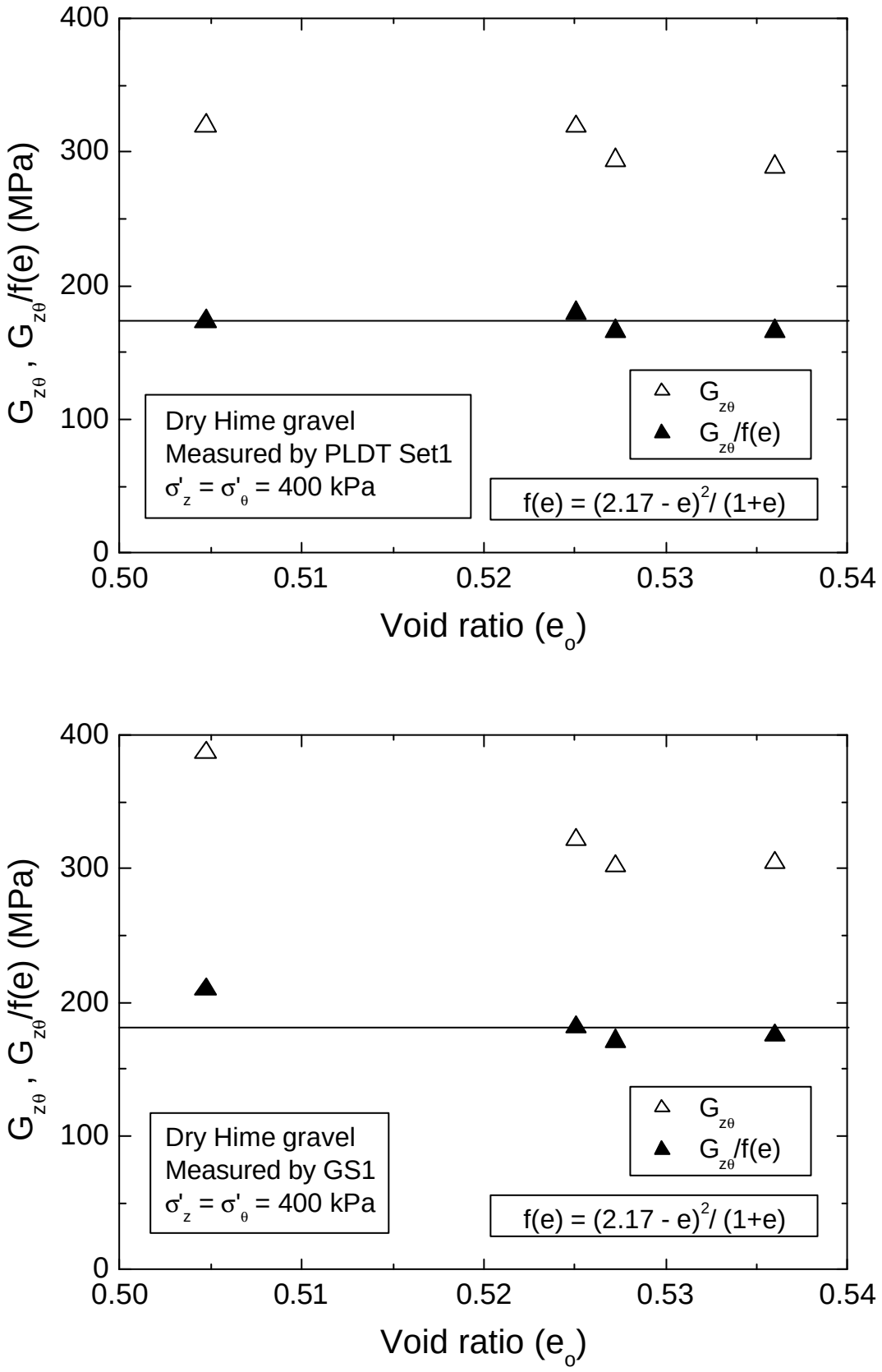

Fig. 5.23b $G_{z\theta}$, $G_{z\theta}$/f(e) vs initial void ratio (e_o) at a typical stress state

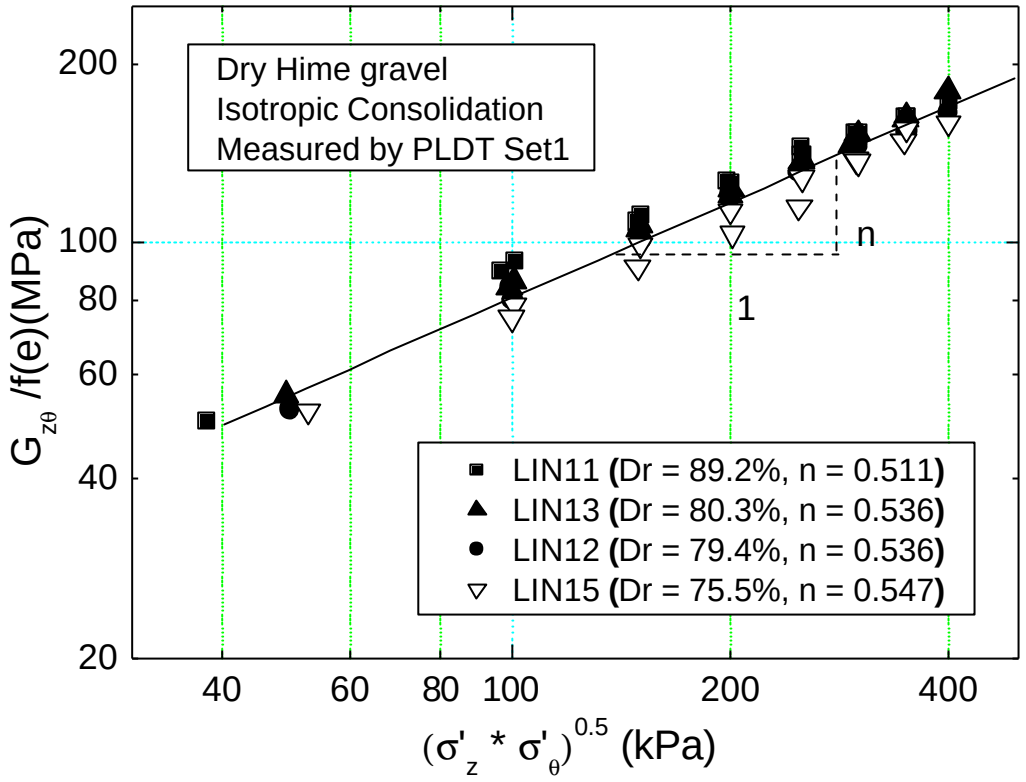

Fig. 5.24 $G_{z\theta}$/f(e) during IC measured using PLDT Set1

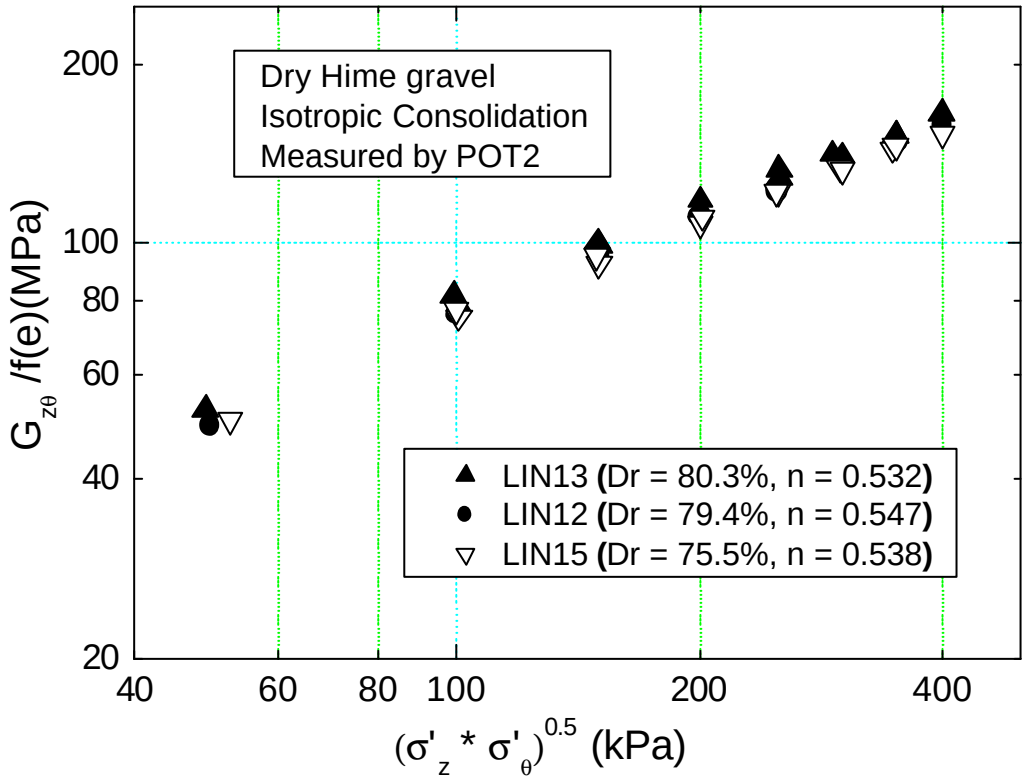

Fig. 5.25 $G_{z\theta}$/f(e) during IC measured using POT2

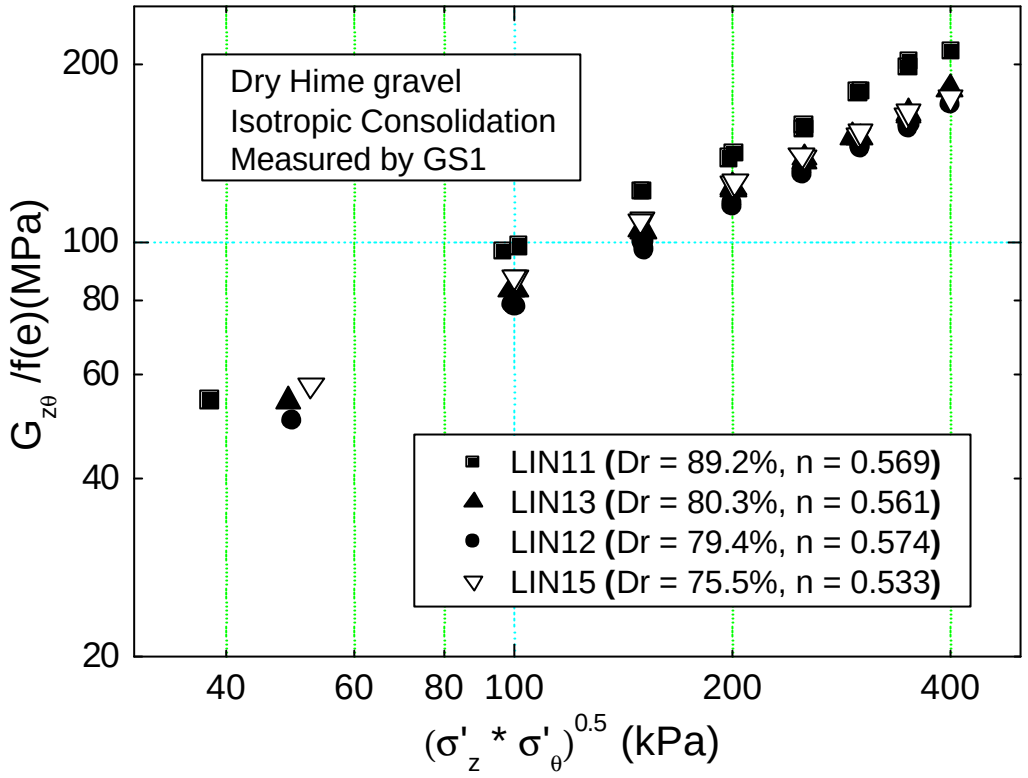

Fig. 5.26 $G_{z\theta}/f(e)$ during IC measured using GS1

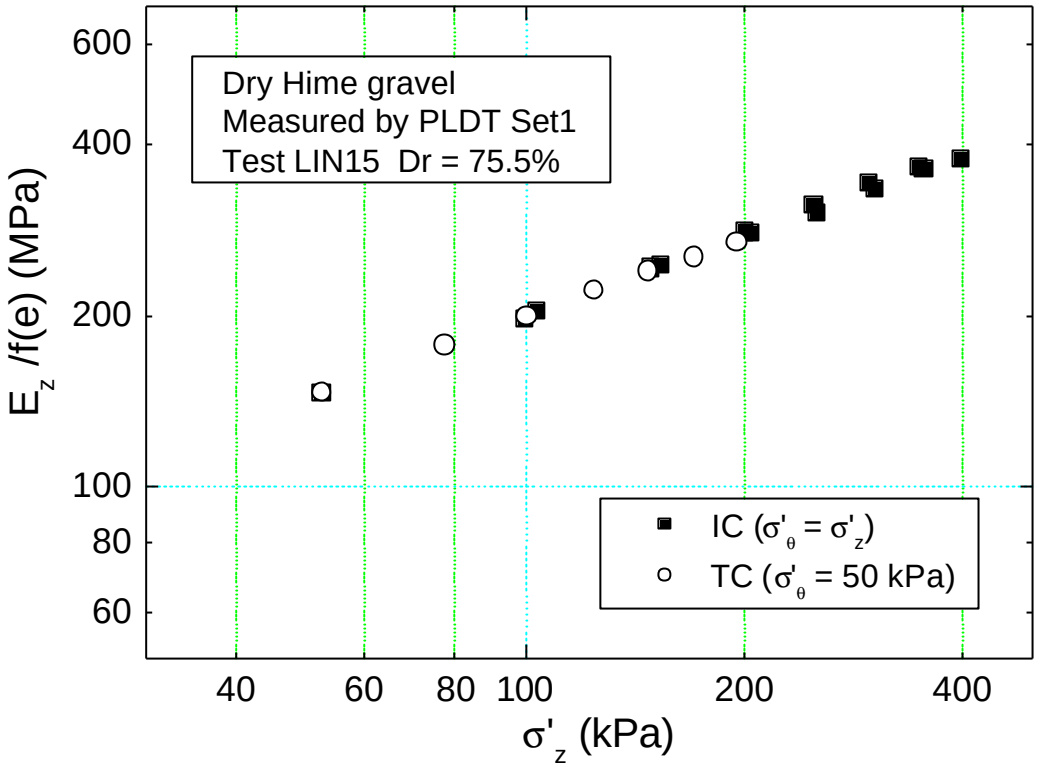

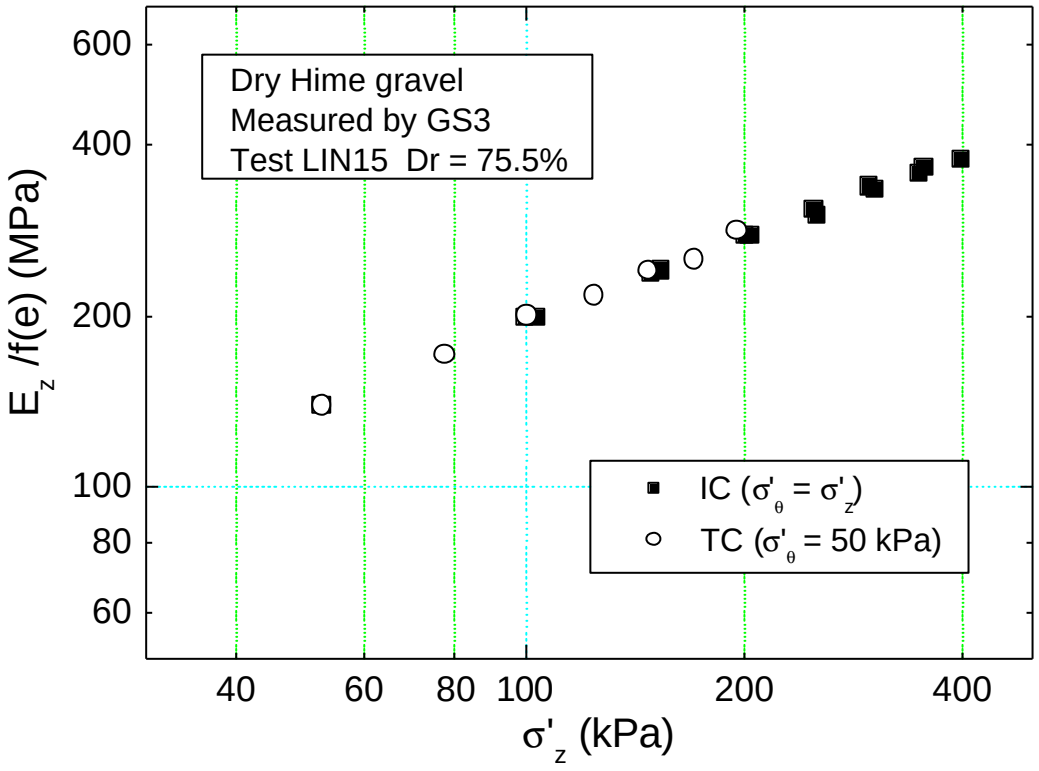

Fig. 5.27 $E_z/f(e)$ vs σ'_z during IC and TC

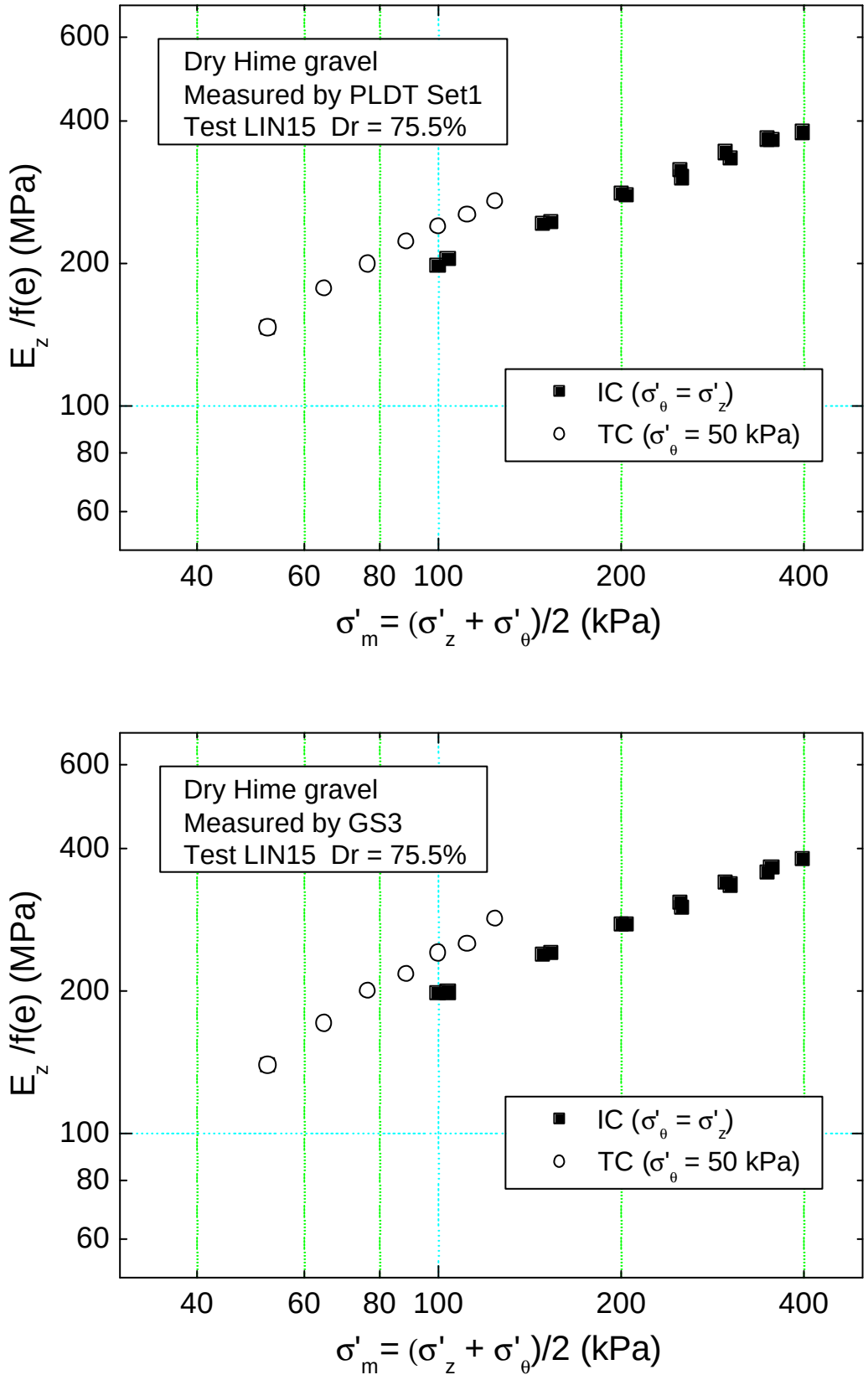

Fig. 5.28 $E_z/f(e)$ vs σ'_m during IC and TC

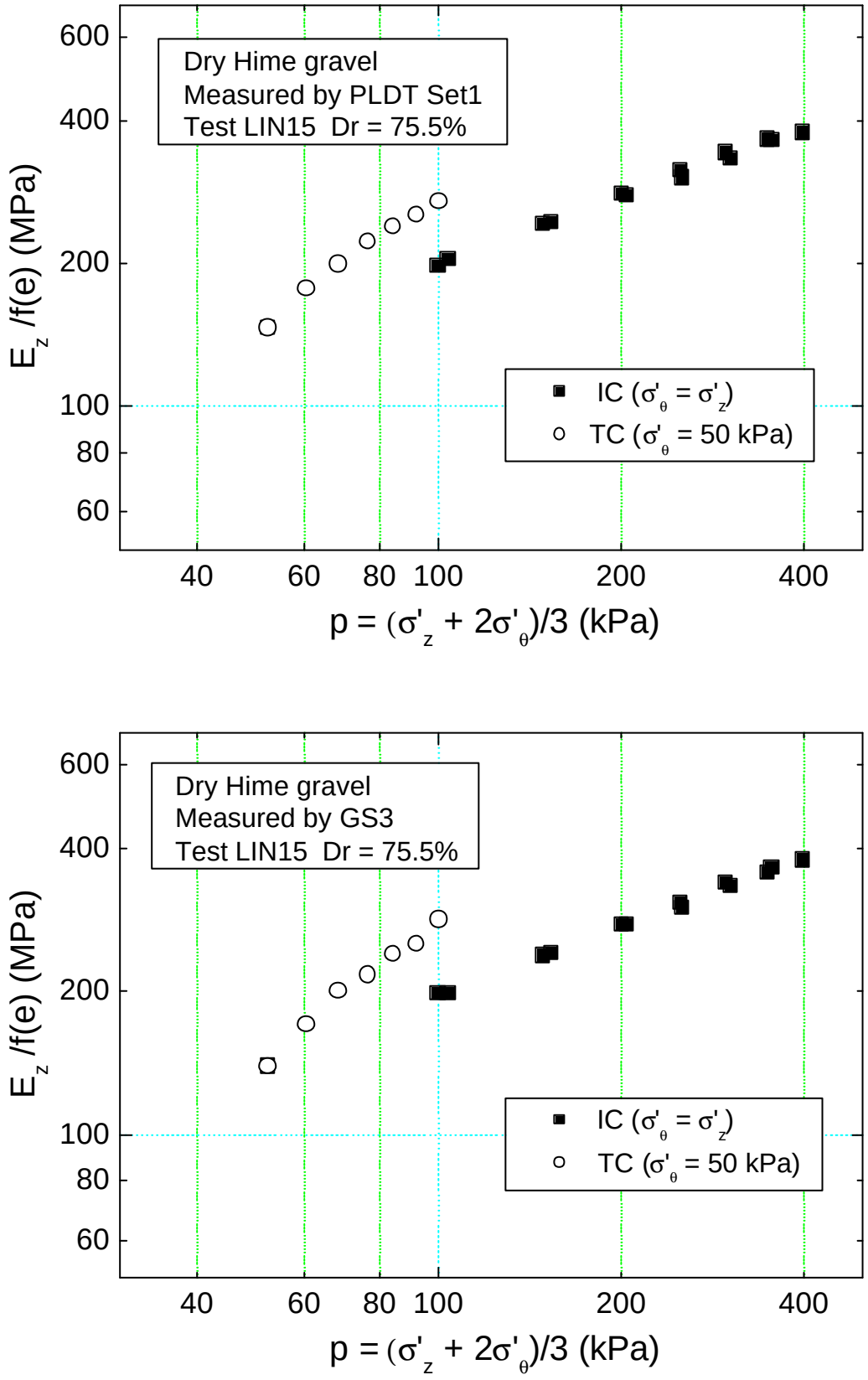

Fig. 5.29 $E_z/f(e)$ vs p during IC and TC

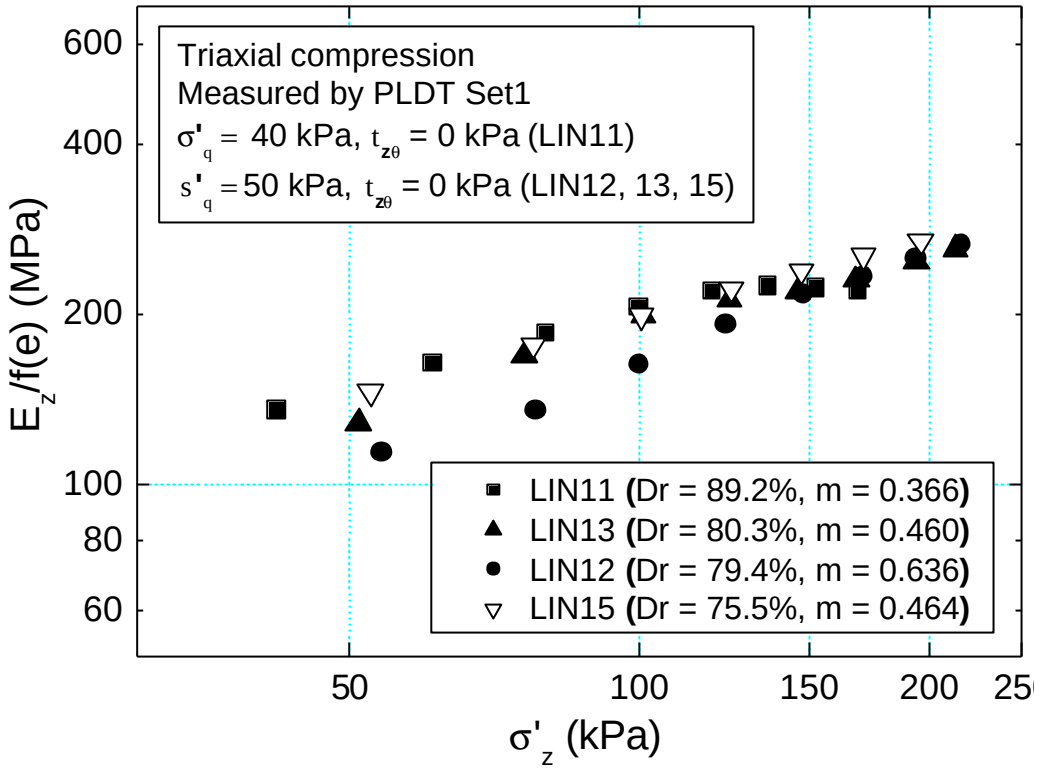

Fig. 5.30 $E_z/f(e)$ vs σ'_z during TC measured using PLDT Set1

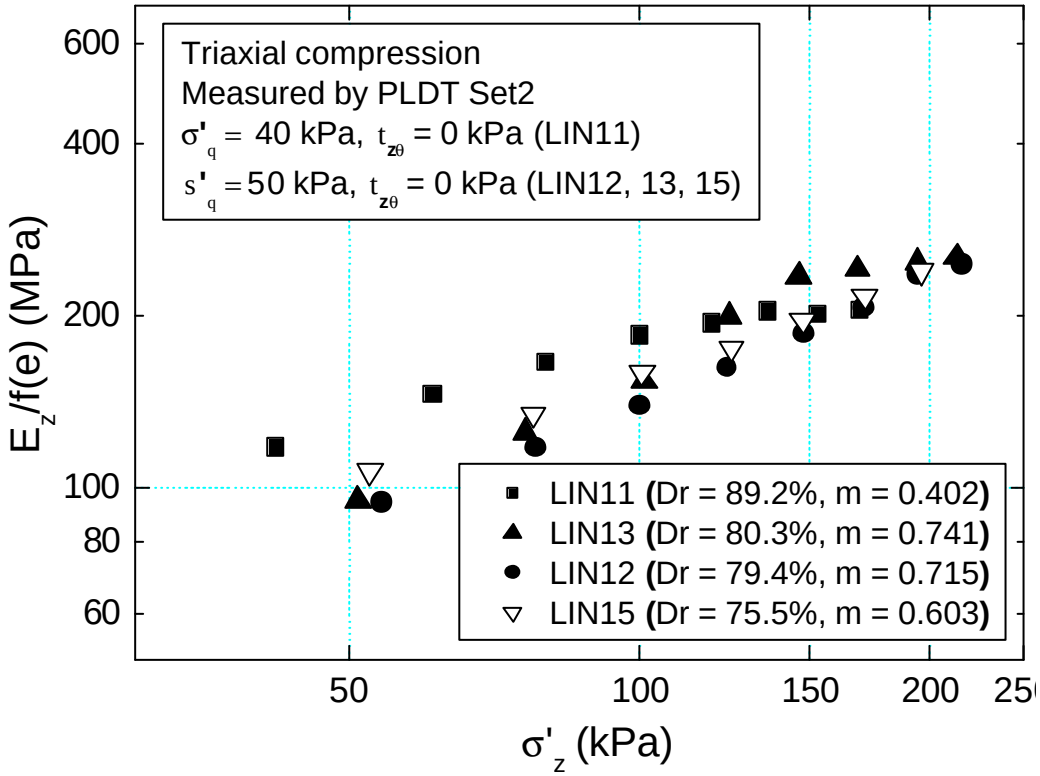

Fig. 5.31 $E_z/f(e)$ vs σ'_z during TC measured using PLDT Set2

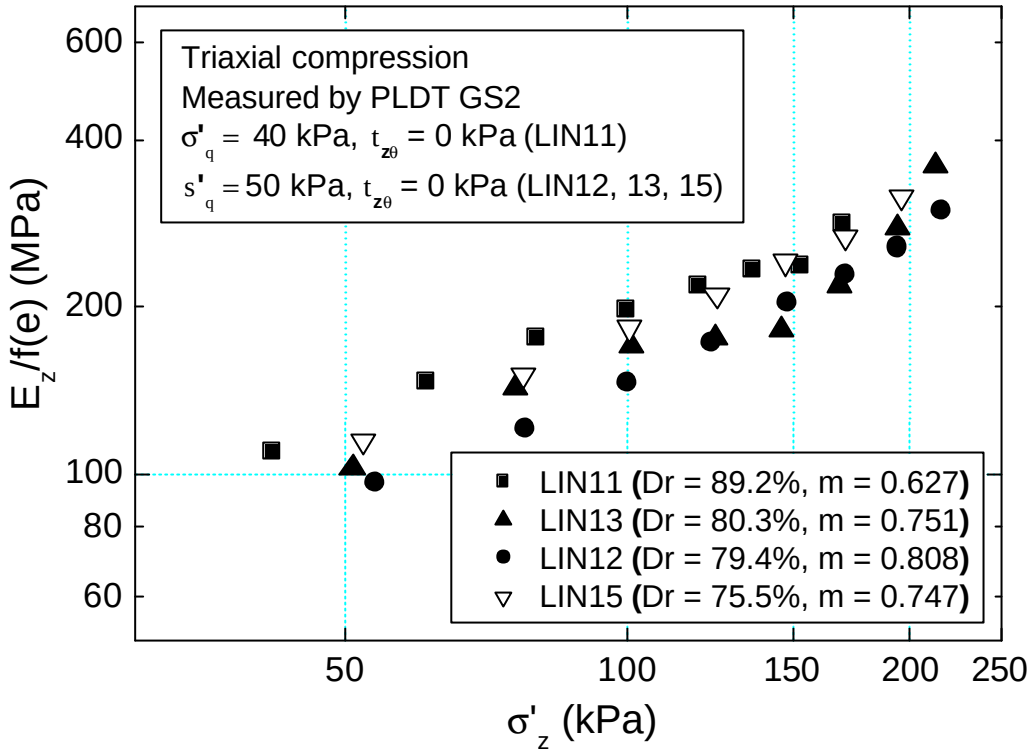

Fig. 5.32 $E_z/f(e)$ vs σ'_z during TC measured by GS2

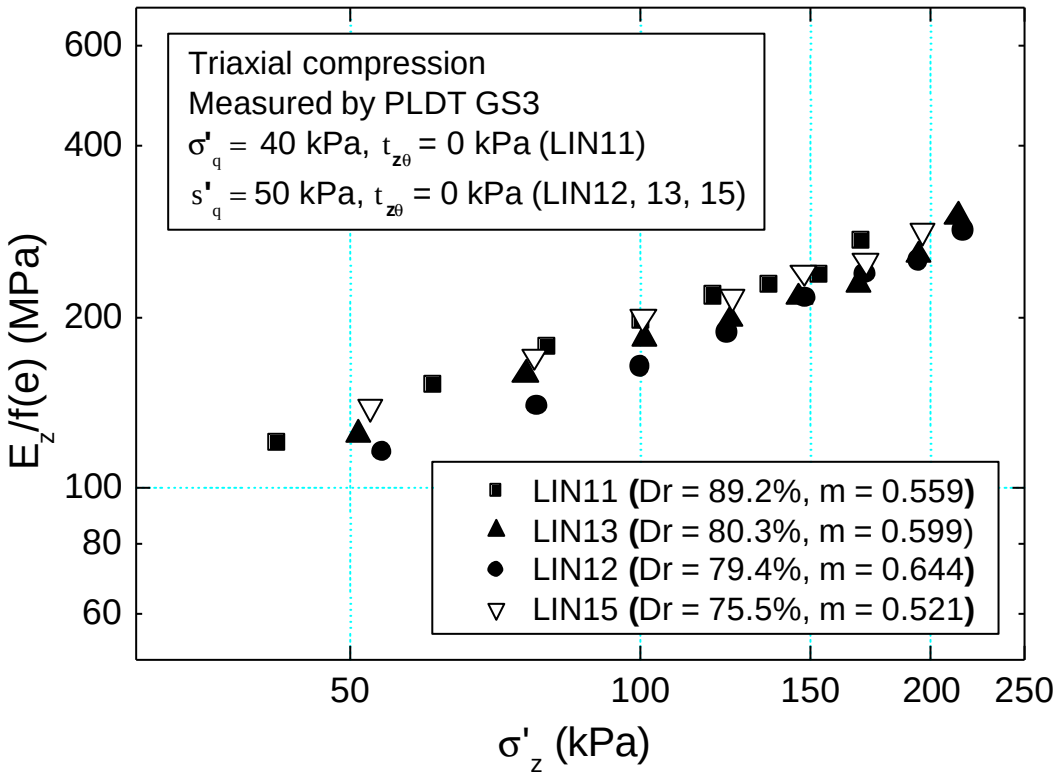

Fig. 5.33 $E_z/f(e)$ vs σ'_z during TC measured by GS3

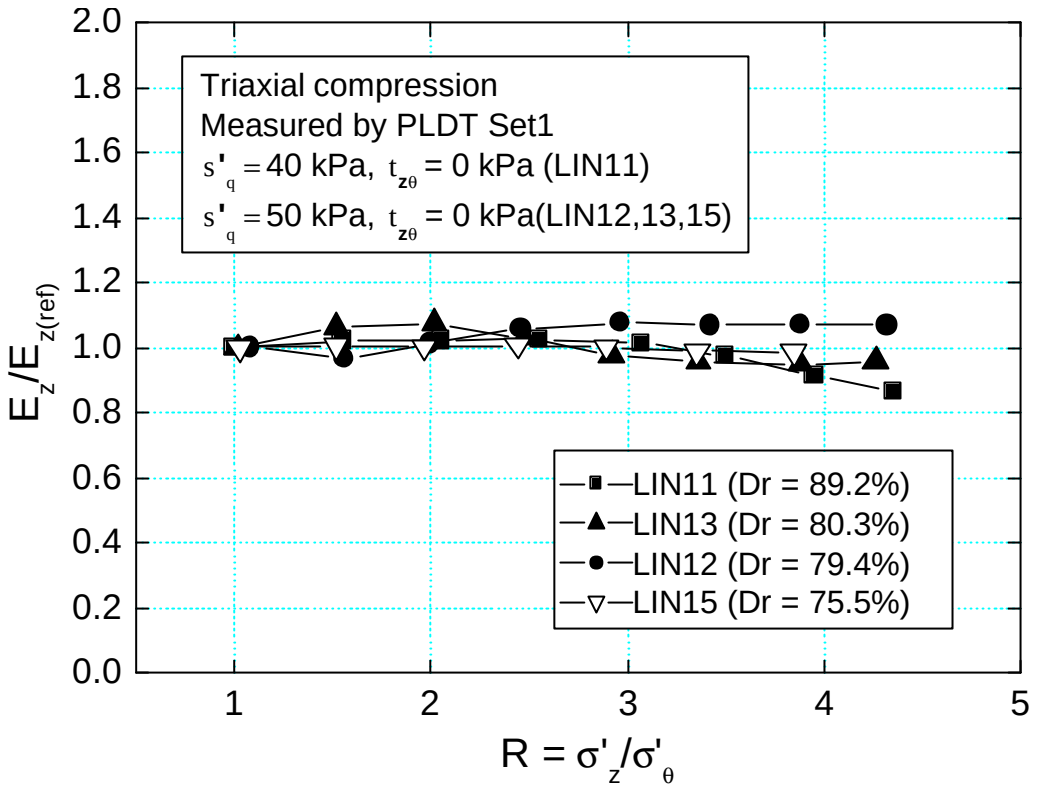

Fig. 5.34 $E_z/E_{z(ref)}$ vs R during TC measured using PLDT Set1

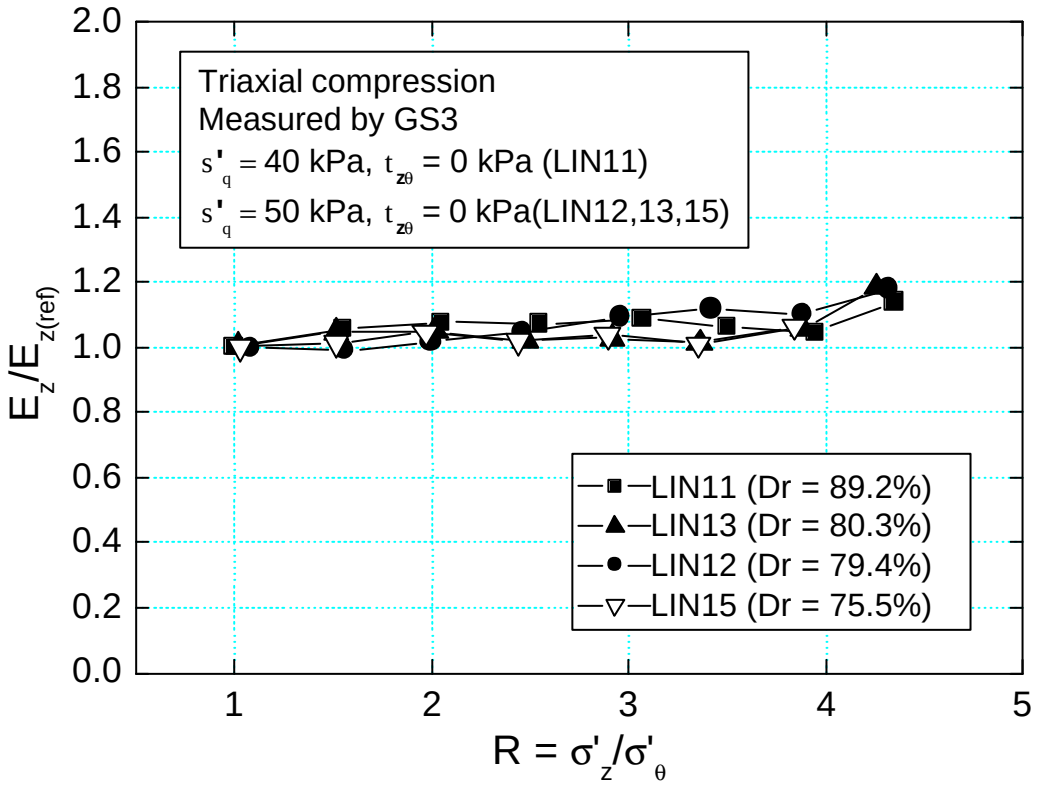

Fig. 5.35 $E_z/E_{z(ref)}$ vs R during TC measured using GS3

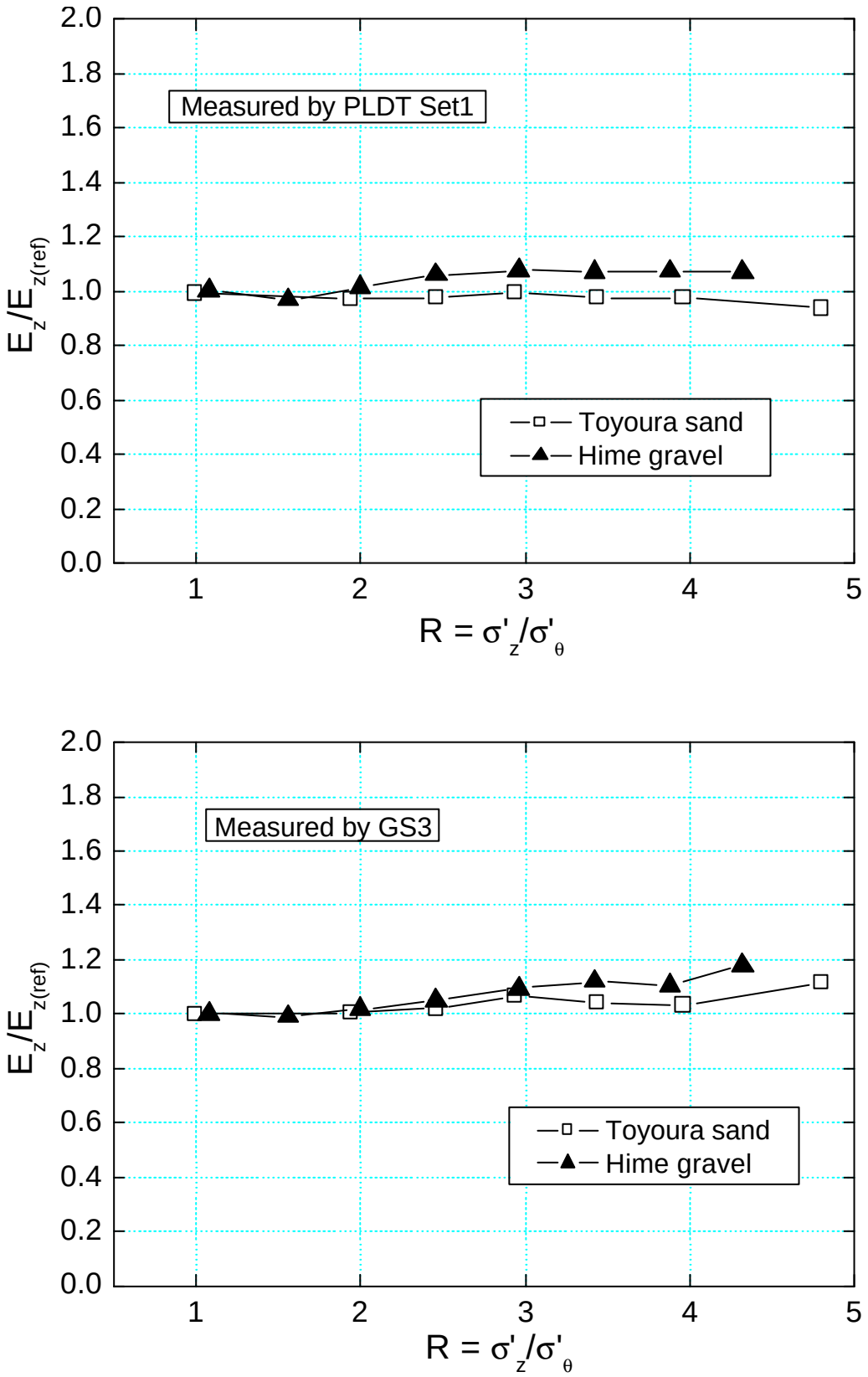

Fig. 5.36 Comparison of $E_z/E_{z(ref)}$ vs R between Toyoura sand and Hime gravel

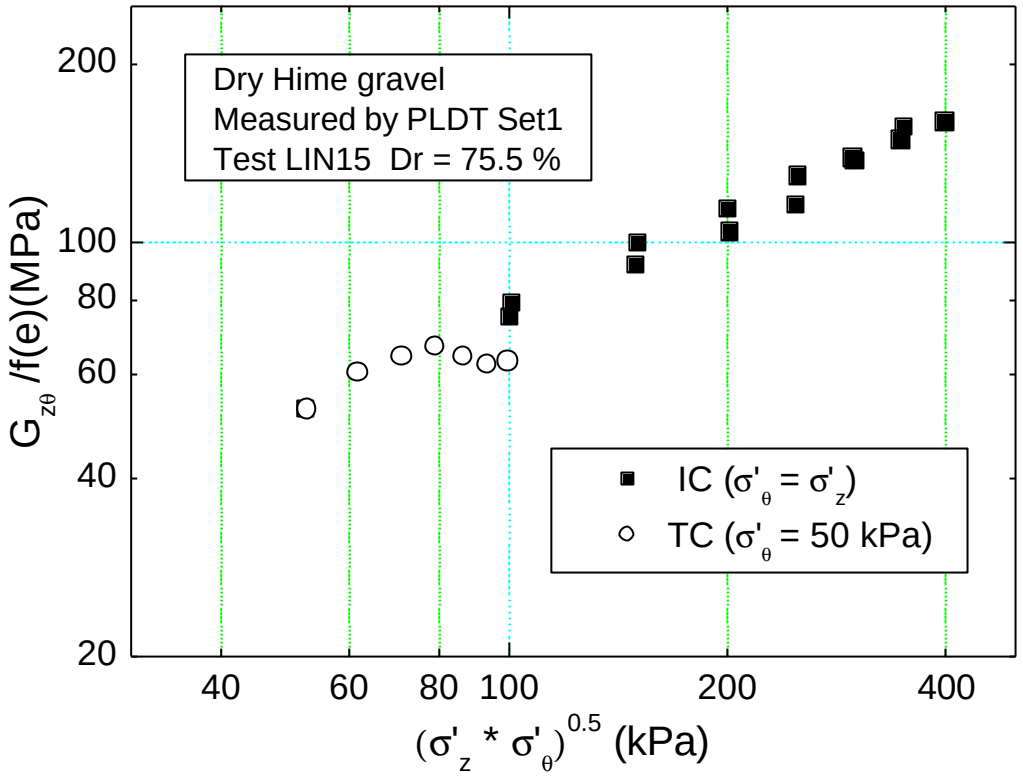

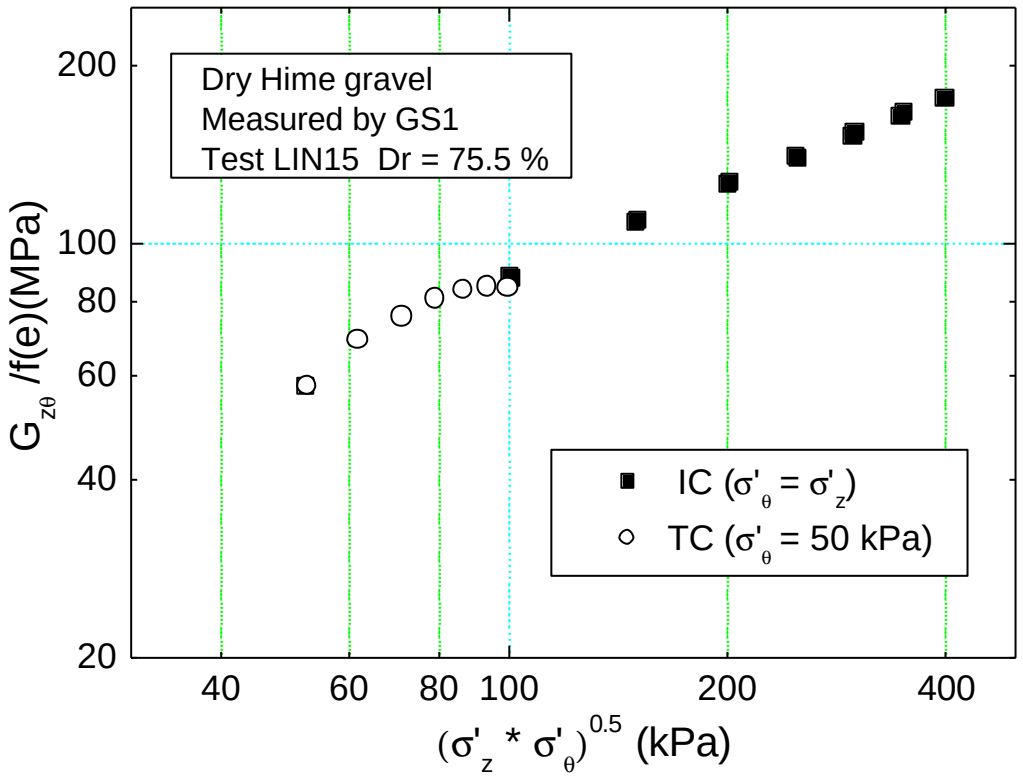

Fig. 5.37 $G_{z\theta}/f(e)$ vs $(\sigma'_z * \sigma'_\theta)^{0.5}$ during IC and TC

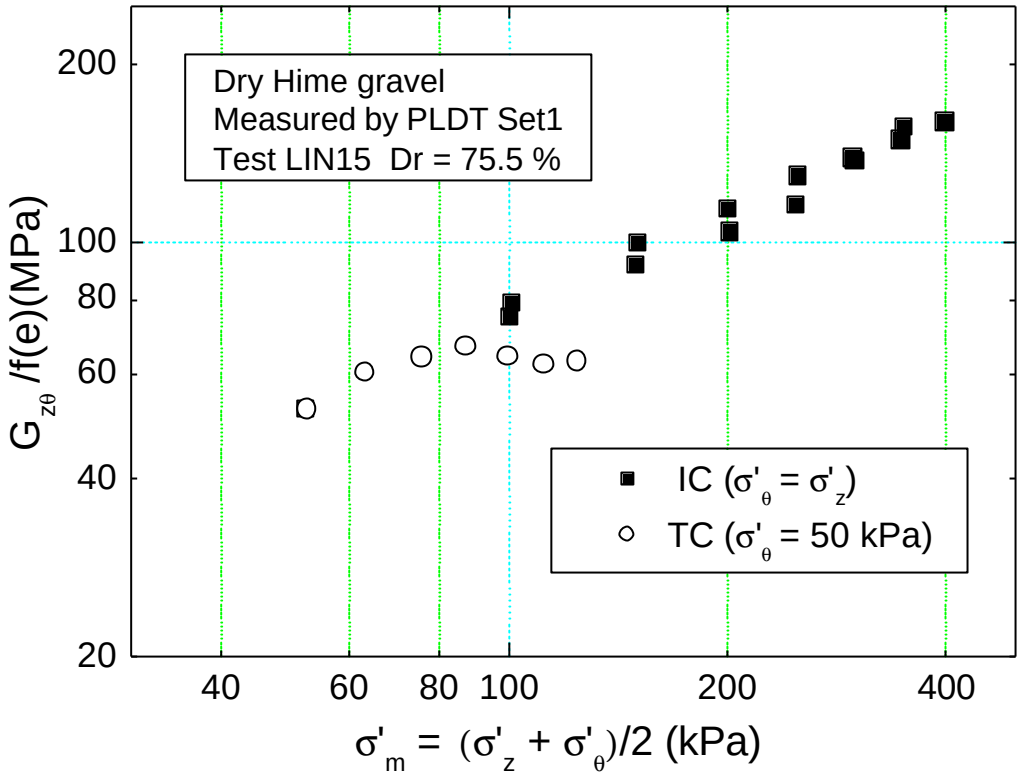

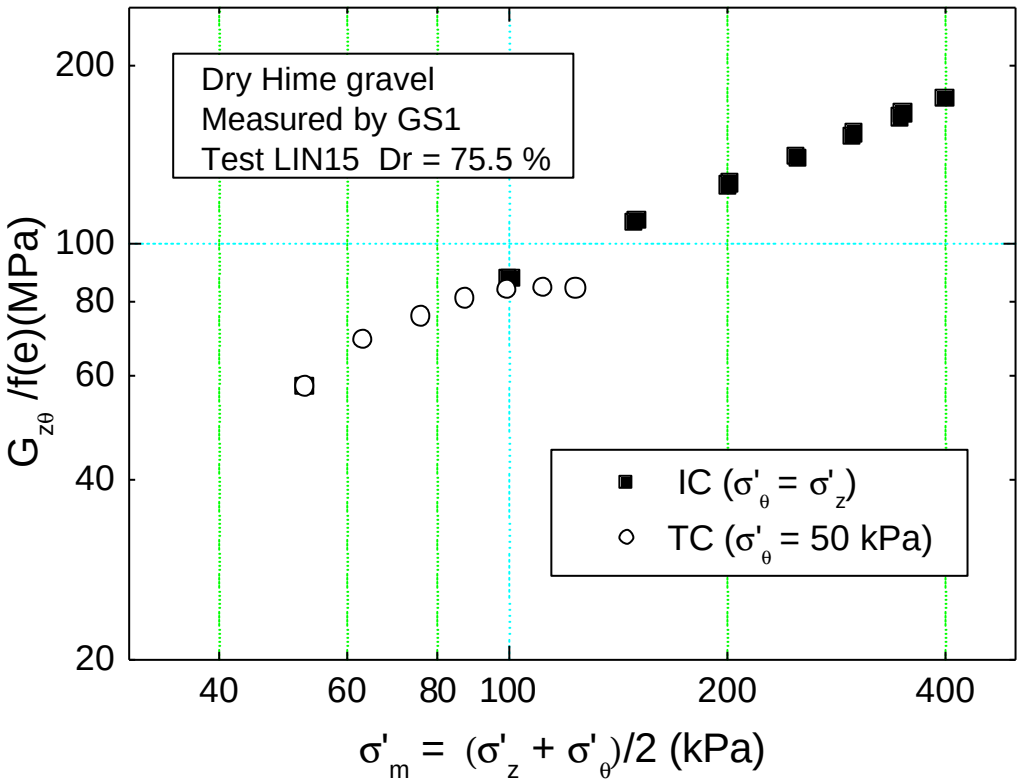

Fig. 5.38 $G_{z\theta}/f(e)$ vs σ'_m during IC and TC

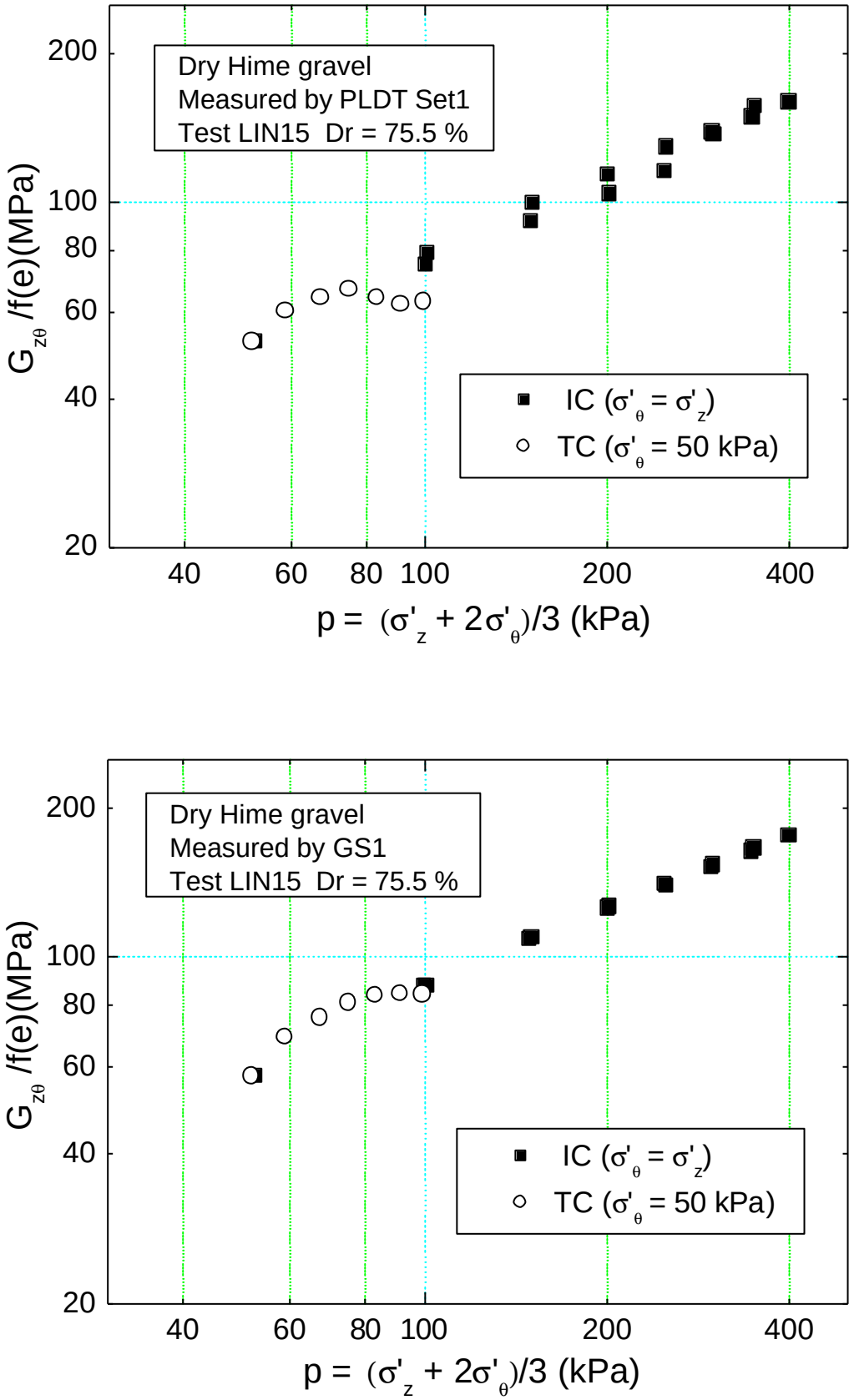

Fig. 5.39 $G_{z\theta}/f(e)$ vs p during IC and TC

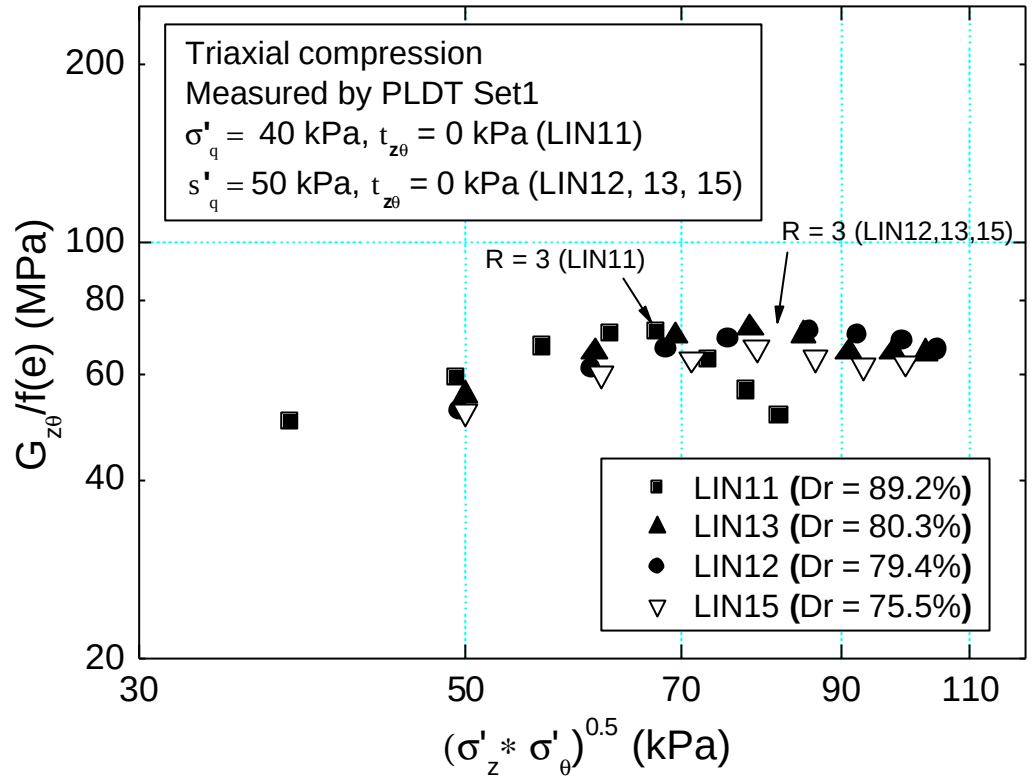

Fig. 5.40 $G_{z\theta}/f(e)$ vs $(\sigma'_z * \sigma'_\theta)^{0.5}$ during TC measured by PLDT Set1

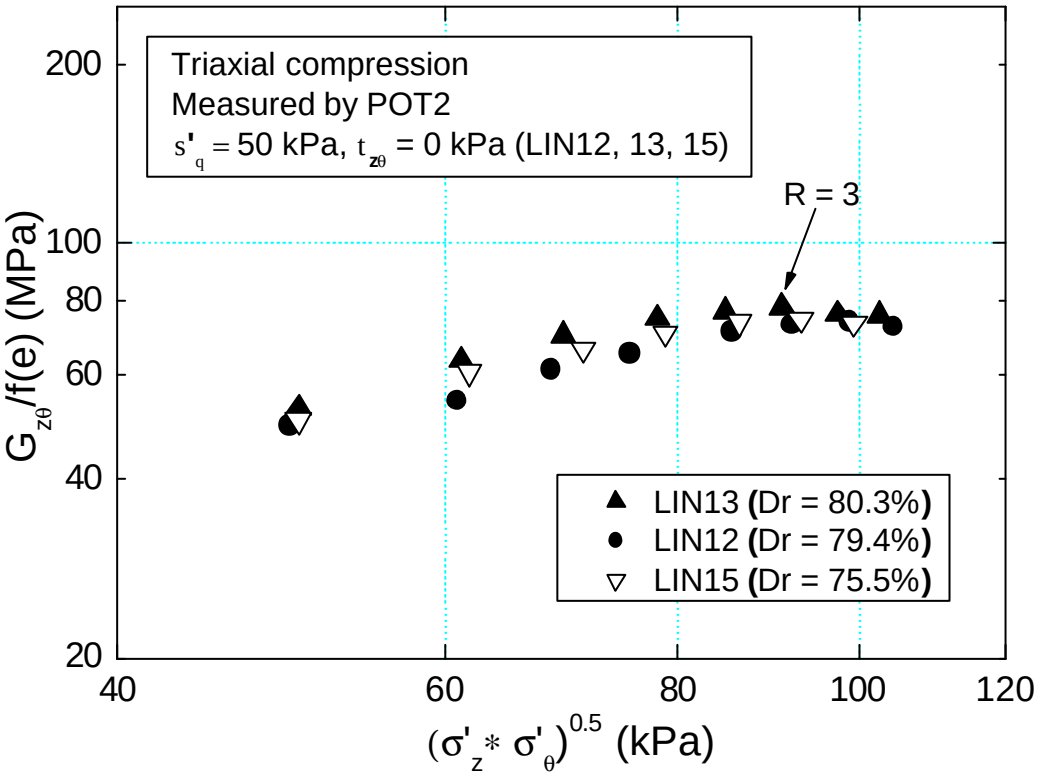

Fig. 5.41 $G_{z\theta}/f(e)$ vs $(\sigma'_z * \sigma'_\theta)^{0.5}$ during TC measured by POT2

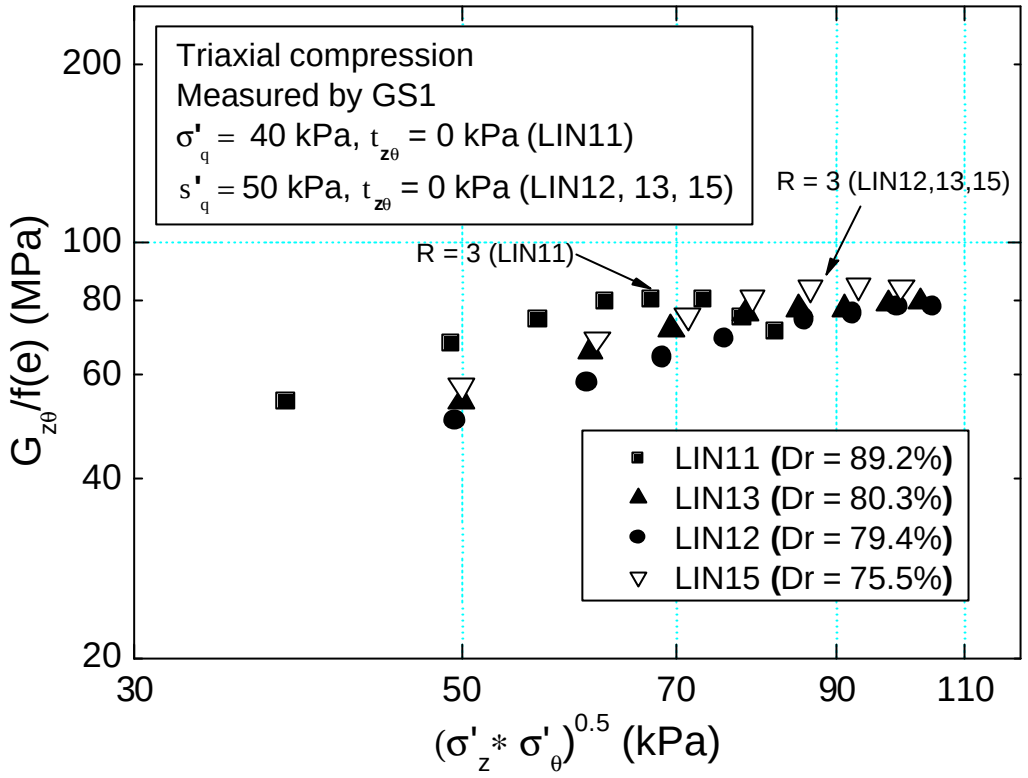

Fig. 5.42 $G_{z\theta}/f(e)$ vs $(\sigma'_z * \sigma'_\theta)^{0.5}$ during TC measured by GS1

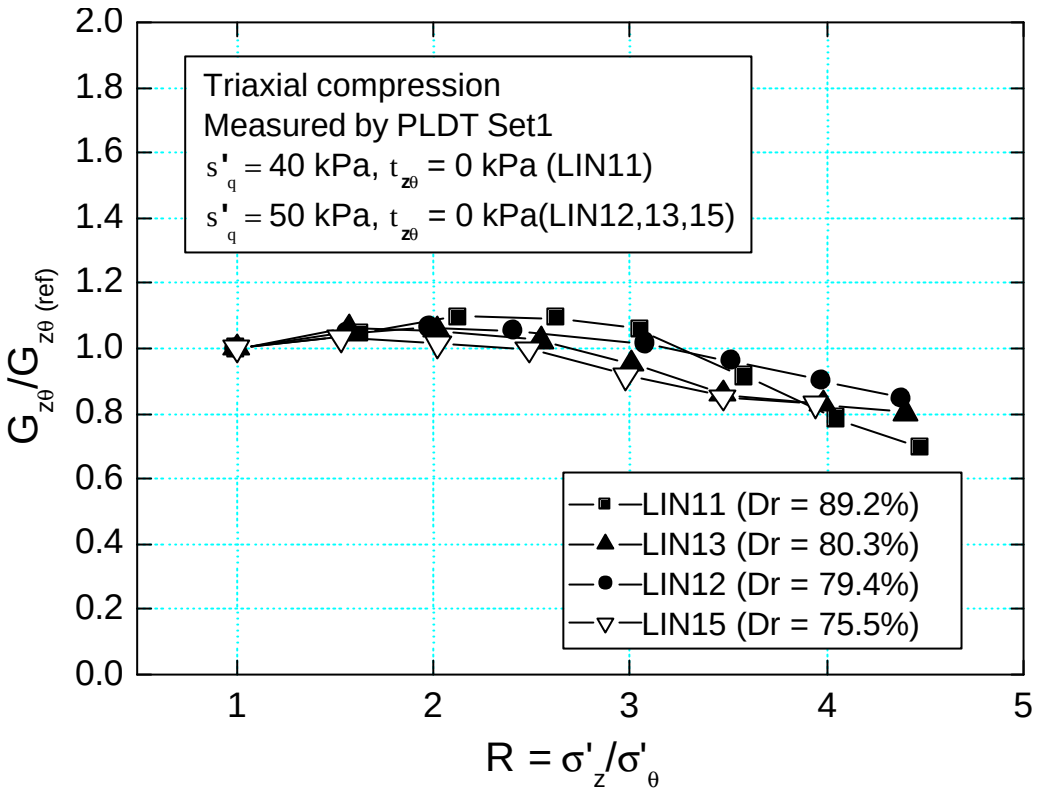

Fig. 5.43 $G_{z\theta}/ G_{z\theta\ (ref)}$ vs R during TC measured using PLDT Set1

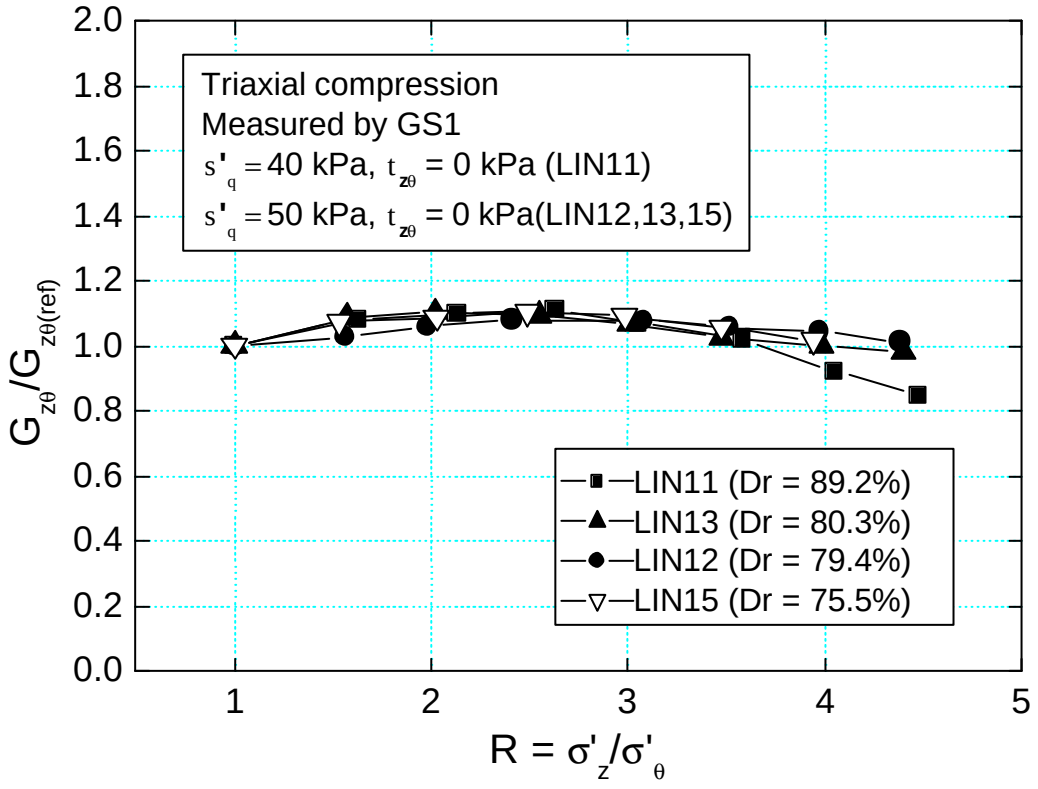

Fig. 5.44 $G_{z\theta}/ G_{z\theta\ (ref)}$ vs R during TC measured using GS1

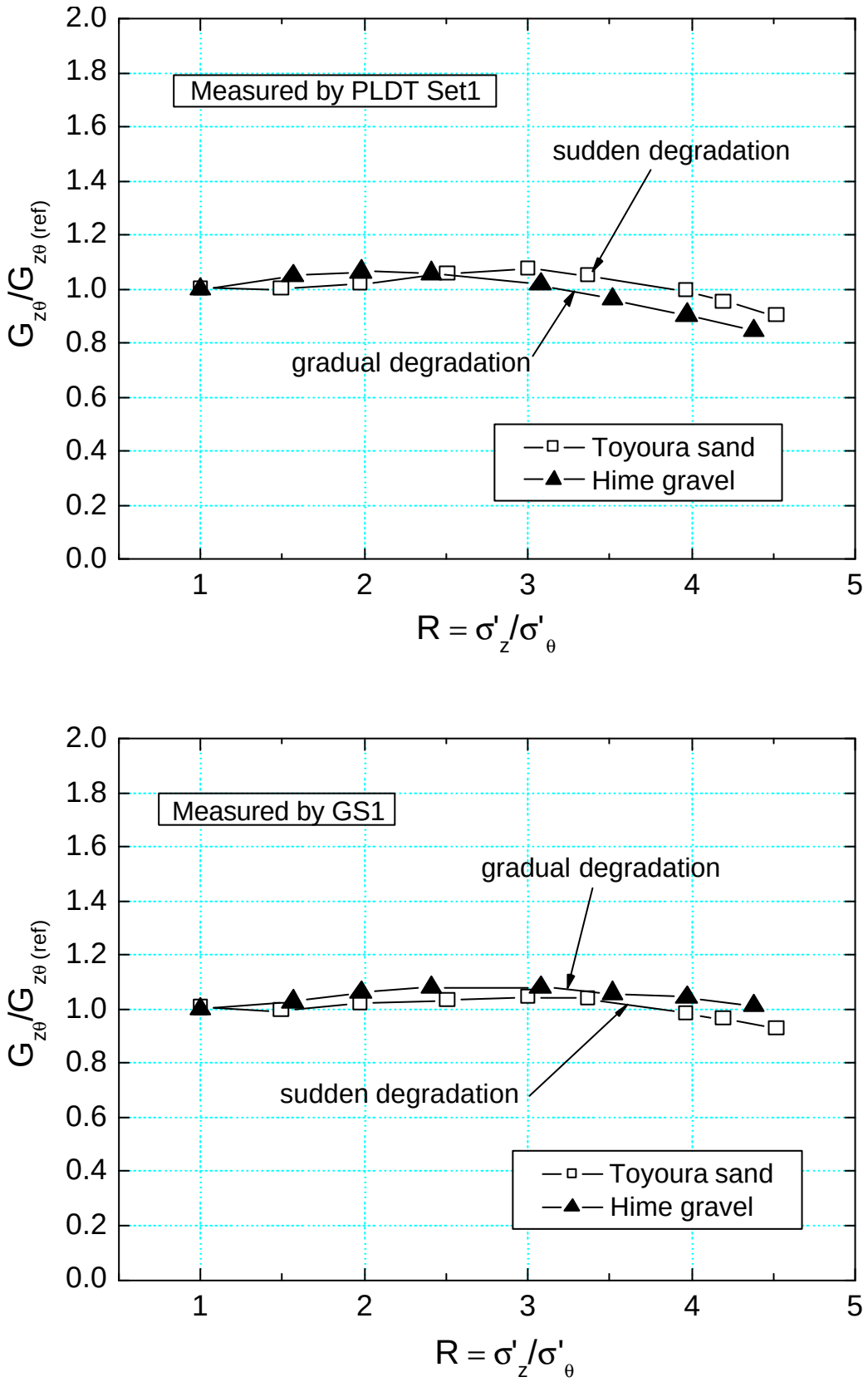

Fig. 5.45 Comparison of $G_{z\theta}/ G_{z\theta\,(ref)}$ vs R between Toyoura sand and Hime gravel

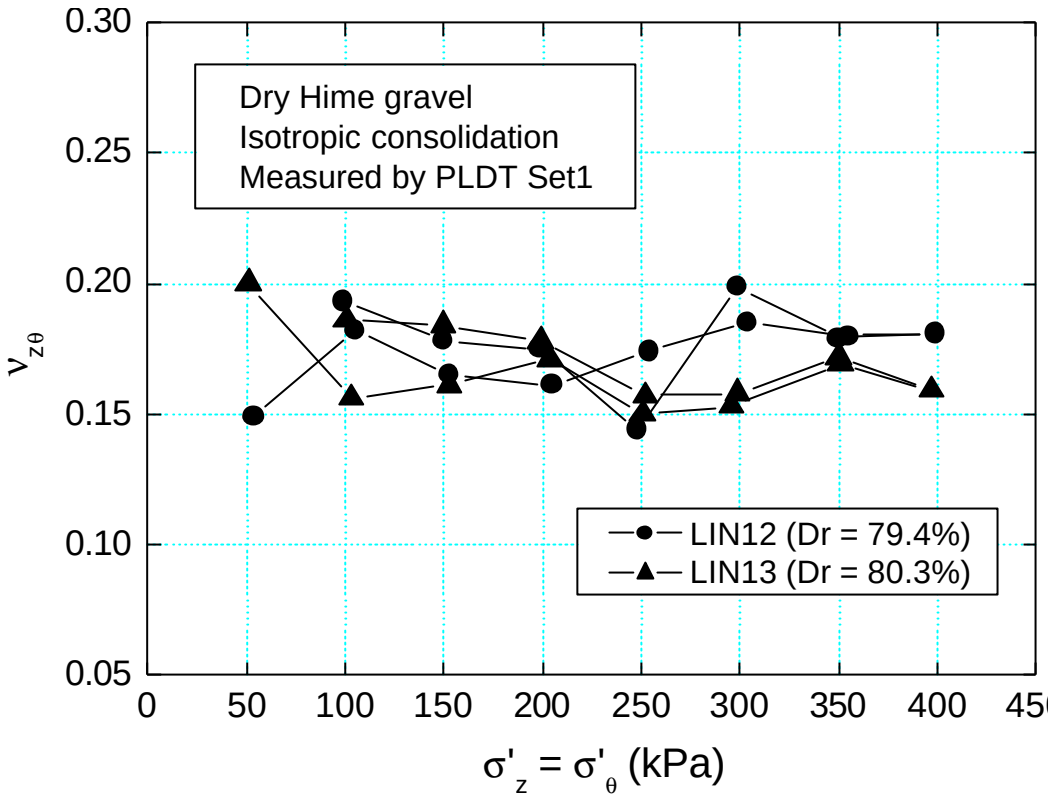

Fig. 5.46 $\nu_{z\theta}$ during IC measured by PLDT Set1

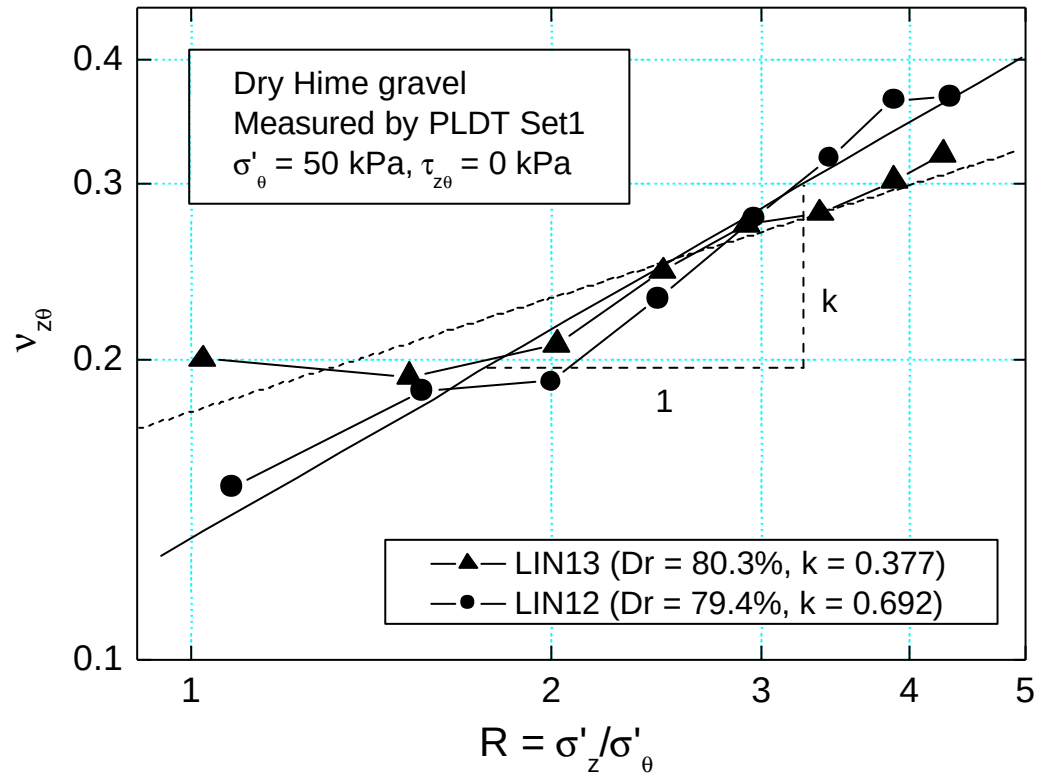

Fig. 5.47 $\nu_{z\theta}$ during TC measured by PLDT Set1

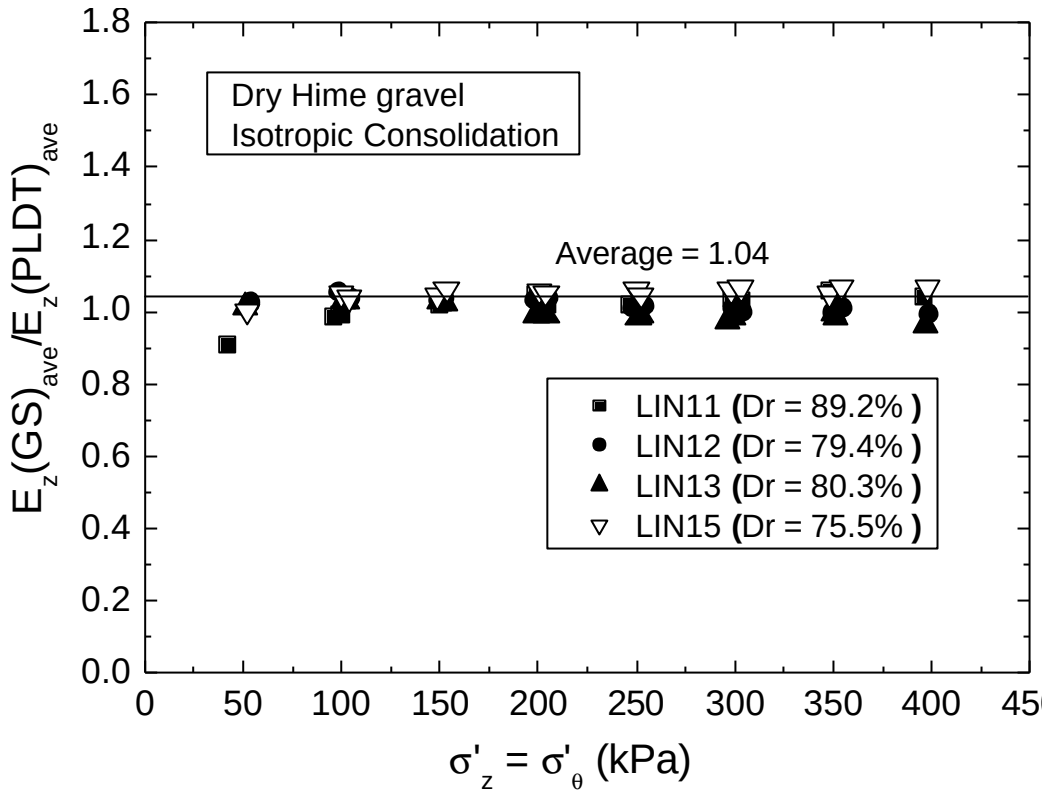

Fig. 5.48 E_z (GS_{ave})/ E_z ($PLDT_{ave}$) during IC

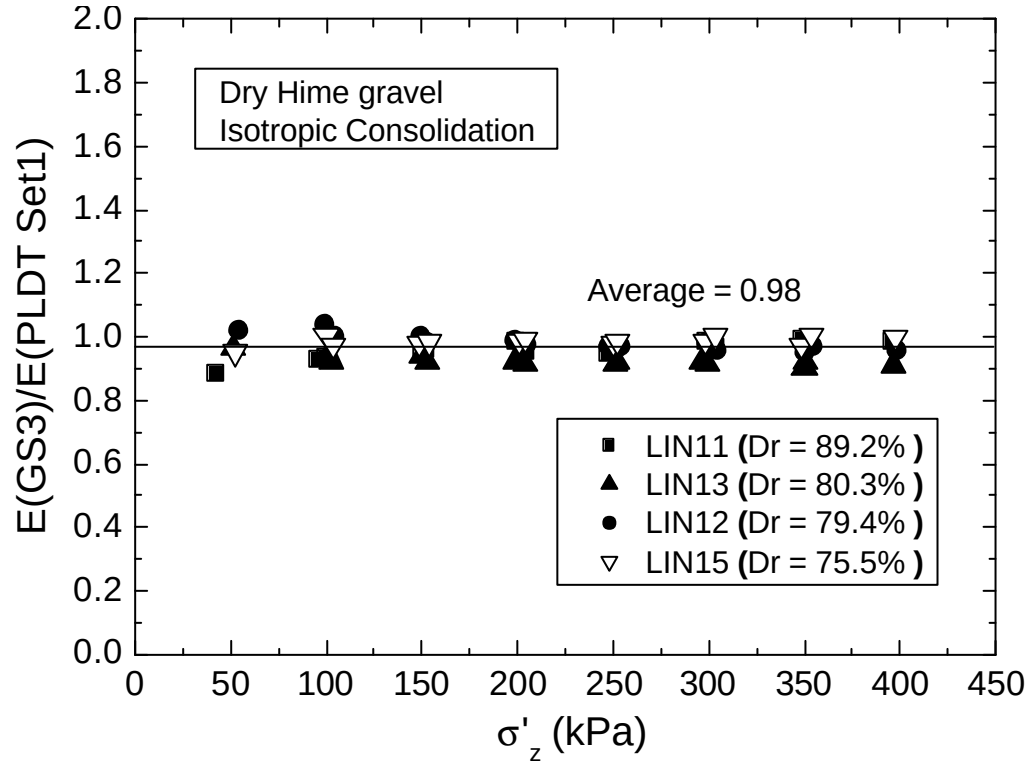

Fig. 5.49 E_z (GS3)/ E_z (PLDT Set1) during IC

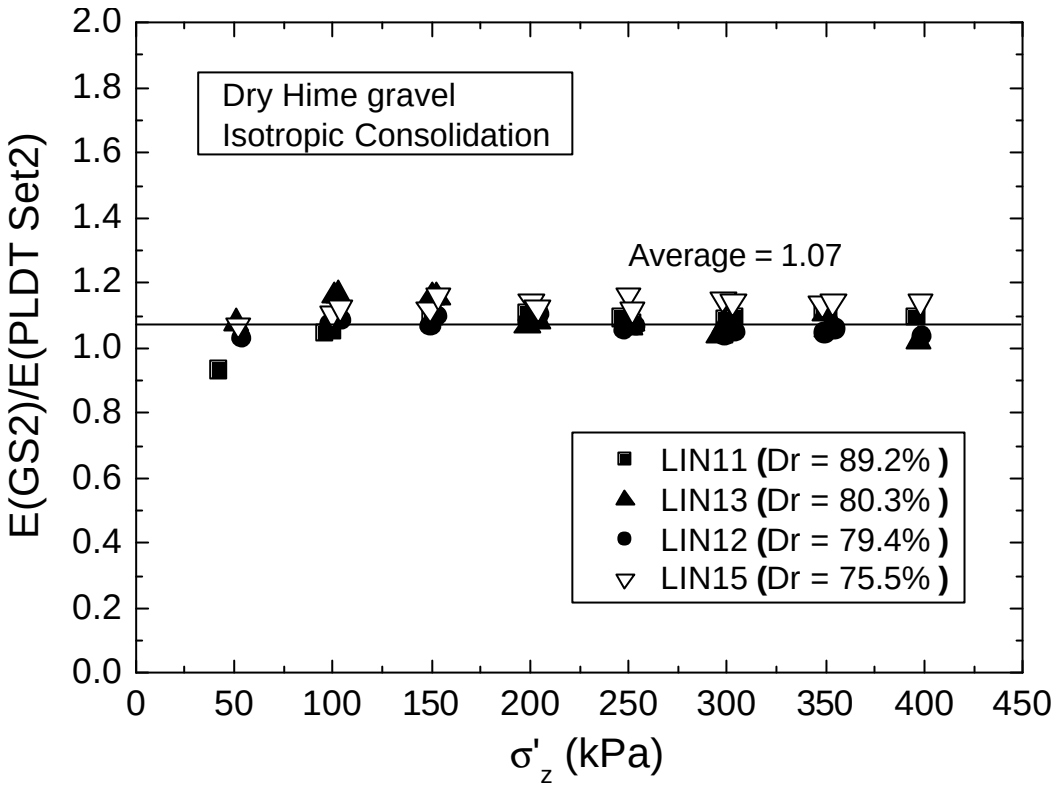

Fig. 5.50 E_z (GS2)/ E_z (PLDT Set2) during IC

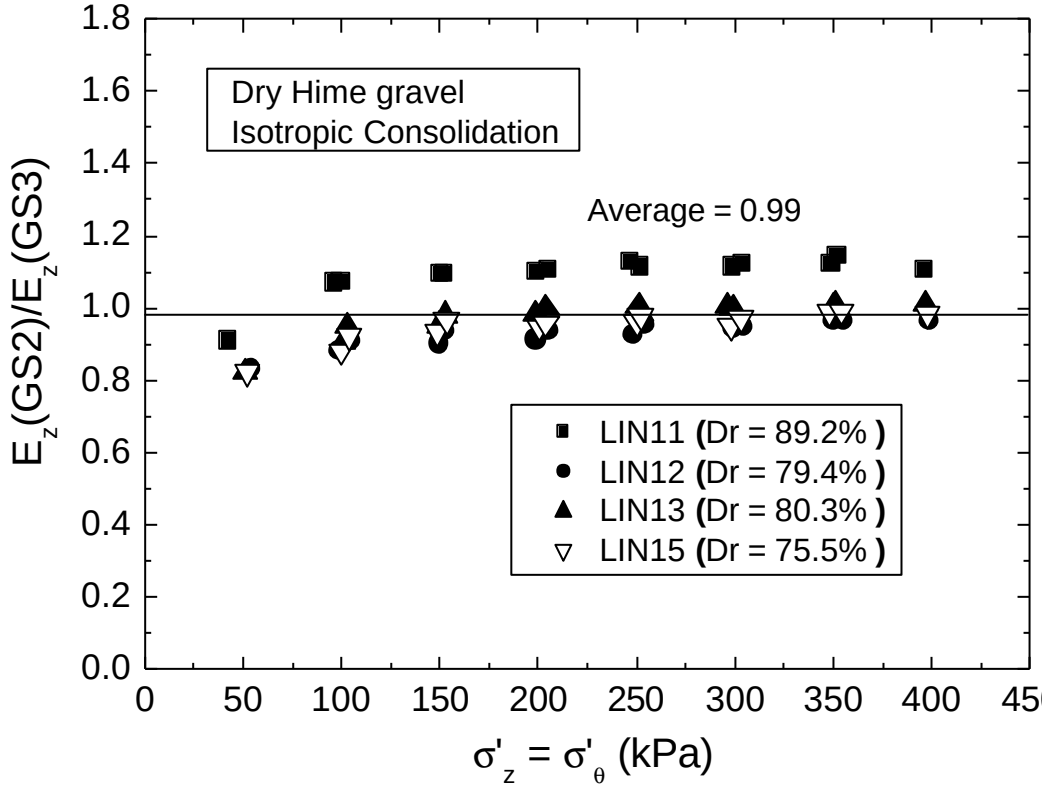

Fig. 5.51 E_z (GS2)/ E_z (GS3) during IC

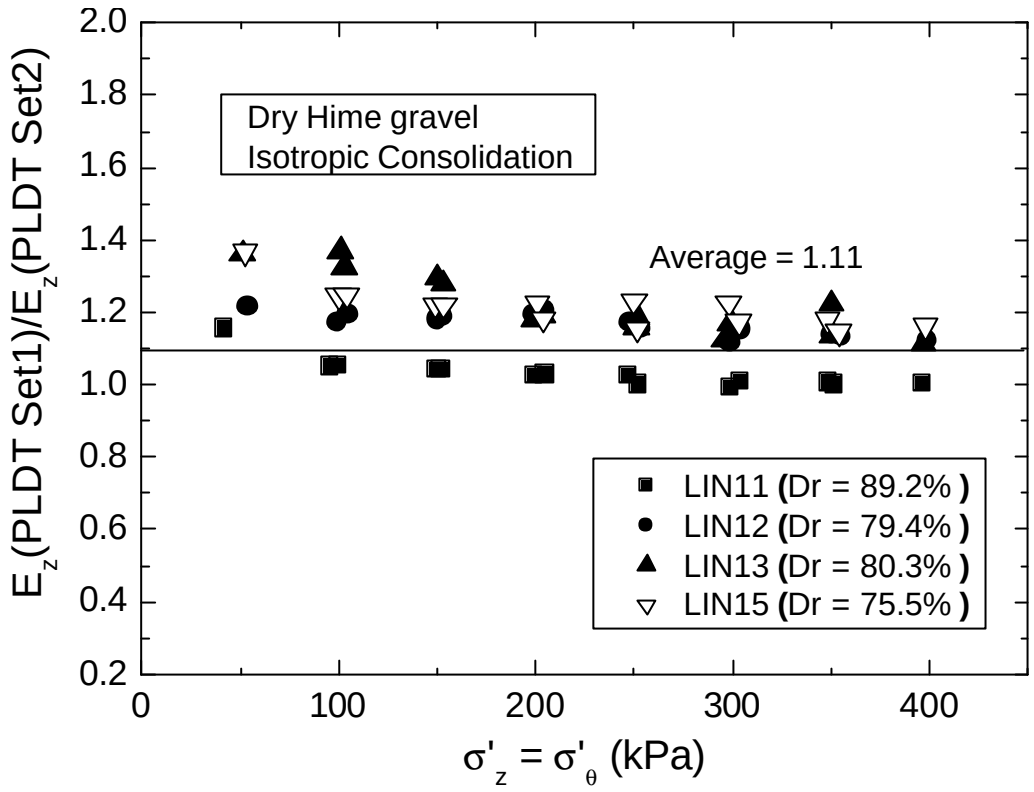

Fig. 5.52 E_z (PLDT Set1)/ E_z (PLDT Set2) during IC

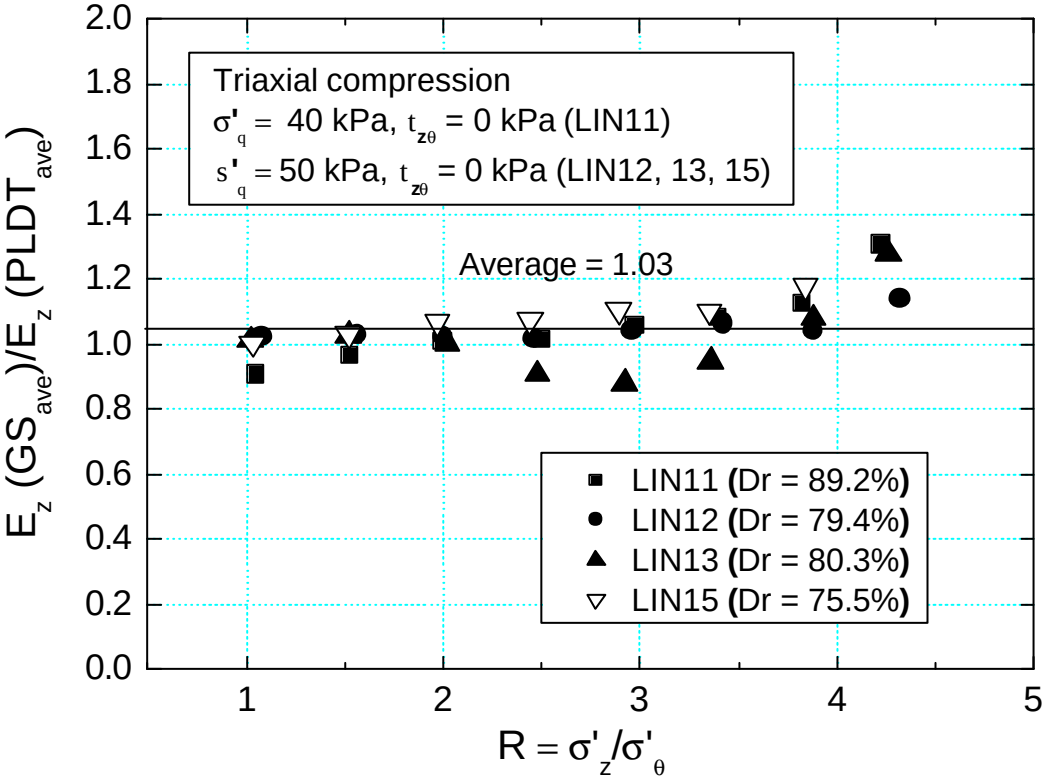

Fig. 5.53 E_z (GS_{ave})/E_z ($PLDT_{ave}$) during TC

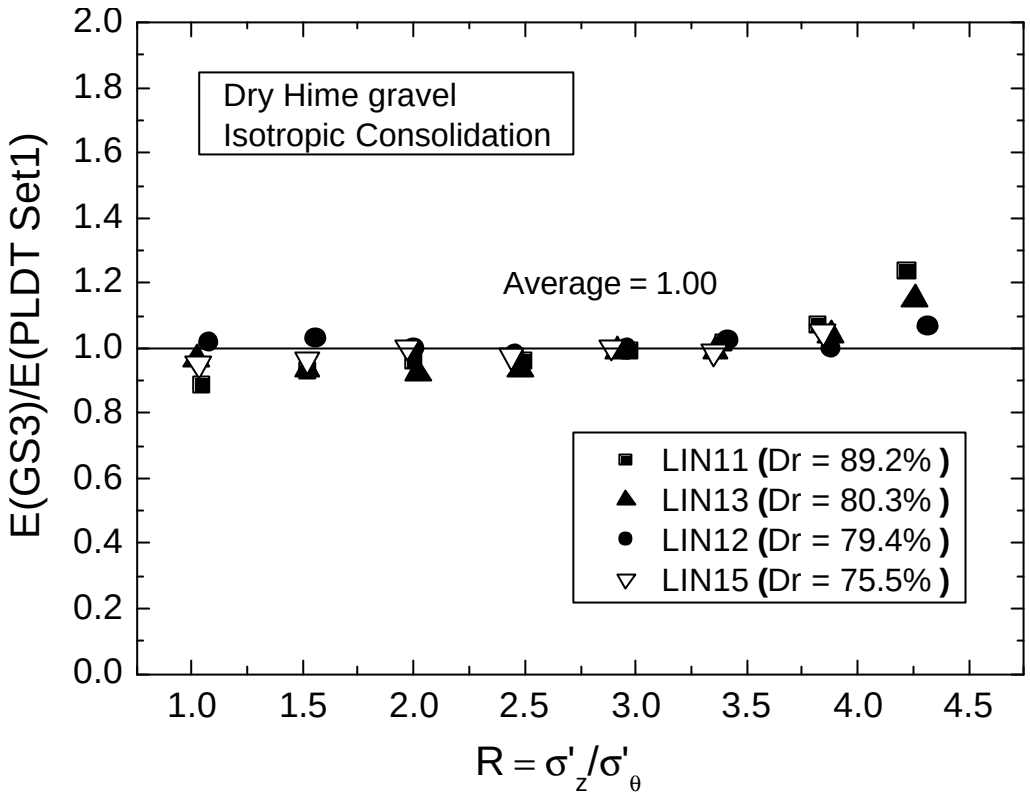

Fig. 5.54 E_z (GS3)/ E_z (PLDT Set1) during TC

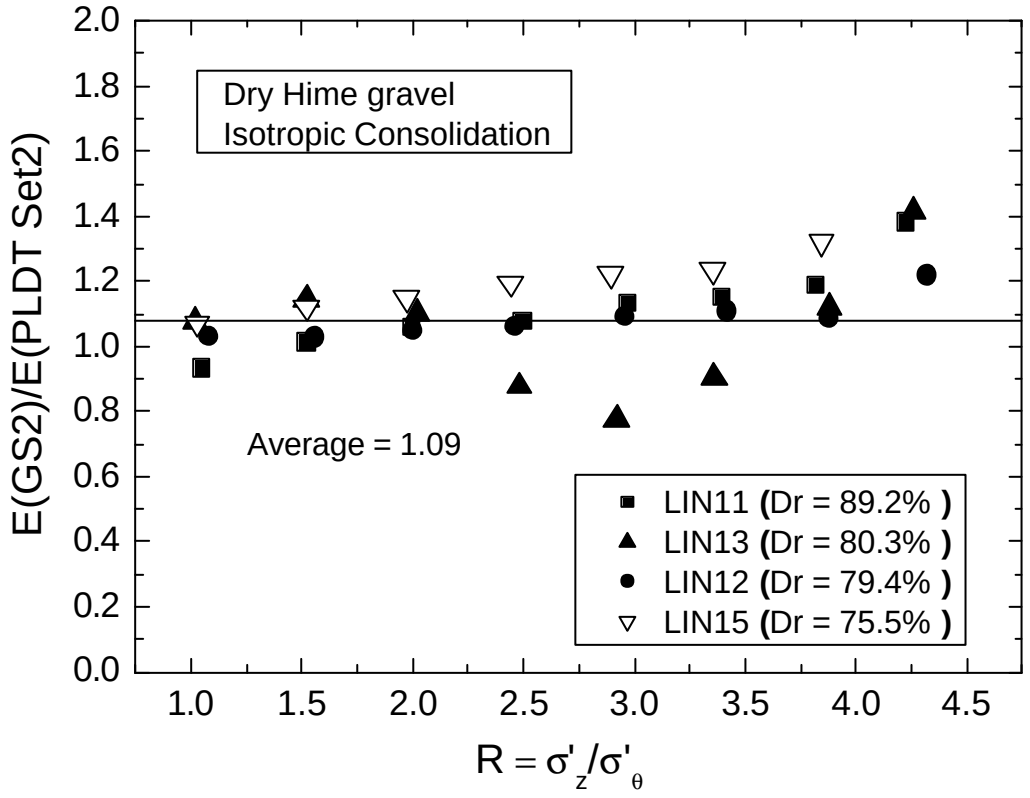

Fig. 5.55 E_z (GS2)/ E_z (PLDT Set2) during TC

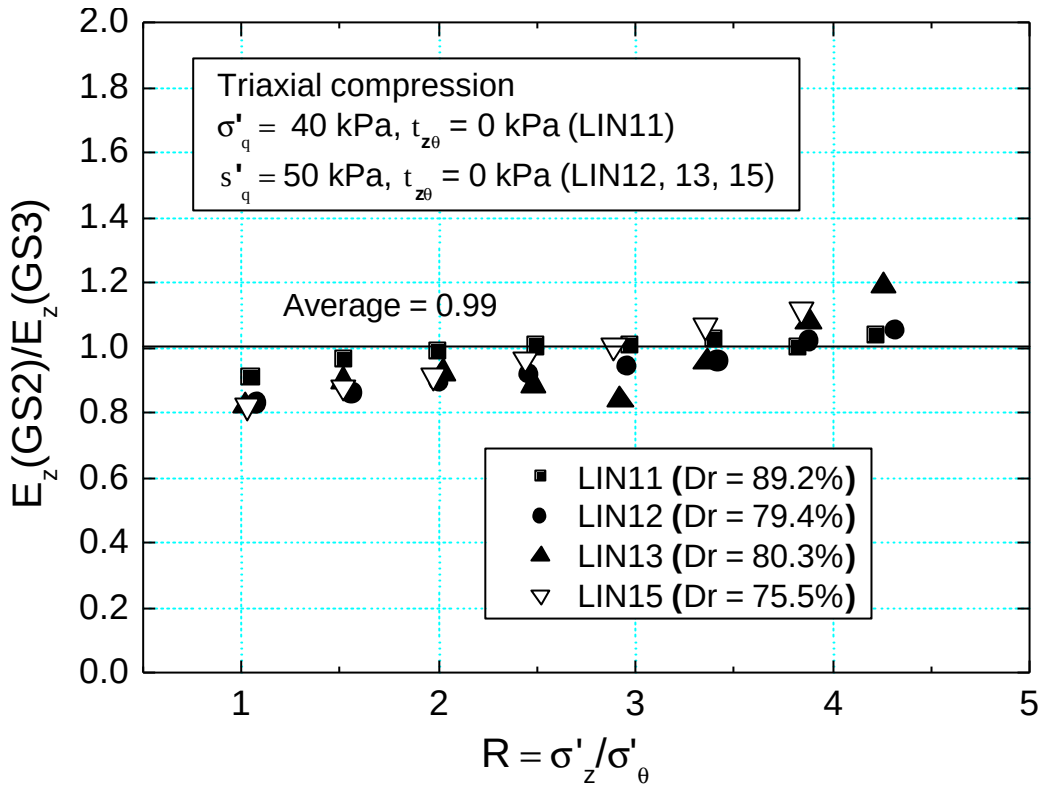

Fig. 5.56 E_z (GS2)/ E_z (GS3) during TC

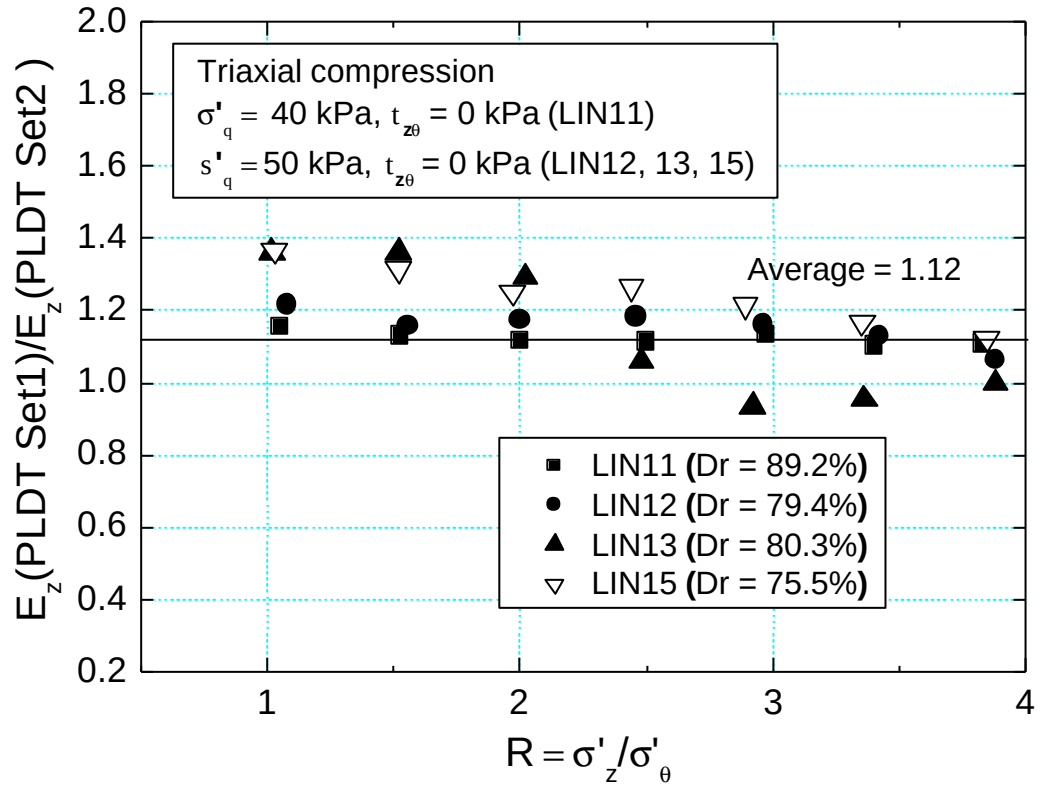

Fig. 5.57 E_z (PLDT Set1)/ E_z (PLDT Set2) during TC

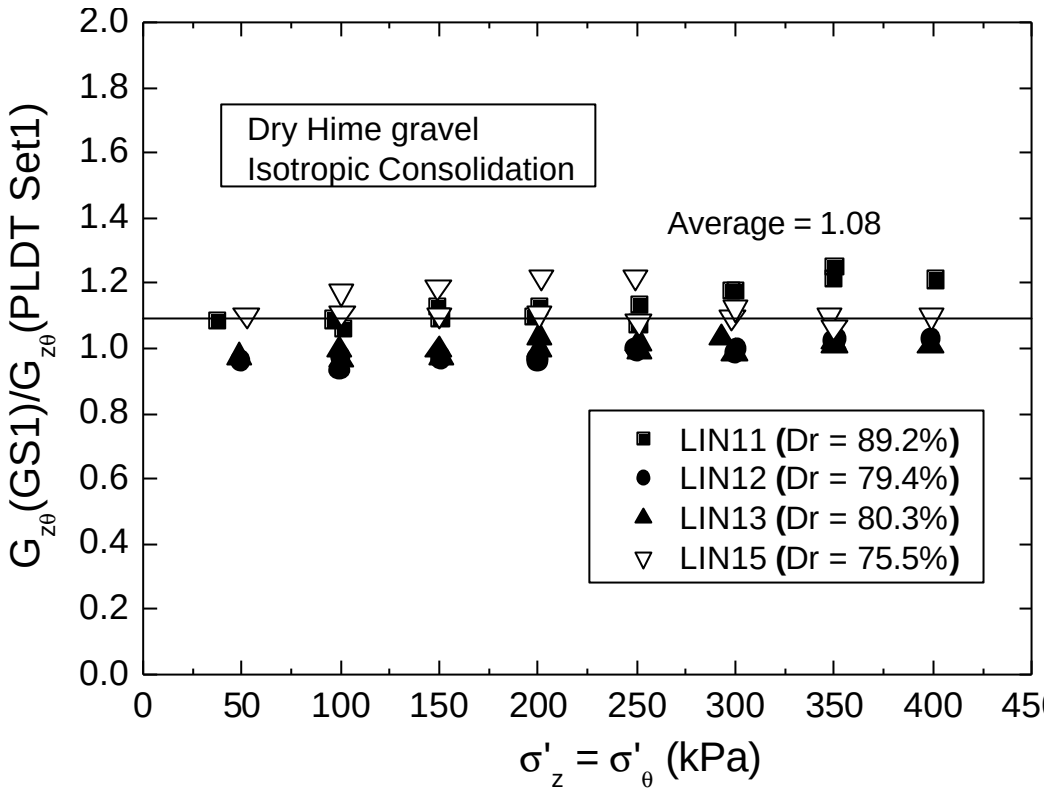

Fig. 5.58 $G_{z\theta}$ (GS1)/$G_{z\theta}$ (PLDT Set1) during IC

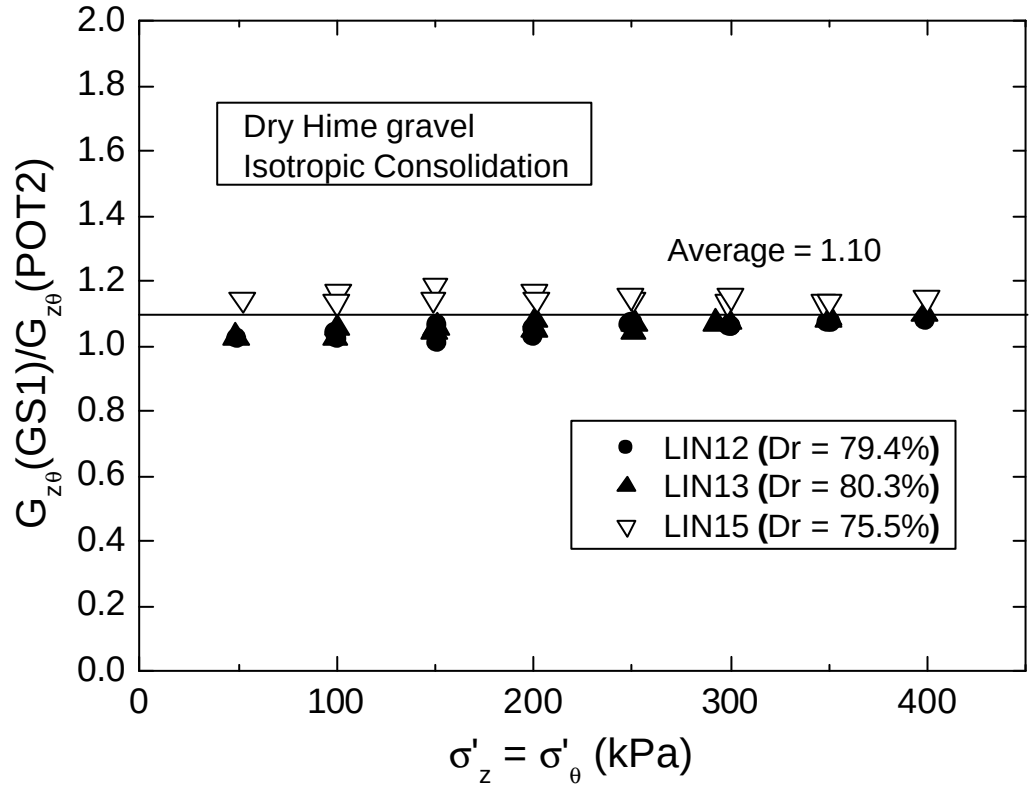

Fig. 5.59 $G_{z\theta}$ (GS1)/$G_{z\theta}$ (POT2) during IC

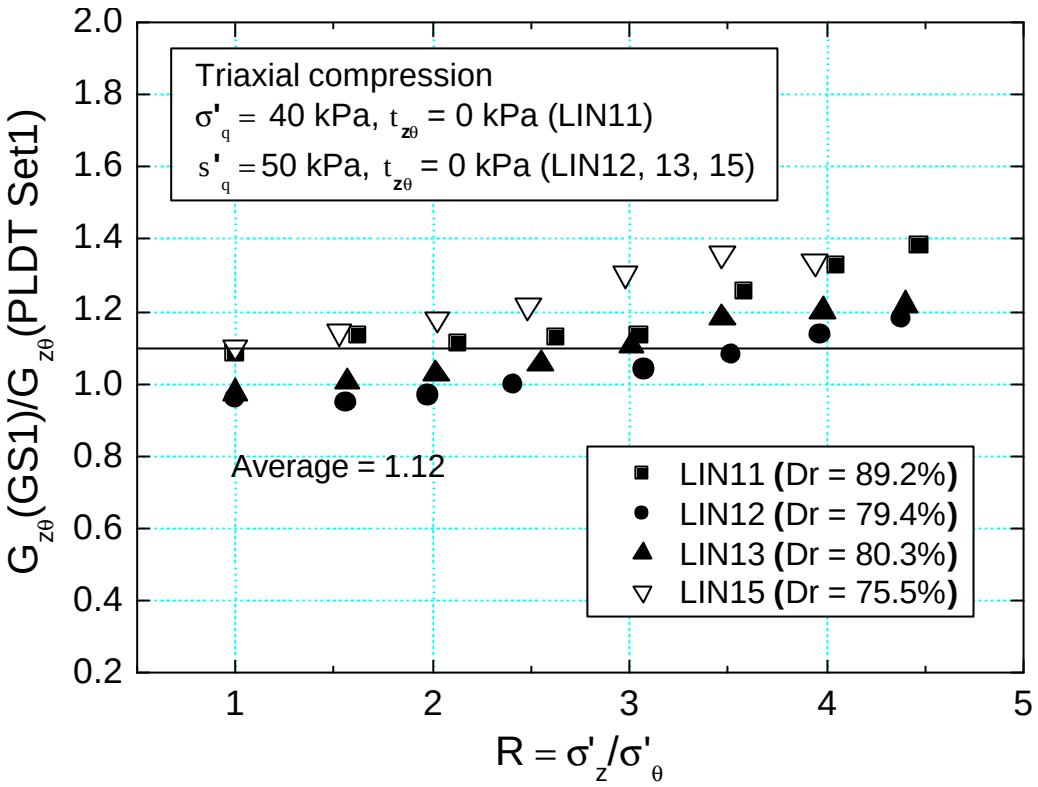

Fig. 5.60 $G_{z\theta}$ (GS1)/$G_{z\theta}$ (PLDT Set1) during TC

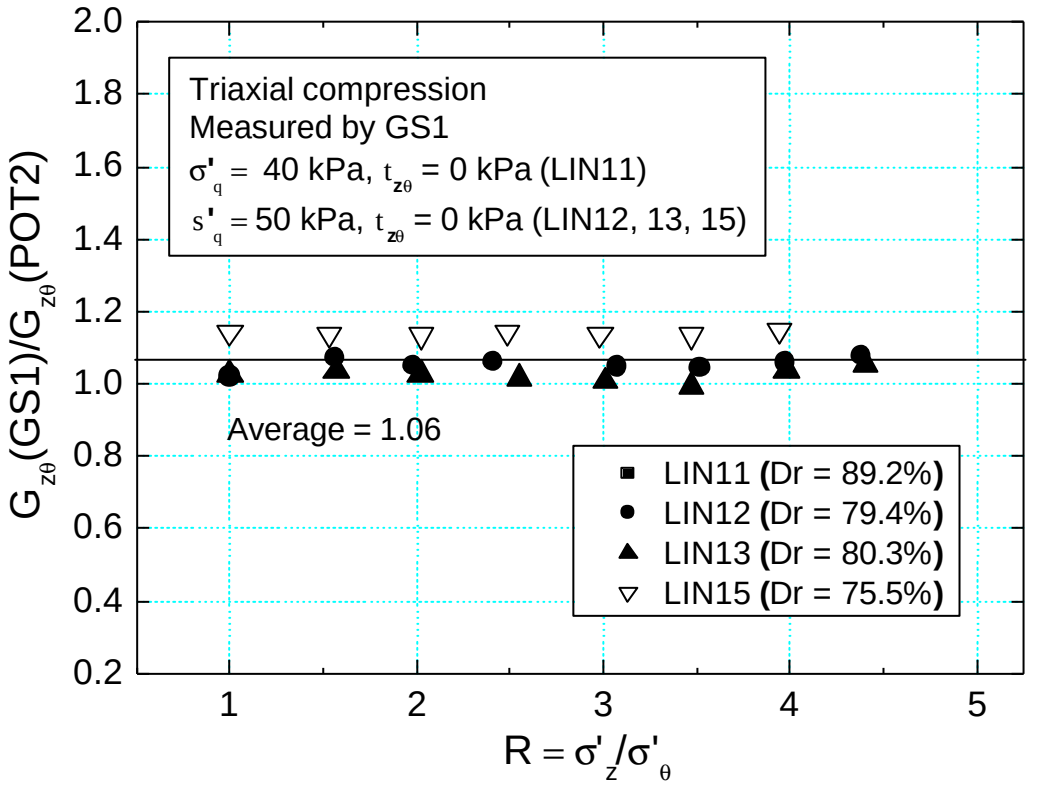

Fig. 5.61 $G_{z\theta}$ (GS1)/$G_{z\theta}$ (POT2) during TC

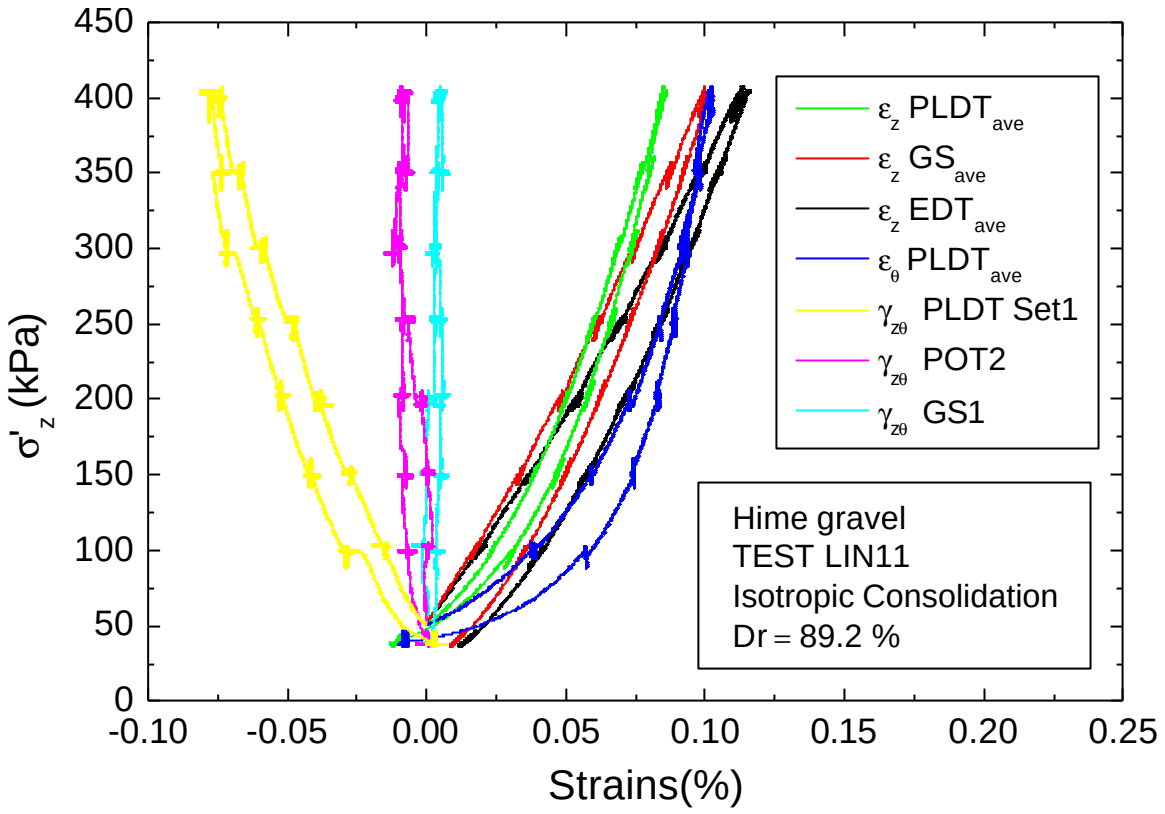

Fig. 5.62 Global strains of test LIN11 during IC

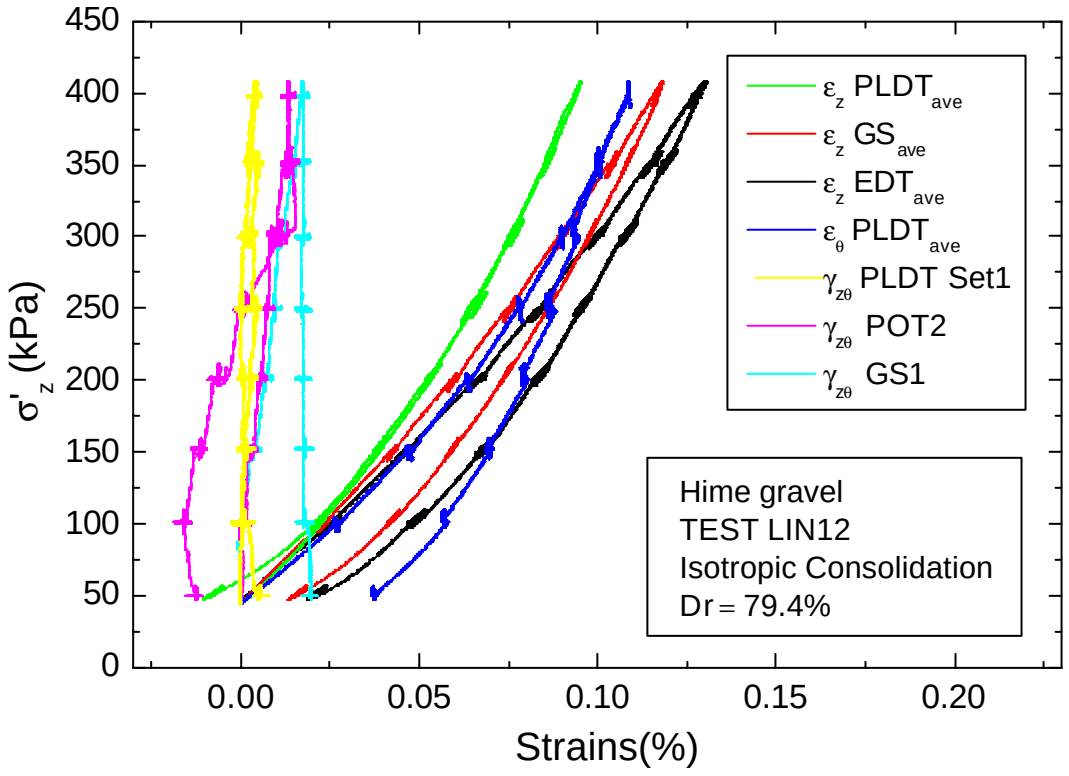

Fig. 5.63 Global strains of test LIN12 during IC

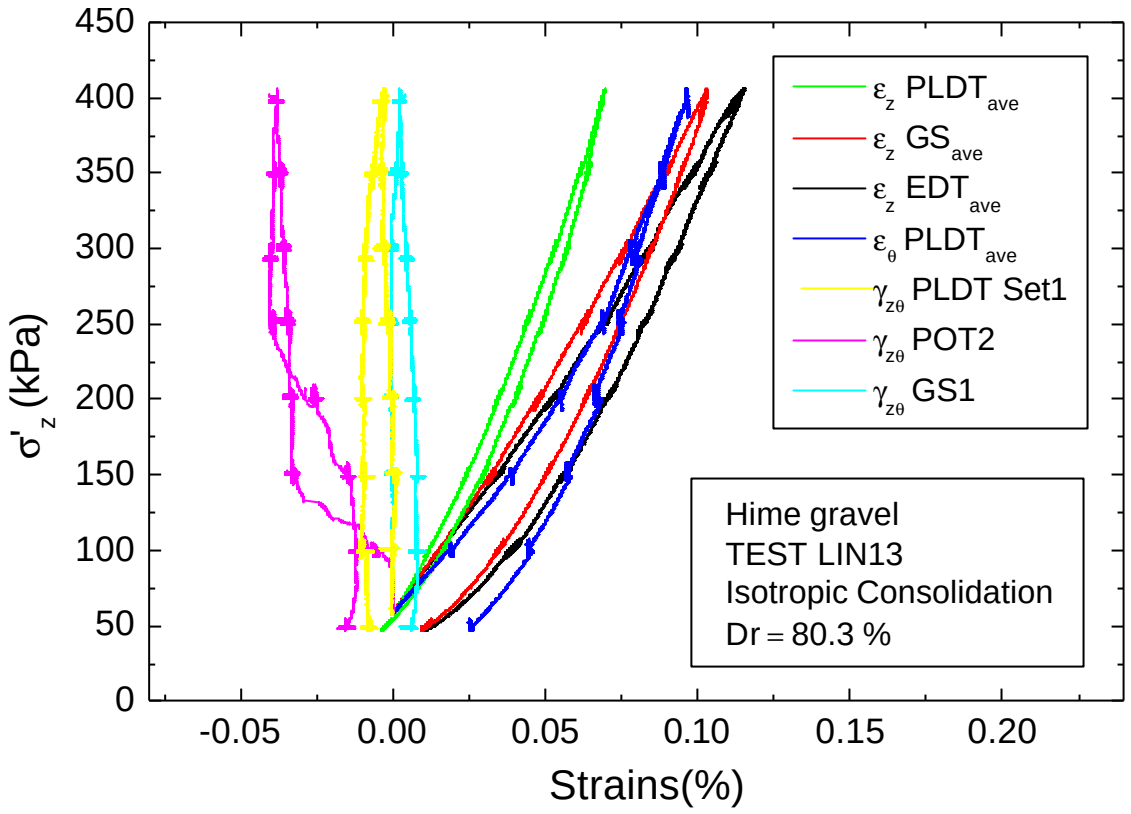

Fig. 5.64 Global strains of test LIN13 during IC

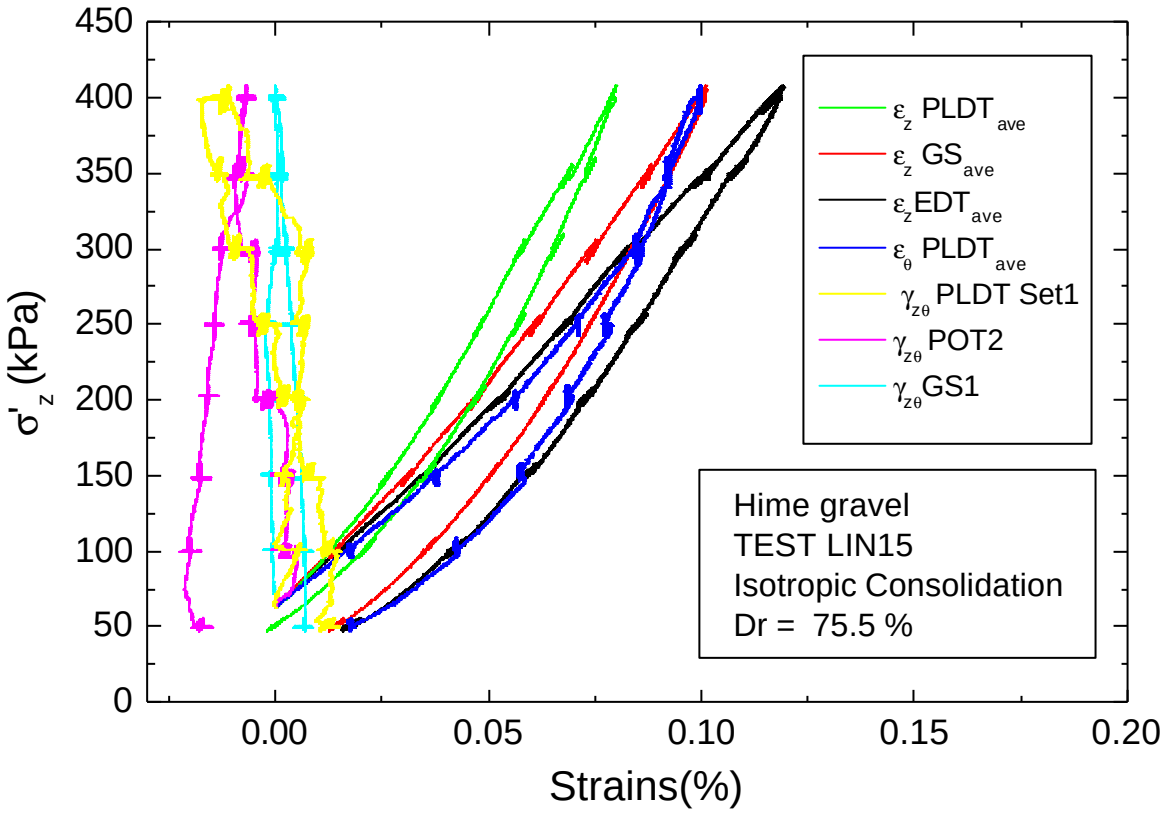

Fig. 5.65 Global strains of test LIN15 during IC

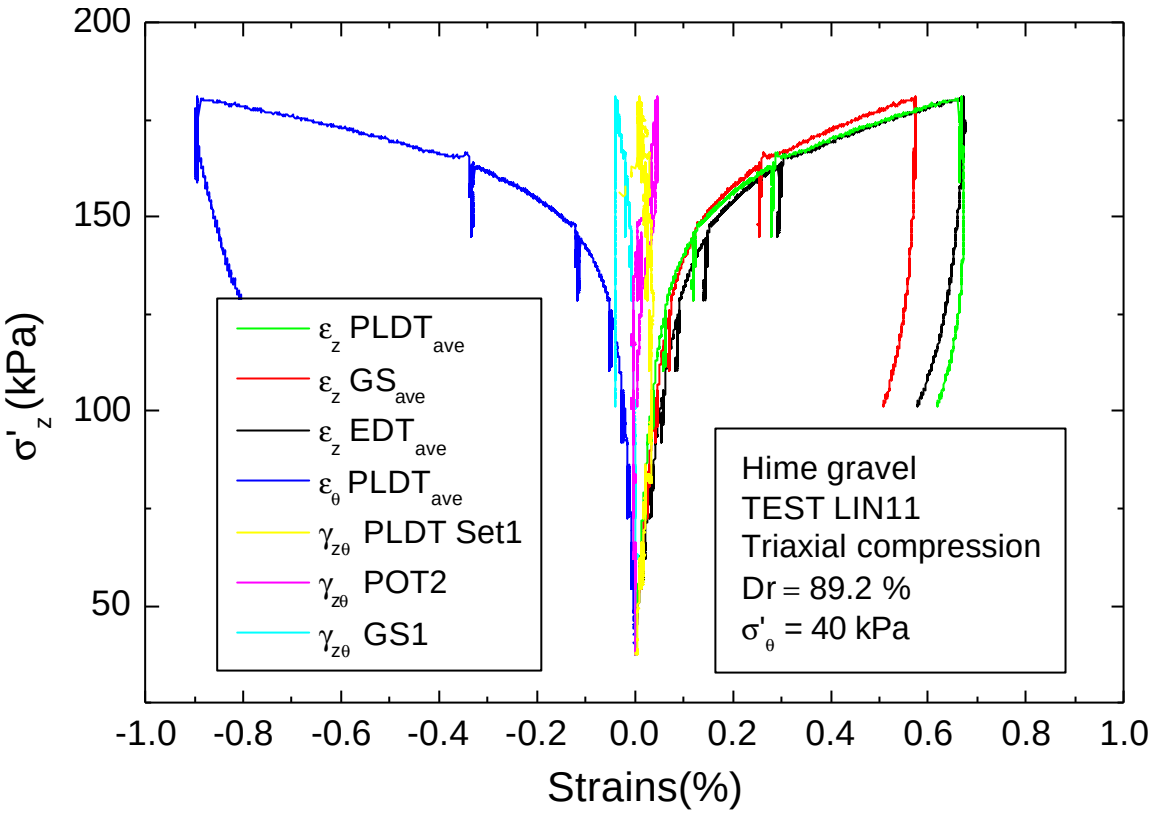

Fig. 5.66 Global strains of test LIN11 during TC

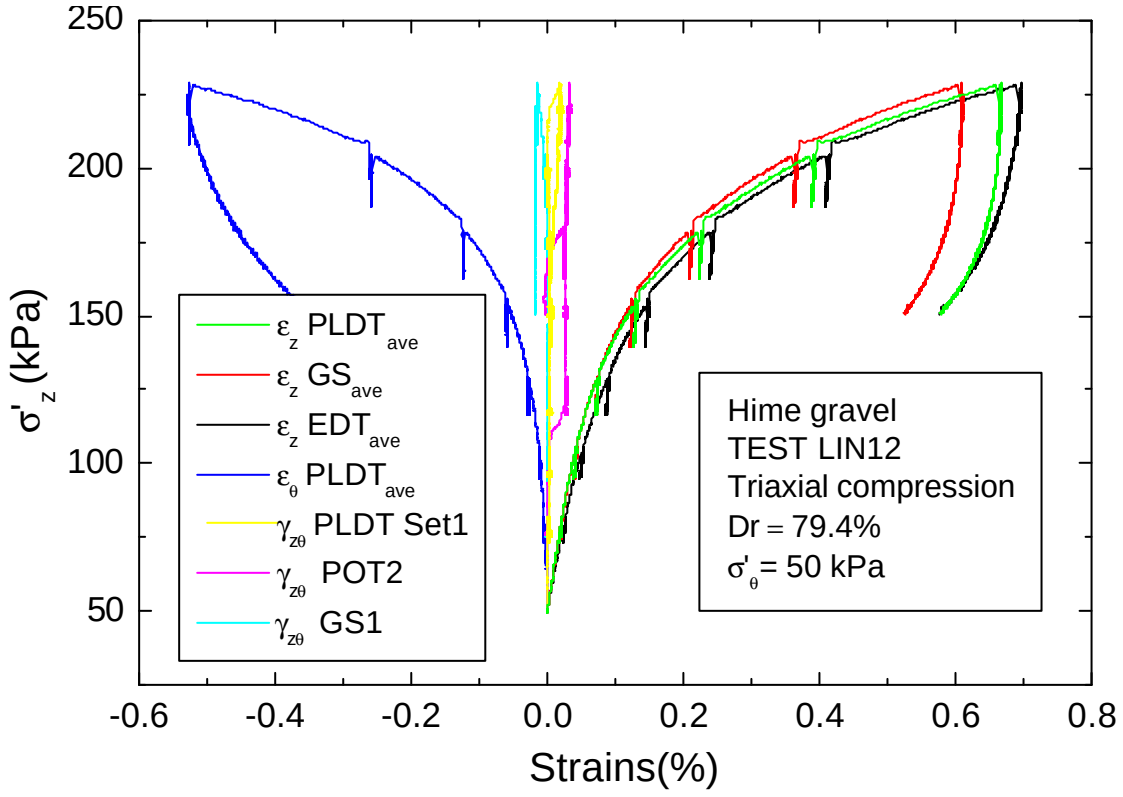

Fig. 5.67 Global strains of test LIN12 during TC

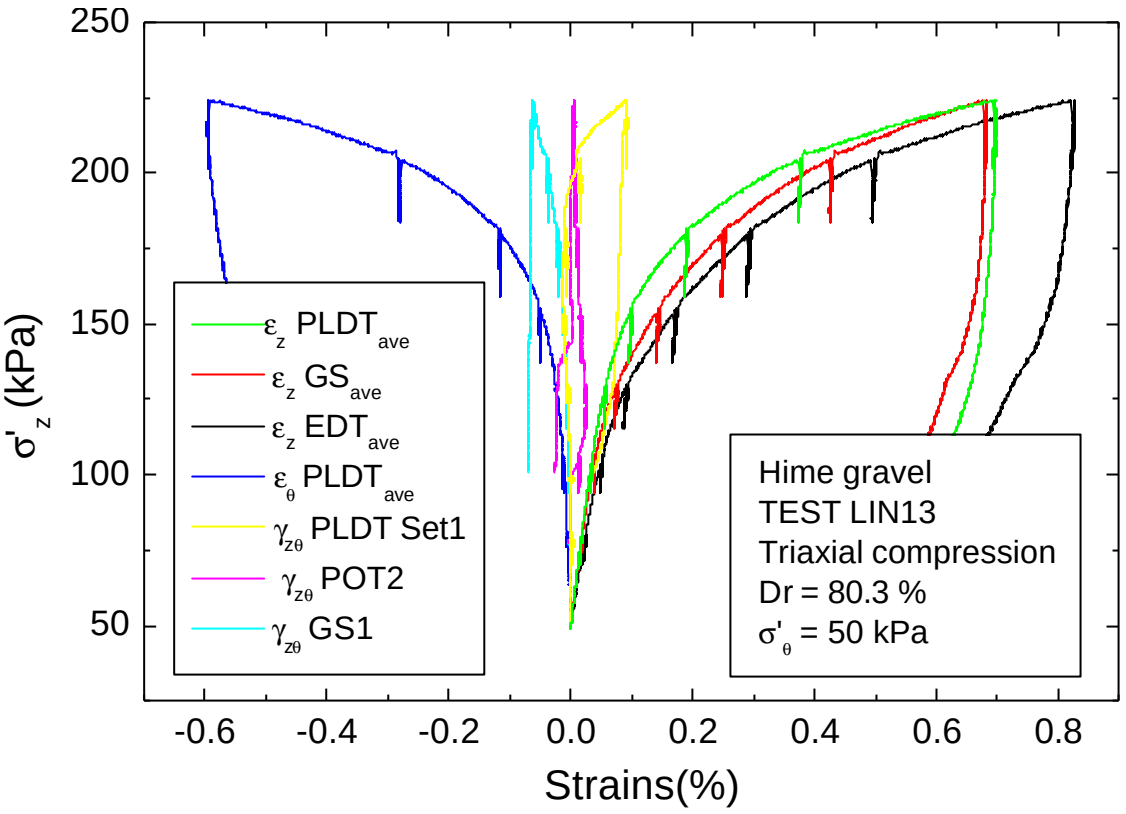

Fig. 5.68 Global strains of test LIN13 during TC

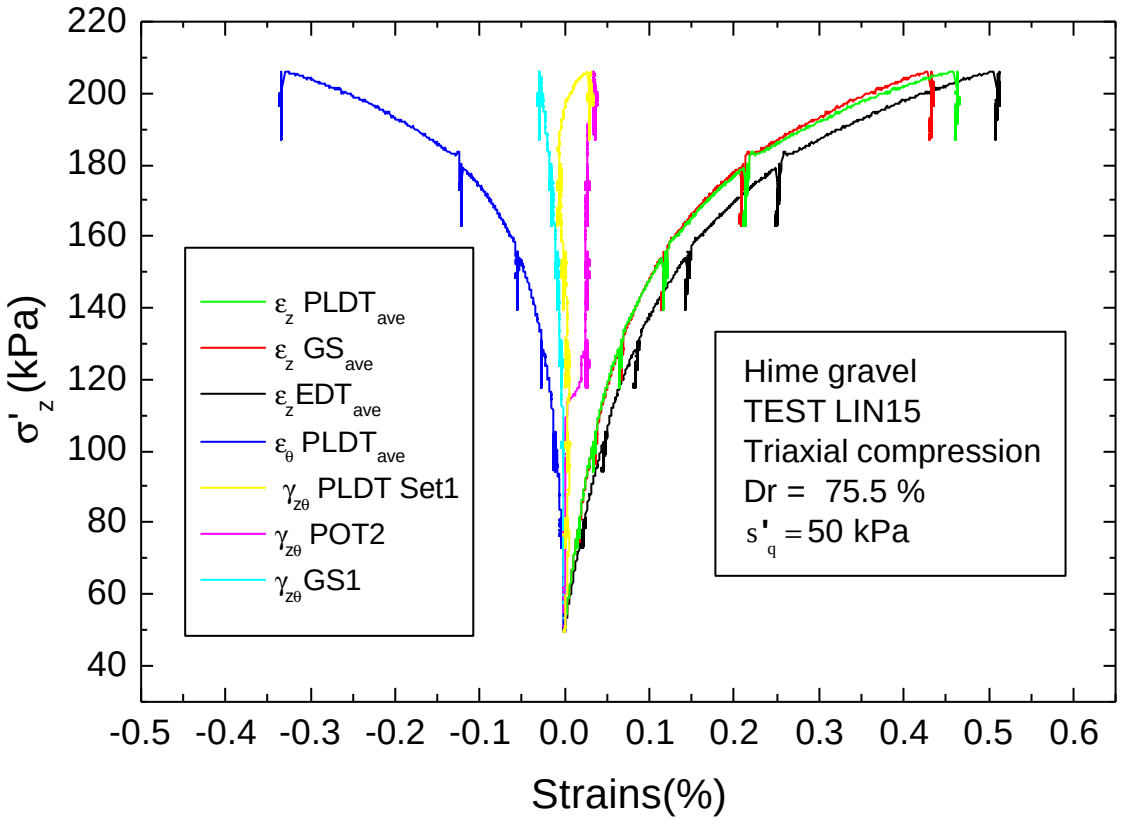

Fig. 5.69 Global strains of test LIN15 during TC

Appendix 5.1: $E_z/f(e)$ and $G_{zq}/f(e)$ vs principal stress ratio, R

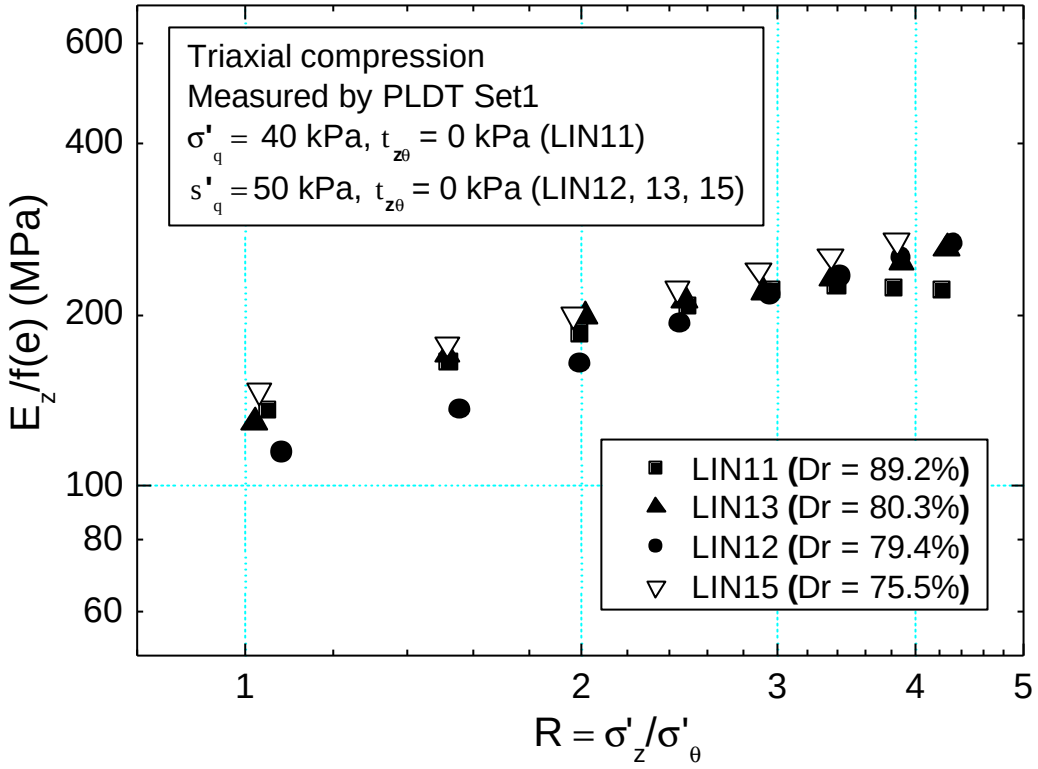

Fig. A.5.1 $E_z/f(e)$ vs R during TC measured using PLDT Set1

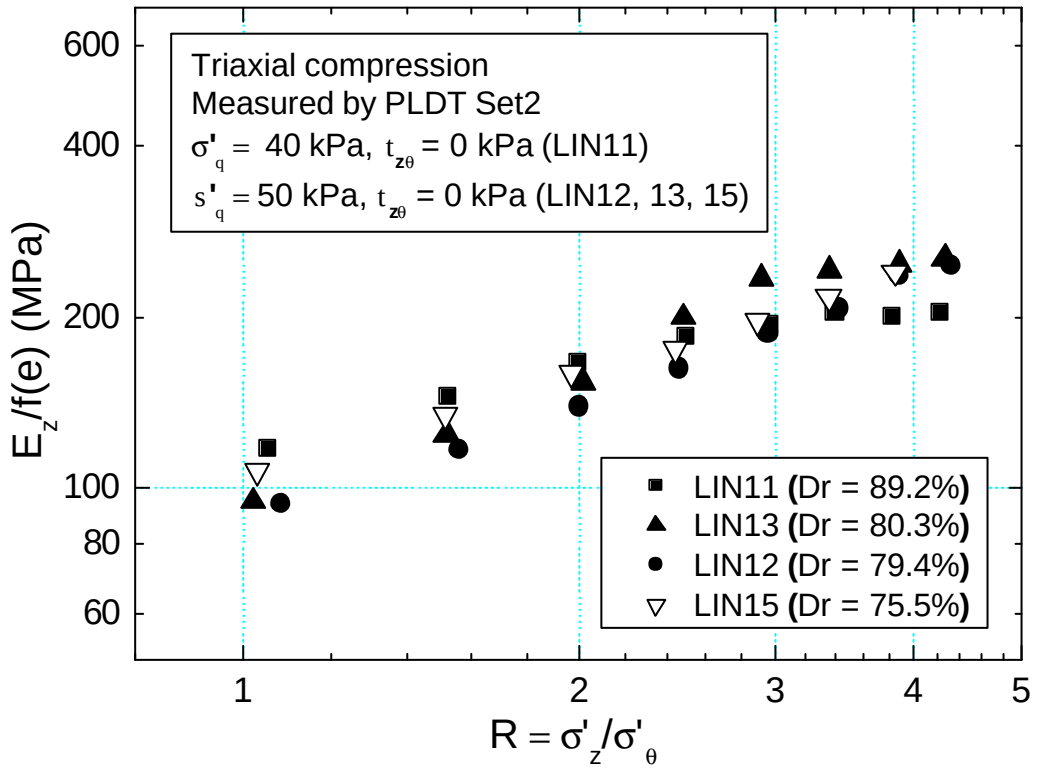

Fig. A.5.2 $E_z/f(e)$ vs R during TC measured using PLDT Set2

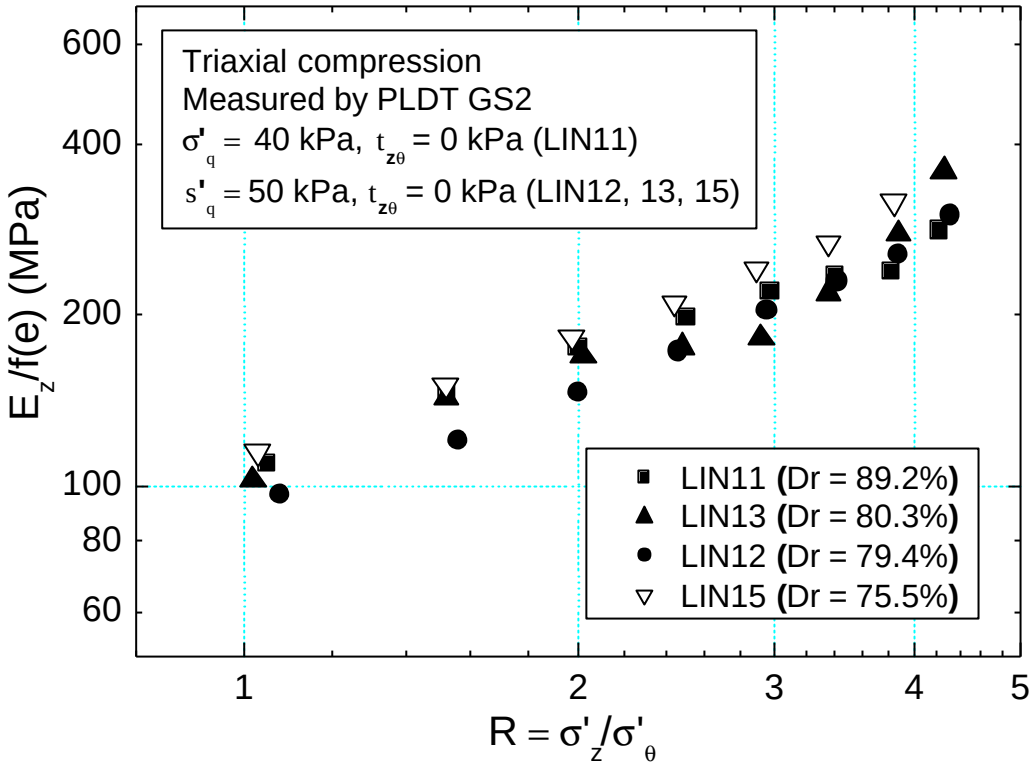

Fig. A.5.3 $E_z/f(e)$ vs R during TC measured using GS2

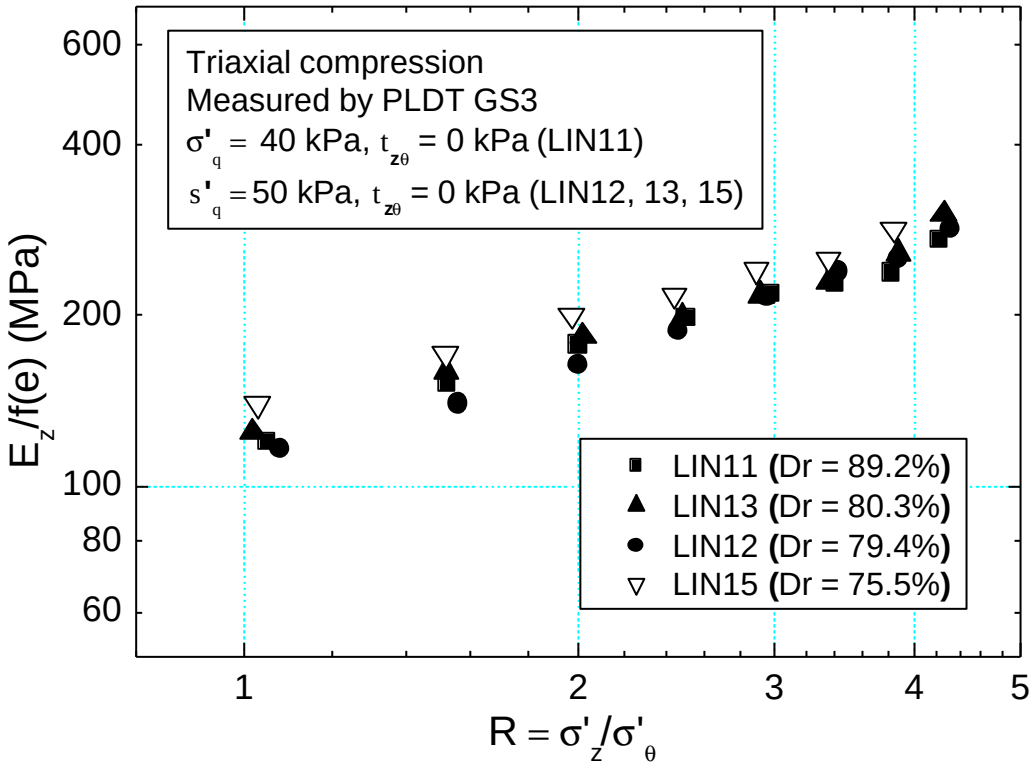

Fig. A.5.4 $E_z/f(e)$ vs R during TC measured using GS3

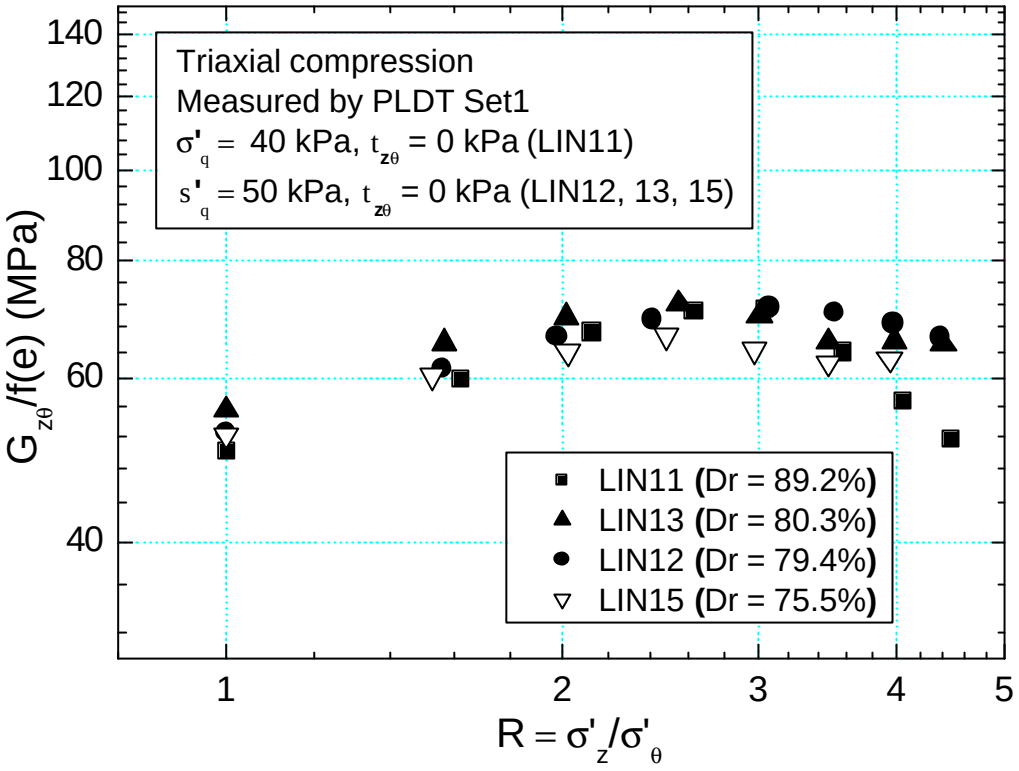

Fig. A.5.5 $G_{z\theta}/f(e)$ vs R during TC measured using PLDT Set1

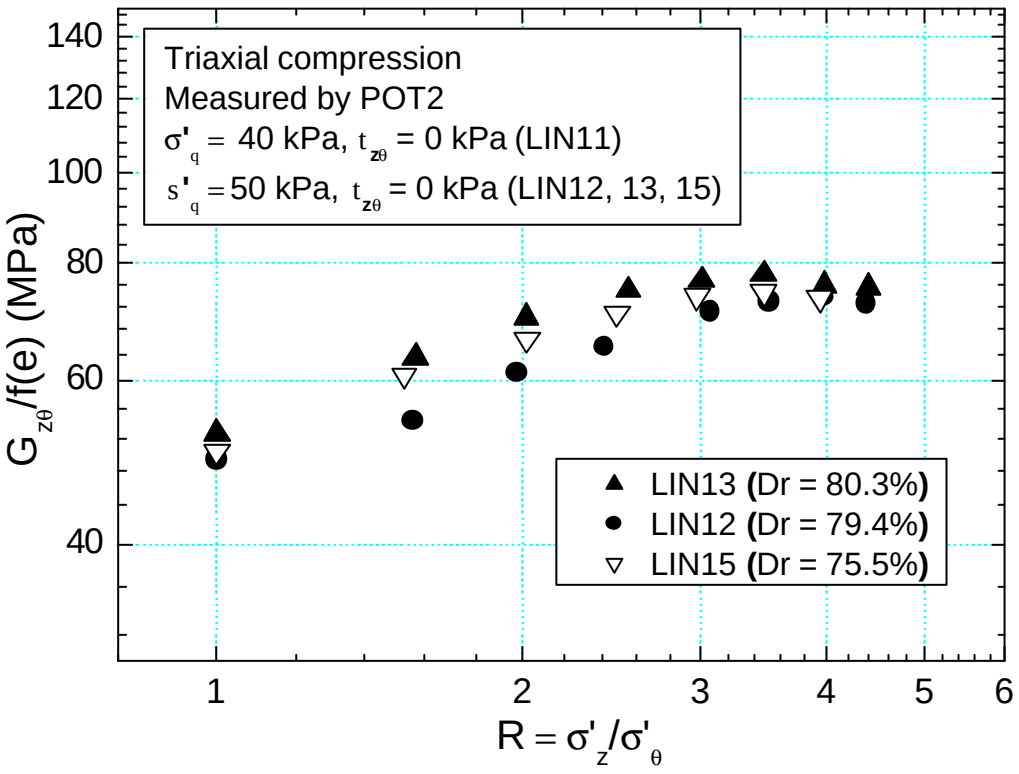

Fig. A.5.6 $G_{z\theta}/f(e)$ vs R during TC measured using POT2

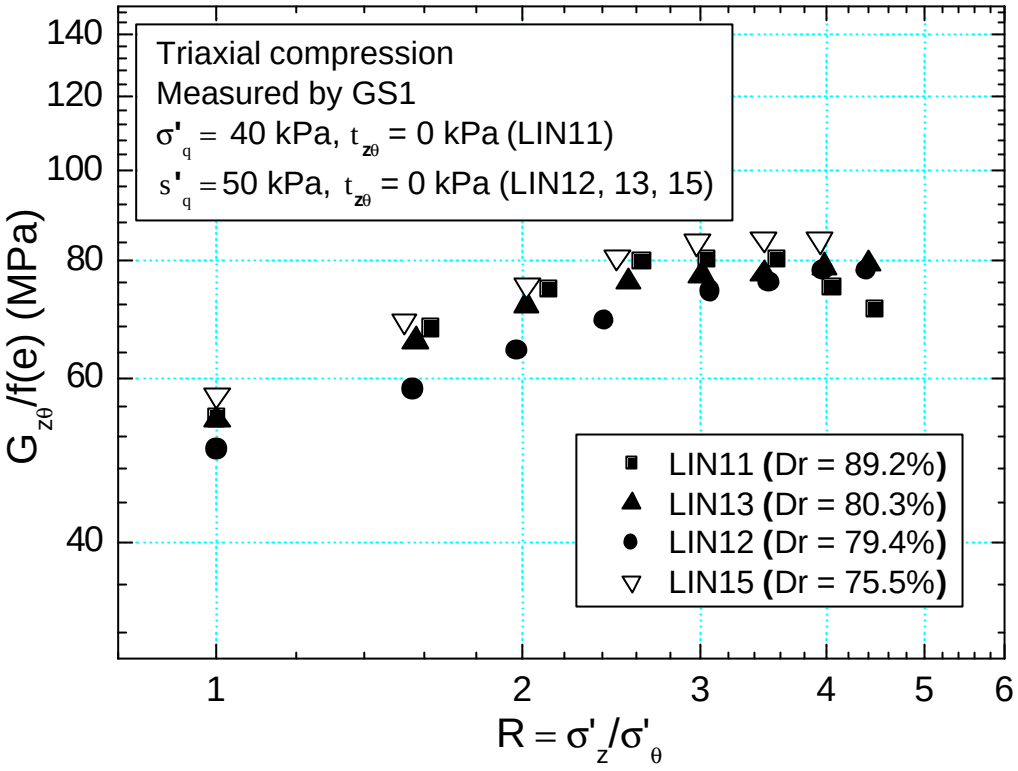

Fig. A.5.7 $G_{z\theta}/f(e)$ vs R during TC measured using GS1

Appendix 5.2: Applicability of $f(e) = (2.17-e)^2/(1+e)$ (Hardin & Richart, 1963) at different stress levels

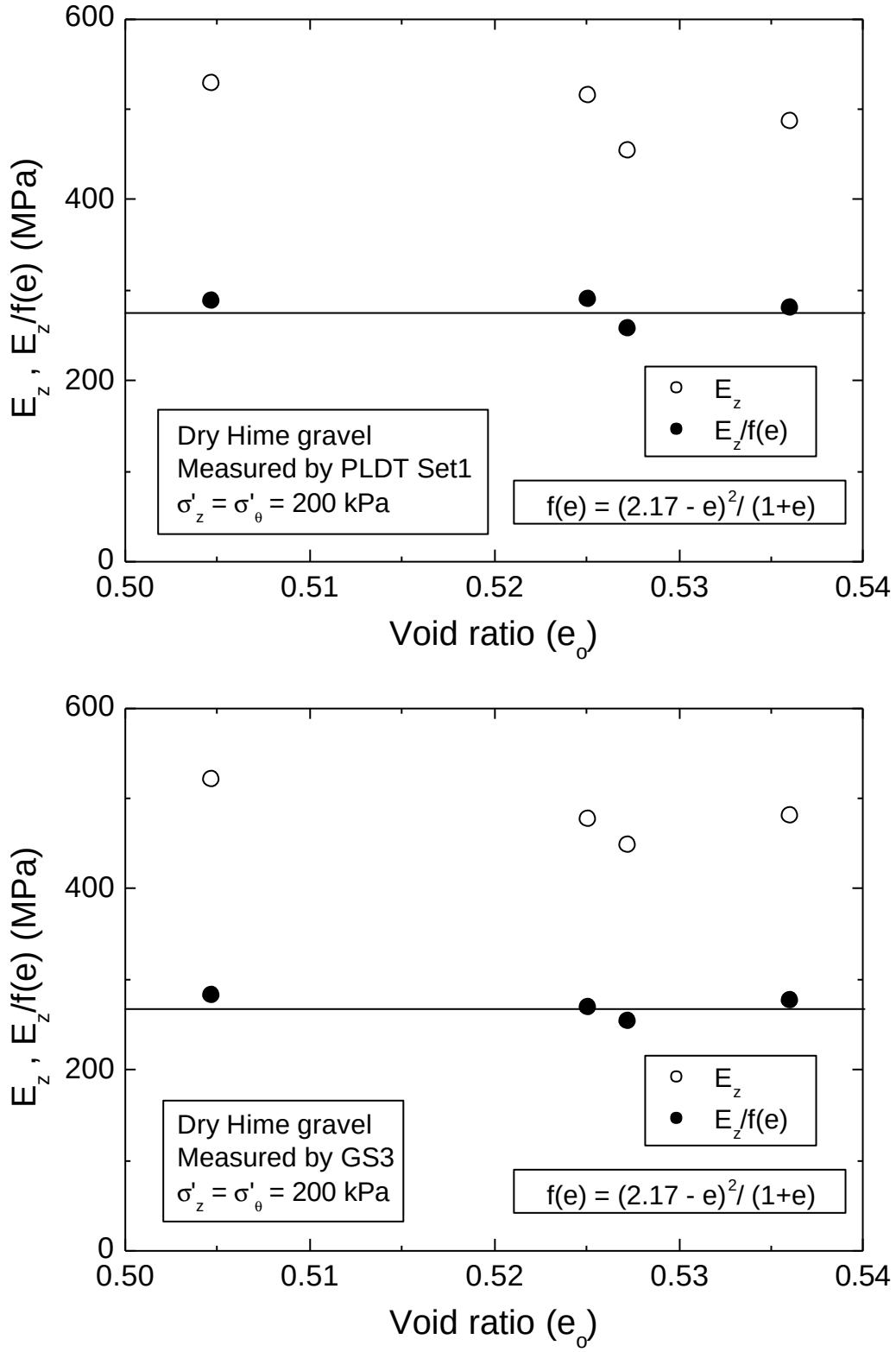

Fig. A.5.8 E_z, $E_z/f(e)$ vs initial void ratio (e_o) at a $\sigma'_z = \sigma'_\theta$ = 200 kPa

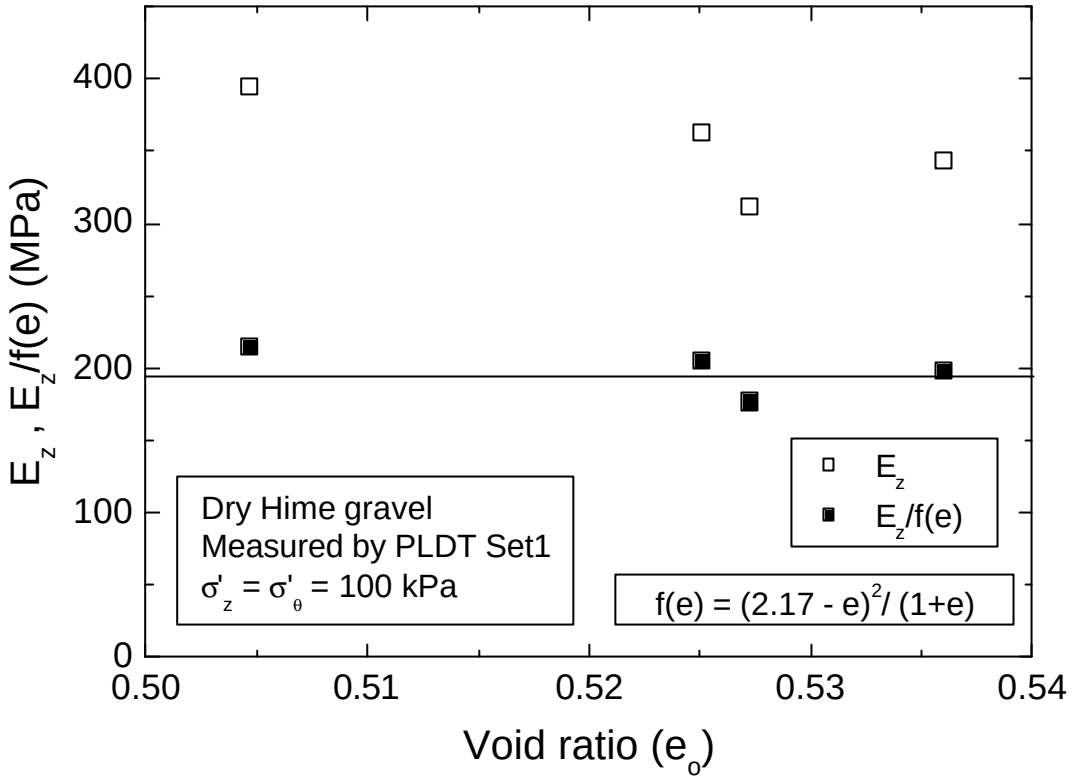

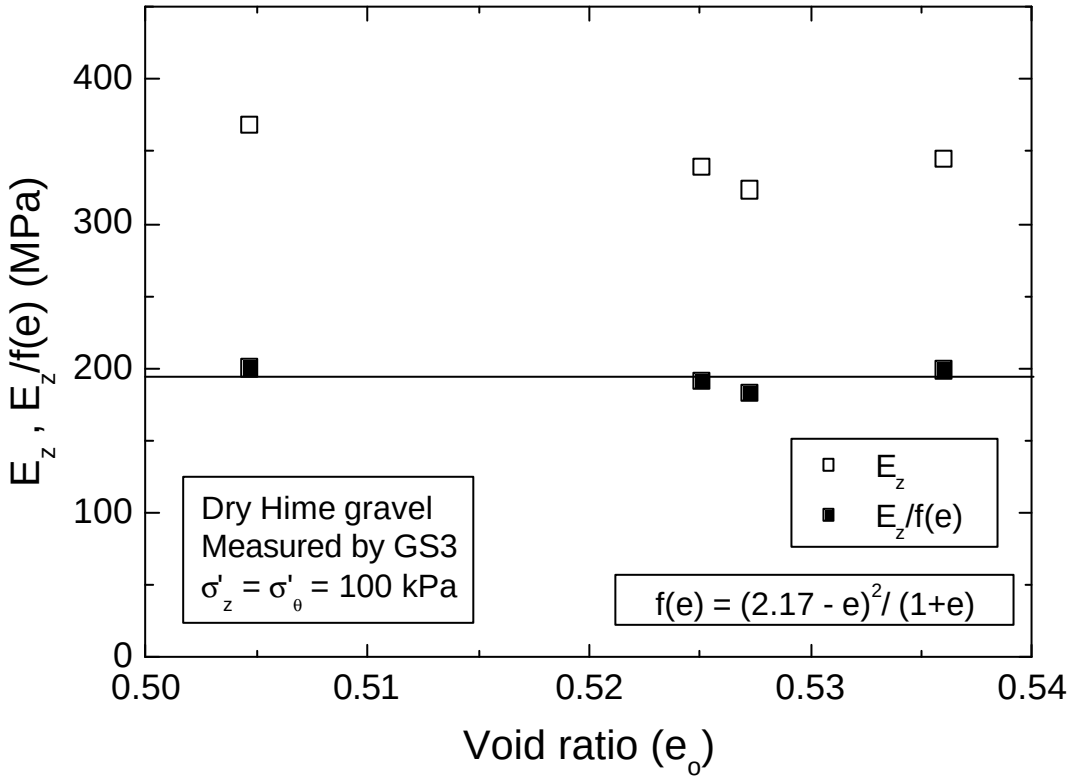

Fig. A.5.9 E_z, E_z/f(e) vs initial void ratio (e_o) at a $\sigma'_z = \sigma'_\theta$ = 100 kPa

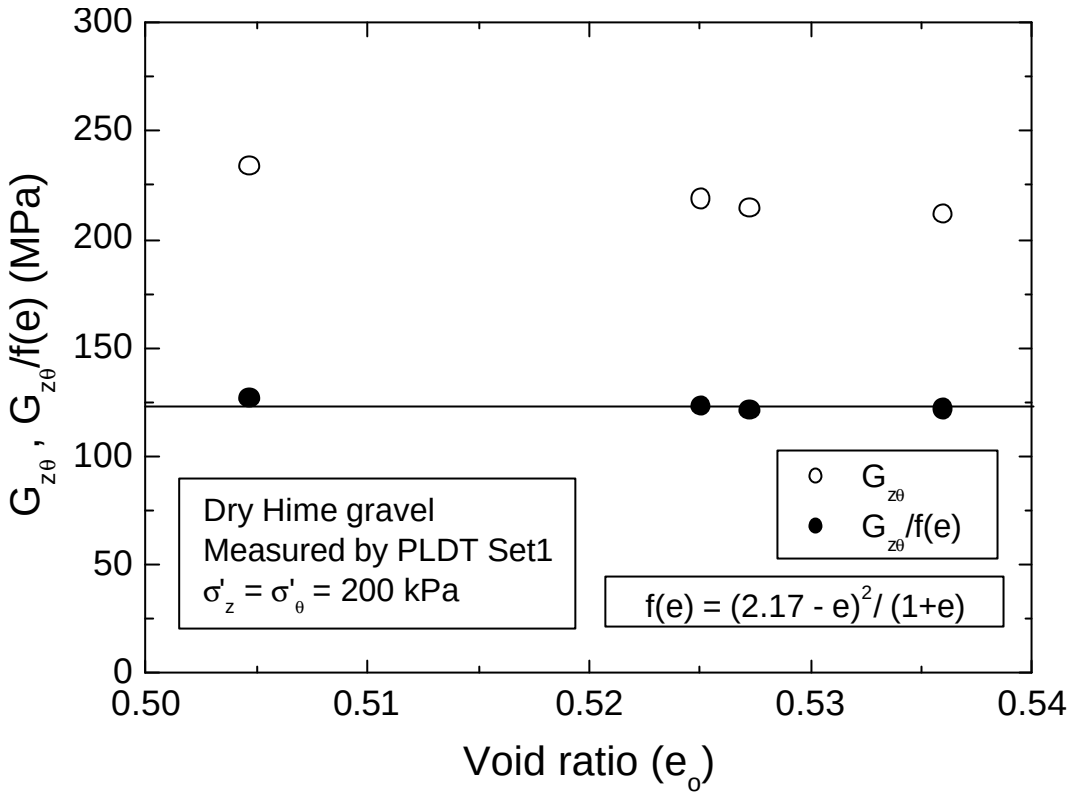

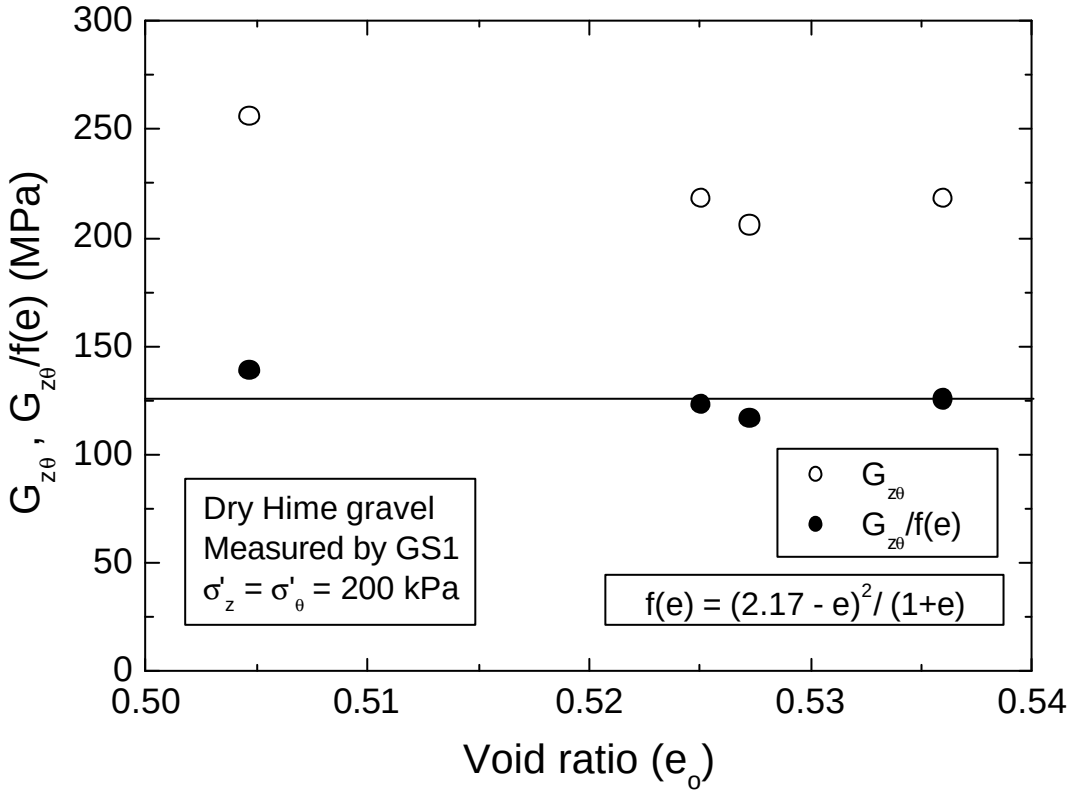

Fig. A.5.10 $G_{z\theta}$, $G_{z\theta}$ /f(e) vs initial void ratio (e_o) at a $\sigma'_z = \sigma'_\theta$ = 200 kPa

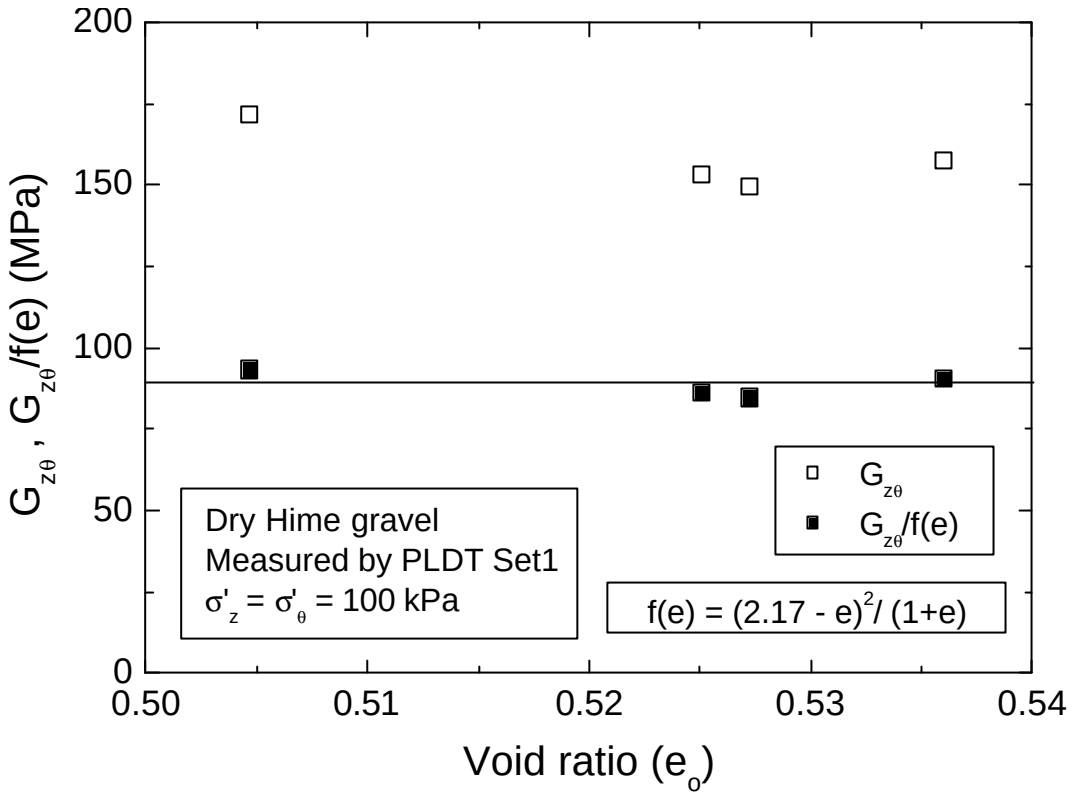

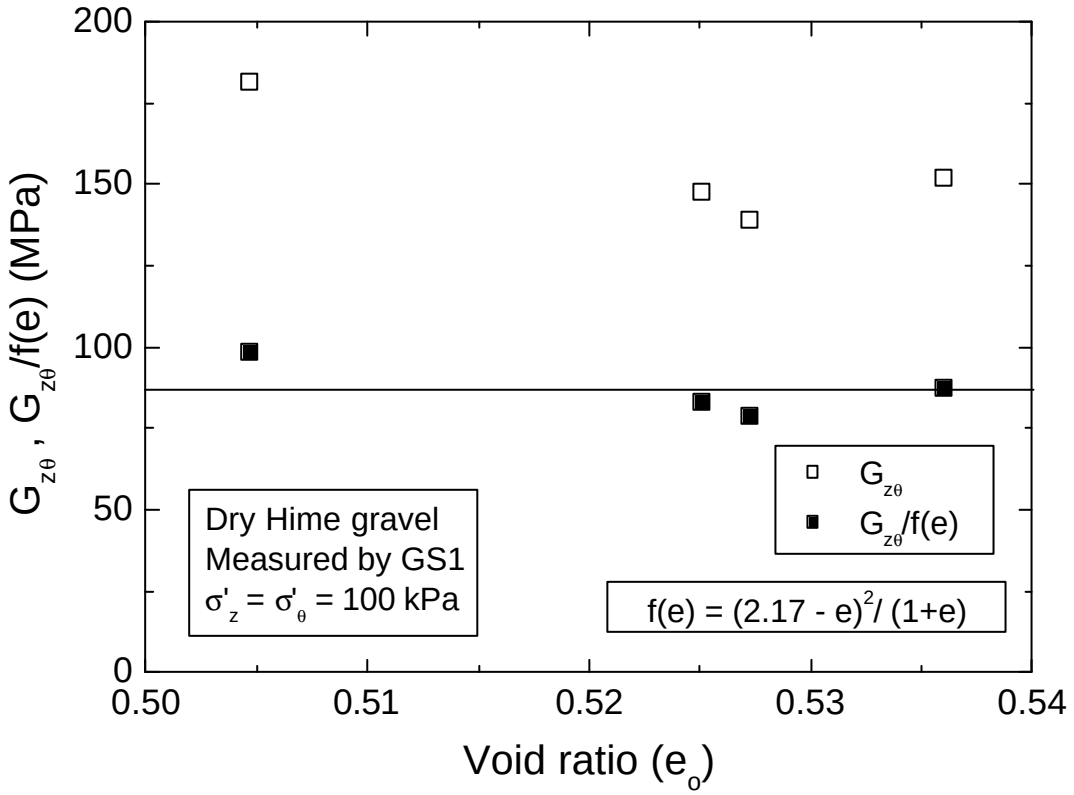

Fig. A.5.11 $G_{z\theta}$, $G_{z\theta}$ /f(e) vs initial void ratio (e_o) at a $\sigma'_z = \sigma'_\theta$ = 100 kPa

Appendix 5.3: $-\Delta\varepsilon_q/\Delta\varepsilon_z$ vs principal stress ratio, $R = \sigma'_z/\sigma'_q$

Fig.A.5.12 through Fig.A.5.15 show $-\Delta\varepsilon_\theta/\Delta\varepsilon_z$ vs principal stress ratio for all the Hime gravel specimens. As described in detail in Appendix 4.4 for Toyoura sand, a similar gradual dilation during triaxial compression was observed in Hime gravel specimens also. Therefore, results of Hime gravel specimens verify the observation that the sudden degradation of shear modulus observed after principal stress ratio become greater than three was not caused by the sudden dilation of the specimen. Some unknown factor seems to be the governing factor for this sudden degradation.

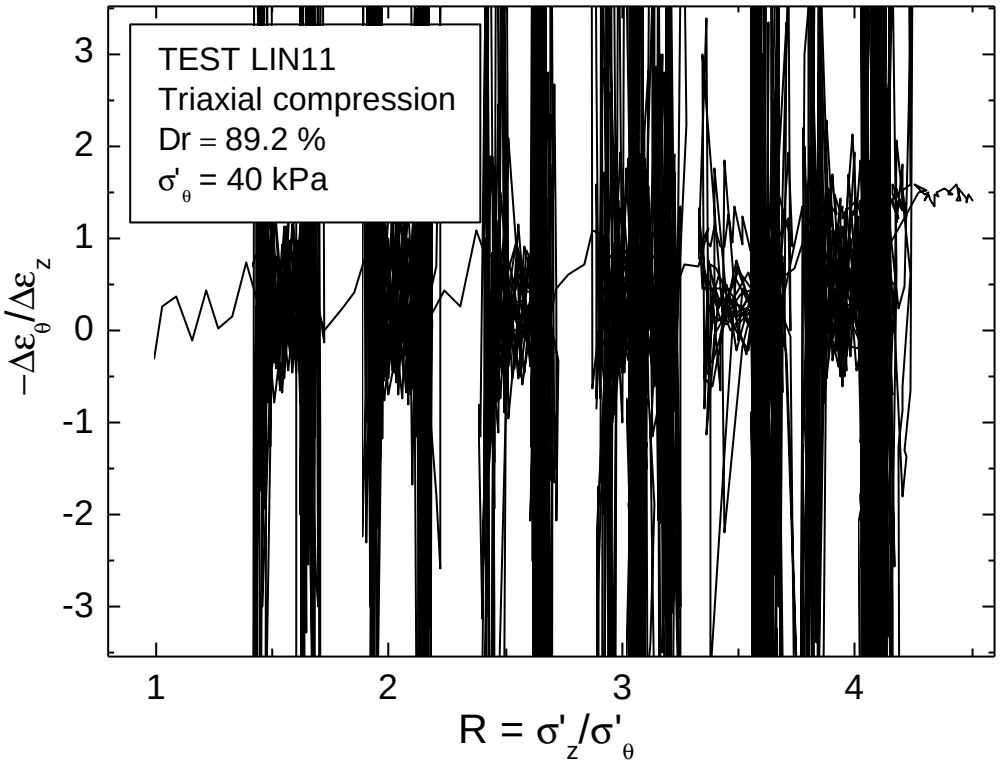

Fig. A.5.12 $-\Delta\varepsilon_\theta/\Delta\varepsilon_z$ vs $R = \sigma'_z/\sigma'_\theta$ for Test LIN11

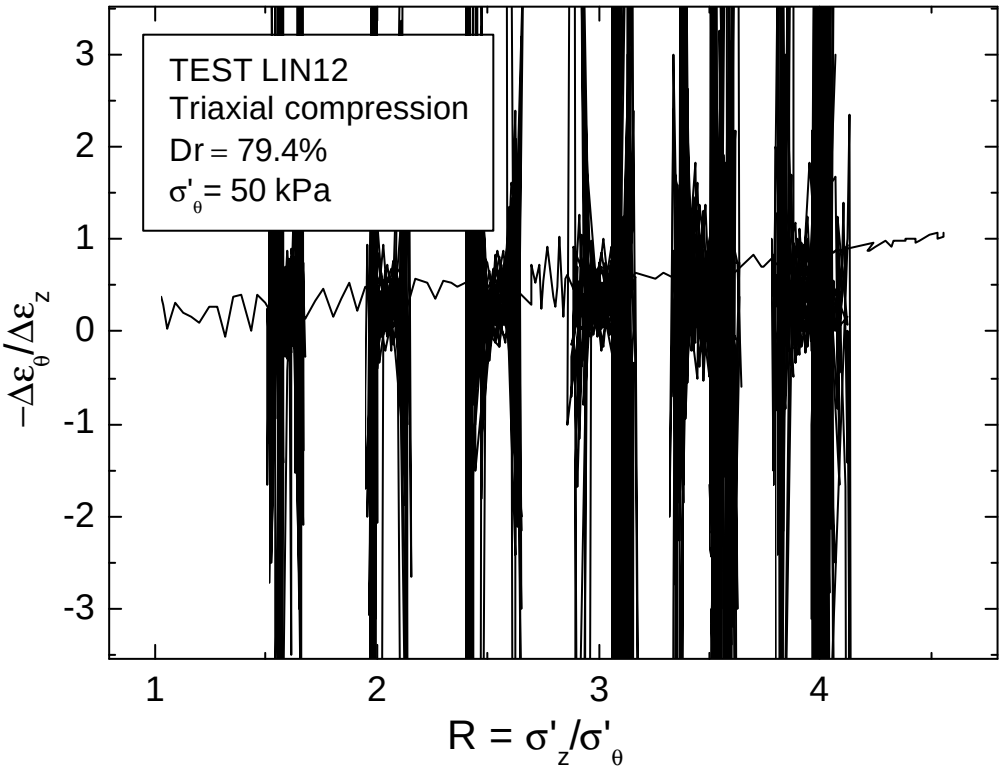

Fig. A.5.13 $-\Delta\varepsilon_\theta/\Delta\varepsilon_z$ vs $R = \sigma'_z/\sigma'_\theta$ for Test LIN12

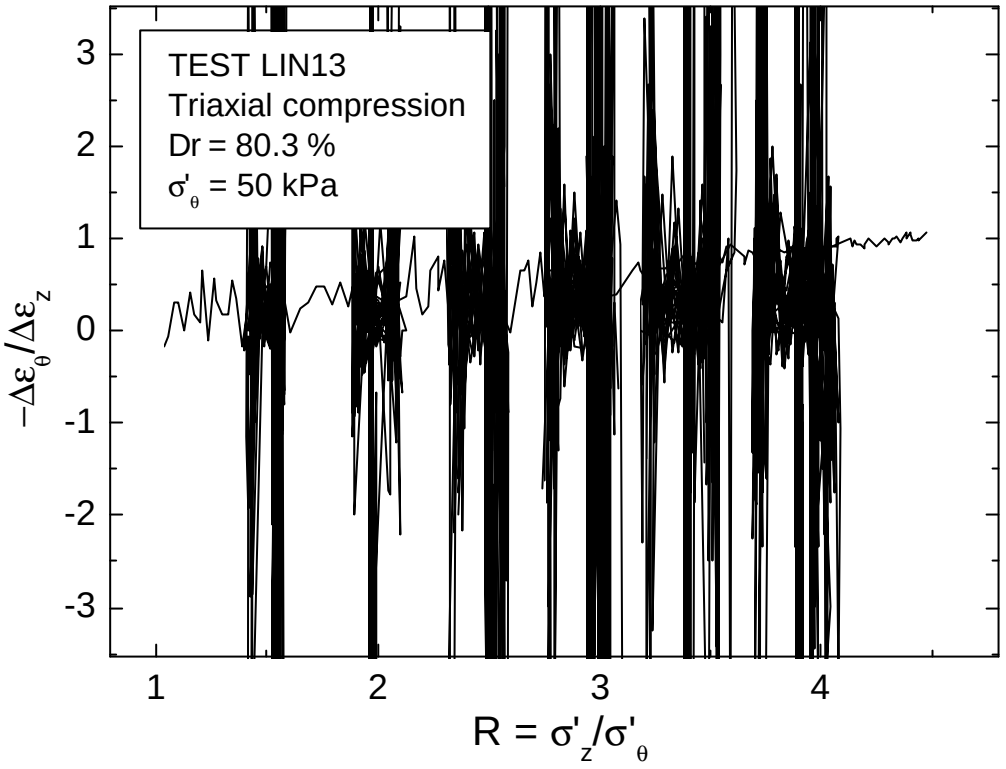

Fig. A.5.14 $-\Delta\varepsilon_\theta/\Delta\varepsilon_z$ vs $R = \sigma'_z/\sigma'_\theta$ for Test LIN13

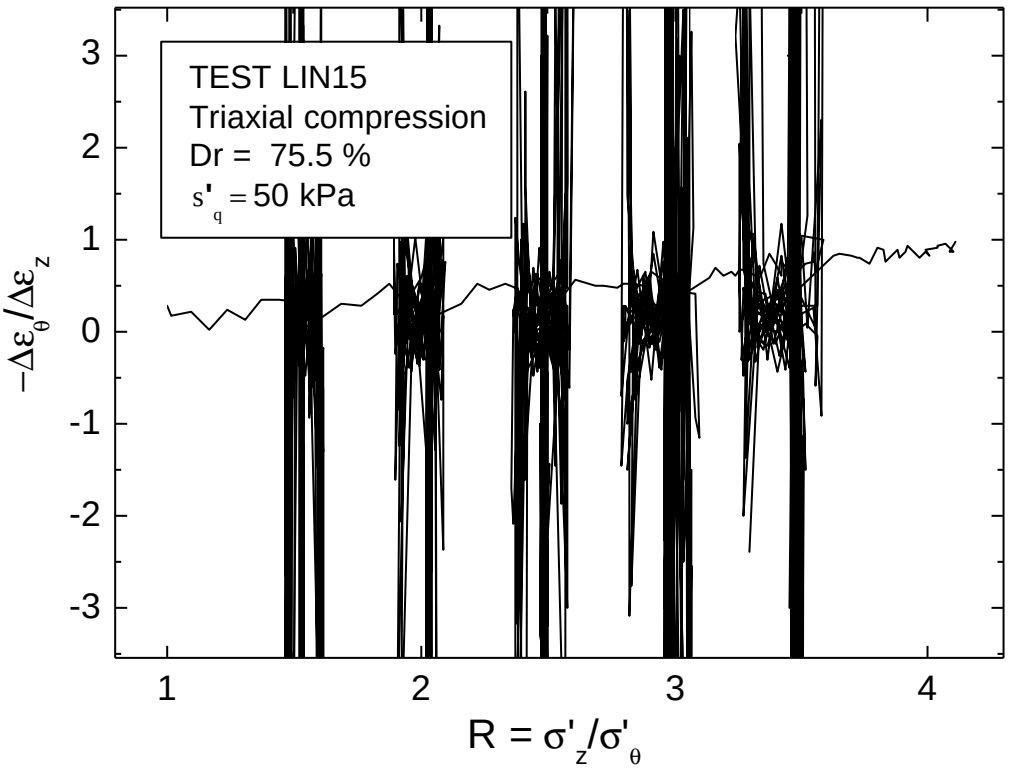

Fig. A.5.15 $-\Delta\varepsilon_\theta/\Delta\varepsilon_z$ vs $R = \sigma'_z/\sigma'_\theta$ for Test LIN15

CHAPTER 6: SIMULATION OF THE SMALL STRAIN BEHAVIOR OF HOLLOW CYLINDER SPECIMENS

6.1 Introduction

As observed experimentally, shear modulus measured locally is on average 10 %- 15 % less than that measured externally, while Young's modulus shows almost similar result between local and external measurements. This phenomenon is attributed to be due to the effects of end restraint. However, the reason why the effects of end restraint could be seen only in shear modulus is still unknown. In order to explain this observation, it would be helpful to simulate the small strain behavior of hollow cylinder specimen in 3-D by taking into account the effects of end restraint. Therefore an attempt was made in this study to simulate the small strain behavior of hollow cylinder sand specimen under vertical and torsional loading by a 3-D elastic analysis.

The dimension of the model specimen for simulation is 15 cm in outer diameter, 9 cm in inner diameter and 30 cm in height. The full model has 6480 elements, as shown in Fig. 6.2. In the radial direction, the model thickness is divided in to 3 layers so that one layer has a thickness of 1 cm. In the circumferential direction, the model is divided into sectors having a central angle of 5 degrees so that there are 72 sectors in total for one radial layer. Full height is divided into 1 cm high hollow cylinders so that there are 30 such cylinders in total. A finite element code named Mudian, which is developed at Research Institute of Takenaka Corporation to model the elastic behaviour of soils in 3-D, was used for the analysis.

The analysis was performed for two cases in order to understand the effect of the blades on the small strain behavior of hollow cylinder specimens, which are attached to the top cap and

the pedestal. In the first case the presence of the blades at the top and bottom layers was not considered and in the second case the presence of six blades each on the top and bottom layers was considered. In each case the model was subjected to vertical and torsional displacement in two steps.

In the first case, the elastic model parameters for vertical loading were selected as follows. E_o = 234 MPa and ν = 0.2 at σ'_o = 10 kPa, isotropy is assumed, then $G_o = E_o/2(1+\nu)$ = 97.5 MPa, and E was expressed as a function of $\sigma'^{0.5}_z$ (Hardin.,1978). In the second case, the presence of stiffer elements was introduced into the model, as shown in Fig. 6.7, by assuming for simplicity that a certain region (0.65 cm to 0.39 cm in width and 1 cm in height) around each blade is stiffened by the presence of the blade. E_o and G_o of the stiffer material was assumed to be 2340 MPa and 975 MPa, which is ten times larger than that of the rest of the elements. On the other hand, the effect of vertical stress on Young's modulus was not considered in the second case. Poisson's ratio is taken as 0.200 and, the initial confining stress is assumed to be zero in both the cases.

First, a vertical displacement of 0.006 mm, which is equal to a vertical strain of 0.002 %, is applied in six equal intervals of 0.001mm to the nodes of the top layer elements. Then, a rotation of 0.00015 rad, which is equal to a shear strain of 0.003 % was applied in five equal steps to the nodes of top layer elements. In order to model the end restraint, bottom layer nodes were fixed in all three directions during vertical and torsional loading. Top layer nodes were fixed in two horizontal directions during vertical loading. During torsional loading, horizontal displacement of the top layer nodes was allowed only in the circumferential direction. Vertical direction of the top layer nodes was fixed during torsional loading. Evaluation of vertical and shear strains after application of displacements to the model in both the cases is depicted in section 6.2.

6.2 Evaluation of local and external strains of the model

The same set of equations that were employed for evaluating local strains using PLDTs were used to evaluate the local strains of the model. Selection of the coordinate system is shown in Fig. 6.1. Displacements of the hinge points O, A and B in X, Y and Z directions were obtained from the analysis of the 3-D model. Based on these, the new co-ordinates of the hinge points O', A', B' were evaluated, and the lengths O'A', A'B' and O'B' were calculated. Then by using Eq.3-52, Eq.3-56 and Eq.3-58, three local deformations ΔR_o, $\Delta\theta$ and ΔZ_o were evaluated.

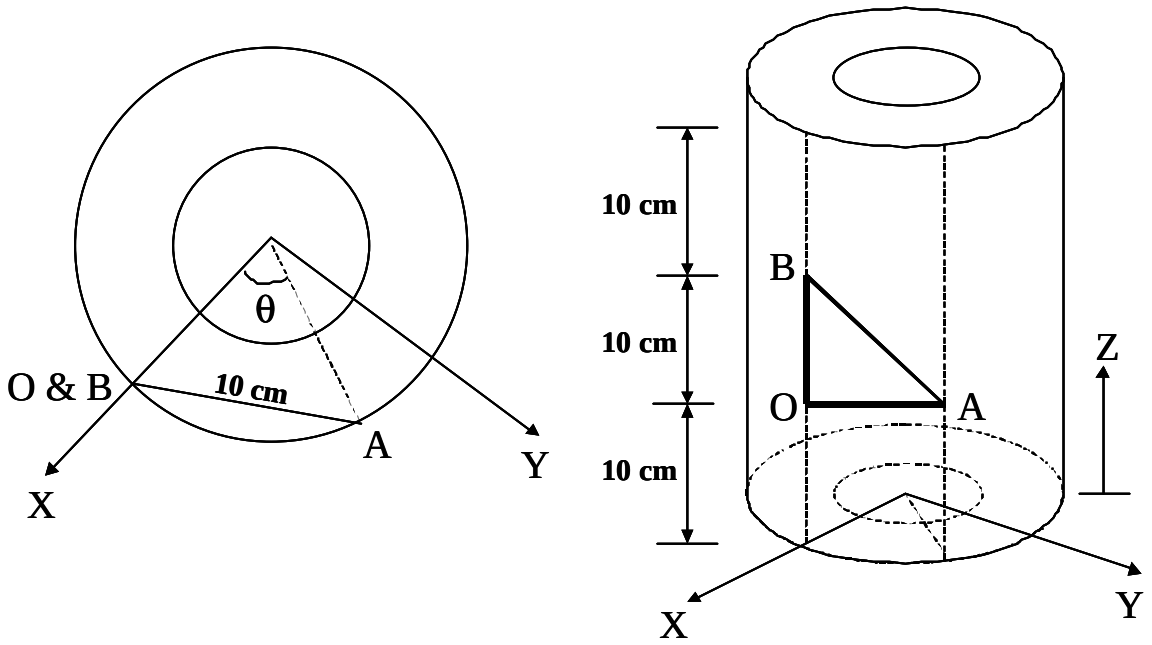

Fig. 6.1 Co-ordinate system of the model specimen

$q_0 = 2 \times sin^{-1}(5/7.5)$

$q_0 = 83.62063^0 = 1.459455 rad$

Initial Co-ordinates of Hinge points O, A and B

$O \equiv (7.5,0,10)$

$B \equiv (7.5,0,20)$

$A \equiv (0.833333,7.453560,10)$

Nodes corresponding to points O, A and B

$O \equiv node10001$

$B \equiv node20001$

$A \equiv node10067.8965$ (between *node* 10065 and *node* 10069)

Note that, point A does not correspond directly to a node. Line OA subtends 83.62063 degrees at the center of the hollow circular cross section of the hollow cylinder model. According to the coordinate system, as shown in Fig. 6.1, node 10065 corresponds to 80 degrees and node 10069 corresponds to 85 degrees. Therefore, a linear interpolation was made between node 10065 and node 10069 to obtain the corresponding node at point A.

Finally, the local strains were obtained by using Eq.3-52, Eq.3-56 and Eq.3-58. They are summarized in Table 6.1.

6.2.1 Evaluation of strains without the blades at the top and the bottom layers (Case 1)

6.2.1.1 Application of vertical loading

Displacements of nodes after application of vertical displacement

Hinge	Node	ΔX (cm)	ΔY (cm)	ΔZ (cm)
O	10001	3.0985E-05	4.9235E-11	-1.9880E-04
B	20001	3.0988E-05	4.9144E-11	-4.0062E-04
A	10067.8965	3.43994E-06	3.076989E-05	-1.988E-04

Coordinates of hinge points after application of vertical displacement

$O' \equiv (7.5 + 3.0985E-05, 4.9235E-11, 10 - 1.9880E-04)$

$B' \equiv (7.5 + 3.0988E-05, 4.9144E-11, 20 - 4.0062E-04)$

$A' \equiv (0.833333 + 3.43994E\text{-}06, 7.453560 + 3.076989E\text{-}05, 10 - 1.988E\text{-}04)$

Then,

$O'A' = 10.0000413$ cm

$O'B' = 9.99979818$ cm

$A'B' = 14.14202212$ cm

ΔR_o, $\Delta\theta$ and ΔZ_o can be evaluated using the following equations

$\Delta R_o = R_{oo}\,(\overline{O'A'}/\overline{OA} - 1) = 3.09734E\text{-}04$ cm

$\Delta q = q_o/2 - \arcsin\{[\overline{A'B'}^2 - \overline{O'B'}^2]\,/\,[4R_o^2 \sin(q_o/2)]\} = 3.12187E\text{-}09$ rad

$\Delta Z_o = [\overline{O'B'}^2 - 2R_o^2(1 - \cos q)]^{0.5} - Z_{oo} = -0.00020182$ cm

Where $R_{oo} = 7.5$ cm, $R_o = 7.5 + 3.0985E-05$ cm and $Z_{oo} = 10$ cm

Evaluation of ε_θ, ε_z and $\gamma_{z\theta}$

$\varepsilon_\theta = \Delta R_o / R_{oo} * 100\,(\%) = 0.000412979$ %

$\varepsilon_z = -\Delta Z_o / Z_{oo} * 100\,(\%) = 0.002018202$ %

$\gamma_{z\theta} = \Delta q * (R_{oo} + R_{io})/2Z_{oo} * 100\,(\%) = 1.87312E\text{-}07$ %, where $R_{io} = 4.5$ cm

$\nu_{z\theta} = \varepsilon_\theta/\varepsilon_z = 0.205$

Externally applied $\varepsilon_z = 0.006/300 * 100\,(\%) = 0.002$ %

Therefore the difference between locally and externally calculated ε_z is 0.9 %

6.2.1.2 Application of torsional loading

Displacements of nodes after application of torsional displacement

Hinge	Node	ΔX (cm)	ΔY (cm)	ΔZ (cm)
O	10001	-2.47E-10	3.74E-04	-6.55E-10
B	20001	-2.84E-10	7.51E-04	-6.08E-10
A	10067.8965	-0.000371805	4.157E-05	-1.34147E-10

Coordinates of hinge points after application of torsional displacement

$O' \equiv (7.5 - 2.47\text{E-}10, 3.74\text{E-}04, 10 - 6.55\text{E-}10)$

$B' \equiv (7.5 - 2.84\text{E-}10, 7.51\text{E-}04, 20 - 6.08\text{E-}10)$

$A' \equiv (0.833333 - 3.718\text{E-}04, 7.453560 + 4.157\text{E-}05, 10\text{-}1.34147\text{E-}10)$

Then,

A'B' = 14.14193743 cm

A'O' = 10.00000007 cm

O'B' = 10.00000001 cm

Using the same equations as in the previous case, ε_θ, ε_z and $\gamma_{z\theta}$ can be evaluated

ε_θ = -2.04448E-06 %

ε_z = 5.15499E-10 %

$\gamma_{z\theta}$ = 0.003008373 %

The externally applied $\gamma_{z\theta}$ = 0.001125/7.5* (7.5 + 4.5)/2/30*100 % = 0.003 %.

The difference between locally and externally calculated $\gamma_{z\theta}$ is 0.28 %.

6.2.2 Evaluation of strains with the blades at the top and the bottom layers (Case 2)

6.2.2.1 Application of vertical loading

Displacements of nodes after application of vertical displacement

Hinge	Node	ΔX (cm)	ΔY (cm)	ΔZ (cm)
O	10001	3.142E-05	2.4851E-10	-1.9772E-04
B	20001	3.142E-05	2.4851E-10	-4.0228E-04
A	10067.8965	3.48965E-06	3.12087E-05	-1.97710E-04

Coordinates of hinge points after application of vertical displacement

$O' \equiv (7.5 + 3.142\text{E-}05, 2.4851\text{E-}10, 10 - 1.9772\text{E-}04)$

$B' \equiv (7.5 + 3.142\text{E-}05, 2.4851\text{E-}10, 20 - 4.0228\text{E-}04)$

$A' \equiv (0.833333 + 3.48965\text{E-}06, 7.453560 + 3.12087\text{E-}05, 10 - 1.97710\text{E-}04)$

Then,

$O'A' = 10.00004188$ cm

$O'B' = 9.99979544$ cm

$A'B' = 14.14202059$ cm

Then the local strains, ε_θ, ε_z and $\gamma_{z\theta}$ can be obtained as follows

Evaluation of ε_θ, ε_z and γ

ε_θ = 0.000418816 %

ε_z = 0.0020456 %

$\gamma_{z\theta}$ = 2.32733E-07 %

$\nu_{z\theta} = \varepsilon_\theta / \varepsilon_z$ = 0.205

Externally applied ε_z = 0.006/300 *100 (%) = 0.002 %

Therefore the difference between locally and externally calculated ε_z is 2.28 %

6.2.2.2 Application of torsional loading

Displacements of nodes after application of torsional displacement

Hinge	Node	ΔX (cm)	ΔY (cm)	ΔZ (cm)
O	10001	-1.26460E-09	3.7213E-04	-4.8425E-10
B	20001	3.6314E-10	7.5287E-04	-4.1707E-10
A	10067.8965	-3.69543E-04	4.13168E-05	-2.45738E-10

Coordinates of hinge points after application of torsional displacement

$O' \equiv (7.5 - 1.26460\text{E-}09, 3.7213\text{E-}04, 10 - 4.8425\text{E-}10)$

$B' \equiv (7.5 - 3.6314\text{E-}10, 7.5287\text{E-}04, 20 - 4.1707\text{E-}10)$

$A' \equiv (0.833333 - 3.69543\text{E-}04, 7.453560 + 4.13168\text{E-}05, 10 - 2.45738\text{E-}10)$

Then,

A'B' = 14.14193483 cm

A'O' = 9.9999998 cm

O'B' = 10.00000001 cm

Using the same equations as in the previous case, ε_θ, ε_z and $\gamma_{z\theta}$ can be evaluated

ε_θ = -2.00084E-06 %

ε_z = 5.79501E-10 %

$\gamma_{z\theta}$ = 0.003047859 %

The externally applied $\gamma_{z\theta}$ = 0.001125/7.5* (7.5 + 4.5)/2/30*100 % = 0.003 %.

The difference between locally and externally calculated $\gamma_{z\theta}$ is 1.595 %.

6.3 Discussion

Distribution of σ'_{zz} and ε_{zz} throughout the model specimen in Case 1 after the application of vertical displacement is shown in Fig. 6.3 and Fig. 6.4, respectively. It can be observed that there is a considerable concentration of stress and strain at the top and bottom layer elements compared to the elements in the other parts of the model. Distribution of stress and strain along the radial direction is also not uniform. The difference of locally and externally evaluated vertical strain in the case without blade elements is 0.91 %. On the other hand, the distribution of σ'_{zx} and ε_{zx}, after the application of torsional displacement as shown in Fig. 6.5 and Fig. 6.6, respectively, shows almost uniform distribution of stress and strain throughout the model specimen. The difference of locally and externally evaluated shear strain is 0.28 %. It is smaller than the difference in vertical strain. This tendency is completely opposite to what we have observed experimentally.

Distribution of σ'_{zz} and ε_{zz} after application of vertical displacement in Case 2 is shown in Fig. 6.8 and Fig. 6.9, respectively. The concentration of σ'_{zz} just beneath and in between the blade elements is significant while ε_{zz} of the blade elements show almost zero vertical strain. The difference of locally and externally evaluated vertical strain in Case 2 is 2.28 %, which is about 2.5 times greater than that of in Case 1. Therefore it can be observed that there is some effect of end restraint on Young's modulus. Fig. 6.10 and Fig. 6.11 show the distribution of σ_{zx} and ε_{zx} in Case 2 after the application of torsional displacement, respectively. As similar to the case without blade elements, it shows almost uniform distribution of σ_{zx} and ε_{zx}. However the difference between the locally and externally evaluated shear strains is 1.595 %, which is about 5.7 times larger than that of in Case 1. Therefore a significant increase in the effect of end restraint on shear strain after the introduction of blades is observed. But still the effects of end restraint on vertical strain is greater than that on shear strain, which is completely the opposite to the tendency observed experimentally. Therefore it seems that the difference of locally and externally measured shear modulus as observed experimentally, cannot be explained only by considering the effects of end restraint alone. It may be necessary to take the concentration of vertical stress and strain after the application of vertical displacement in to account when modeling the torsional behavior of the specimen. This was not considered in the present study.

However, this analysis confirmed that the set of equations used in the original and modified versions of PLDT systems to evaluate ε_θ, ε_z, and $\gamma_{z\theta}$ are correct.

Table 6.1 Local and external strains obtained from simulation

		Local		External	
		e_z (%)	g_{zq} (%)	e_z (%)	g_{zq} (%)
Case 1	Vertical	0.002018202	1.87312E-07	0.002	0.000
	Torsional	5.15499E-10	0.003008373	0.000	0.003
Case 2	Vertical	0.0020456	2.32733E-07	0.002	0.000
	Torsional	5.79501E-10	0.003047859	0.000	0.003

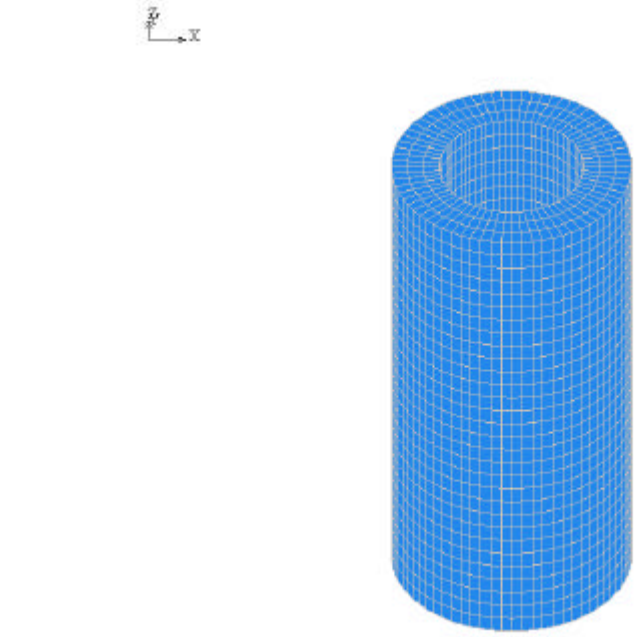

Fig. 6.2 Elements of the model

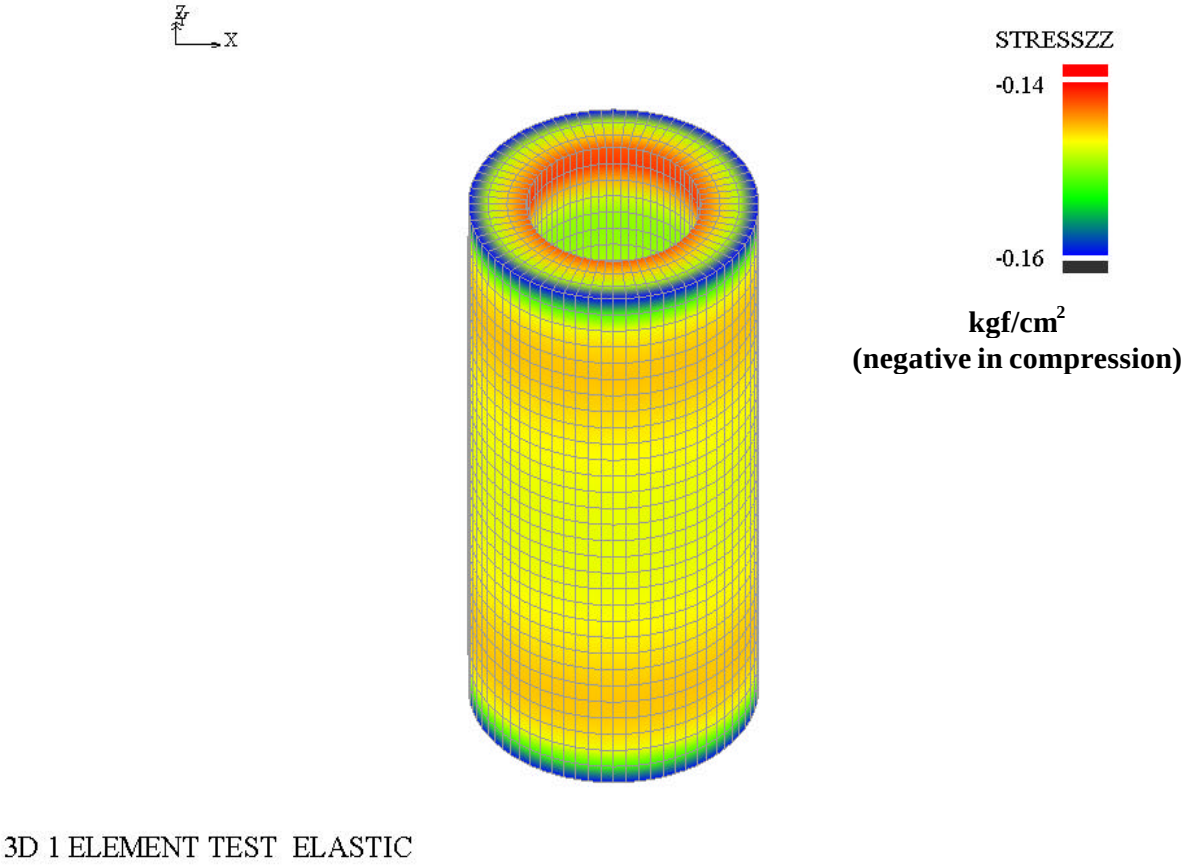

Fig. 6.3 Distribution of σ'_{zz} in Case 1 after application of vertical displacement

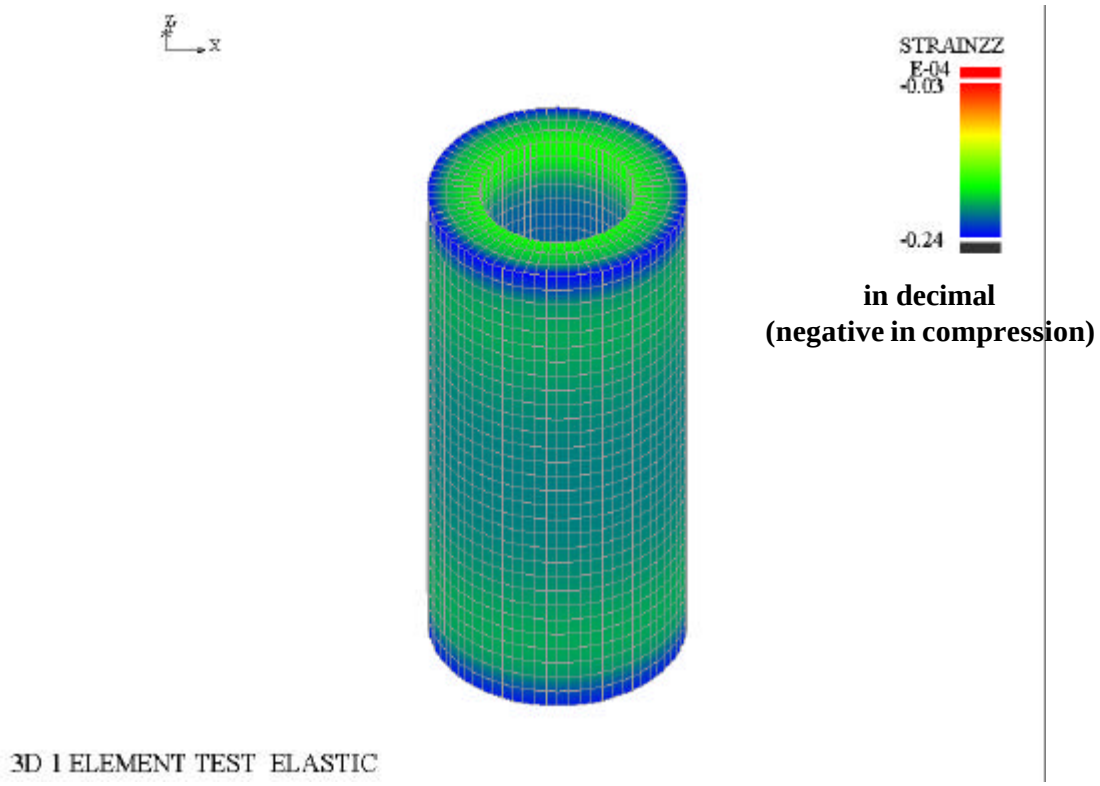

Fig. 6.4 Distribution of ε_{zz} in Case 1 after application of vertical displacement

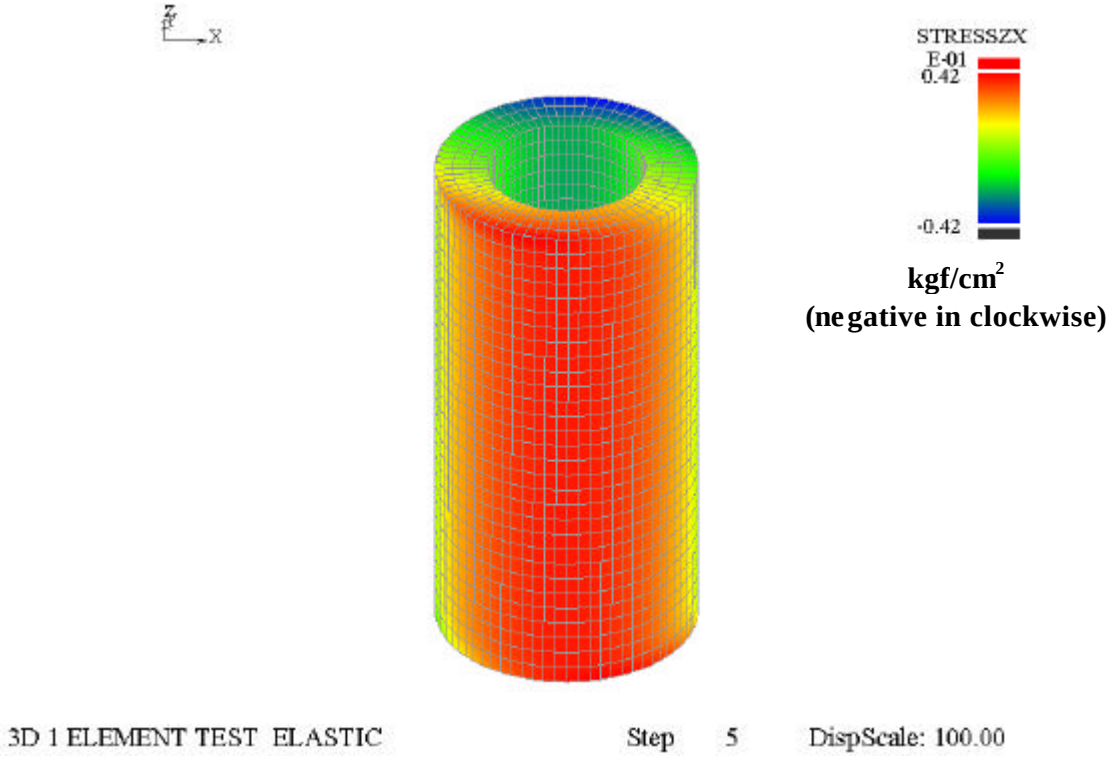

Fig. 6.5 Distribution of σ_{zx} in case 1 after application of torsional displacement

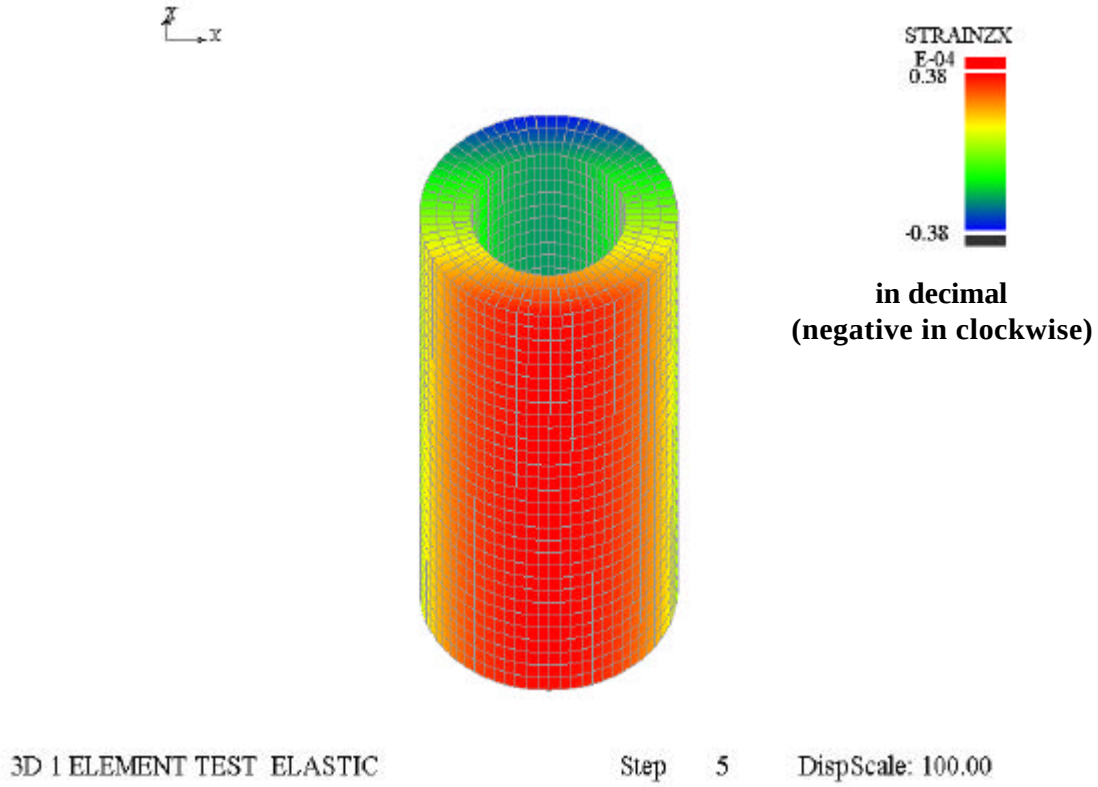

Fig. 6.6 Distribution of ε_{zx} in case 1 after application of torsional displacement

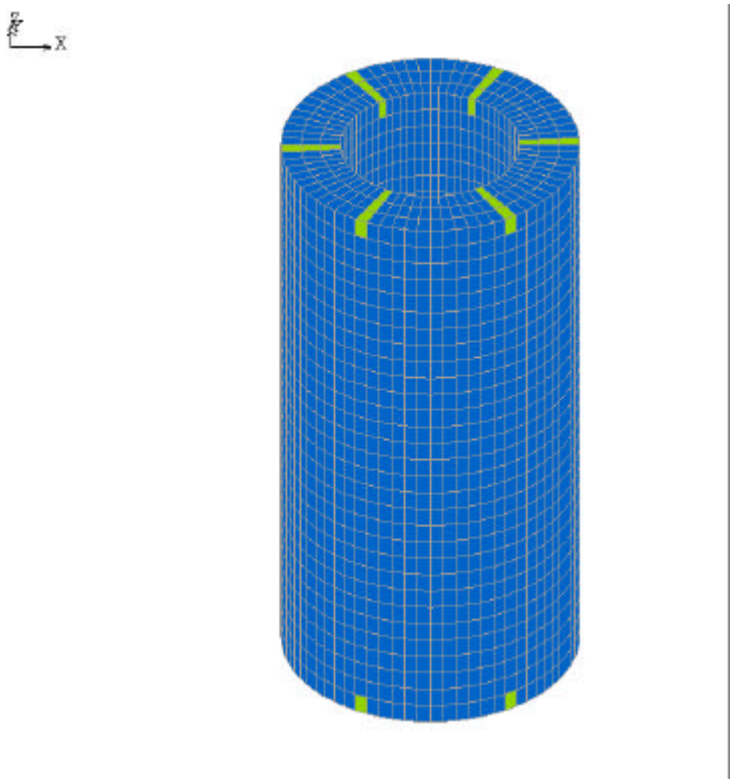

Fig. 6.7 Model with stiffer elements at the top and bottom layers

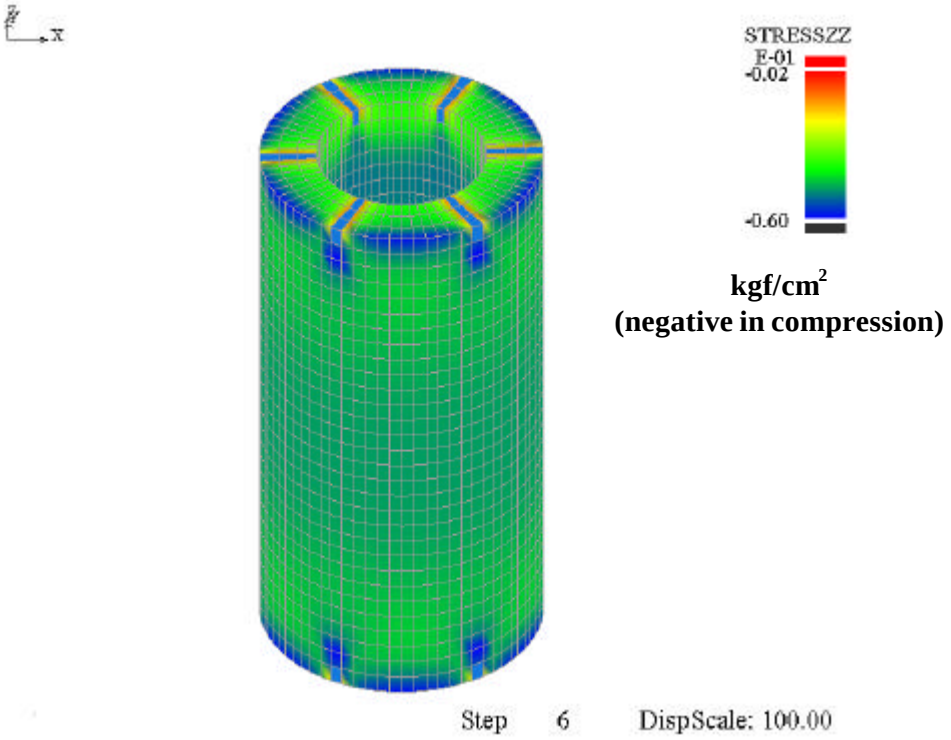

Fig. 6.8 Distribution of σ'_{zz} in Case 2 after application of vertical displacement

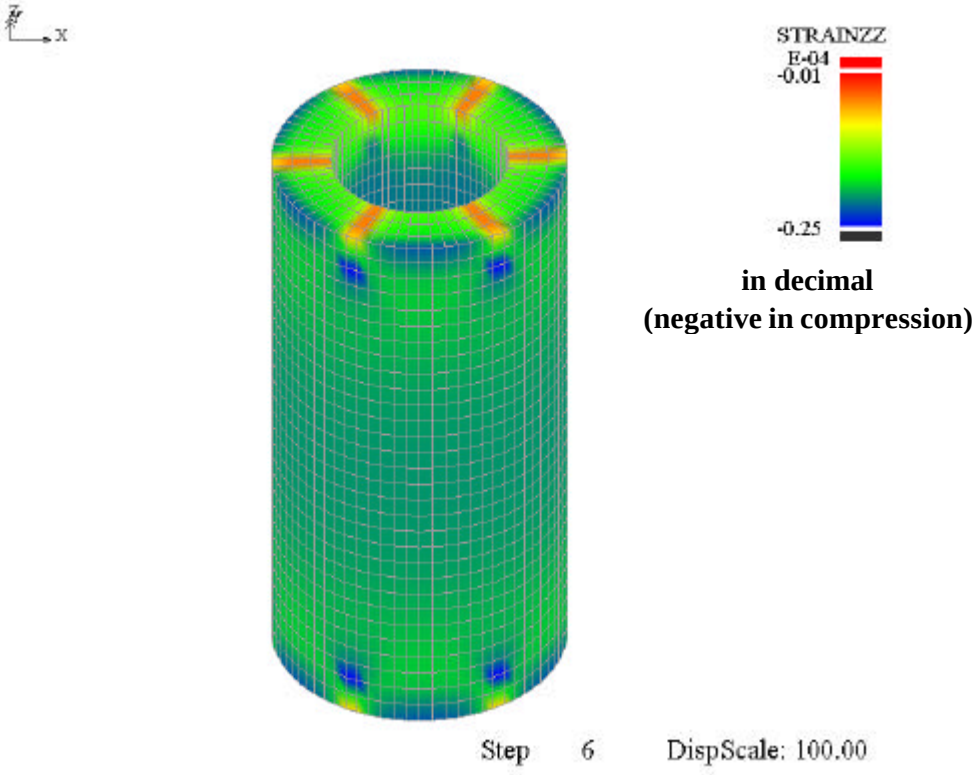

Fig. 6.9 Distribution of ε_{zz} in Case 2 after application of vertical displacement

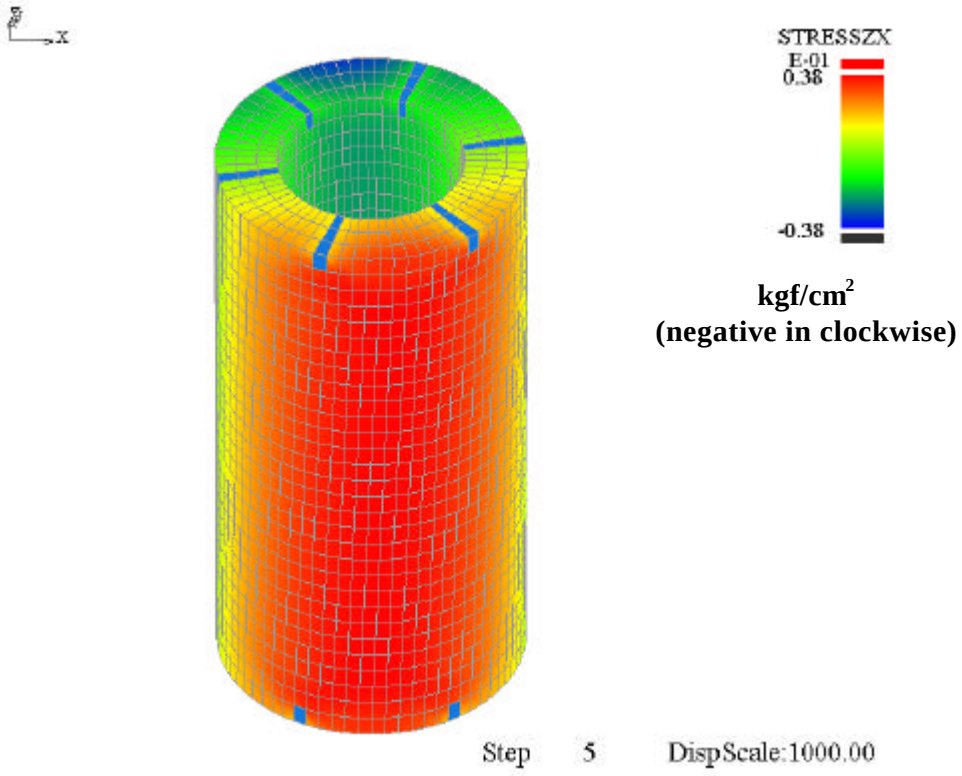

Fig. 6.10 Distribution of σ_{zx} in case 2 after application of torsional displacement

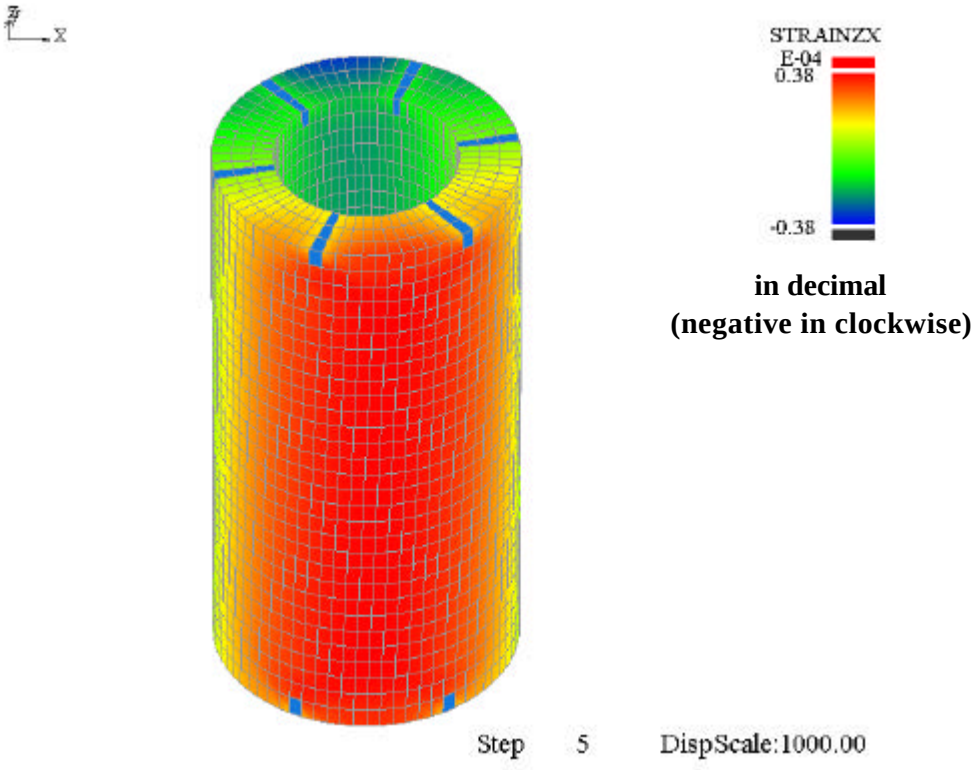

Fig. 6.11 Distribution of ε_{zx} in case 2 after application of torsional displacement

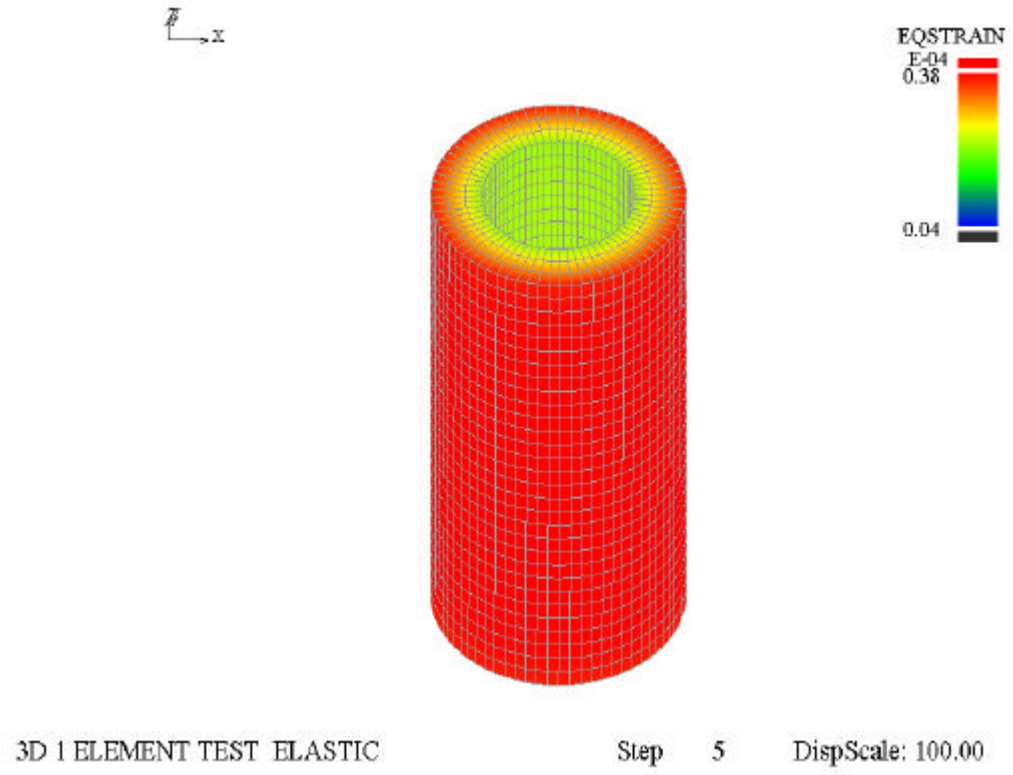

Fig.6.6 Distribution of equivalent strain in Case 1 after application of torsional displacement

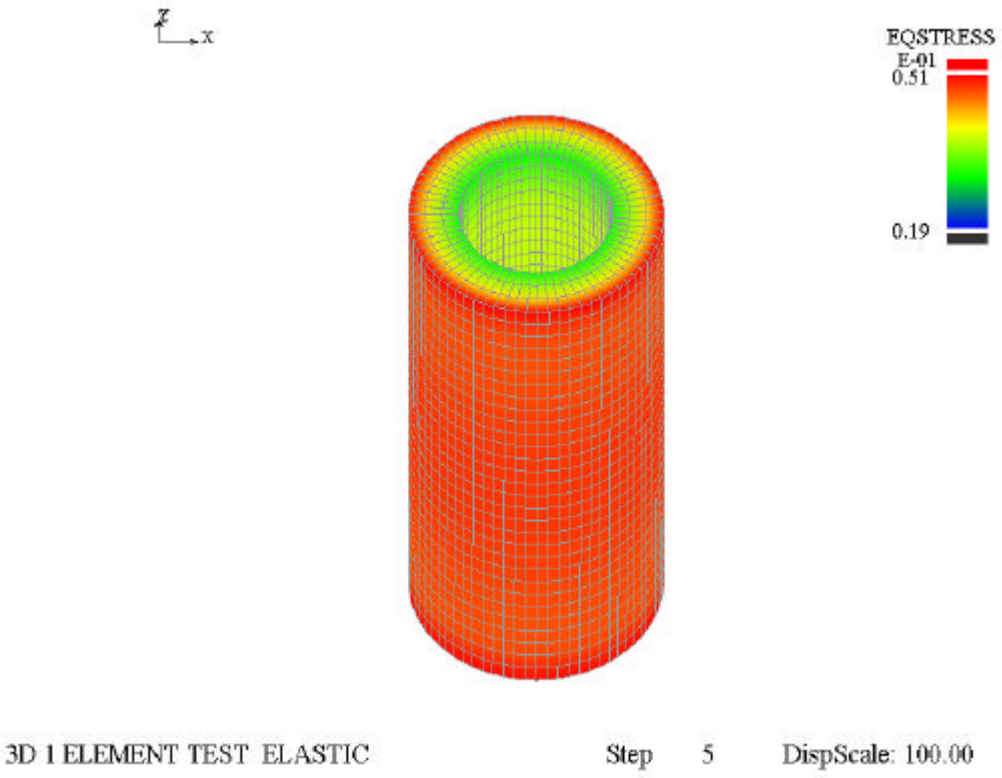

Fig.6.7 Distribution of equivalent stress after application of torsional displacement

7. CONCLUSIONS AND RECOMMENDATIONS

7.1 Conclusions

7.2 Recommendations

7.1 Conclusions

This study is mainly focused on the determination of quasi-elastic and global deformation properties of Dry Toyoura sand and Dry Hime gravel both locally and externally using medium-sized hollow cylinder specimens with different densities.

Local measurement of strains is gaining popularity among the researchers in the geotechnical engineering field due to its closeness to the actual soil deformation. But it should be noted that the application of local strain measurement in hollow cylinder specimens is still very limited due to the presence of technical difficulties like change of measuring direction and curvature of the specimen. Conventional local strain measuring techniques face difficulties in dealing with those.

On the other hand, recently developed Pin-typed Local Deformation Transducer system (Hong Nam and Koseki, 2004) is an effective technique that can deal with the change of curvature and measuring direction of hollow cylinder specimens. In this study, this version of PLDT is referred as the original version of PLDTs. Since it was found that this system was not working properly for specimens with outer diameter less than 20 cm, in the present study, the original version was modified and used for the evaluation of quasi-elastic and global deformation properties of sand and gravel at different densities. The conclusions that can be derived from the results of the present study are depicted below.

- It was confirmed that the modified version of PLDT system could be effectively used to evaluate quasi-elastic and global deformation properties of soil locally. In addition, the modified version of PLDTs offers an improved flexibility in fixing them up on the specimen. Moreover, the reaction forces at the hinges can be greatly reduced by employing the modified version of PLDT system.

- Locally and externally measured Young's modulus of both Toyoura sand and Hime gravel shows almost similar values with an average difference of 2% while that of shear modulus shows an average difference of 15 % in the case of Toyoura sand. This confirms the results of Hong Nam (2004). Conversely, locally and externally measured shear modulus of Hime gravel shows almost similar results. Compared to the width of the top cap and pedestal blades, the size of a Hime gravel particle is large. Therefore the effects of end restraint in Hime gravel may be lesser than that of Toyoura sand. According to the Toyoura sand results, it seems that the effects of bedding error on Young's modulus is not so significant while the effect of end restraint on shear modulus is significant. Blades attached to the top cap and pedestal seemed to be generating non-uniform distribution of shear strain along the specimen during small cyclic torsional loading, yielding a difference between locally and externally measured shear modulus.

- As expected, Young's and shear moduli at a particular stress level are increasing with the increase of density in both materials.

- Among the different void ratio functions proposed in the literature, it was verified that the void ratio function proposed by Harding and Richart for granular particles (1963) is the most appropriate for the comparison of Young's and shear moduli at different densities for both Toyoura sand and Hime gravel. After normalized by the void ratio function proposed by Hardin and Richart for granular particles (1963), results of Young's and shear moduli at different densities show almost unique relationship among each other against their stress levels.

- It was verified that $E_z/f(e)$, $G_{z\theta}/f(e)$ can be expressed as functions of $\sigma'_z{}^m$ and $(\sigma'_z * \sigma'_\theta)^{0.5n}$, respectively. It was confirmed that the locally and externally measured Young's and shear moduli were consistent with each other in terms of their stress state dependency parameters (m and n values) in both Toyoura sand and Hime gravel.

- During triaxial compression, a sudden degradation of shear modulus at principal stress ratio greater than three was observed in Toyoura sand specimens, while Hime gravel specimens show a gradual degradation after principal stress ratio become greater than three. Young's modulus did not show such degradation. This confirms the findings of Yu and Richart (1984). Both local and external transducers show the same tendency of Young's and shear moduli. E/E_{ref} values against stress ratio remains almost close to unity during triaxial compression while G/G_{ref} of all the tests during triaxial compression show a sudden degradation after principal stress ratio three. This is confirming the degradation of shear modulus occurred at principal stress ratios greater than three.

- Young's and shear moduli measured by two PLDT systems at the opposite sides give results almost similar to each other in the case of Toyoura sand while those of Hime gravel show an average difference of 10%. Two vertical gap sensors also show the similar behavior. It should be noted that the Young's modulus values of Hime gravel measured by the PLDT system and gap sensor attached at the same side of the specimen show almost similar results. This suggests possible non-uniformity of Hime gravel specimens caused by the local disturbance during specimen preperation.

- The effect of shear stress on Young's modulus of Toyoura sand at a confining stress of $\sigma_z = \sigma_\theta = 150$ kPa was found to be very small until a shear stress $\tau_{z\theta}$ of 50 kPa and after that a sudden degradation was observed. On the other hand, shear modulus gradually decreased with the shear stress level until a shear stress of 50 kPa, followed by a sudden degradation as observed in Young's modulus. This is possibly due to the damage occurred to the structure after this shear stress level, which corresponds to a principal stress ratio of 2.2. The relationships of E/E_{ref} and G/G_{ref} with $\tau_{z\theta}/\sigma'_\theta$ have a well agreement with that of Hong Nam (2004).

- Preparing a uniform specimen is an important issue in torsional shear testing of soils. In the present study, one Toyoura sand specimen was prepared by pluviting sand in alternative clockwise and anticlockwise directions following the conventional procedure, and the rest of the sand specimens were prepared by pluviating sand particles predominantly and repeatedly in the radial direction, while traveling a

pluviator slowly in the circumferential direction. The traveling of sand from nozzle along the circumferential direction was reversed when each cycle had been completed. Results of the former specimen during isotropic consolidation show a circumferential strain (ε_θ) significantly greater than the vertical strain (ε_z). On the other hand, results of the specimens prepared by pluviating sand in radial direction show a circumferential strain (ε_θ) in the same order as the vertical strain, as observed by Hong Nam (2004). Therefore it can be concluded that the specimens prepared by pluvaiting sand in the radial direction behave more isotropically compared to the specimens prepared by the conventional procedure. In the case of Hime gravel specimens, irrespective of the preperation method, ε_θ and ε_z are found to be in the same order. This may be because the Hime garvel particles are sub-round in shape. Therefore the orientations of the particles are not so relevant for obtaining a uniform specimen as in the case of Toyoura sand.

- Finite element analysis of the small strain behavior of hollow cylinder specimen shows that there is some effect of end restraint on the externally evaluated vertical and shear strains. But the difference in locally and externally evaluated shear strain was not so significant as observed experimentally. This suggests that the effect of end restraint alone is not enough to explain this phenomena and it should be combined with the stress and strain concentration near the top and bottom layers of the model to obtain a more realistic simulation. In addition, it was confirmed from the analysis that the set of equations used in evaluating local strains using PLDTs are correct.

7.2 Recommendations for future research

In spite of the conclusions derived from the present study, a few recommendations can also be made for further investigation.

- Although it is clear that there is a difference in externally and locally measured shear modulus of Toyoura sand, the reason for such difference is still unclear. Therefore it is recommended to test on different materials with different particle shapes and sizes to

further investigate this phenomenon. In addition, modeling the specimen by accurately taking the effects of end restraint and stress concentration into account is suggested.

- Sudden degradation of shear modulus at principal stress ratios greater than three is another issue, which needs further investigation. To understand this, it is recommended to model the quasi-elastic properties by taking into account the damage factors as proposed by Hong Nam and Koseki (2004).

- As stated before, the recently developed medium-sized hollow cylinder apparatus is capable of testing in-situ frozen samples. Therefore examination of the above-mentioned properties and behavior of in-situ frozen samples is strongly suggested. Use of local strain measurement and dynamic methods like bender element and conventional accelerometers in in-situ frozen hollow cylinder specimens is very limited. Thorough investigation of the difference in local and external measurements, comparison of dynamic and static methods, and the sudden degradation of shear modulus at large principal stress ratios in in-situ frozen soils will be helpful in preparing a set of guidelines for soil property characterization for practical applications.

- Effects of the direction of pluviation on specimens made of different materials is another interesting issue. According to the results of the present study, Hime gravel shows no effect on the direction of pluviation. It is assumed that this is because the shape of Hime gravel particles is sub-round. As for verification of this assumption, it is recommended to carryout some tests on specimens with perfectly rounded particles such as glass beads.

- Modelling of plastic volumetric strain under undrained condition and combine it with quasi-elastic modelling of volumetric strain (IIS model, Hong Nam and Koseki, 2004) to obtain an overall understanding of undrain behavior of soil is also left for future.

.

REFERENCES

Anh Dan, L. Q., Effects of Stress History and Time on the Deformation of Gravelly Soil. M.Eng Thesis, Department of Civil Engineering, The University of Tokyo, Japan, 1998.

Burland, J. B., Small is Beautiful- the Stiffness of Soil at Small Strains. Ninth Laurits Bjerrum memorial lecture, Canadian Geotechnical Journal, Vol. 26, 1989. pp. 499-516.

Di Benedetto, H., Geoffroy, H. and Sauzeat, Viscous and Non Viscous Behavior of Sand Obtained from Hollow Cylinder Tests. Advanced Laboratory Stress-strain Testing of Geomaterials, ISBN 90 2651 843 9, 2001, Balkema, pp. 217-226.

Goto, S., Tatsuoka, F., Shibuya, S., Kim, Y.S. and Sato, T., A Simple Gauge for Local Small Strain Measurement in the Laboratory. Soils and Foundations, 31-1, 1991, pp. 169-180.

Hardin, B. O. and Richart, F.E., Elastic Wave Velocities in Granular Soils. Journal of Soil Mechanics and Foundations, ASCE, 89-1, 1963, pp. 33-65.

Hight, D. W., Gens, A. and Symes, M. J. The Development of a New Hollow Cylinder Apparatus for Investigating the Effects of Principal Stress Rotation in Soils. Geotechnique, 33- 4,1983, pp. 255-383.

Hong Nam, N. and Koseki, J., Measurement of Local Strains of Toyoura Sand Using Hollow Cylindrical Specimen. Proceedings of 56th annual meeting of JSCE, 3(A), 2001, pp. 60-61.

Hong Nam, N. and Koseki, J., Quasi-elastic Shear Modulus of Toyoura Sand with Local Strain Measurement. Proc. of the Fifth International Summer Symposium, JSCE, Tokyo, 2003, pp. 237-240.

Hong Nam, N., Development of Local Strain Measurement System for Hollow Cylindrical Specimen of Soils Subjected to Torsion and Axial Load. M.Eng Thesis, Department of civil engineering, The University of Tokyo, Japan, 2001.

Hong Nam, N., Locally Measured Deformation Properties of Toyoura Sand in Cyclic Triaxial and Torsional Loadings and Their Modelling. PhD Thesis, Department of Civil Engineering, The University of Tokyo, Japan, 2004.

Hong Nam, N., Sato, T. and Koseki, J., Development of Triangular Pin-typed LDTs for Hollow Cylindrical Specimen. Proceedings of 36th annual meeting of JGS, 2001, pp. 441-442.

Hoque, E., Elastic Deformation of Sands in Triaxial Tests. Ph.D. thesis, Department of Civil Engineering, The University of Tokyo, Japan, 1996.

Hoque, E., Tatsuoka, F., Sato, T., Measuring Anisotropic Elastic Properties of Sand Using a Large Triaxial Specimen. Geotechnical Testing Journal, ASTM, 19-4, 1996, pp. 411-420.

Jardine, R. J., Zdravkovic, L., Provic, E., Panel Contribution: Anisotropic Consolidation Including Principal Stress Axis Rotation: Experiments, Results and Practical Implications.

Kamegai, Y., Deformation Characteristics of sands by Plane Strain Compression Tests. M.Eng Thesis, Department of Civil Engineering, The University of Tokyo, Japan, 1994 (In Japanese)

Koseki, J., Kawakami, S., Nagayama, H., Sato, T., Change of Small-Strain Quasi-elastic Deformation Properties during Undrained Cyclic Torsional Shear and Triaxial Tests of Toyoura Sand. Soils and Foundations, 40-3, 2000, pp. 101-110.

Mimura, M., Characteristics of Some Japanese Natural Sands- Data from Undisturbed Frozen Samples. Characterization and Engineering Properties of Natural Soils, ISBN 90 5809 537 1, 2003, Balkema, pp. 1149-1168.

Saada, A. S., Hollow Cylinder Torsional Devices: Their Advantages and Limitations. State of the Art Paper. In Advanced Triaxial Testing of Soil and Rock, ASTM STP 977, Donaghe, R., T., Chaney, R. C. and Silver, M. L. (eds.), ASTM, 1988, pp. 766-795.

Santucci de Magistris, F., Koseki, J., Amaya, M., Hamaya, S., Sato, T. and Tatsuoka, F., A, Triaxial Testing System to Evaluate Stress-Strain Behaviour of Soils for Wide Range of Strain and Strain Rate. Geotechnical Testing Journal, ASTM, 22-1, 1999, pp. 44-60.

Scholey, G. K., Frost, J. D., Lo Presti, D. C. F. and Jamiolkowski, J., A Review of Instrumentation for Measuring Small Strains during Triaxial Testing of Soil Specimen. Geotechnical Testing Journal, ASTM, 18-2, 1995, pp. 137-156.

Tatsuoka, F., Jardine, R. J., Lo Presti, D., Di Benedetto, H. and Kodaka, T., Characterizing the Pre-Failure Deformation Properties of Geomaterials. Theme Lecture for the Plenary Session No.1. Proc. of XIV IC on SMFE, Hamburg,Vol. 4, 1997, pp. 2129-2164.

Tatsuoka, F., Shibuya, S., Kuwano, R., Recent Advances in Stress-Strain Testing of Geomaterials in the Laboratory – Background and History of TC – 29 for 1994 – 2001-. Advanced Laboratory Stress-Strain Testing of Geomaterials, ISBN 90 2651 843 9, 2001, Balkema, pp. 1-12.

Tatsuoka, F., Sonoda, S., Hara, H., Fukushima, S., Pradhan, T. B. S., Failure and Deformation of Sand in Torsional Shear. Soils and Foundations, 26-4, 1986, pp. 79-97.

Yu, P. and Richart, F.E., Jr., Stress Ratio Effects on Shear Modulus of Dry Sands. Journal of Geotechnical Engineering, ASCE, 110-3, 1984, pp. 331-345.

APPENDIX

1. Some important considerations in local small strain measurements

There are some important points to mention on the application of the modified version of PLDT system in hollow cylinder specimens. Before making and calibrating PLDTs, there should be an understanding about the size of the specimen, which they are going to be used. Length of the horizontal and diagonal PLDTs can be determined by using the criteria given by Hong Nam (2001). Pinned ends of the PLDTs should be as sharp as possible to avoid any unforeseen friction between the pinned end of the PLDT and conical hole of the hinge.

Electrical noise is a big problem in small strain measurement. The minimum voltage that can be displayed on the digital display is 1 mV. According to my experience there should be at least 8 mV change of voltage needed to get noise free data. Keeping that point in mind, the calibration range of PLDTs can be determined. For example, 0.002 % of vertical strain of a vertically set PLDT of 10 cm in length corresponds to 0.002 mm of vertical displacement. If we assume that this amount of displacement corresponds to a voltage change of 10 mV, taking into account the facts that the range of amplifier is from –5 V to +5 V (10000 mV) and assuming a linear variation of displacement with voltage, the PLDT should be calibrated for a range less than 0.002/10*10000 = 2 mm. A similar approximated calculation can be done for horizontal and diagonal PLDTs as well. When setting the PLDTs, a care should be taken to set them at an initial voltage close of –5 V to take the advantage of the curved nature of the calibration curve. But at the same time it is a must to ensure that the PLDT and hinge has a proper contact because there is a risk that at a voltage close to –5 V the contact between PLDT and the hinge may be lost. Therefore according to my experience the best initial voltage of a PLDT should be within –1.5 V and -2.5 V.

The position of the conical hole in a hinge is another important thing. If the distance between the center of the conical hole and the base of the hinge is large, a large level arm is created and the moment applied by the PLDT to the hinge may be significant. This will affect the measurement of strain at large stress levels. But at the same time there should be some reasonable distance between the center of the conical hole and the base of the hinge to

accommodate horizontal and diagonal PLDTs particularly. This is crucial in the case of horizontal PLDTs. Therefore a special attention should be paid in setting up the horizontal PLDT and it is recommended to set it first. The diagonal PLDT should be set at an angle approximately 45^0 to the horizontal plane to optimize shear strain measurement. If this is not done, the change of length of diagonal PLDT during small torsional cyclic loading may be insufficient to yield a reasonable change of voltage. In addition, it should be ensured that none of the PLDTs are touching the specimen. This might be the case in horizontal and diagonal PLDTs. In order to prevent that a phosphor bronze strip should be glued to the specimen to function as a guide for the horizontal and diagonal PLDTs.

When the modified version of PLDT system is applied for specimens with large particles like gravel, the effect of membrane penetration should be taken into account. For example, Hime gravel has a D_{50} of 1.73 mm and the width of normal hinge base is just 5 mm. Therefore this hinge base is covering just less than 6 gravel particles, in which unusual movement of one particle will affect the whole measurement. Therefore it is recommended to glue a base plate of at least 1 cm * 1 cm to the membrane first and fix the hinge on the base plate. It is better if the base plates have the same curvature as the specimen outer diameter.

2. Some photos of the apparatus, specimen and PLDTs

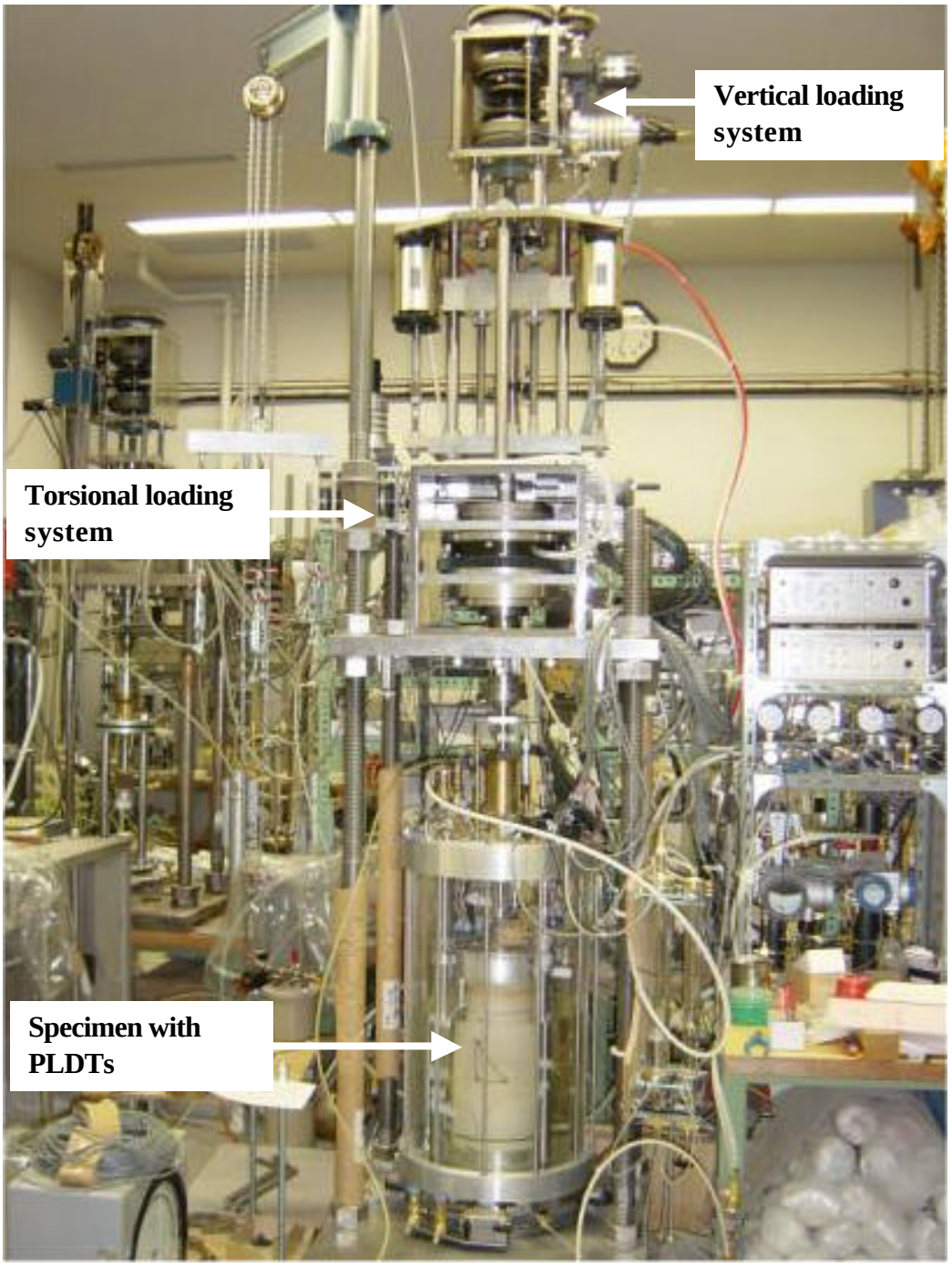

Photo 1. High capacity medium-sized hollow cylinder apparatus

Photo 2. Metal ring and inner membrane

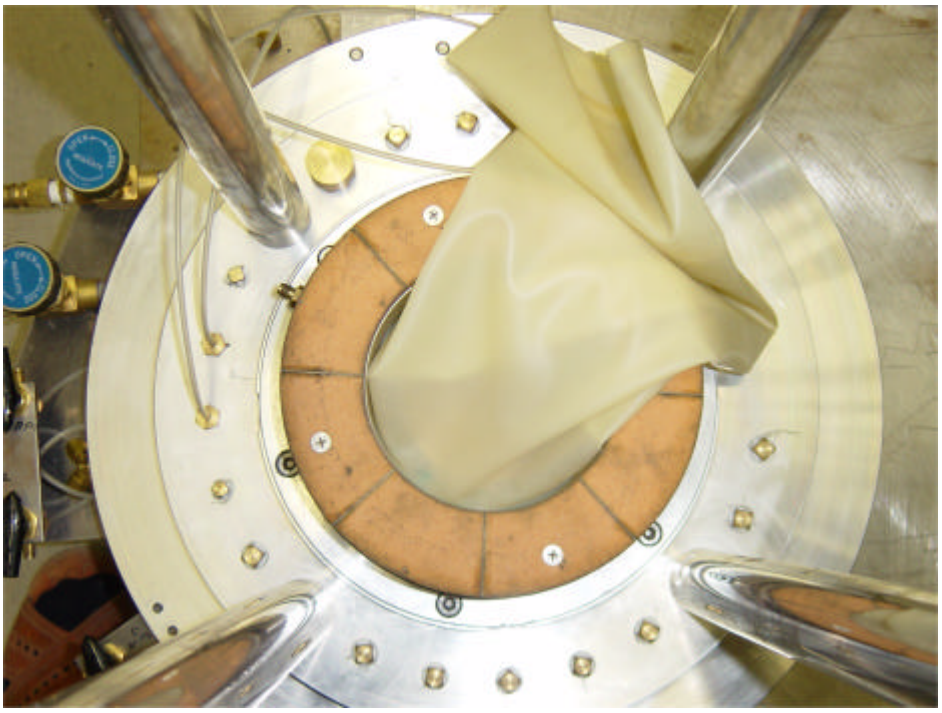

Photo 3. After putting the pedestal over the metal ring

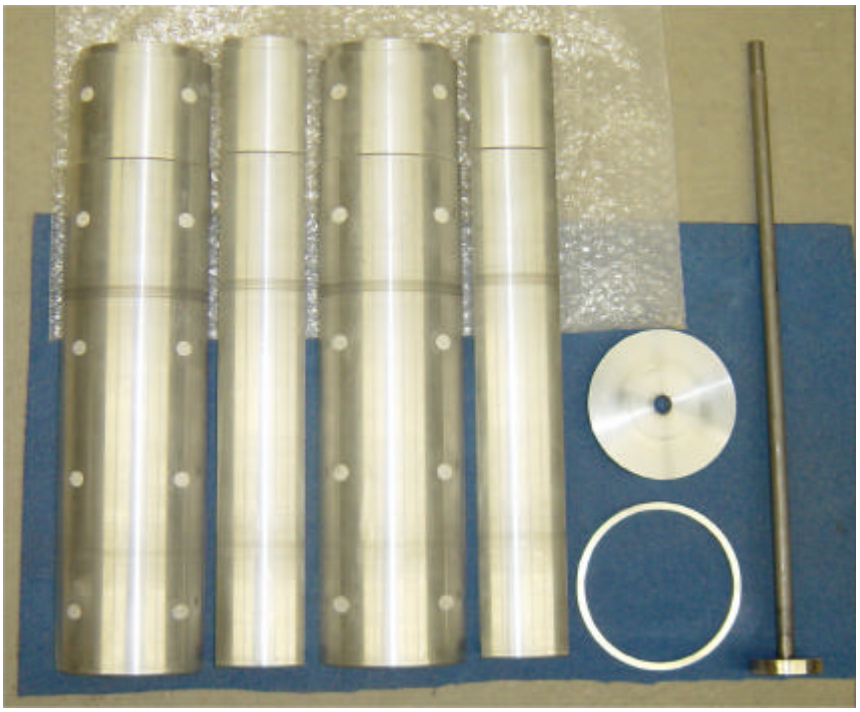

Photo 4. Components of the inner mould

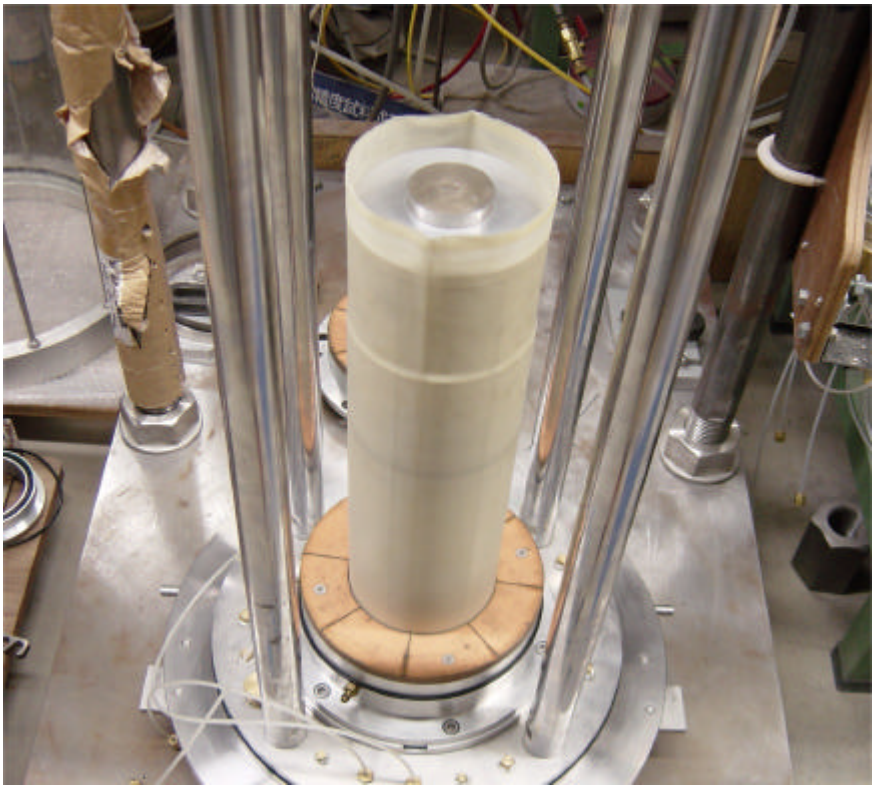

Photo 5. After setting the inner mould

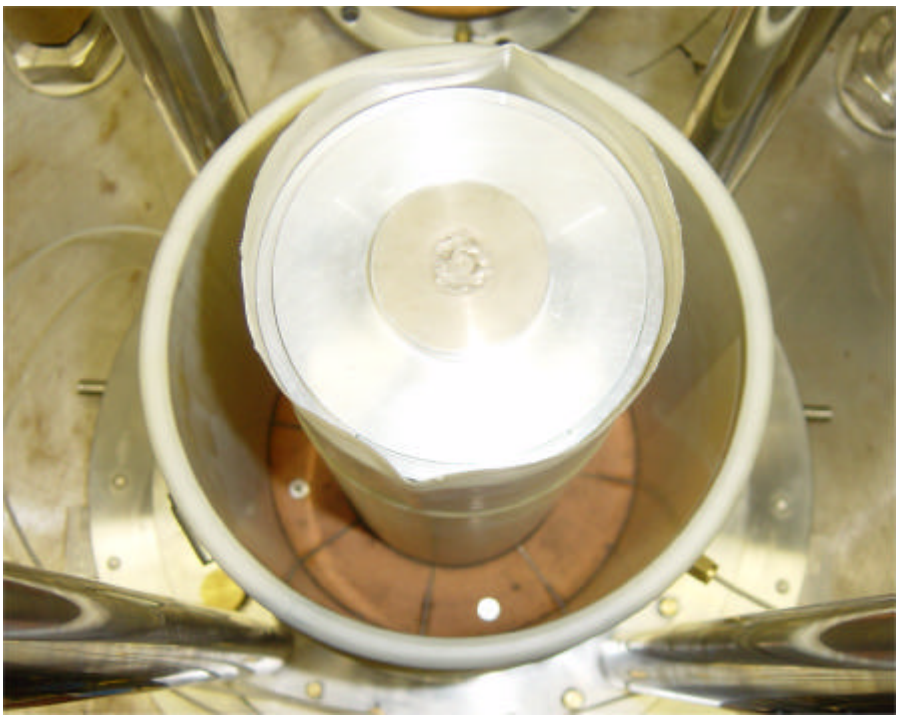

Photo 6. After setting the outer mould

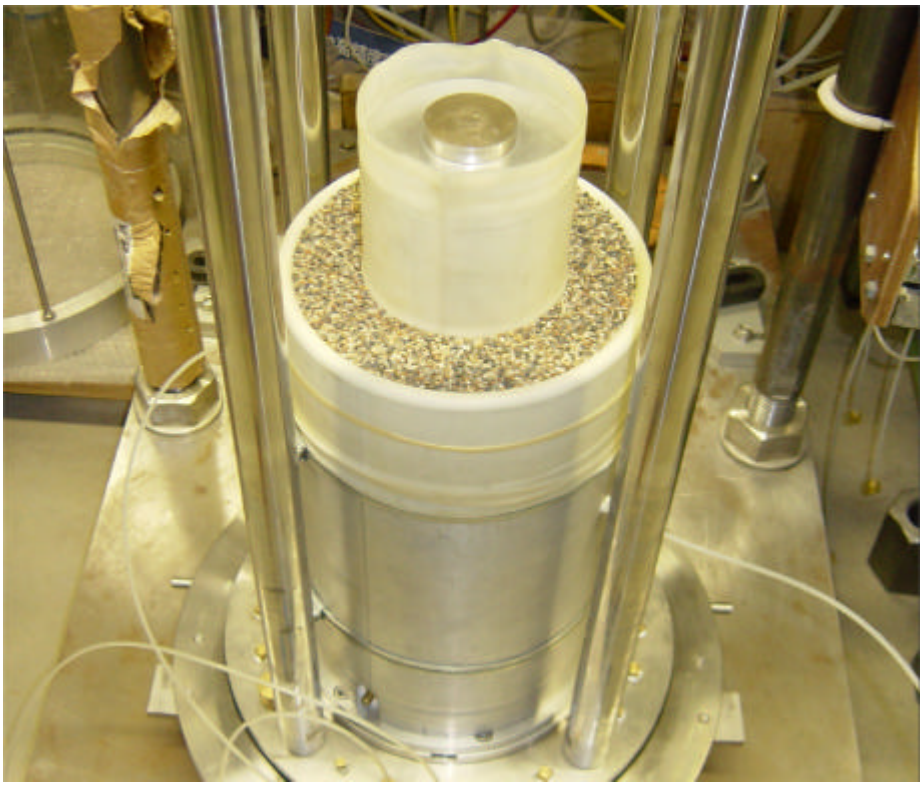

Photo 7. After pluviating gravel into the space between inner and outer moulds

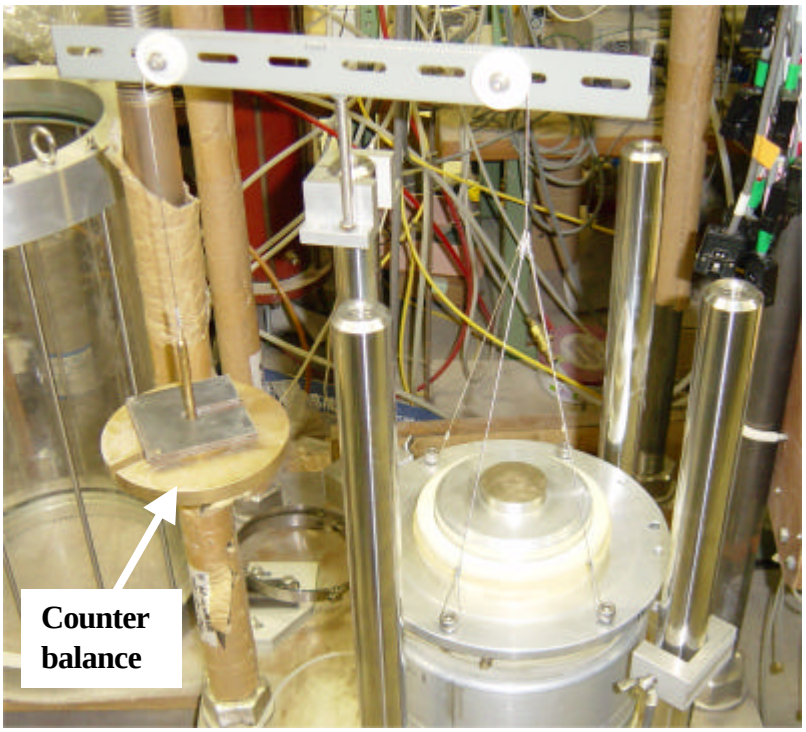

Photo 8. Placing the top cap over the specimen

Photo 9. Specimen under vacuum

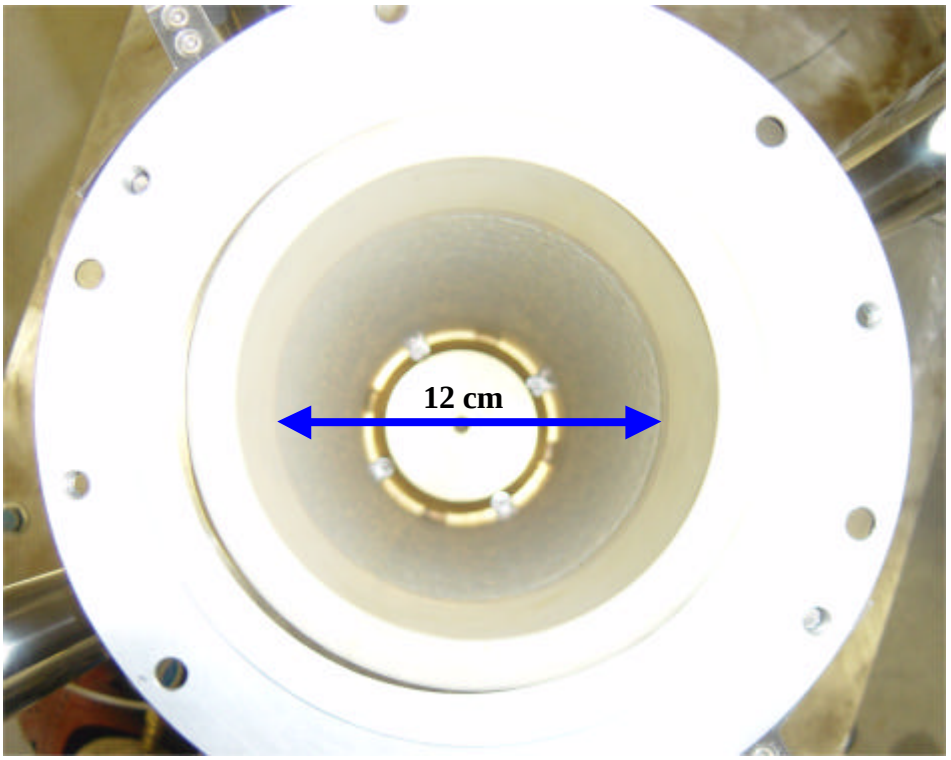

Photo 10. After removing the inner mould

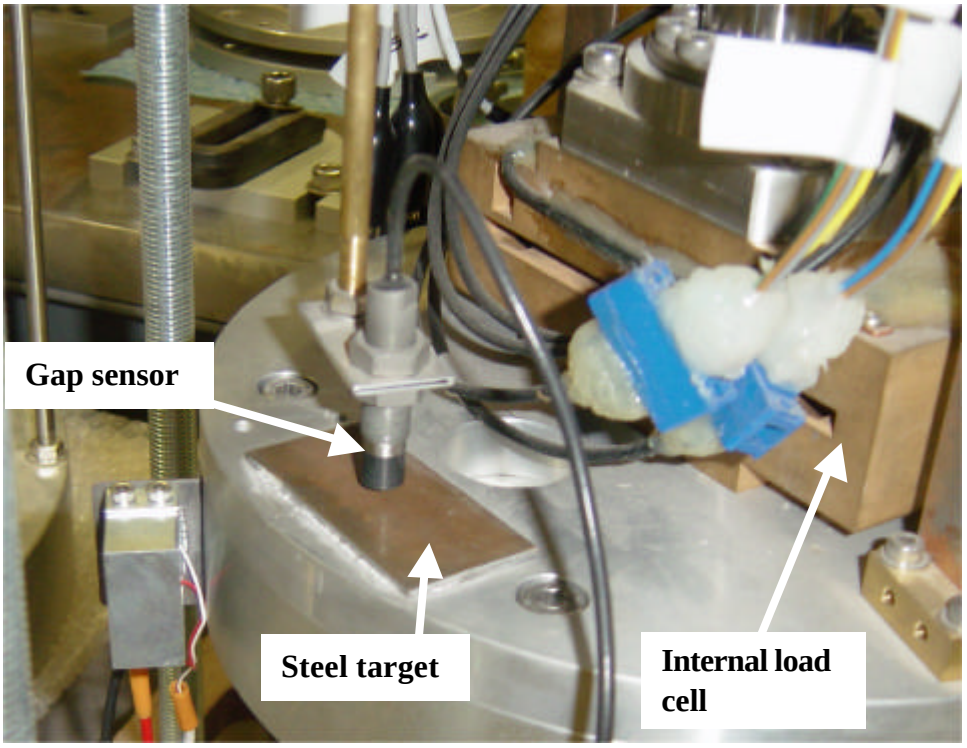

Photo 11. Vertical gap sensor and internal load cell

Photo 12. The original version of PLDTs

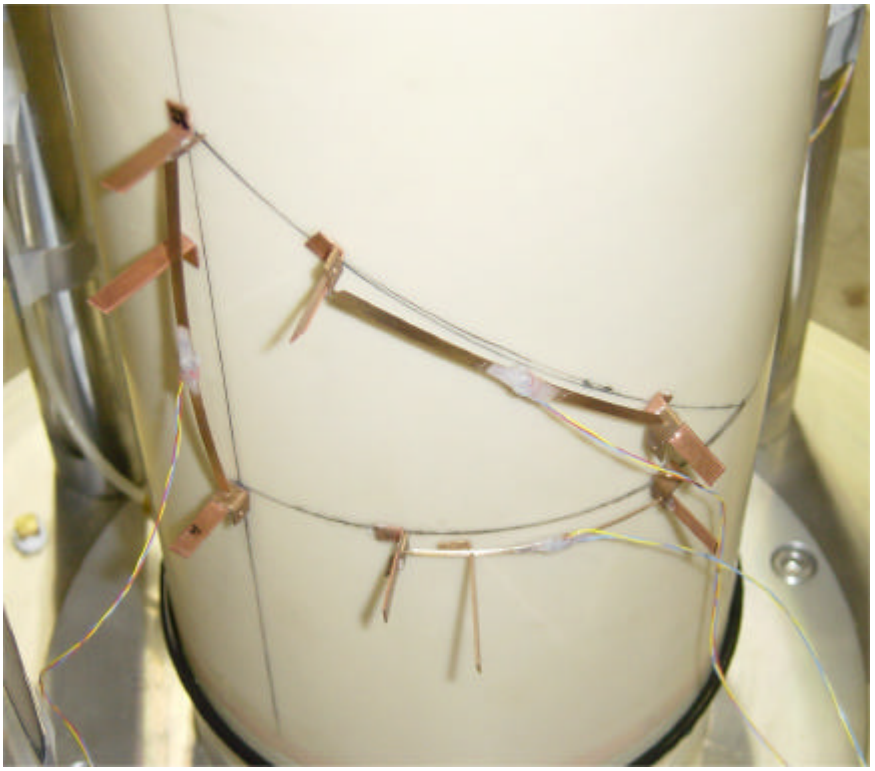

Photo 13. The modified version of PLDTs

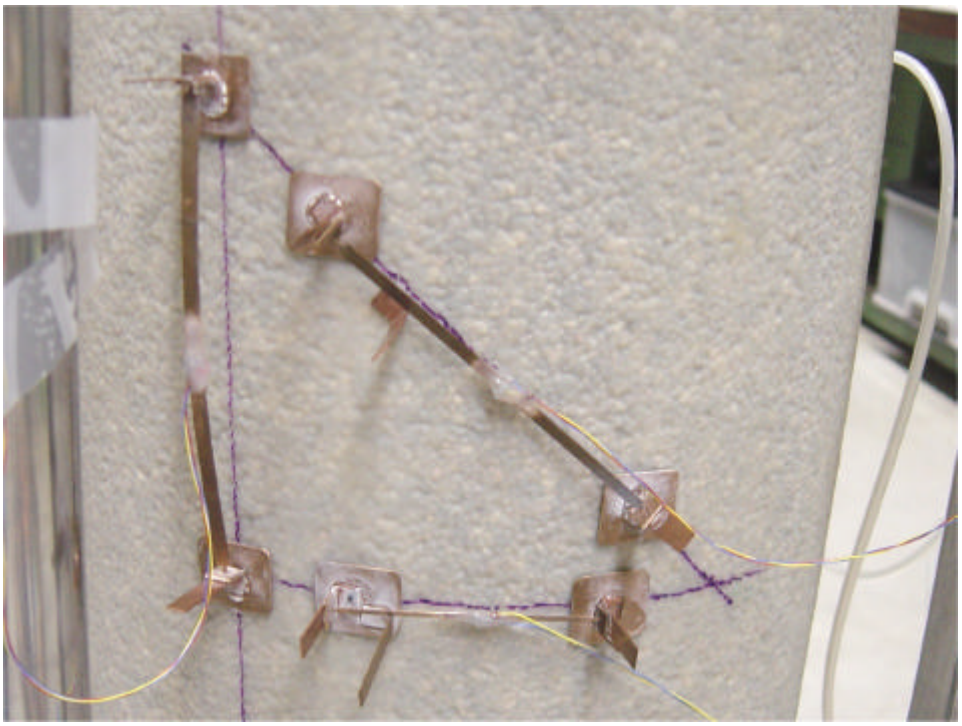

Photo 14. The modified version of PLDTs with base plates

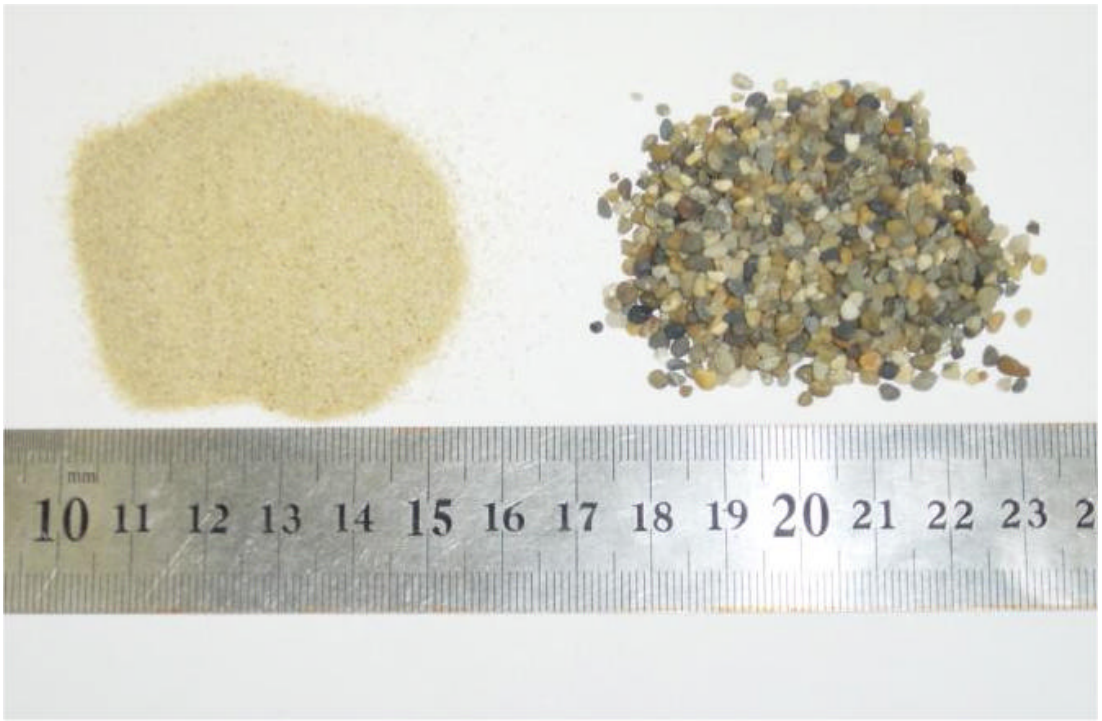

Photo 15. Toyoura sand and Hime gravel